REPORT DOCUMENTATION PAGE

2

Form Approved OMB NO. 0704-0188

1. REPORT DATE (DD-MM-YYYY)	2. REPORT TYPE	3. DATES COVERED (From - To)
08-09-2014	Ph.D. Dissertation	-

4. TITLE AND SUBTITLE	5a. CONTRACT NUMBER
Metal-Organic Framework-Metal Oxide Composites for Toxic Gas Adsorption and Sensing	W911NF-10-1-0079
	5b. GRANT NUMBER
	5c. PROGRAM ELEMENT NUMBER
	611103

6. AUTHORS	5d. PROJECT NUMBER
Katrina Stults	
	5e. TASK NUMBER
	5f. WORK UNIT NUMBER

7. PERFORMING ORGANIZATION NAMES AND ADDRESSES	8. PERFORMING ORGANIZATION REPORT NUMBER
Georgia Tech Research Corporation 505 Tenth Street NW Atlanta, GA 30332 -0420	

9. SPONSORING/MONITORING AGENCY NAME(S) AND ADDRESS (ES)	10. SPONSOR/MONITOR'S ACRONYM(S)
U.S. Army Research Office P.O. Box 12211 Research Triangle Park, NC 27709-2211	ARO
	11. SPONSOR/MONITOR'S REPORT NUMBER(S)
	57995-CH-PCS.14

12. DISTRIBUTION AVAILIBILITY STATEMENT

Approved for public release; distribution is unlimited.

13. SUPPLEMENTARY NOTES

The views, opinions and/or findings contained in this report are those of the author(s) and should not contrued as an official Department of the Army position, policy or decision, unless so designated by other documentation.

14. ABSTRACT

Metal organic frameworks (MOFs) and metal oxide-MOF composites were investigated for adsorption and oxidation of carbon monoxide. Metal oxides were successfully included in MOFs via both impregnation and encapsulation. UiO-66, a zirconium-based MOF, was impregnated with magnesium or cobalt oxide. Cobalt oxide in UiO-66 increases the room temperature CO capacity and shows increased adsorption at 65°C due to strong cobalt-CO interactions. Titania and magnetic nanoparticles were encapsulated in HKUST-1, a copper-based MOF. Including titania in HKUST-1 lowers the CO oxidation onset temperature by over 100°C compared with HKUST-1

15. SUBJECT TERMS

composites MOFs

16. SECURITY CLASSIFICATION OF:			17. LIMITATION OF ABSTRACT	15. NUMBER OF PAGES	19a. NAME OF RESPONSIBLE PERSON
a. REPORT	b. ABSTRACT	c. THIS PAGE			Krista Walton
UU	UU	UU	UU		19b. TELEPHONE NUMBER
					404-894-5254

Metal-Organic Framework-Metal Oxide Composites for Toxic Gas Adsorption and Sensing

ABSTRACT

Metal organic frameworks (MOFs) and metal oxide-MOF composites were investigated for adsorption and oxidation of carbon monoxide. Metal oxides were successfully included in MOFs via both impregnation and encapsulation. UiO-66, a zirconium-based MOF, was impregnated with magnesium or cobalt oxide. Cobalt oxide in UiO-66 increases the room temperature CO capacity and shows increased adsorption at 65°C due to strong cobalt-CO interactions. Titania and magnetic nanoparticles were encapsulated in HKUST-1, a copper-based MOF. Including titania in HKUST-1 lowers the CO oxidation onset temperature by over 100°C compared with HKUST-1, and the composite reaches complete conversion by 250°C. HKUST-1 with magnetic nanoparticles shows enhanced structural stability and increased room temperature adsorption of CO and hexane. MOF-74, an isostructural family with coordinatively unsaturated metal centers of cobalt, magnesium, nickel, or zinc, was investigated for the metal center's impact on stability and adsorption. Pre-treatment conditions to optimize accessibility were found that maximize solvent removal while retaining structural integrity. The impact of air exposure on equilibrium CO capacity was investigated, and these predictions were compared to dynamic conditions, separating CO from nitrogen or air at room temperature. The cobalt analog loses only 25% of its CO capacity with air exposure, retaining higher capacity than the other analogs under ideal conditions. Unlike cobalt, the magnesium analog does not follow the predicted trends with air exposure, having higher dynamic capacities with pre-exposed samples. Under all dynamic conditions, the nickel analog oxidized a portion of the carbon monoxide feed.

METAL ORGANIC FRAMEWORK-METAL OXIDE COMPOSITES FOR TOXIC GAS ADSORPTION AND SENSING

A Dissertation
Presented to
The Academic Faculty

by

Katrina A. Stults

In Partial Fulfillment
of the Requirements for the Degree
Doctor of Philosophy in the
School of Chemical and Biomolecular Engineering

Georgia Institute of Technology
MAY 2014

METAL ORGANIC FRAMEWORK-METAL OXIDE COMPOSITES

FOR TOXIC GAS ADSORPTION AND SENSING

Approved by:

Dr. Krista S. Walton, Advisor
School of Chemical and Biomolecular
Engineering
Georgia Institute of Technology

Dr. Christopher W. Jones
School of Chemical and Biomolecular
Engineering
Georgia Institute of Technology

Dr. Yoshiaki Kawajiri
School of Chemical and Biomolecular
Engineering
Georgia Institute of Technology

Dr. Amyn Teja
School of Chemical and Biomolecular
Engineering
Georgia Institute of Technology

Dr. Z. John Zhang
School of Chemistry
Georgia Institute of Technology

Date Approved: [April 05, 2014]

ACKNOWLEDGEMENTS

TABLE OF CONTENTS

LIST OF TABLES

LIST OF FIGURES

NOMENCLATURE

BDC	Benzene dicarboxylate, benzene dicarboxylic acid, terephthalic acid
BET	Branauer Emmett Teller
BTC	1,3,5-benzenetricarboxylate, 1,3,5-benzenetricarboxylic acid
cc/g	cubic centimeter per gram
$Co(NO_3)_2$	cobalt nitrate
Co_3O_4	cobalt oxide
CPO	coordination polymer of Oslo
$Cu(NO_3)_2$	copper nitrate
CUS	coordinatively unsaturated sites
CVD	chemical vapor deposition
DA	Dubinin-Astakhov
DFT	density functional theory
DMF	n,n-dimethylformamide
DOBDC	dioxybenzenedicarboxylate
dthp	dioxyterephthalic acid
g	gram
H_4DOBDC	2,5-dihydroxyterephthalic acid
HKUST	Hong Kong University of Science and Technology
ICP-MS	inductively coupled plasma mass spectrometry
IGA	Intelligent Gravimetric Analyzer
IRMOF	Isoreticular metal organic framework
K	Kelvin
kJ/mol	kilojoule per mole

m^2/g	square meter per gram
MFC	mass flow controller
$Mg(NO_3)_2$	magnesium nitrate
MgO	magnesium oxide
MIL	Materiaux de Institut Lavoisier
mL	milliliter
mL/min	milliliter per min
MMO	mixed metal oxide
MNP	magnetic nanoparticle
mmol/g	millimole per gram
MO	metal oxide
MOF	metal organic framework
$Ni(NO_3)_2$	nickel nitrate
NOx	nitrogen oxides
NP	nanoparticle
OMS	open metal site
OSHA	Occupational Health and Safety Administration
PEL	permissible exposure limit
PID	proportional-integral derivative
PXRD	powder X-ray diffraction
SEM	scanning electron microscopy
SOx	sulfur oxides
TEM	transmission electron microscopy
TGA-DSC	thermogravimetric analysis-differential scanning calorimetry
TWA	8-hour time weighted average

UiO	University in Oslo
ZIF	zeolitic imidazolate framework
$Zn(NO_3)_2$	zinc nitrate
$ZrCl_4$	zirconium chloride

SUMMARY

Metal organic frameworks (MOFs) and metal oxide-MOF composites were investigated for adsorption and oxidation of carbon monoxide. Metal oxides were successfully included in MOFs via both impregnation and encapsulation. UiO-66, a zirconium-based MOF, was impregnated with magnesium or cobalt oxide. Cobalt oxide in UiO-66 increases the room temperature CO capacity and shows increased adsorption at 65°C due to strong cobalt-CO interactions. Titania and magnetic nanoparticles were encapsulated in HKUST-1, a copper-based MOF. Including titania in HKUST-1 lowers the CO oxidation onset temperature by over 100°C compared with HKUST-1, and the composite reaches complete conversion by 250°C. HKUST-1 with magnetic nanoparticles shows enhanced structural stability and increased room temperature adsorption of CO and hexane. MOF-74, an isostructural family with coordinatively unsaturated metal centers of cobalt, magnesium, nickel, or zinc, was investigated for the metal center's impact on stability and adsorption. Pre-treatment conditions to optimize accessibility were found that maximize solvent removal while retaining structural integrity. The impact of air exposure on equilibrium CO capacity was investigated, and these predictions were compared to dynamic conditions, separating CO from nitrogen or air at room temperature. The cobalt analog loses only 25% of its CO capacity with air exposure, retaining higher capacity than the other analogs under ideal conditions. Unlike cobalt, the magnesium analog does not follow the predicted trends with air exposure, having higher dynamic capacities with pre-exposed samples. Under all dynamic conditions, the nickel analog oxidized a portion of the carbon monoxide feed.

CHAPTER 1

INTRODUCTION

1.1. Metal Organic Frameworks

Metal-organic frameworks (MOFs) are a relatively new class of porous adsorbents that could potentially be used to solve a myriad of separations challenges, ranging from purifying gases for energy production, waste stream remediation, low temperature catalysis, shape- and size-based liquid and gas separations, and air purification. Consisting of metal nodes connected via organic linkers, the theoretical porous structures that can be created are practically endless, and the structures that have been synthesized number in the thousands. The narrow pore size distribution is attractive for size selectivity, and the wide variety of metal centers and functionalized organic linkers that can be used provide the opportunity for designer materials targeting specific molecules.

The highly porous structures have low overall densities. Lightweight materials are attractive for high gravimetric capacities, but this means there is also a relatively low density of active sites. For some applications, the high surface area and small pore sizes provide sufficient non-specific interactions. However, for interactions relying on strong interactions between the adsorbate and the active site, the low active site density coupled with larger pores results in 'wasted' space in the interior of the pore system. Several approaches have been considered to address this issue: selectively choosing metals and ligands to maximize favorable host-guest interactions, such as coordinatively unsaturated metal centers; altering or increasing the functionality of the ligand linkers; creating

interpenetrated networks; and including active guest molecules into the MOF framework.

This work focuses on including metal oxide guest molecules to increase the density of

active sites while maintaining the structural framework and minimally increasing material

weight. Additionally, MOF-74, a family of isostructural MOFs, contains high densities

of active metal sites intrinsically, with the difference between members being only the

metal node. These unsaturated metal centers are investigated for their impact on

adsorption, particularly their impact on low pressure interactions and the variables that

alter their adsorption capacity.

1.1.1. MOFs Synthesis on Particles and Substrates

As the MOF field matures from primarily identifying new materials to thoroughly

characterizing materials and applying them in meaningful ways, interest has grown in

synthesizing MOFs on substrates and particles for thin film or membrane applications

and additional functionality. MOF-5 and HKUST-1, among others, have been

synthesized on substrates using several synthesis methods: direct solvothermal synthesis,

layer-by-layer growth, assembly of preformed nanocrystals, electrochemical synthesis

and gel-layer synthesis.[1] Most promising for growth on nanoparticles are solvothermal

and layer-by-layer methods.

Solvothermal synthesis is the most straightforward synthesis method; a substrate or

particle is placed in the MOF precursor solution, and the synthesis progresses similarly to

the standard synthesis for that MOF. The substrate can be functionalized, for instance

with hydroxide or carboxylate groups, or seeded with nanocrystals of the desired MOF to

assist in growth. Functionalization can impact not only where the MOF grows but also the crystal orientation, as demonstrated for HKUST-1 on gold that had been functionalized with –OH, –COOH, and –CH$_3$. Films grown on the –OH functionalization preferentially oriented along the [111] direction, –COOH functionalization grew MOF preferring the [100], and methyl functionalization showed no preferred orientation.[2] HKUST-1 has also been grown on a number of other supports, including silicon,[3] alumina,[4,5] gold,[5,6] copper,[7] and silica,[5,8-10] with varying functional groups. Microwave-assisted synthesis has been used to synthesize MOF-5 only in the vicinity of a substrate suspended in the mother solution as a seed layer for subsequent solvothermal growth.[11]

Layer-by-layer growth takes advantage of SAM (self-assembled monolayer)-synthesis techniques. In this method, a substrate is sequentially immersed in a ligand-containing solution and a metal precursor solution.[1] Layer-by-layer growth leads to highly-oriented, homogeneous growth. This method has been used to successfully create thin films of HKUST-1,[12] ZIF-8,[13] and Zn- and Cu-DABCO.[14] Additionally, this method has been used to create a non-interpenetrated form of MOF-508,[15] which is only produced as interpenetrated networks when synthesized solvothermally.

HKUST-1 has been successfully synthesized on nanoparticles. In 2010, HKUST-1 was synthesized on gold nanoparticles via a layer-by-layer approach for CO_2 and SF_6 sensing.[16] They found that encapsulating the sensor nanoparticle in HKUST-1 caused an order of magnitude increase in sensitivity to CO_2 because the MOF served to concentrate the target prior to reaching the sensor.   The sensor used localized surface plasmon

resonance (LSPR) spectroscopy, which measures small changes in the refractive index via tiny shifts in extinction. Rather than chemically interacting with the sensor particle, the mere presence of the target gas near the nanoparticle changes the local refractive index. By adsorbing CO_2, the MOF serves to increase the local concentration, thereby increasing the index shift. In contrast, SF_6 sensing is adversely affected by MOF encapsulation. MOF thickness was also shown to impact the sensor: increasing thickness initially increased the CO_2 signal, indicating an optimum thickness for concentrating the target gas around the sensor.

More recently, HKUST-1, DUT-4, and DUT-5 were synthesized on magnetite nanoparticles for drug delivery applications.[17] DUT-4 and -5 are aluminum-based MOFs, and magnetite is a magnetic iron oxide. The MOFs were synthesized on the nanoparticle surface, which retained its superparamagentic properties. The composites possessed surface areas only slightly lower than values reported for the unfunctionalized MOFs and morphologies similar to the parent MOF. In addition to being easily separated from solution via the magnetic functionalization, the composite materials heat up to 55°C in an alternating magnetic field, showing their promise for hyperthermia treatments or triggered drug release: the magnetic field strength controls the composite's temperature, which affects the rate of drug delivery.

1.1.2. Metals and Oxides in MOFs

Metal oxides such as MgO and Co_3O_4 have been synthesized in a wide variety of mesoporous carbons and silicas to form nanoparticles and inverse replicas by many

groups who used the composite materials for catalytic oxidation[18-20] and electrochemical applications.[21,22] Most commonly, metal nitrates in water[23-28] or ethanol[18,20-22,29-31] have been used to impregnate the mesoporous material, followed by heating to decompose the nitrate into the metal hydroxide or oxide. The solution-based synthesis methods used for including magnesium and cobalt oxides in mesoporous materials are used as the starting point for my work on oxide inclusion in MOFs.

Metal nanoparticles such as Pd, [32-40] Ru,[41] Cu,[42] Au, [43-47] Ni,[48] and Pt;[49-53] metal oxide nanoparticles of ZnO,[54,55] TiO$_2$,[56] iron oxides,[45,57], and vanadium oxide;[58] and biologically relevant molecules have successfully been synthesized in the cavities of MOFs such as MIL-100,[39,44] MIL-101,[34,42,46,49,50,52,59] ZIFs,[43,45] MOF-5,[32,37,48] MIL-53,[36] IRMOFs,[33] and UiO-66[40,47] via gas phase and solution based impregnation for primarily catalytic applications[60,61] or controlled drug delivery.[62,63] In some cases, the MOF serves as a sacrificial template or precursor to metal oxide formation rather than a participant or support.[64-68]

Synthesizing composites consisting of active species in MOFs can be realized through gas-phase or solution based methods. Gas phase impregnation often results in higher single-step loadings, but solution-phase impregnation allows finer control over the final particle loading.[60] Solution-based techniques can be divided into two general types: wet impregnation and incipient wetness. For wet impregnation, the MOF is placed in an excess of low concentration precursor solution and mixed or sonicated to assist in pore filling. In the incipient wetness technique, a small amount of a higher concentration

solution is used, with just enough solution added to completely wet the MOF and just enough precursor to fill the pore space to the desired loading. Incipient wetness is appealing for MOFs because of the shorter liquid contact time. Additionally, it has been demonstrated in the synthesis of Pd@MIL-101 and Cu@MIL-101 that incipient wetness leads to nanoparticle formation preferentially within the pore system as opposed to predominately on the surface for wet impregnation.[69] A number of techniques have been examined to improve solution-phase loading and preferential formation within the pore space, including sonication-assisted impregnation, vacuum-assisted impregnation, and microwave-assisted reaction.[69]

In a study that impregnated HKUST-1 with barium salts via wet methods, it was shown that the precursor selection is important for framework stability and composite properties.[70] Composites produced from nitrate and acetate precursors retained the parent HKUST-1 structure per PXRD measurements, with a change in intensity attributed to the guest species. However, the PXRD measurement for the composite material produced from the chloride precursor indicates considerable structural degradation, and SEM images indicate salts external to the framework. Rather than use the barium salts as precursors to metal or metal oxide particles, this study investigated the salt-MOF composite for SO_2 uptake. They found that the Ba/HKUST-1(Cl) decomposition product outperformed current SO_2 adsorbents. However, it lost the regular porous nature that is an attractive characteristic for MOFs, making it less attractive for applications where confinement could be beneficial or porosity is necessary. The acetate composite had similar loadings to the chloride composite while retaining the MOF structure, while the

nitrate composite and parent MOF had about half the uptake but still exceeded supported

barium carbonate materials.

Fischer and coworkers have included ZnO and TiO_2 in MOF-5 for catalytic applications

via gas-phase loading.[56,71] The (Cu/ZnO)@MOF-5 composite was ultimately

unsuccessful as a catalyst due to the instability of MOF-5 in water. However, this study

demonstrates the interactions between included solid guests and the MOF's metal sites:

copper in the absence of zinc oxide shows no activity for methanol synthesis, but copper

nanoparticles included in MOF-5 show catalytic activity similar to copper supported on

zinc oxide. The zinc centers of MOF-5, in this case, provide similar promoting effects to

uncoordinated zinc oxide. Including ZnO as well in MOF-5 increases the catalytic

activity over Cu@MOF-5, further indicating the benefit of additional active sites within

the MOF framework. Titania included in MOF-5 had optical properties similar to

supported nanoparticles, but in this case, too, the MOF-5 framework degraded on

exposure to water.

1.2. Metal Organic Frameworks and Metal Oxides for Toxic Gas Adsorption

1.2.1. Metal Oxides for TIC Removal

Metal oxides including MgO,[72-79] Al_2O_3,[75,76] CaO,[72,75,78] CuO,[80] NiO,[80] ZnO,[81] and mixed

metal oxides (MMOs) have been considered for reactive adsorption of toxic gases for

some time, including traditional chemical warfare agents (CWAs)[73-75,77-86] and

industrially relevant gases or toxic industrial chemicals (TICs).[73,78,80,81,87] A major

drawback to their implementation is low surface areas obtained by traditional synthesis

methods, on the order of tens to hundreds of square meters per gram. Nanoparticles

possessing a higher density of edge and defect sites are more reactive than traditionally

synthesized oxides. Additionally, it has been shown that intimately mixed alkaline earth

metals and alumina are more reactive against SO_2, CCl_4, and paraoxon, a CWA mimic

used for materials testing, than the oxides alone or in mixtures of preformed oxides.[76,86]

Additionally, Klabunde and coworkers demonstrated that MgO will adsorb more than

three times the amount of SO_2 as CO_2 on a per-surface area basis; they propose that SO_2,

the more acidic gas, probes all basic sites while CO_2 interacts more selectively.[84]

1.2.2. MOFs for TIC Removal

There is current interest in MOFs for toxic gas removal from air. MOFs can be tailored

to target specific gases through varying pore size, open metal sites, and functionality. A

benchmark study of dynamic adsorption of TICs in a series of pristine MOFs under dry

conditions was conducted by Yaghi and coworkers in 2008.[88] As a representative

selection of TICs, they tested sulfur dioxide, ammonia, chlorine, tetrahydrothiophene,

benzene, dichloromethane, and ethylene oxide. Their test MOFs included ultra-high

surface areas (MOF-5, MOF-177), open metal sites (Zn-MOF-74, HKUST-1), and pore

functionality (IRMOF-3, IRMOF-62). They determined that for each target gas, at least

one MOF equaled or out-performed the BPL carbon baseline, finding functionality and

open metal sites to be critical. IRMOF-3, an amine functionalized MOF, performed best

against ammonia and chlorine, outperforming BPL carbon by 105 and 1.76 times,

respectively. The MOFs with open metal sites performed best against the other target

gases, with Zn-MOF-74 outperforming BPL carbon by 5.88 times against sulfur dioxide and HKUST-1 outperforming for all other target gases.

More recently, a series of MOF-74 analogs was tested against ammonia, cyanogen chloride, octane, and sulfur dioxide under dry and humid conditions.[89] It was shown that for all four test gases, the Mg and Co analogs outperformed the Ni and Zn analogs. Co-MOF-74 outperformed Mg-MOF-74 against cyanogen chloride under dry conditions and ammonia under humid conditions, while Mg-MOF-74 performed better for the other gases and conditions. Compared to the standard adsorbents BPL carbon and zeolite 13X, the cobalt and magnesium MOF-74 analogs adsorbed several times the amount of ammonia and retained significantly more under desorption. Retention is critical for breathing air applications; off-gassing could lead to incapacitation of the individual the filter is designed to protect.

By comparing the Zn-MOF-74 results for sulfur dioxide and ammonia between the two studies, the effect of ambient conditions can be easily seen. In the first study, all MOFs were stored and tested under an inert atmosphere.[88] In the second study, they intentionally stored the materials under atmospheric conditions to more closely represent the conditions under which the materials would need to function in a respirator application.[89] The MOF stored under atmospheric conditions loses a third of its capacity for ammonia compared with the material stored under inert and over 90% of its sulfur dioxide capacity. However, Zn-MOF-74 outperformed the other MOFs in the first study against sulfur dioxide, and both Co-MOF-74 and Mg-MOF-74 outperform Zn-MOF-74

under comparable conditions. Additionally, under dry conditions, Co-MOF-74 and Mg-MOF-74 outperform IRMOF-3 stored under inert against ammonia.

In a different study, HKUST-1 impregnated with barium chloride, nitrate, and acetate were investigated for SO_2 uptake and storage.[70] Impregnation with the barium salts increases the SO_2 uptake over the parent MOF, with the acetate and chloride compounds outperforming the commercial sorbent, too. However, for the chloride-containing compound, the MOF structure is severely degraded during synthesis. HKUST-1 decomposes around 573 K, and the maximum uptake for each material was measured at 773 K, indicating that the HKUST-1 decomposition products (copper ions) intimately mix with barium ions to play a considerable role in SO_2 uptake. For the intact framework below its decomposition temperature, HKUST-1 compares to other MOFs, and uptake is only enhanced for the barium acetate composite.

1.2.3. MOFs for CO Adsorption and Oxidation

Removing toxic gases from ambient air mixtures has a wide variety of applications, including respirators and environmental air quality control.[90-93] Carbon monoxide and VOCs such as hexane are prevalent candidates for capture to improve air quality. Carbon monoxide removal from gas mixtures is also relevant to a wide range of other applications, including energy and industrial applications. Here, the application of interest is air purification: removing toxic CO from an air stream at low concentration and pressure. Of particular interest are two applications: personal respirators operating at ambient temperature and larger beds associated with fixed sites or vehicles where waste

heat from HVAC or other systems may be available.[18-21] Carbon monoxide adsorption and catalysis has been studied on HKUST-1;[9,22-24] materials supported on HKUST-1, including PdO_2[25] and Ag;[26] and the decomposition products of HKUST-1.[27]

Titania is a common support for nanoparticles for carbon monoxide oxidation and other catalytic reactions,[28,29] showing little activity towards CO oxidation on its own but enhancing the activity of the supported material, with CuO/TiO_2 showing higher activity than other metal oxide systems, with an onset temperature around 60°C and complete conversion reached around 150°C.[30] In another study looking at copper oxide supported on titania and zirconia alloys, the CuO/TiO_2 system reached complete conversion at about 200°C, with an onset temperature around 50°C.[31]

1.2.4. MOFs for Combined Adsorption and Sensing

Within the diverse family of metal-organic frameworks are structures with interesting magnetic or optical properties. These properties can be used as indicators of small molecule adsorption. An adsorption event can alter the local magnetic field, and there are multiple examples of MOFs that change color or luminesce when certain molecules are adsorbed.

Yaghi and coworkers report a color change for HKUST-1;[88] a deep violet when activated, it reverts to a light blue on exposure to atmosphere. An identical change is observed for the activated HKUST-1 on exposure to ammonia, but this change is not reversible. Also observed were permanent color changes in Zn-MOF-74 in the presence of sulfur dioxide,

IRMOF-3 in chlorine and ammonia, and IRMOF-62 in ammonia.[88] Simple color changes provide an indicator to the extent of penetration of the adsorbent bed and could be used as a built-in indicator for single-pass respirators, giving a more precise metric for filter life.

Lanthanide metals have shown luminescent properties that are highly dependent on their coordination environment and the adjacent functional groups.[94] MOFs are an attractive way to take advantage of lanthanides' well-known coordination chemistry and explore new coordination environments. Of particular interest are the effects of crystal structure and guest molecules on luminescence. It has been shown for Eu-BTC that the solvent can enhance, in the case of DMF, or quench, in the case of acetone, fluorescence.[95] Eu-BTC has been shown to exhibit quenching in the presence of several nitroaromatic explosive compounds,[94] demonstrating a broad range of potential sensing applications. Interestingly, a zinc-based MOF, [Zn4(dmf)(ur)2(ndc)4] (ndc2- = 2,6-naphtalenedicarboxylate, ur = urotropin, dmf = N,N¢-dimethylformamide), exhibited strong blue emission as-synthesized, activated, and loaded with benzene. When loaded with ferrocene, in contrast, emissions were quenched.[96] The change in bulk refractive index with adsorption has been taken advantage of in thin films of ZIF-8: shifts in visible light occur upon adsorption of propane and ethanol but not upon exposure to water.[97] There is also a concentration dependence on the peak shift up to pore saturation.

Electromagnetic properties are also useful in molecular sensing. Composites of cobalt oxide and carbon nanotubes have been investigated for sensing NO_x, taking advantage of the change in resistivity of the material with adsorbed molecules.[98] Changes in magnetic

properties can also occur in so-called 'breathing' MOFs, in which the framework expands upon guest adsorption and shrinks on desorption.[99] This has been demonstrated for copper-based MOROF-1 (Metal-Organic Radical Open Framework): the solvated crystal has a higher magnetic response than the desolvated, amorphous material.[100] Interestingly, the amorphous desolvated material will regain crystallinity upon adsorption of water or alcohols but does not take up any other hydrocarbon tested. Cobalt iron oxide magnetic nanoparticles (MNPs) have demonstrated changes in magnetic field with adsorbed species.[101] Including such species into MOFs couples a selective, high-capacity adsorbent with a nonselective indicator to provide information about exposure and device lifetime.

1.3. Objectives and Overview of this Work

The overall goal of this work is to synthesize next-generation adsorbents for toxic gas removal from breathing air by combining metal oxides with metal-organic frameworks (MOFs) in order to preserve life and minimize performance degradation of military and first-responders. This goal is realized through three objectives: (1) include metal oxides within the pore system of MOFs for enhanced TIC adsorption; (2) synthesize MOFs around metal oxide nanoparticles whose diameters exceed the MOF pore size to provide selectivity and enhance MOF adsorption; and (3) investigate MOF properties for TIC adsorption and practical gas separations. Objective 1 is addressed in Chapter 3 and Appendix B using cobalt oxide and magnesium oxide in two MOF systems. Objective 2 is covered in Chapters 4 and 5 with the same MOF but different metal oxides. Chapters 6 and 7 address Objective 3, with an isostructural family of MOFs providing insight.

Chapter 2 outlines the materials and experimental methods used throughout this work,

beginning with details on the MOF systems used: HKUST-1/Cu-BTC, UiO-66, and M-

MOF-74/CPO-27-M/M-DOBDC (M=Co, Mg, Ni, Zn). HKUST-1 is a copper-based

MOF consisting of paddlewheel clusters connected by BTC linkers into a three-

dimensional structure. UiO-66 is a zirconium-based three-dimensional MOF with

terephthalic acid (BDC) linkers that has been shown to be relatively thermally and

hydrodynamically stable. MOF-74 is a family of isostructural MOFs with DOBDC

linkers that form a one-dimensional honeycomb pore structure. This family is useful for

investigating the impact of changing the metal center while the underlying architecture

remains identical. In both HKUST-1 and MOF-74, solvent molecules coordinated to the

metal center can be removed upon activation, resulting in coordinatively unsaturated sites

(CUS) or open metal sites (OMS).

This chapter continues with descriptions of the two methods of guest inclusion used in

this work, impregnation and encapsulation. For the former, the MOF is synthesized per

standard synthesis methods, and metal oxide precursors are added to the MOF and

subsequently decomposed. Several methods of impregnation are considered, with the

precursor concentration and method of impregnation both impacting the resulting

composite. With the latter method, fully formed metal oxide particles are added to the

MOF precursor solution. These particles are kept suspended during the MOF synthesis to

allow precursor access to the particle surface, upon which the MOF should grow.

Experimental methods, including characterization via powder X-ray diffraction, nitrogen physisorption, thermogravimetric analysis, and scanning and transmission microscopy are then detailed. Methods and apparatus for adsorption isotherms are discussed. Isotherms were measured up to 5 bar for CO_2 and CO at 25-65°C. Dynamic adsorption and catalysis experiments conducted on the breakthrough system are explained. Generally, mixtures of air and CO or nitrogen and CO were passed through a packed bed at temperatures ranging from room temperature up to 250˚C, and the outlet was monitored for the feed gases and possible products.

Chapter 3 considers metal oxide impregnation into UiO-66 and the impact on adsorption. Composites consisting of cobalt oxide or magnesium oxide in UiO-66 were synthesized and characterized, with particular attention on the impact of the oxide guest on the MOF structure and accessibility to the pore space. Adsorption isotherms were measured to determine the impact of the included oxide on capacity.

Chapter 4 discusses a MOF-metal oxide system consisting of HKUST-1 encapsulating titania. This composite is synthesized by adding titania to the MOF precursor solution. The composite and parent material are characterized and investigated for adsorption interactions with carbon monoxide. Under dynamic conditions, the parent MOF and composite material are interrogated with air-CO mixtures at a range of temperatures to investigate the separation potential and onset of oxidation.

Chapter 5 covers a MOF-metal oxide system of pre-formed magnetic nanoparticles encapsulated in HKUST-1. This composite is synthesized identically to the HKUST-1-titania system. This system was investigated for the impact of the nanoparticles on the structure and stability of the material, as well as the capacity for gases and vapors.

Chapter 6 looks at the impact of activation conditions on carbon monoxide adsorption in the MOF-74 family, particularly the cobalt, magnesium, nickel, and zinc analogs. Activation temperature and duration are critical to activate these materials, as evidenced by obtainable surface area. Open metal site accessibility was investigated through carbon monoxide adsorption over a range of activation temperatures.

The investigation on MOF-74 continues in Chapter 7 by investigating the impact of air exposure on the equilibrium and dynamic adsorption capacities of MOF-74 materials in order to investigate their suitability for real-world systems. Equilibrium isotherms were measured on pristine and air exposed samples to quantify the loss in capacity associated with air exposure. These results were compared to breakthrough experiments with and without air exposure to determine the impact on air exposure to the predictive nature of the isotherms.

Chapter 8 covers trends, conclusions, and recommendations for future work. All of the metal oxide-MOF systems discussed are un-optimized. Different oxides, precursors, and concentrations could further enhance activity against specific targets, and different metal combinations as MOF-oxide systems could be tailored to increase adsorption against a

range of targets. Additionally, functionalizing the organic linker of the MOF in addition to oxide impregnation has the potential to enhance adsorption in interesting ways, too.

Appendix A discusses metal oxide impregnation in a mesoporous silica, SBA-15. The resulting changes in porosity are discussed, as well as the impact on the dynamic adsorption of a series of test gases, including ammonia, sulfur dioxide, cyanogen chloride, and octane.

Appendix B combines the investigations into MOF-74 with metal oxide impregnation, resulting in a series of metal-oxide-MOF composites. The results with this material are contrasted with the impregnations on UiO-66.

Appendix C contains the data used to generate the preceding chapters. It is broken down by MOF or MOF-nanoparticle system in the same order as it occurs in the text. Tabulated data for all isotherms are included; PXRD, TGA-DSC, and breakthrough data are omitted due to length but are available upon request.

1.4. References

(1)   Shekhah, O.; Liu, J.; Fischer, R. A.; Woll, C. *Chem. Soc. Rev.* **2011**, *40*, 1081.

(2)   Biemmi, E.; Scherb, C.; Bein, T. *J. Am. Chem. Soc.* **2007**, *129*, 8054.

(3)   Redel, E.; Wang, Z.; Walheim, S.; Liu, J.; Gliemann, H.; Woell, C. *Appl. Phys. Lett.* **2013**, *103*.

(4)   Granato, T.; Testa, F.; Olivo, R. *Microporous Mesoporous Mat.* **2012**, *153*, 236.

(5)   Stavila, V.; Volponi, J.; Katzenmeyer, A. M.; Dixon, M. C.; Allendorf, M. D. *Chem. Sci.* **2012**, *3*, 1531.

(6)   Zhuang, J.-L.; Ceglarek, D.; Pethuraj, S.; Terfort, A. *Adv. Funct. Mater.* **2011**, *21*, 1442.

(7)   Jeremias, F.; Henninger, S. K.; Janiak, C. *Chem. Commun.* **2012**, *48*, 9708.

(8)   Sachse, A.; Ameloot, R.; Coq, B.; Fajula, F.; Coasne, B.; De Vos, D.; Galarneau, A. *Chem. Commun.* **2012**, *48*, 4749.

(9)   Ahmed, A.; Forster, M.; Clowes, R.; Bradshaw, D.; Myers, P.; Zhang, H. *Journal of Materials Chemistry A* **2013**, *1*, 3276.

(10)   Shekhah, O.; Fu, L.; Sougrat, R.; Belmabkhout, Y.; Cairns, A. J.; Giannelis, E. P.; Eddaoudi, M. *Chem. Commun.* **2012**, *48*, 11434.

(11)   Yoo, Y.; Lai, Z. P.; Jeong, H. K. *Microporous Mesoporous Mat.* **2009**, *123*, 100.

(12)   Shekhah, O.; Wang, H.; Kowarik, S.; Schreiber, F.; Paulus, M.; Tolan, M.; Sternemann, C.; Evers, F.; Zacher, D.; Fischer, R. A.; Woll, C. *J. Am. Chem. Soc.* **2007**, *129*, 15118.

(13)   Shekhah, O.; Eddaoudi, M. *Chem. Commun.* **2013**, *49*, 10079.

(14)   Shekhah, O.; Hirai, K.; Wang, H.; Uehara, H.; Kondo, M.; Diring, S.; Zacher, D.; Fischer, R. A.; Sakata, O.; Kitagawa, S.; Furukawa, S.; Woell, C. *Dalton Trans.* **2011**, *40*, 4954.

(15)   Shekhah, O.; Wang, H.; Paradinas, M.; Ocal, C.; Schupbach, B.; Terfort, A.; Zacher, D.; Fischer, R. A.; Woll, C. *Nat. Mater.* **2009**, *8*, 481.

(16)   Kreno, L. E.; Hupp, J. T.; Van Duyne, R. P. *Anal. Chem.* **2010**, *82*, 8042.

(17)   Lohe, M. R.; Gedrich, K.; Freudenberg, T.; Kockrick, E.; Dellmann, T.; Kaskel, S. *Chem. Commun.* **2011**, *47*, 3075.

(18)   Garcia, T.; Agouram, S.; Sanchez-Royo, J. F.; Murillo, R.; Mastral, A. M.; Aranda, A.; Vazquez, I.; Dejoz, A.; Solsona, B. *Appl. Catal. A-Gen.* **2010**, *386*, 16.

(19)   Lopes, I.; Davidson, A.; Thomas, C. *Catal. Commun.* **2007**, *8*, 2105.

(20)   Xia, Y. S.; Dai, H. X.; Jiang, H. Y.; Zhang, L. *Catal. Commun.* **2010**, *11*, 1171.

(21)   Wang, G. X.; Liu, H.; Horvat, J.; Wang, B.; Qiao, S. Z.; Park, J.; Ahn, H. *Chemistry-a European Journal* **2010**, *16*, 11020.

(22)   Zhang, H. J.; Tao, H. H.; Jiang, Y.; Jiao, Z.; Wu, M. H.; Zhao, B. *J. Power Sources* **2010**, *195*, 2950.

(23)   Bhagiyalakshmi, M.; Lee, J. Y.; Jang, H. T. *International Journal of Greenhouse Gas Control* **2010**, *4*, 51.

(24)   Deng, J. G.; Zhang, L.; Dai, H. X.; Xia, Y. S.; Jiang, H. Y.; Zhang, H.; He, H. *J. Phys. Chem. C* **2010**, *114*, 2694.

(25)   Khodakov, A. Y.; Zholobenko, V. L.; Bechara, R.; Durand, D. *Microporous Mesoporous Mat.* **2005**, *79*, 29.

(26)   Roggenbuck, J.; Koch, G.; Tiemann, M. *Chem. Mat.* **2006**, *18*, 4151.

(27)   Roggenbuck, J.; Tiemann, M. *J. Am. Chem. Soc.* **2005**, *127*, 1096.

(28)   Roggenbuck, J.; Waitz, T.; Tiemann, M. *Microporous Mesoporous Mat.* **2008**, *113*, 575.

(29)   Rumplecker, A.; Kleitz, F.; Salabas, E. L.; Schuth, F. *Chem. Mat.* **2007**, *19*, 485.

(30)   Shu, P.; Ruan, J. F.; Gao, C. B.; Li, H. C.; Che, S. N. *Microporous Mesoporous Mat.* **2009**, *123*, 314.

(31)   Tuysuz, H.; Lehmann, C. W.; Bongard, H.; Tesche, B.; Schmidt, R.; Schuth, F. *J. Am. Chem. Soc.* **2008**, *130*, 11510.

(32)   Esken, D.; Zhang, X.; Lebedev, O. I.; Schroder, F.; Fischer, R. A. *J. Mater. Chem.* **2009**, *19*, 1314.

(33)   Gutierrez, I.; Diaz, E.; Ordonez, S. *Thermochim. Acta* **2013**, *567*, 79.

(34)   Hermannsdofer, J.; Kempe, R. *Chemistry-a European Journal* **2011**, *17*, 8071.

(35)   Huang, Y. B.; Lin, Z. J.; Cao, R. *Chemistry-a European Journal* **2011**, *17*, 12706.

(36)   Huang, Y. B. A.; Zheng, Z. L.; Liu, T. F.; Lu, J.; Lin, Z. J.; Li, H. F.; Cao, R. *Catal. Commun.* **2011**, *14*, 27.

(37)   Sabo, M.; Henschel, A.; Froede, H.; Klemm, E.; Kaskel, S. *J. Mater. Chem.* **2007**, *17*, 3827.

(38)   Zhang, L. J.; Su, Z. X.; Jiang, F. L.; Zhou, Y. F.; Xu, W. T.; Hong, M. C. *Tetrahedron* **2013**, *69*, 9237.

(39)   Zlotea, C.; Campesi, R.; Cuevas, F.; Leroy, E.; Dibandjo, P.; Volkringer, C.; Loiseau, T.; Ferey, G.; Latroche, M. *J. Am. Chem. Soc.* **2010**, *132*, 2991.

(40)   Shen, L. J.; Wu, W. M.; Liang, R. W.; Lin, R.; Wu, L. *Nanoscale* **2013**, *5*, 9374.

(41)   Schroeder, F.; Esken, D.; Cokoja, M.; van den Berg, M. W. E.; Lebedev, O. I.;
         van Tendeloo, G.; Walaszek, B.; Buntkowsky, G.; Limbach, H. H.; Chaudret, B.;
         Fischer, R. A. *J. Am. Chem. Soc.* **2008**, *130*, 6119.

(42)   Wu, F.; Qiu, L. G.; Ke, F.; Jiang, X. *Inorg. Chem. Commun.* **2013**, *32*, 5.

(43)   Esken, D.; Turner, S.; Lebedev, O. I.; Van Tendeloo, G.; Fischer, R. A. *Chem.
         Mat.* **2010**, *22*, 6393.

(44)   Ke, F.; Zhu, J. F.; Qiu, L. G.; Jiang, X. *Chem. Commun.* **2013**, *49*, 1267.

(45)   Lu, G.; Li, S. Z.; Guo, Z.; Farha, O. K.; Hauser, B. G.; Qi, X. Y.; Wang, Y.;
         Wang, X.; Han, S. Y.; Liu, X. G.; DuChene, J. S.; Zhang, H.; Zhang, Q. C.; Chen,
         X. D.; Ma, J.; Loo, S. C. J.; Wei, W. D.; Yang, Y. H.; Hupp, J. T.; Huo, F. W.
         Nat. Chem. **2012**, *4*, 310.

(46)   Gu, X. J.; Lu, Z. H.; Jiang, H. L.; Akita, T.; Xu, Q. *J. Am. Chem. Soc.* **2011**, *133*,
         11822.

(47)   Wu, R. B.; Qian, X. K.; Zhou, K.; Liu, H.; Yadian, B.; Wei, J.; Zhu, H. W.;
         Huang, Y. Z. *Journal of Materials Chemistry A* **2013**, *1*, 14294.

(48)   Zhao, H. H.; Song, H. L.; Chou, L. J. *Inorg. Chem. Commun.* **2012**, *15*, 261.

(49)   Aijaz, A.; Akita, T.; Tsumori, N.; Xu, Q. *J. Am. Chem. Soc.* **2013**, *135*, 16356.

(50)   Khajavi, H.; Stil, H. A.; Kuipers, H.; Gascon, J.; Kapteijn, F. *ACS Catal.* **2013**, *3*,
         2617.

(51)   Pan, H. Y.; Li, X. H.; Zhang, D. M.; Guan, Y. J.; Wu, P. *J. Mol. Catal. A-Chem.*
         2013, *377*, 108.

(52)   Pan, Y. Y.; Ma, D. Y.; Liu, H. M.; Wu, H.; He, D. H.; Li, Y. W. *J. Mater. Chem.*
         2012, *22*, 10834.

(53)   Wang, P.; Zhao, J.; Li, X. B.; Yang, Y.; Yang, Q. H.; Li, C. *Chem. Commun.*
         2013, *49*, 3330.

(54)   Muller, M.; Turner, S.; Lebedev, O. I.; Wang, Y. M.; van Tendeloo, G.; Fischer,
         R. A. *Eur. J. Inorg. Chem.* **2011**, 1876.

(55)   Muller, M.; Lebedev, O. I.; Fischer, R. A. *J. Mater. Chem.* **2008**, *18*, 5274.

(56)   Muller, M.; Zhang, X. N.; Wang, Y. M.; Fischer, R. A. *Chem. Commun.* **2009**,
         119.

(57)   Zhang, T.; Zhang, X. F.; Yan, X. J.; Kong, L. Y.; Zhang, G. C.; Liu, H. O.; Qiu, J.
         S.; Yeung, K. L. *Chem. Eng. J.* **2013**, *228*, 398.

(58)   Fazaeli, R.; Aliyan, H.; Moghadam, M.; Masoudinia, M. *J. Mol. Catal. A-Chem.* **2013**, *374*, 46.

(59)   Park, K. S.; Ni, Z.; Cote, A. P.; Choi, J. Y.; Huang, R. D.; Uribe-Romo, F. J.; Chae, H. K.; O'Keeffe, M.; Yaghi, O. M. *Proc. Natl. Acad. Sci. U. S. A.* **2006**, *103*, 10186.

(60)   Schroder, F.; Fischer, R. A. In *Functional Metal-Organic Frameworks: Gas Storage, Separation and Catalysis*; Springer-Verlag Berlin: Berlin, 2010; Vol. 293, p 77.

(61)   Meilikhov, M.; Yusenko, K.; Esken, D.; Turner, S.; Van Tendeloo, G.; Fischer, R. A. *Eur. J. Inorg. Chem.* **2010**, 3701.

(62)   Cunha, D.; Gaudin, C.; Colinet, I.; Horcajada, P.; Maurin, G.; Serre, C. *J. Mat. Chem. B* **2013**, *1*, 1101.

(63)   Devautour-Vinot, S.; Martineau, C.; Diaby, S.; Ben-Yahia, M.; Miller, S.; Serre, C.; Horcajada, P.; Cunha, D.; Taulelle, F.; Maurin, G. *J. Phys. Chem. C* **2013**, *117*, 11694.

(64)   Zamaro, J. M.; Perez, N. C.; Miro, E. E.; Casado, C.; Seoane, B.; Tellez, C.; Coronas, J. *Chem. Eng. J.* **2012**, *195*, 180.

(65)   Kim, J. Y.; Jin, M.; Lee, K. J.; Cheon, J. Y.; Joo, S. H.; Kim, J. M.; Moon, H. R. *Nanoscale Res. Lett.* **2012**, *7*.

(66)   Das, R.; Pachfule, P.; Banerjee, R.; Poddar, P. *Nanoscale* **2012**, *4*, 591.

(67)   Akhbari, K.; Morsali, A. *J. Coord. Chem.* **2011**, *64*, 3521.

(68)   Qin, F. X.; Jia, S. Y.; Liu, Y.; Han, X.; Ren, H. T.; Zhang, W. W.; Hou, J. W.; Wu, S. H. *Mater. Lett.* **2013**, *101*, 93.

(69)   El-Shall, M. S.; Abdelsayed, V.; Khder, A.; Hassan, H. M. A.; El-Kaderi, H. M.; Reich, T. E. *J. Mater. Chem.* **2009**, *19*, 7625.

(70)   Dathe, H.; Peringer, E.; Roberts, V.; Jentys, A.; Lercher, J. A. *C. R. Chim.* **2005**, *8*, 753.

(71)   Muller, M.; Hermes, S.; Kaehler, K.; van den Berg, M. W. E.; Muhler, M.; Fischer, R. A. *Chem. Mat.* **2008**, *20*, 4576.

(72)   Livraghi, S.; Paganini, M. C.; Giamello, E. *J. Mol. Catal. A-Chem.* **2010**, *322*, 39.

(73)   Stark, J. V.; Klabunde, K. J. *Chem. Mat.* **1996**, *8*, 1913.

(74)   Rajagopalan, S.; Koper, O.; Decker, S.; Klabunde, K. J. *Chemistry-a European Journal* **2002**, *8*, 2602.

(75) Khaleel, A.; Kapoor, P. N.; Klabunde, K. J. *Nanostructured Materials* **1999**, *11*, 459.

(76) Carnes, C. L.; Kapoor, P. N.; Klabunde, K. J.; Bonevich, J. *Chem. Mat.* **2002**, *14*, 2922.

(77) Li, Y. X.; Klabunde, K. J. *Langmuir* **1991**, *7*, 1388.

(78) Li, Y. X.; Li, H.; Klabunde, K. J. *Environ. Sci. Technol.* **1994**, *28*, 1248.

(79) Wagner, G. W.; Bartram, P. W.; Koper, O.; Klabunde, K. J. *Journal of Physical Chemistry B* **1999**, *103*, 3225.

(80) Carnes, C. L.; Stipp, J.; Klabunde, K. J. *Langmuir* **2002**, *18*, 1352.

(81) Carnes, C. L.; Klabunde, K. J. *Langmuir* **2000**, *16*, 3764.

(82) Li, Y. X.; Koper, O.; Atteya, M.; Klabunde, K. J. *Chem. Mat.* **1992**, *4*, 323.

(83) Lucas, E.; Decker, S.; Khaleel, A.; Seitz, A.; Fultz, S.; Ponce, A.; Li, W. F.; Carnes, C.; Klabunde, K. J. *Chemistry-a European Journal* **2001**, *7*, 2505.

(84) Stark, J. V.; Park, D. G.; Lagadic, I.; Klabunde, K. J. *Chem. Mat.* **1996**, *8*, 1904.

(85) Utamapanya, S.; Klabunde, K. J.; Schlup, J. R. *Chem. Mat.* **1991**, *3*, 175.

(86) Medine, G. M.; Zaikovskii, V.; Klabunde, K. J. *J. Mater. Chem.* **2004**, *14*, 757.

(87) Karwacki, C. J., Jones, P.; ECBC, Ed. Aberdeen Proving Ground, MD, 2000.

(88) Britt, D.; Tranchemontagne, D.; Yaghi, O. M. *Proc. Natl. Acad. Sci. U. S. A.* **2008**, *105*, 11623.

(89) Glover, T. G.; Peterson, G. W.; Schindler, B. J.; Britt, D.; Yaghi, O. *Chem. Eng. Sci.* **2011**, *66*, 163.

(90) Asimakopoulou, E. K.; Kolaitis, D. I.; Founti, M. A. *Indoor Built Environ.* **2013**, *22*, 750.

(91) Guerrero, P. A.; Corsi, R. L.; Ashrae In *Ashrae: Transactions 2011, Vol 117, Pt 1*; Amer Soc Heating, Refrigerating and Air-Conditioning Engs: Atlanta, 2011; Vol. 117, p 419.

(92) Kartel, M. T.; Savelyev, Y. V.; Kanellopoulos, N. In *Methods and Techniques for Cleaning-up Contaminated Sites*; Annable, M. D., Teodorescu, M., Hlavinek, P., Diels, L., Eds.; Springer: Dordrecht, 2008, p 187.

(93) Menzies, K. T., Randel, M.A., Quill, A.L., Roberts, W.C.; Command, U. S. A. M. R. a. D., Ed. Fort Detrick, Frederick, MD, 1989.

(94)   Liu, T. F.; Zhang, W. J.; Sun, W. H.; Cao, R. *Inorg. Chem.* **2011**, *50*, 5242.

(95)   Chen, B. L.; Yang, Y.; Zapata, F.; Lin, G. N.; Qian, G. D.; Lobkovsky, E. B. *Advanced Materials* **2007**, *19*, 1693.

(96)   Sapchenko, S. A.; Samsonenko, D. G.; Dybtsev, D. N.; Melgunov, M. S.; Fedin, V. P. *Dalton Trans.* **2011**, *40*, 2196.

(97)   Lu, G.; Hupp, J. T. *J. Am. Chem. Soc.* **2010**, *132*, 7832.

(98)   Li, W.; Jung, H.; Nguyen, D. H.; Kim, D.; Hong, S. K.; Kim, H. *Sens. Actuator B-Chem.* **2010**, *150*, 160.

(99)   Qiu, S. L.; Zhu, G. S. *Coord. Chem. Rev.* **2009**, *253*, 2891.

(100)   Maspoch, D.; Ruiz-Molina, D.; Wurst, K.; Domingo, N.; Cavallini, M.; Biscarini, F.; Tejada, J.; Rovira, C.; Veciana, J. *Nat. Mater.* **2003**, *2*, 190.

(101)   Glover, T. G.; Sabo, D.; Vaughan, L. A.; Rossin, J. A.; Zhang, Z. J. *Langmuir* **2012**, *28*, 5695.

(102)   Chowdhury, P.; Bikkina, C.; Meister, D.; Dreisbach, F.; Gumma, S. *Microporous Mesoporous Mat.* **2009**, *117*, 406.

(103)   Li, Z.-Q.; Wang, A.; Guo, C.-Y.; Tai, Y.-F.; Qiu, L.-G. *Dalton Trans.* **2013**, *42*, 13948.

(104)   Majano, G.; Perez-Ramirez, J. *Advanced Materials* **2013**, *25*, 1052.

(105)   Rubes, M.; Grajciar, L.; Bludsky, O.; Wiersum, A. D.; Llewellyn, P. L.; Nachtigall, P. *ChemPhysChem* **2012**, *13*, 488.

(106)   Schlichte, K.; Kratzke, T.; Kaskel, S. *Microporous Mesoporous Mat.* **2004**, *73*, 81.

(107)   Seo, Y.-K.; Hundal, G.; Jang, I. T.; Hwang, Y. K.; Jun, C.-H.; Chang, J.-S. *Microporous Mesoporous Mat.* **2009**, *119*, 331.

(108)   Tranchemontagne, D. J.; Hunt, J. R.; Yaghi, O. M. *Tetrahedron* **2008**, *64*, 8553.

(109)   van der Meer, J.; Bardez-Giboire, I.; Mercier, C.; Revel, B.; Davidson, A.; Denoyel, R. *J. Phys. Chem. C* **2010**, *114*, 3507.

(110)   Hicks, J. C.; Drese, J. H.; Fauth, D. J.; Gray, M. L.; Qi, G. G.; Jones, C. W. *J. Am. Chem. Soc.* **2008**, *130*, 2902.

CHAPTER 2

EXPERIMENTAL MATERIALS AND METHODS

2.1. Materials

2.1.1. Metal-Organic Framework Synthesis

The following MOFs were synthesized using solvothermal methods based on published

procedures, except where noted.

2.1.1.1. HKUST-1

HKUST-1, also known as Cu-BTC or MOF-199, is a copper-based MOF consisting of

paddlewheel clusters connected by BTC (benzene tricarboxylate) linkers into a three-

dimensional structure as shown in **Figure 2.1**. It has been widely studied for a variety of

applications and can be synthesized under a variety of conditions.[1-11] Solvent molecules
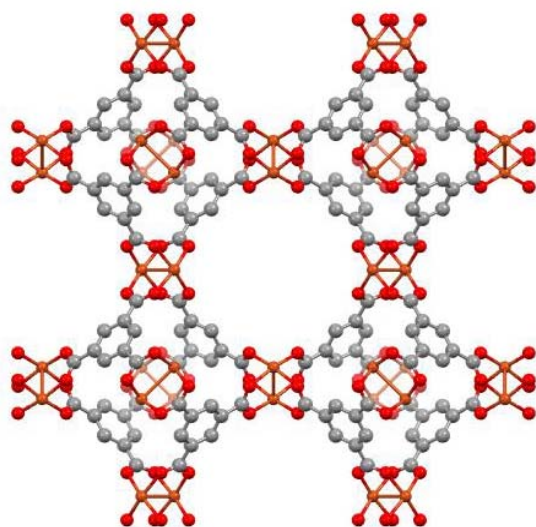
Figure 2.1. HKUST-1.

coordinated to the copper can be removed upon activation, resulting in coordinatively unsaturated sites (CUS) favorable for adsorption. HKUST-1 generally has a surface area in the range of 1400-1700 m^2/g[11] and pore volume in the range of 0.4-0.8 cc/g.[11]

HKUST-1 is synthesized in a method adapted from literature,[7] except where otherwise noted. Benzene tricarboxylate dissolved in ethanol is mixed with copper nitrate dissolved in water. The solution is sealed and heated to 120°C for 15-18 hours. Once cool, the blue crystals are washed daily with ethanol for three days, filtered, and dried. After activation overnight at 200°C, the material turns violet.

2.1.1.2. UiO-66

UiO-66 is a zirconium-based three-dimensional MOF with terephthalic acid (BDC) linkers. **Figure 2.2**. shows the structure. The zirconium is 8-coordinated, making the structure quite hydrodynamically and thermally stable, with a decomposition temperature above 500°C. It possesses a cubic "Maltese star"[13] coordination environment, with very small particles and BET surface areas around 1000-1200 m^2/g.

A standard synthesis adapted from literature[13] consists of adding DMF to a mixture of $ZrCl_4$ and BDC. Sealed vessels are placed in a 120°C oven for 24-48 hours. Once cool, the crystals are washed three times with DMF and three times with methanol over six days. The samples are dried at room temperature under air prior to activation at 200°C under vacuum.
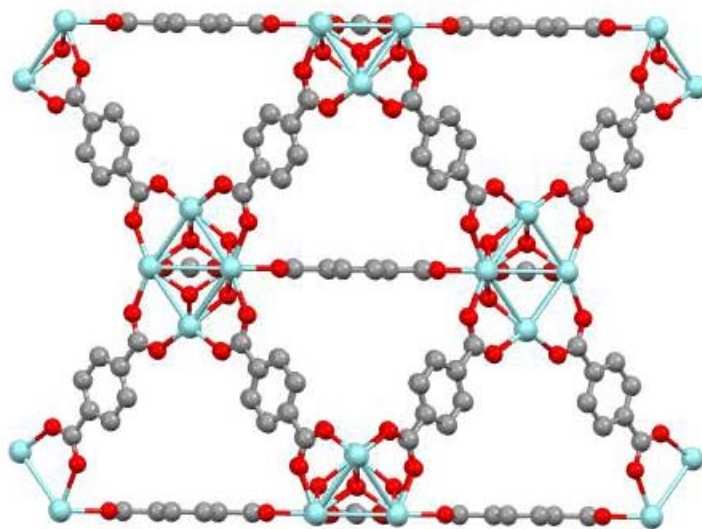
Figure 2.2. UiO-66.

2.1.1.3. M-MOF-74 / M-DOBDC / M-CPO-27 (M=Co, Mg, Ni, Zn)

This is a family of isostructural MOFs with DOBDC (dioxyterephthalate) linkers

connecting various metals into a one-dimensional honeycomb pore structure as seen in

Figure 2.3. This family is useful for investigating the impact of changing the metal

center of CUS-containing MOFs while the underlying architecture remains identical.

Surface areas range from 800 m^2/g for Zn-MOF-74[15] up to 1550 m^2/g for Mg-MOF-74,[16]

with Co- and Ni-MOF-74 having intermediate values.

In a standard synthesis based on literature procedures,[17] the metal nitrate is combined

with the H_4DOBDC ligand in a mixture of DMF, ethanol, and water. The solution is

placed in a sealed vessel and heated for several days. The ratios of solvents, synthesis

temperature, and duration vary for each analog. After cooling, the resulting crystals are

washed daily, three times with DMF and three times with methanol. Because of the
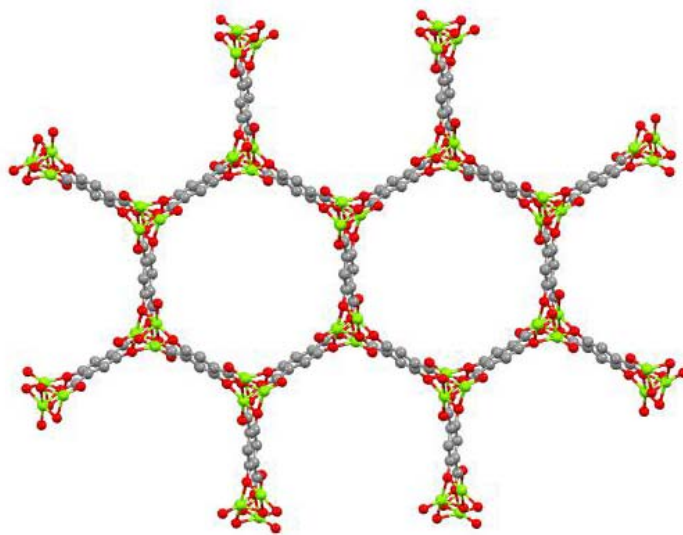
Figure 2.3. M-MOF-74.

limited stability in air, this series of MOFs is kept under methanol until use and activated

to 250°C under vacuum immediately prior to measurements.

2.1.2 Metal Oxide-Metal-Organic Framework Composite Synthesis

Metal-oxide-MOF composites were synthesized in two ways: impregnation and

encapsulation. **Figure 2.4** shows a simplified schematic of these methods to highlight the

differences. The goal of both methods is to yield materials where the oxide resides

within the MOF. With impregnation, a fully formed MOF is impregnated with an oxide

precursor solution. The precursor is then decomposed into the oxide, with the oxide

remaining in the MOF pore space. In encapsulation, a pre-formed oxide is added to the

MOF precursor solution. The oxide provides nucleation sites, and the MOF should

subsequently grow around the oxide, fully encapsulating it. Additional details for each

method, along with strengths and weaknesses, follow.

a) Impregnation
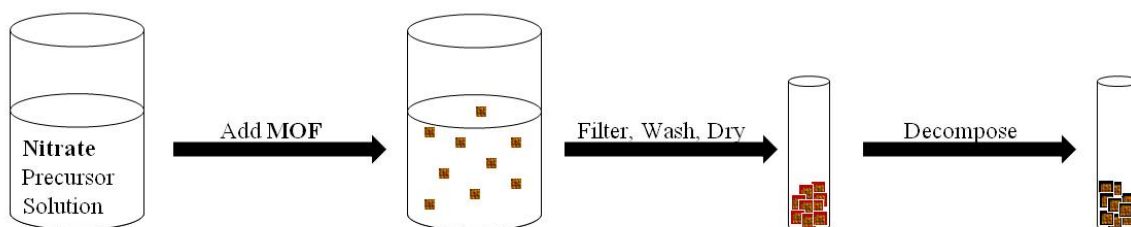
b) Encapsulation
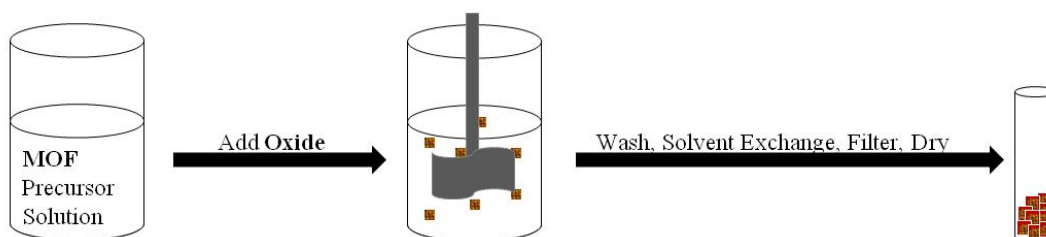
Figure: 2.4. Schematic showing composite synthesis methods, a) impregnation, b) encapsulation.

2.1.2.1. Impregnation

Oxide-MOF composites are realized by the impregnation method by adding metal nitrate

precursor solutions to fully formed MOF structures, and the resulting materials are heat-

treated to decompose the nitrates. In this work, cobalt and magnesium oxides were

formed within the pore systems of UiO-66 and MOF-74 via this method. For both

MOFs, a solution of the nitrate dissolved in ethanol was used. For UiO-66, which is

quite stable when exposed to air, the nitrate solution was added to the dried and activated

MOF. This was then stirred or sonicated. After 24 hours, the materials were filtered,

washed in ethanol, and dried in air prior to decomposition at 200°C. The resulting

product was stored in air until activation prior to subsequent measurements. For MOF-

74, which does not have the same long-term stability in air, the procedure was altered

slightly. The methanol in which the MOF was stored was decanted and the nitrate

solution was added. This mixture was allowed to stand for 24 hours, then placed directly from this solution into each instrument with minimal liquid accompaniment. The remaining liquid was evaporated off under vacuum. Then the material was activated directly from this state in situ at 250°C for 12 hours, coupling MOF activation and nitrate decomposition.

Impregnation is attractive for several reasons. This method allows characterization of the MOF prior to subsequent loading to ensure quality samples are used. It has been shown that impregnation provides a high level of control over the final oxide loading[18] through repeated loadings with low concentration solutions. Additionally, some MOFs are synthesized under harsh conditions that would decompose oxides. For example, mixing $ZrCl_4$ and DMF, the precursor and solvent for UiO-66 synthesis, results in the formation of HCl, making this solution acidic enough to decompose iron oxide into iron chloride when added. Impregnation allows for the pursuit of such composites using standard MOF synthesis procedures by adding the oxide after the MOF is removed from the harsh conditions.

Solution-based impregnation also has several drawbacks. It is difficult to ensure good distribution of the oxides within the pore system with this method. The oxides generated thusly tend to be distributed within the upper layers of each MOF particle rather than throughout the crystals when the MOF particles are large.[18] UiO-66 was chosen for this work in part because of the small particle size, increasing the fraction of each particle that falls within the accessible outer layer. There is also a greater likelihood of agglomeration

and pore blockage, and high loadings may completely block access to the MOF pore

space by covering the surface or completely filling the void space. To minimize these

drawbacks, low loadings are generally deemed preferable.

2.1.2.2. Encapsulation

The encapsulation method uses a preformed oxide added to the MOF precursor solution.

In this work, HKUST-1 has been synthesized with TiO_2 and magnetic $CoFeO_4$

nanoparticles. The standard HKUST-1 synthesis method was altered to allow for

constant stirring to keep the nanoparticles suspended, allowing MOF precursors access to

all sides of the nanoparticles. After the ligand and metal were dissolved in ethanol and

water, respectively, they were combined at room temperature and stirred for 30 minutes.

The oxide was added to this solution, and this mixture was placed in a preheated bath.

The mixture was stirred constantly at 50 rpm to keep the oxide particles suspended in the

solution. In the case of magnetic nanoparticles, magnetic stirring was unsuitable, so an

impeller was used. After the synthesis was completed and the mixture cooled to room

temperature, the resulting material was removed and washed several times with ethanol

over several days before drying and subsequent use.

There are several benefits to encapsulation for making MOF-oxide composites. First, the

MOF grows around the oxide, resulting in complete encapsulation and removing the

difficulties associated with minimizing agglomeration. Additionally, the oxide particles

can be larger than the MOF void spaces, but access to the oxide surface is restricted to

molecules that fit within the pore system. This is attractive for sensing applications

where non-selective oxides may be good sensing materials, and the MOF can add selectivity by restricting access to the oxide surface.

There are several potential drawbacks to encapsulation. First, the oxide must be compatible with the MOF synthesis. This means that MOFs with harsh synthesis conditions, such as UiO-66, are not suitable because the oxide is destroyed while the MOF is created. Additionally, the oxide must not alter the environment to the point that conditions are no longer favorable to MOF formation. These difficulties may be addressed through alternate synthesis schemes. If capping agents are used to make the particle surface more attractive for MOF formation, they must be easily removable. A drawback often seen with metal nanoparticles is that such capping agents are often too large to be effectively removed. This problem can be avoided with metal oxides, as the MOF ligands coordinate readily.

2.2. Experimental Methods

2.2.1. Material Characterization

General structure characterization was conducted using powder X-ray-diffraction (PXRD), nitrogen adsorption at 77K, thermogravimetric analysis-differential scanning calorimetry (TGA-DSC), scanning electron microscopy (SEM), and transmission electron microscopy (TEM).

2.2.1.1. PXRD

PXRD was conducted to verify crystal structure of synthesized MOFs and determine the impact of the addition of oxides on the MOF structure. PXRD involves interrogating a powder sample with X-rays at a series of well-defined angles. When an X-ray contacts a plane of molecules within a crystalline structure, it diffracts at the same angle reflected through a perpendicular plane. Parallel planes of molecules diffract at the same angle, resulting in constructive interference. This constructive interference results in a 'peak' measured at twice the incident angle for each parallel plane of molecules. Crystalline structures have a characteristic pattern of these peaks, and this pattern can be used to identify a material, and to some extent, the quality of it. PXRD patterns were measured on a PANalytical X'Pert Pro (CuKα).

2.2.1.2. Nitrogen Physisorption

Nitrogen isotherms were measured on a Quantachrome Quadrasorb Porous Material Analyzer for pore structure characterization. A known mass of sample is activated in a Quantachrome FloVac Degasser at temperatures up to 250°C under vacuum. After back-filling the sample tube with nitrogen, up to four samples are placed into the Quadrasorb. The instrument measures isotherm points from a relative pressure of 0.0005 up to 1. It is capable of calculating the BET surface area, pore volume, and pore radius from the isotherm using user-defined points, and the software can also apply DFT, DA, HK, and other models using standard reference models, which may have limited applicability to MOFs compared to the materials from which the models were derived.

The BET surface area is calculated using the method of Branauer Emmett and Teller. It is derived assuming a monolayer coverage of adsorbate, using the relative pressure range of 0.05-0.3. For small pore materials like MOFs, this definition does not strictly hold, as pore filling may be a more realistic model than layer-by-layer coverage. However, it has been shown that the method can be applied to microporous materials in general and MOFs in particular[19] if the relative pressure range is chosen appropriately to include the 'knee' of the isotherm. A range of 0.005-0.03 is generally appropriate for these materials. While it no longer meets the strict definition of surface area in the model, the calculated areas are still useful to evaluate samples for success in removing impurities, extent of activation, and accessibility of the pore system.

2.2.1.3. TGA-DSC

Coupled Thermogravimetry Analysis-Differential Scanning Calorimetry (TGA-DSC) experiments were conducted on a Netzsch STA449 Jupiter under flowing helium or air at 20 mL/min. A sample is placed in a chamber through which the carrier gas flows while the sample is heated through a precise profile, ramping 2-10°C/min up to maximum temperatures from 600-1000°C. To obtain the thermogravimetry data, the sample weight is monitored throughout the heating profile, and the mass loss can be used to identify solvent loss and sample decomposition. The differential scanning calorimetry data is obtained through the use of an adjacent blank cell. The software monitors the amount of energy needed to raise the sample temperature relative to a blank cell. Exothermic and endothermic peaks can be identified and attributed to solvent losses, decomposition, and phase changes.

2.2.1.4. Electron Microscopy

Scanning electron microscopy (SEM) and transmission electron microscopy (TEM) were used to verify particle size and shape and investigate changes with oxide addition. SEM provides images showing the surfaces of particles, which proves useful for identifying large-scale agglomeration of metal oxide on the surfaces of large particles or unaffiliated with the parent particle. SEM was conducted on a LEO 1530 operated at 5 kV on samples that had been sputter-coated with gold to reduce sample charging. TEM was conducted on a JEOL 100 CX II at 100keV. This imaging method provides additional information about the location and size of included nanoparticles. Using select area diffraction patterns, combined with brightfield and darkfield images, the host material can, in some cases, be differentiated from the metal oxide guest.

2.2.2. Adsorption Isotherms

Single component isotherms for CO_2, N_2, and O_2 were measured on a Hiden Intelligent Gravimetric Analyzer (IGA) capable of in situ activation, a wide range of available temperatures, and fine pressure control. Isotherms were measured at temperatures from 25-65°C over pressure ranges from 12 mbar to 5 bar.

Carbon monoxide isotherms at temperatures up to 65°C and pressures up to 5 bar were measured on a lab-built pressure decay system, shown in **Figure 2.5**. In this system, two samples can be run simultaneously. A sample is placed in the sample cell and can be activated in situ by using heat tape controlled via a PID in lieu of the water bath. The sample and reference cells are placed in a water bath to maintain the temperature set
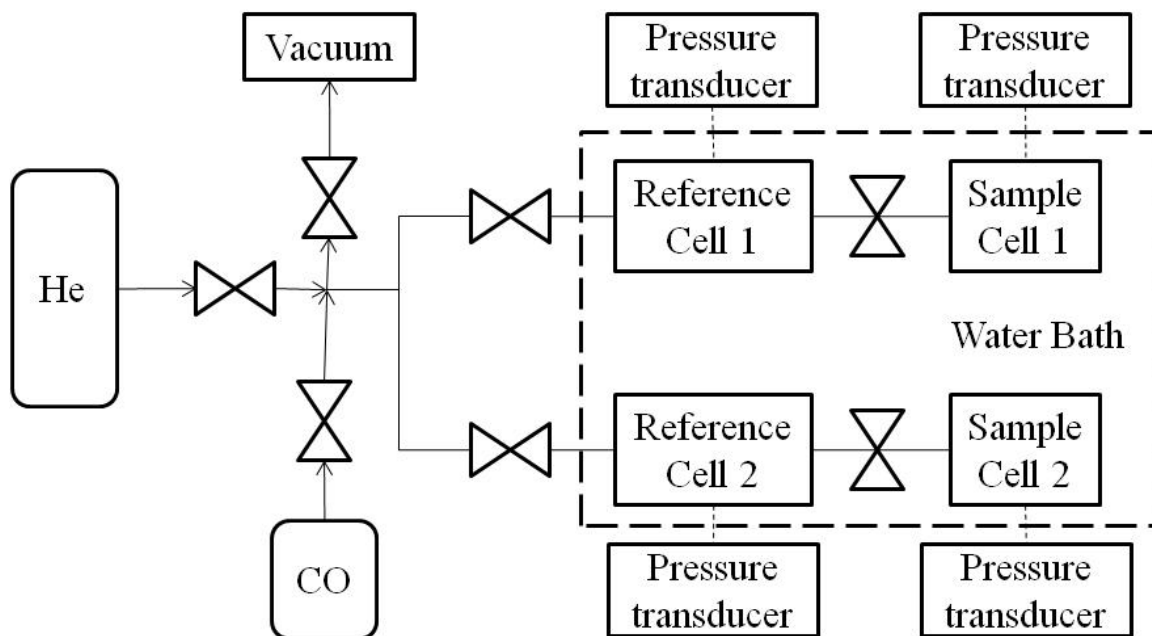
Figure 2.5. Pressure decay system.

point. Valves serve to isolate each cell, and transducers on each cell provide pressure readouts. For each point on the isotherm, the reference cell is charged with gas and allowed to reach thermal equilibrium. The gas is then allowed to enter the sample cell, which is then isolated. Once the pressure reaches equilibrium, a mass balance and the Peng-Robinson equation of state are used to determine the difference between the expected amount of gas in the sample cell from the amount the reference cell is reduced by and the actual amount of gas in that state as measured by the sample cell pressure. This difference corresponds to the amount adsorbed by the sample.

2.2.3. Dynamic Adsorption and Oxidation

Breakthrough and oxidation experiments were conducted on a lab-built apparatus consisting of a packed bed flowing to a Hiden DSMS. See **Figure 2.6** for a schematic.
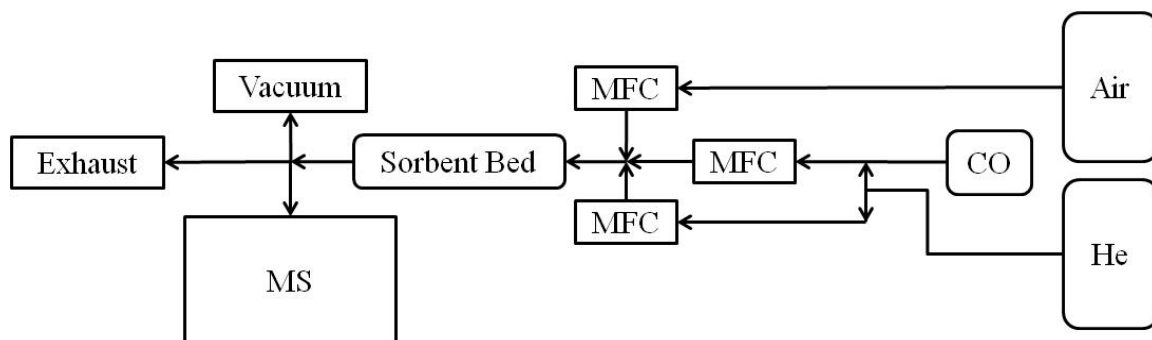
Figure 2.6. Breakthrough system.

Three MKS MFCs are controlled manually through a control box, allowing helium flow rates 0-140 mL/min, air or nitrogen 0-100 mL/min, and carbon monoxide 0-10 mL/min. The gas streams are mixed and preheated before entering the packed bed of sorbent. At the bed outlet, the stream is monitored via the MS using Hiden MasSoft Pro on a PC. The bed temperature is regulated using a heating element with thermocouple controlled via a PID.

The system is capable of in situ activation under vacuum or inert up to 250°C. Experiments were conducted predominantly with 1% CO in air or nitrogen at a total flow rate of 50 mL/min and temperatures ranging up to 250°C on 30-100 mg samples. Breakthrough criteria were defined as 1% of the feed concentration. In the case of CO, this corresponds to 50 ppm, which is the OSHA permissible exposure limit (PEL) 8-hour time weighted average (TWA).[20]

2.3. References

(1)   Chowdhury, P.; Bikkina, C.; Meister, D.; Dreisbach, F.; Gumma, S. *Microporous Mesoporous Mat.* **2009**, *117*, 406.

(2)   Jeremias, F.; Henninger, S. K.; Janiak, C. *Chem. Commun.* **2012**, *48*, 9708.

(3)   Li, Z.-Q.; Wang, A.; Guo, C.-Y.; Tai, Y.-F.; Qiu, L.-G. *Dalton Trans.* **2013**, *42*, 13948.

(4)   Majano, G.; Perez-Ramirez, J. *Helvetica Chimica Acta* **2012**, *95*, 2278.

(5)   Majano, G.; Perez-Ramirez, J. *Advanced Materials* **2013**, *25*, 1052.

(6)   Rubes, M.; Grajciar, L.; Bludsky, O.; Wiersum, A. D.; Llewellyn, P. L.; Nachtigall, P. *ChemPhysChem* **2012**, *13*, 488.

(7)   Schlichte, K.; Kratzke, T.; Kaskel, S. *Microporous Mesoporous Mat.* **2004**, *73*, 81.

(8)   Seo, Y.-K.; Hundal, G.; Jang, I. T.; Hwang, Y. K.; Jun, C.-H.; Chang, J.-S. *Microporous Mesoporous Mat.* **2009**, *119*, 331.

(9)   Tranchemontagne, D. J.; Hunt, J. R.; Yaghi, O. M. *Tetrahedron* **2008**, *64*, 8553.

(10)   Zhuang, J.-L.; Ceglarek, D.; Pethuraj, S.; Terfort, A. *Adv. Funct. Mater.* **2011**, *21*, 1442.

(11)   Liu, J. C.; Culp, J. T.; Natesakhawat, S.; Bockrath, B. C.; Zande, B.; Sankar, S. G.; Garberoglio, G.; Johnson, J. K. *J. Phys. Chem. C* **2007**, *111*, 9305.

(12)   Cai, Y.; Zhang, Y. D.; Huang, Y. G.; Marder, S. R.; Walton, K. S. *Crystal Growth & Design* **2012**, *12*, 3709.

(13)   Cavka, J. H.; Jakobsen, S.; Olsbye, U.; Guillou, N.; Lamberti, C.; Bordiga, S.; Lillerud, K. P. *J. Am. Chem. Soc.* **2008**, *130*, 13850.

(14)   Dietzel, P. D. C.; Panella, B.; Hirscher, M.; Blom, R.; Fjellvag, H. *Chem. Commun.* **2006**, 959.

(15)   Eddaoudi, M.; Kim, J.; Rosi, N.; Vodak, D.; Wachter, J.; O'Keeffe, M.; Yaghi, O. M. *Science* **2002**, *295*, 469.

(16)   Rosi, N. L.; Kim, J.; Eddaoudi, M.; Chen, B. L.; O'Keeffe, M.; Yaghi, O. M. *J. Am. Chem. Soc.* **2005**, *127*, 1504.

(17)   Glover, T. G.; Peterson, G. W.; Schindler, B. J.; Britt, D.; Yaghi, O. *Chem. Eng. Sci.* **2011**, *66*, 163.

(18)   Schroder, F.; Fischer, R. A. In *Functional Metal-Organic Frameworks: Gas Storage, Separation and Catalysis*; Springer-Verlag Berlin: Berlin, 2010; Vol. 293, p 77.

(19)   Duren, T.; Millange, F.; Ferey, G.; Walton, K. S.; Snurr, R. Q. *J. Phys. Chem. C* **2007**, *111*, 15350.

(20)   In *29 CFR Toxic and Hazardous Substances*; OSHA: 2013.

CHAPTER 3

METAL OXIDES INCLUDED IN UIO-66 FOR ENHANCED ADSORPTION

3.1. Introduction

Metal-organic frameworks are a relatively new class of porous materials consisting of metal nodes connected via organic linkers into a wide range of crystalline geometries. The highly structured materials possess well-defined pore systems, tight pore size distributions, and, in some cases, well defined active sites attractive for targeted adsorption applications. The attractiveness of these materials is evident in the wide body of literature reporting new structures and the ever-growing body of literature investigating these materials for specific applications ranging from gas storage and separations to catalysis, sensing, and drug delivery.

However, accompanying the seemingly limitless potential MOFs possess, there are several substantial drawbacks. Many MOFs are unstable or only partially stable in humidity, restricting their utility in real-world applications such as CO_2 removal from flue gas or toxic gas removal from air. This is being addressed through several paths: by strengthening the metal-ligand bond by replacing the carboxylate linker with an imidazolate linker as in the well-known ZIFs,[1] by shielding the metal-ligand bond through functionalization with bulky groups,[2] and by using metals with higher coordination numbers to increase stability. An exemplar of this third path towards water

stability is UiO-66, a zirconium-based MOF that coordinates with benzene dicarboxylate (BDC) into a three-dimensional structure.[3] It has been shown to not only be relatively stable in humidity,[4] but also possesses a high capacity for several gases of interest, including CO_2,[5,6] NO_2,[7] and H_2.[5,8]

A unique quality to MOFs, unlike some other well-studied porous materials such as activated carbons, is that their adsorption capacity does not always scale linearly with surface area.[9] Interactions with the pore walls can be more critical than raw surface area available. For many small gas molecules, the molecules group around favorable sites along the pore walls, leaving a void space in the interior of the pore, an inefficient use of the porosity. There are several paths to reducing this void space: network interpenetration, where two or more identical networks are fractionally offset within the crystal; ligand functionalization, where functional groups are added to the structural ligands before or after synthesis; and placing something in the pore space to reduce the void and provide additional, diverse active sites. UiO-66 has been researched extensively for ligand functionalization due to the relative ease with which isostructures can be generated with functionalized BDC linkers.[10] It is also an attractive platform for impregnation. To date, the majority of studies investigating the impregnation of MOFs with nanoparticles and molecules cover noble metals such as gold,[11-15] platinum,[16-20] palladium,[21-29] copper,[30] and nickel[31] for adsorption or catalytic applications in MIL-100,[12,28] MIL-101,[1,14,16,17,19,23,30] ZIFs,[11,13] MOF-5,[21,26,31] MIL-53,[25] IRMOFs,[22] and UiO-66[15,29] or biologically relevant molecules for controlled delivery.[32,33] Relatively few studies have looked at zinc oxide,[34,35] iron oxides,[13,36] titania,[37] or vanadium oxide[38] in

MOFs for catalysis, with several more using MOFs as a sacrificial template or precursor to metal oxide formation.[39-43]

Impregnation of porous materials is conducted via gas or solution based techniques. CVD has successfully been used to impregnate MOFs with noble metals[11,44] using highly reactive, air sensitive precursors. Solution-based techniques are an attractive approach to avoid specialized sensitive precursors, as the same salts used for MOF synthesis can be used for subsequent metal oxide impregnation. There are two general types of solution-base impregnation: wet impregnation and incipient wetness impregnation.[45] Wet impregnation involves placing the MOF in a solution of low concentration precursor and mixing or sonicating to assist in pore filling. Incipient wetness involves contacting the MOF with just enough solution to fill the pores. It has been demonstrated that incipient wetness can lead to nanoparticle formation preferentially within the pore system,[46] but the lower loading associated with wet impregnation may lead to reduced pore blocking.

Metal oxides incorporated into metal-organic frameworks allude to the intimate contact between disparate oxides found in mixed metal oxides (MMOs), where the whole is quite often greater than the sum of its parts. Additionally, the pore system limits growth and agglomeration, resulting in a relatively higher portion of surface sites and defects for the included metal oxide. UiO-66 is an attractive platform for such composites as zirconia is often a substrate or component of metal oxide and mixed metal oxide systems. Magnesium and cobalt oxides and MOFs based on these metals have shown attractive adsorption characteristics towards many small molecules,[47-67] but their oxides generally

possess quite low surface areas and the MOFs are generally unstable in humidity. In particular, these materials show very high affinities for carbon monoxide in conditions under which they are stable. To couple the high affinities with a stable platform, we have impregnated UiO-66 with magnesium oxide and cobalt oxide through several pathways and investigated the impact on carbon dioxide and carbon monoxide adsorption.

3.2. Experimental Methods

3.2.1. Synthesis Procedures

Ethanol was obtained from VWR. All other chemicals were obtained from Sigma Aldrich. All chemicals were used as received. UiO-66 was synthesized as reported previously.[3] To synthesize the composite materials, UiO-66 was activated under vacuum at 200°C overnight and allowed to cool to room temperature. For wet impregnation, 5 mL of 1 or 2 M magnesium nitrate or cobalt nitrate in ethanol was added to the activated, room temperature MOF (denoted -#w). The samples were sonicated for 5 minutes and allowed to stand overnight. For incipient wetness impregnation, 1 or 2 M solution of the metal nitrate in ethanol was added to the activated MOF, with the liquid volume being just enough to fully wet the MOF (denoted –#i). The samples were left to stand overnight. Each sample was filtered and rinsed with ethanol to remove excess nitrate. When dry, the samples were heated at 5°C/min to 200°C and held there for 3 hours to decompose the nitrates.[68] Before use, each sample was activated overnight at 200°C. Samples are identified as follows: UiO-M#m, where M = Co, Mg; # denotes nitrate concentration; m=w, i for the impregnation method used. For example, UiO-Co1w denotes the sample derived from wet impregnation with 1 M $Co(NO_3)_2$ solution. For

samples with multiple impregnations, a final number is added to denote the number of impregnation steps used; UiO-Co1w2 repeats the wet impregnation with 1M solution a second time.

3.2.2. Experimental Methods

N_2 isotherms at 77K were measured on a Quantachrome Quadrasorb Porous Material Analyzer for pore structure characterization. BET surface areas were calculated over the relative pressure range 0.005-0.03. Powder X-ray diffraction profiles were measured on a PANalytical X-ray diffractometer. Carbon dioxide isotherms were measured on a Hiden IGA-001 Gas Sorption Analyzer. Carbon monoxide isotherms were measured on a lab-built pressure decay system. Metal loadings were determined via ICP-MS.

3.3. Results & Discussion

3.3.1. Composite Characterization

Initially, eight samples were synthesized, consisting of UiO impregnated with a 1 or 2 M cobalt nitrate or magnesium nitrate solution via wet impregnation or incipient wetness impregnation. All samples gained weight consistent with the addition of their respective oxides, and the cobalt oxide samples showed a color change from the pink nitrate to gray indicative of the black oxide mixed with the white UiO-66. The final compositions are listed in **Table 3.1**. Oxide loadings range from 0.1 wt% up to 4 wt%. For the cobalt samples, the highest loading corresponded to the 2M solution included via incipient wetness, with the wet samples having loadings comparable to each other. With the

Table 3.1. BET Surface Area and Metal Loadings for UiO-Metal Oxide Composites.

Sample	BET Surface Area m²/g	M*/sample mg/g	M*/Zr mol/mol
UiO-66	999		
UiO-Co1w	902	6.0	0.034
UiO-Co2w	681	5.9	0.036
UiO-Co1i	1384	3.4	0.019
UiO-Co2i	90	41.9	0.239
UiO-Mg1w	820	1.8	0.023
UiO-Mg2w	719	10.3	0.147
UiO-Mg1i	901	1.0	0.012
UiO-Mg2i	860	1.6	0.022

M=Co, Mg

magnesium samples, the maximum loading was 1 wt% for the 2M wet impregnation, with the other three cases having comparable loadings of 0.1-0.2 wt%.

Each UiO-metal oxide sample was characterized via PXRD and N_2 physisorption at 77K. PXRD shows that the UiO-66 remained intact under all treatment conditions (see **Figure 3.1**). No peaks are present that can be indexed to cobalt oxide or magnesium oxide. The lack of sufficient long-range order to register in the XRD pattern hints at dispersion of the oxides within the pore space rather than agglomeration independently from the MOF or on the particle surfaces. The obtainable BET surface areas (**Table 3.1**) are generally
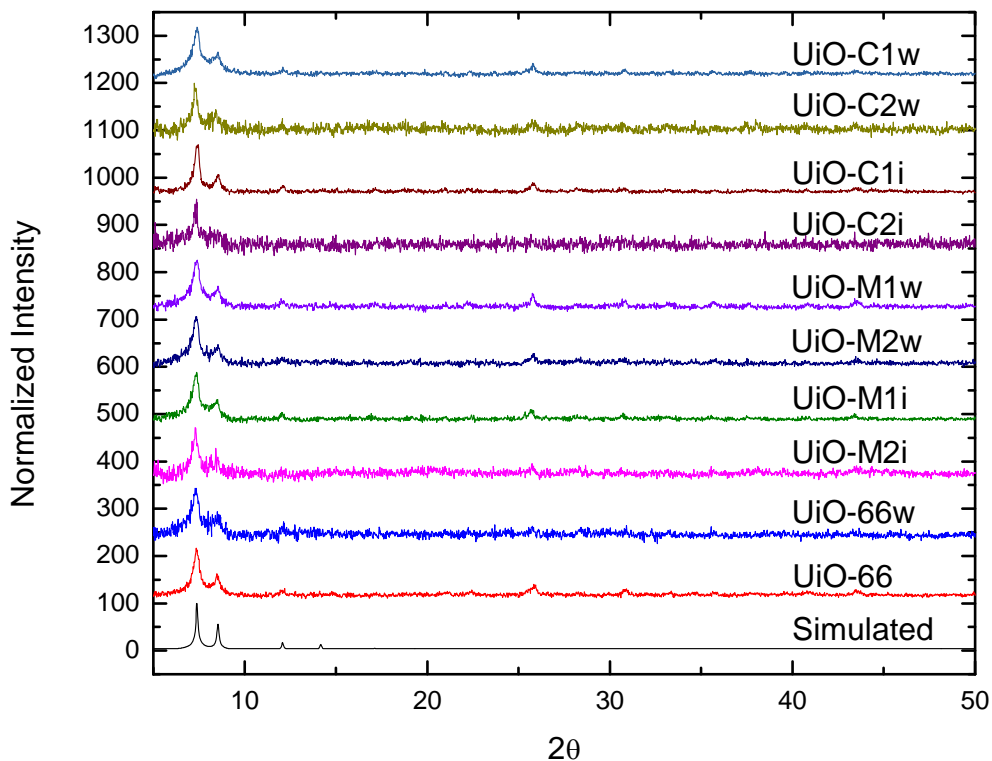
Figure 3.1. Powder XRD patterns for UiO-66 and UiO-66-Co$_3$O$_4$ and UiO-66-MgO composites.

comparable to the parent material, with a considerable loss for UiO-Co2i. This sample had the highest oxide loading, 4 wt% compared to 1 wt% or less for the other composites. Even at this relatively low loading, poor distribution within the outer layers of the MOF particles could lead to considerable pore blockage For both metals, there is generally an inverse correlation between oxide loading and BET surface area, as expected.

3.3.2. Carbon Dioxide and Carbon Monoxide Adsorption

Carbon dioxide isotherms were measured at room temperature and pressures up to 5 bar. All composites show a loss in CO$_2$ capacity compared to the parent UiO-66, with capacities ranging from 57% to 77% of the parent material at 1 bar. The UiO-Mg2w

sample shows the greatest loss in capacity (**Figure 3.2**, top), and UiO-Mg1i, which has the lowest metal loading, shows the least. UiO-Mg2w has the highest loading, corresponding to the largest loss in pore space accessibility.

In contrast with carbon dioxide, the carbon monoxide capacities at 25°C for all samples are higher or comparable to the unmodified UiO-66, as shown in **Figure 3.2** (bottom) for the UiO-MgO samples. The enhanced adsorption is sufficient to overcome the added weight of the oxide, exceeding the capacity of the parent MOF in most cases. UiO-Mg1i had the lowest oxide loading of any sample and showed the least loss in CO_2 capacity. It
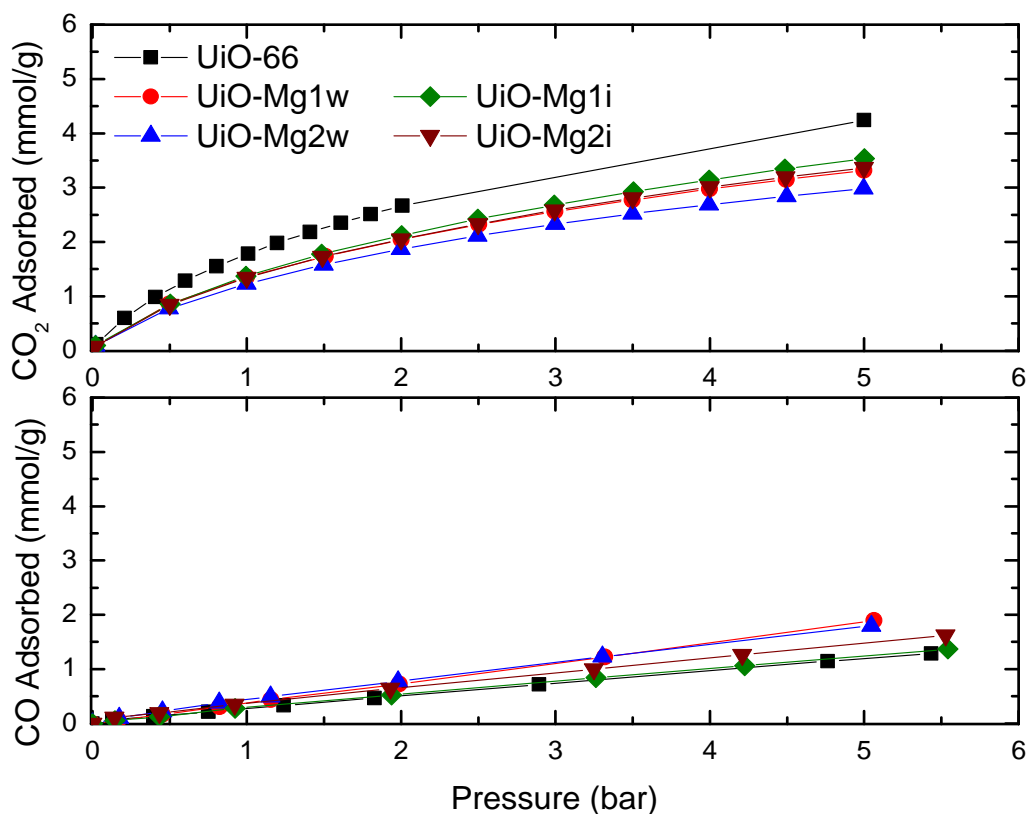
Figure 3.2. CO_2 (top) and CO (bottom) adsorption at 25°C, for UiO-MgO samples, UiO-66[10].

alone shows no enhancement in CO capacity over the parent UiO-66 across the entire

pressure range measured. Both wet-impregnated magnesium oxide samples show

increased adsorption, with UiO-Mg2w having the highest CO capacity of the magnesium

samples at 1 bar (0.45 mmol/g) and UiO-Mg1w exceeding its capacity at higher pressures

to reach 1.87 mmol/g at 5 bar. The higher metal oxide loading in UiO-Mg2w dominates

slightly in the low pressure region, but the reduced pore space is more critical at moderate

pressures. UiO-Mg2i and UiO-Mg1w have similar oxide loadings, but the sample

formed via incipient wetness has a lower CO capacity. In the case of magnesium in UiO-

66 for CO adsorption, there are no apparent benefits to incipient wetness over wet

impregnation like have been seen in metal-MOF systems.[46]

Carbon dioxide isotherms for UiO-Co samples are shown in **Figure 3.3** (top). Like UiO-

Mg, all samples show a loss in CO_2 capacity with the -Co2w sample showing the greatest

loss and the -Co1i sample, with the lowest metal loading, showing the least. In contrast

to UiO-Mg, the Co sample with the highest loading is not the sample with the lowest

capacity. This may indicate more agglomeration on the surface and subsequent pore

blocking for UiO-Co2w rather than distribution within the pore system.

For carbon monoxide in the cobalt oxide samples, all show enhancement over

unmodified UiO-66, with similar capacities above 1.5 bar, regardless of loading or

synthesis method, as shown in **Figure 3.3** (bottom). Of particular interest, in the low

pressure region below 0.5 bar (see inset), UiO-Co1w shows considerable enhancement

over all materials sampled, reaching the same capacity at 0.15 bar that is not obtained in
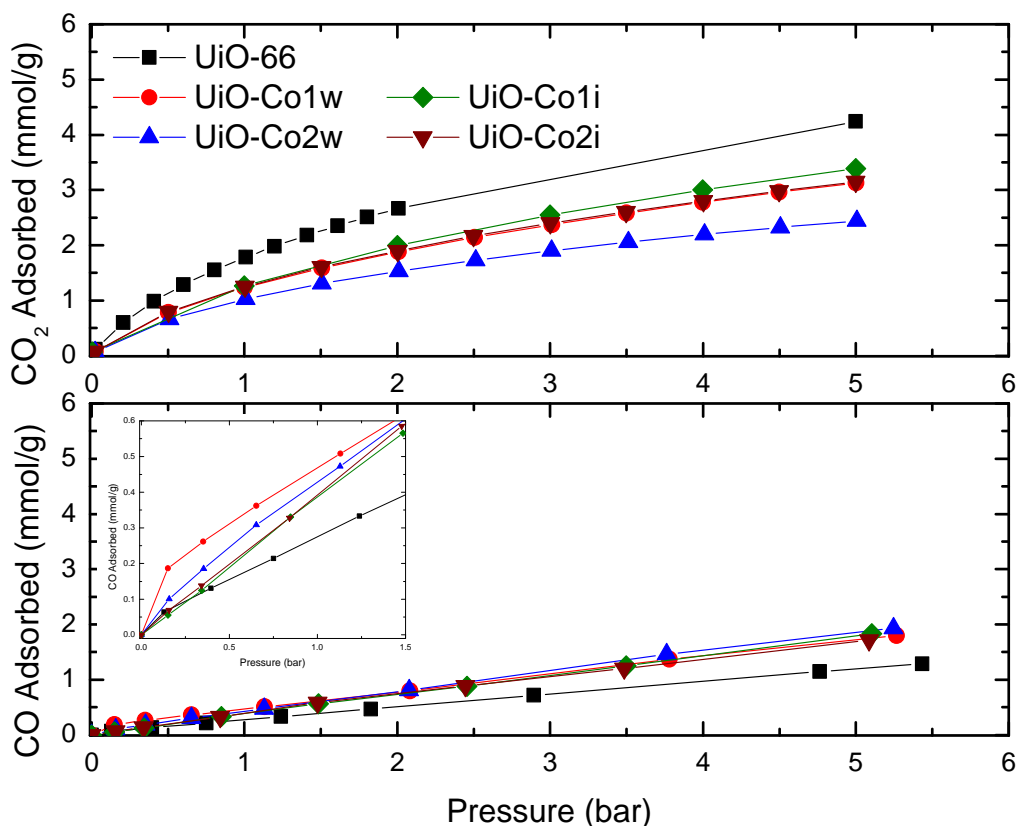
Figure 3.3. CO_2 (top) and CO (bottom) adsorption at 25°C, for $UiO-Co_3O_4$ samples, $UiO-66$[10]. Low pressure region of CO isotherm inset.

the unmodified MOF until 0.75 bar. This is of particular interest for applications involving the removal of CO from breathing air where the partial pressure of CO would likely be well below 0.15 bar. Below 1.5 bar, both wet-impregnated samples outperform the incipient wetness-impregnated samples. The varying concentration makes little difference for wet impregnation, with both having about 6 mg Co/g MOF. By 2 bar, UiO-Co2w slightly exceeds Co1w, and by 5 bar, all cobalt-containing samples reach 1.65-1.85 mmol CO/g.

In an effort to increase the loading stepwise to minimize the likelihood of agglomeration on the surface, repeat impregnation steps were conducted for -1w and -2w samples. The resulting CO capacities are shown in **Figure 3.4**. For no cases did the repeat impregnation enhance adsorption over a single impregnation step. It has been shown that solution-based impregnation generally results in particles being located within the top layer of the MOF pore system and UiO-66 possesses relatively small pores. Therefore, the oxides produced during the first round of impregnation likely block the precursors from entering the remainder of the pore system, resulting in blockage and surface agglomeration for multiple-step impregnations.
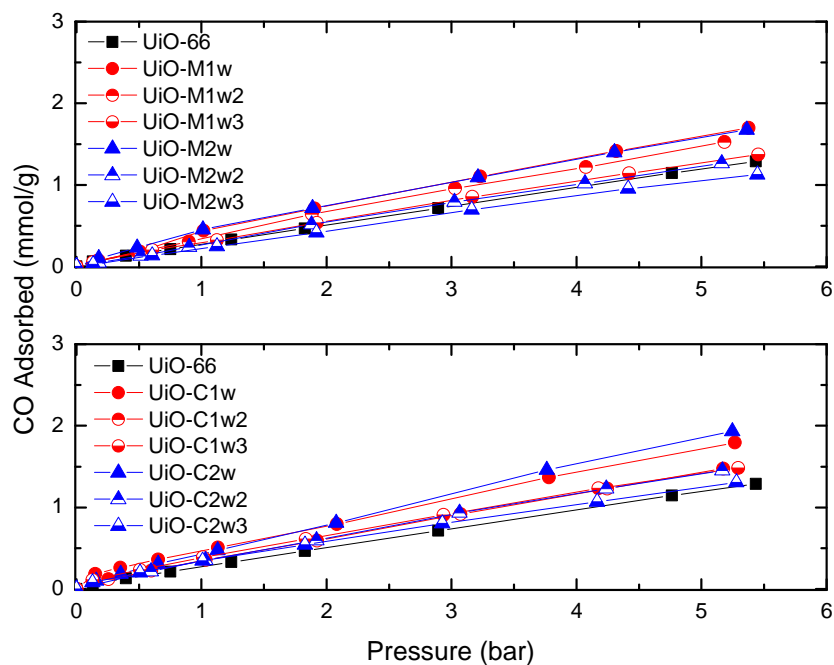
Figure 3.4. CO adsorption at 25°C, repeated impregnations

Carbon monoxide isotherms were also measured at 65°C, shown in **Figure 3.5**. All magnesium oxide samples show a decrease in carbon monoxide capacity compared to isotherms at 25°C, as expected. The general trends between the samples are unchanged.

In contrast, all cobalt oxide samples show an increase in CO capacity over isotherms measured at 25°C. At this temperature, the differences in capacity between the samples become more pronounced. UiO-Co1w, -Co2w, and -Co1i all show strong low pressure interactions, with capacities at 0.15 bar of 0.67, 0.37, and 0.87 mmol/g and at 1 bar of 1.7, 1.2, and 1.4 mmol/g respectively. The spread between the samples at 4.5 bar goes from the 0.2 mmol/g seen at 25°C to 1.75 mmol/g at 65°C, with UiO-Co2w reaching a loading of 3.75 mmol/g. At this temperature, the pore blocking apparent from the high loading of the Co2i sample is quite apparent: it is almost unchanged from the isotherm at lower temperatures.

Generally, adsorption capacity decreases with increasing temperature. The unexpected increase in capacity with increasing temperatures in the cobalt-containing samples is indicative of a transition from physisorption at 25°C to chemisorption at 65°C, with higher temperature needed to overcome the activation energy. This also implies the cobalt oxide is well-dispersed within the pore system of the UiO-66 for low metal oxide loadings as it must be highly accessible to the CO to obtain these carbon monoxide loadings.
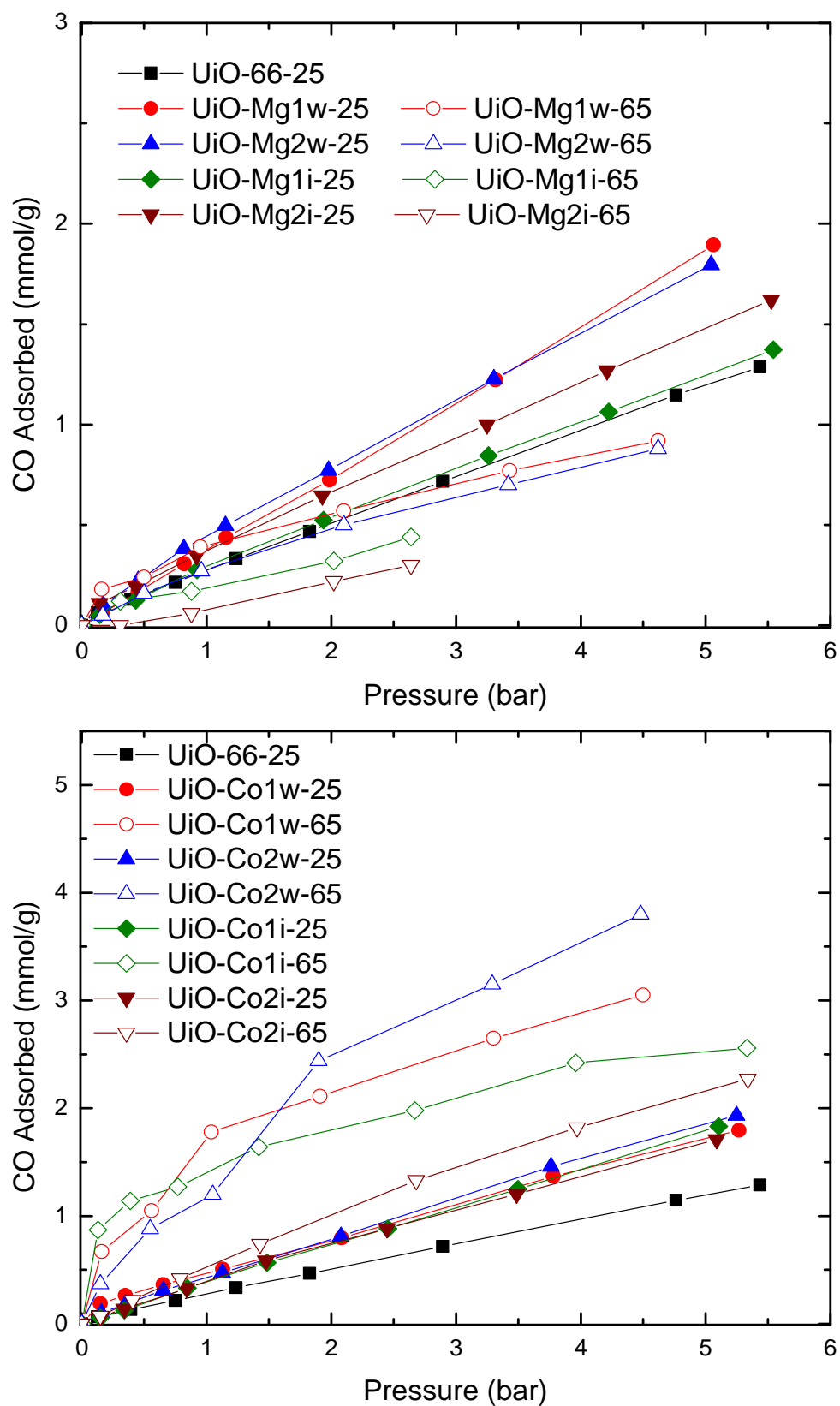
Figure 3.5. CO adsorption at 25 and 65°C.

3.4. Conclusions

Impregnating MOFs with low concentrations of metal nitrates and decomposing them in situ can successfully improve the low pressure capacity of UiO-66 towards carbon monoxide. We found a decrease in carbon dioxide capacity with particle inclusion indicative of partial blocking of the pore network. All samples considered show similar or greater carbon monoxide capacities relative to the parent UiO-66. It was found that wet impregnation techniques generally resulted in greater increases in carbon monoxide capacity at room temperature, with one cobalt-containing sample showing strong low pressure interactions with the carbon monoxide. Unexpectedly, at 65°C, the cobalt oxide-containing samples showed increased carbon monoxide capacity relative to room temperature, resulting from the onset of activated adsorption. Additional investigation into this behavior is warranted, but this implies this substrate may be attractive for carbon monoxide oxidation at moderate temperatures. This straightforward impregnation technique shows promise for increasing the adsorbate-adsorbent interactions in porous materials while minimally impacting the pore structure or overall material weight.

3.5. References

(1)   Park, K. S.; Ni, Z.; Cote, A. P.; Choi, J. Y.; Huang, R. D.; Uribe-Romo, F. J.; Chae, H. K.; O'Keeffe, M.; Yaghi, O. M. *Proc. Natl. Acad. Sci. U. S. A.* **2006**, *103*, 10186.

(2)   Jasuja, H.; Huang, Y. G.; Walton, K. S. *Langmuir* **2012**, *28*, 16874.

(3)   Cavka, J. H.; Jakobsen, S.; Olsbye, U.; Guillou, N.; Lamberti, C.; Bordiga, S.; Lillerud, K. P. *J. Am. Chem. Soc.* **2008**, *130*, 13850.

(4)   DeCoste, J. B.; Peterson, G. W.; Schindler, B. J.; Killops, K. L.; Browe, M. A.; Mahle, J. J. *Journal of Materials Chemistry A* **2013**, *1*, 11922.

(5)   Abid, H. R.; Tian, H. Y.; Ang, H. M.; Tade, M. O.; Buckley, C. E.; Wang, S. B. *Chem. Eng. J.* **2012**, *187*, 415.

(6)   Yang, Q. Y.; Guillerm, V.; Ragon, F.; Wiersum, A. D.; Llewellyn, P. L.; Zhong, C. L.; Devic, T.; Serre, C.; Maurin, G. *Chem. Commun.* **2012**, *48*, 9831.

(7)   Ebrahim, A. M.; Levasseur, B.; Bandosz, T. J. *Langmuir* **2013**, *29*, 168.

(8)   Zhao, Q.; Yuan, W.; Liang, J. M.; Li, J. P. *International Journal of Hydrogen Energy* **2013**, *38*, 13104.

(9)   *Metal-Organic Frameworks*; Farrusseng, D., Ed.; Wiley-VCH Verlag & Co: Weinheim, Germany, 2011.

(10)   Cmarik, G. E.; Kim, M.; Cohen, S. M.; Walton, K. S. *Langmuir* **2012**, *28*, 15606.

(11)   Esken, D.; Turner, S.; Lebedev, O. I.; Van Tendeloo, G.; Fischer, R. A. *Chem. Mat.* **2010**, *22*, 6393.

(12)   Ke, F.; Zhu, J. F.; Qiu, L. G.; Jiang, X. *Chem. Commun.* **2013**, *49*, 1267.

(13)   Lu, G.; Li, S. Z.; Guo, Z.; Farha, O. K.; Hauser, B. G.; Qi, X. Y.; Wang, Y.; Wang, X.; Han, S. Y.; Liu, X. G.; DuChene, J. S.; Zhang, H.; Zhang, Q. C.; Chen, X. D.; Ma, J.; Loo, S. C. J.; Wei, W. D.; Yang, Y. H.; Hupp, J. T.; Huo, F. W. *Nat. Chem.* **2012**, *4*, 310.

(14)   Gu, X. J.; Lu, Z. H.; Jiang, H. L.; Akita, T.; Xu, Q. *J. Am. Chem. Soc.* **2011**, *133*, 11822.

(15)   Wu, R. B.; Qian, X. K.; Zhou, K.; Liu, H.; Yadian, B.; Wei, J.; Zhu, H. W.; Huang, Y. Z. *Journal of Materials Chemistry A* **2013**, *1*, 14294.

(16)   Aijaz, A.; Akita, T.; Tsumori, N.; Xu, Q. *J. Am. Chem. Soc.* **2013**, *135*, 16356.

(17)   Khajavi, H.; Stil, H. A.; Kuipers, H.; Gascon, J.; Kapteijn, F. *ACS Catal.* **2013**, *3*, 2617.

(18)   Pan, H. Y.; Li, X. H.; Zhang, D. M.; Guan, Y. J.; Wu, P. *J. Mol. Catal. A-Chem.* **2013**, *377*, 108.

(19)   Pan, Y. Y.; Ma, D. Y.; Liu, H. M.; Wu, H.; He, D. H.; Li, Y. W. *J. Mater. Chem.* **2012**, *22*, 10834.

(20)   Wang, P.; Zhao, J.; Li, X. B.; Yang, Y.; Yang, Q. H.; Li, C. *Chem. Commun.* **2013**, *49*, 3330.

(21)   Esken, D.; Zhang, X.; Lebedev, O. I.; Schroder, F.; Fischer, R. A. *J. Mater. Chem.* **2009**, *19*, 1314.

(22)   Gutierrez, I.; Diaz, E.; Ordonez, S. *Thermochim. Acta* **2013**, *567*, 79.

(23)   Hermannsdofer, J.; Kempe, R. *Chemistry-a European Journal* **2011**, *17*, 8071.

(24)   Huang, Y. B.; Lin, Z. J.; Cao, R. *Chemistry-a European Journal* **2011**, *17*, 12706.

(25)   Huang, Y. B. A.; Zheng, Z. L.; Liu, T. F.; Lu, J.; Lin, Z. J.; Li, H. F.; Cao, R. *Catal. Commun.* **2011**, *14*, 27.

(26)   Sabo, M.; Henschel, A.; Froede, H.; Klemm, E.; Kaskel, S. *J. Mater. Chem.* **2007**, *17*, 3827.

(27)   Zhang, L. J.; Su, Z. X.; Jiang, F. L.; Zhou, Y. F.; Xu, W. T.; Hong, M. C. *Tetrahedron* **2013**, *69*, 9237.

(28)   Zlotea, C.; Campesi, R.; Cuevas, F.; Leroy, E.; Dibandjo, P.; Volkringer, C.; Loiseau, T.; Ferey, G.; Latroche, M. *J. Am. Chem. Soc.* **2010**, *132*, 2991.

(29)   Shen, L. J.; Wu, W. M.; Liang, R. W.; Lin, R.; Wu, L. *Nanoscale* **2013**, *5*, 9374.

(30)   Wu, F.; Qiu, L. G.; Ke, F.; Jiang, X. *Inorg. Chem. Commun.* **2013**, *32*, 5.

(31)   Zhao, H. H.; Song, H. L.; Chou, L. J. *Inorg. Chem. Commun.* **2012**, *15*, 261.

(32)   Cunha, D.; Gaudin, C.; Colinet, I.; Horcajada, P.; Maurin, G.; Serre, C. *J. Mat. Chem. B* **2013**, *1*, 1101.

(33)   Devautour-Vinot, S.; Martineau, C.; Diaby, S.; Ben-Yahia, M.; Miller, S.; Serre, C.; Horcajada, P.; Cunha, D.; Taulelle, F.; Maurin, G. *J. Phys. Chem. C* **2013**, *117*, 11694.

(34)   Muller, M.; Turner, S.; Lebedev, O. I.; Wang, Y. M.; van Tendeloo, G.; Fischer, R. A. *Eur. J. Inorg. Chem.* **2011**, 1876.

(35)   Muller, M.; Lebedev, O. I.; Fischer, R. A. *J. Mater. Chem.* **2008**, *18*, 5274.

(36)   Zhang, T.; Zhang, X. F.; Yan, X. J.; Kong, L. Y.; Zhang, G. C.; Liu, H. O.; Qiu, J. S.; Yeung, K. L. *Chem. Eng. J.* **2013**, *228*, 398.

(37)   Muller, M.; Zhang, X. N.; Wang, Y. M.; Fischer, R. A. *Chem. Commun.* **2009**, 119.

(38)   Fazaeli, R.; Aliyan, H.; Moghadam, M.; Masoudinia, M. *J. Mol. Catal. A-Chem.* **2013**, *374*, 46.

(39)   Zamaro, J. M.; Perez, N. C.; Miro, E. E.; Casado, C.; Seoane, B.; Tellez, C.; Coronas, J. *Chem. Eng. J.* **2012**, *195*, 180.

(40)   Kim, J. Y.; Jin, M.; Lee, K. J.; Cheon, J. Y.; Joo, S. H.; Kim, J. M.; Moon, H. R. *Nanoscale Res. Lett.* **2012**, *7*.

(41)   Das, R.; Pachfule, P.; Banerjee, R.; Poddar, P. *Nanoscale* **2012**, *4*, 591.

(42)   Akhbari, K.; Morsali, A. *J. Coord. Chem.* **2011**, *64*, 3521.

(43)   Qin, F. X.; Jia, S. Y.; Liu, Y.; Han, X.; Ren, H. T.; Zhang, W. W.; Hou, J. W.; Wu, S. H. *Mater. Lett.* **2013**, *101*, 93.

(44)   Turner, S.; Lebedev, O. I.; Schroder, F.; Esken, D.; Fischer, R. A.; Van Tendeloo, G. *Chem. Mat.* **2008**, *20*, 5622.

(45)   Schroder, F.; Fischer, R. A. In *Functional Metal-Organic Frameworks: Gas Storage, Separation and Catalysis*; Springer-Verlag Berlin: Berlin, 2010; Vol. 293, p 77.

(46)   El-Shall, M. S.; Abdelsayed, V.; Khder, A.; Hassan, H. M. A.; El-Kaderi, H. M.; Reich, T. E. *J. Mater. Chem.* **2009**, *19*, 7625.

(47)   Caskey, S. R.; Wong-Foy, A. G.; Matzger, A. J. *J. Am. Chem. Soc.* **2008**, *130*, 10870.

(48)   Cho, H.-Y.; Yang, D.-A.; Kim, J.; Jeong, S.-Y.; Ahn, W.-S. *Catalysis Today* **2012**, *185*, 35.

(49)   Dietzel, P. D. C.; Besikiotis, V.; Blom, R. *J. Mater. Chem.* **2009**, *19*, 7362.

(50)   Garcia, E. J.; Mowat, J. P. S.; Wright, P. A.; Perez-Pellitero, J.; Jallut, C.; Pirngruber, G. D. *J. Phys. Chem. C* **2012**, *116*, 26636.

(51)   Glover, T. G.; Peterson, G. W.; Schindler, B. J.; Britt, D.; Yaghi, O. *Chem. Eng. Sci.* **2011**, *66*, 163.

(52)   Herm, Z. R.; Krishna, R.; Long, J. R. *Microporous Mesoporous Mat.* **2012**, *151*, 481.

(53)   Liu, J.; Tian, J.; Thallapally, P. K.; McGrail, B. P. *J. Phys. Chem. C* **2012**, *116*, 9575.

(54)   Valenzano, L.; Civalleri, B.; Sillar, K.; Sauer, J. *J. Phys. Chem. C* **2011**, *115*, 21777.

(55)   Yu, K.; Kiesling, K.; Schmidt, J. R. *J. Phys. Chem. C* **2012**, *116*, 20480.

(56)   Zhou, W.; Wu, H.; Yildirim, T. *J. Am. Chem. Soc.* **2008**, *130*, 15268.

(57)   Bhagiyalakshmi, M.; Lee, J. Y.; Jang, H. T. *International Journal of Greenhouse Gas Control* **2010**, *4*, 51.

(58) Deng, J. G.; Zhang, L.; Dai, H. X.; Xia, Y. S.; Jiang, H. Y.; Zhang, H.; He, H. *J. Phys. Chem. C* **2010**, *114*, 2694.

(59) Garcia, T.; Agouram, S.; Sanchez-Royo, J. F.; Murillo, R.; Mastral, A. M.; Aranda, A.; Vazquez, I.; Dejoz, A.; Solsona, B. *Appl. Catal. A-Gen.* **2010**, *386*, 16.

(60) Khodakov, A. Y.; Zholobenko, V. L.; Bechara, R.; Durand, D. *Microporous Mesoporous Mat.* **2005**, *79*, 29.

(61) Lopes, I.; Davidson, A.; Thomas, C. *Catal. Commun.* **2007**, *8*, 2105.

(62) Roggenbuck, J.; Koch, G.; Tiemann, M. *Chem. Mat.* **2006**, *18*, 4151.

(63) Rumplecker, A.; Kleitz, F.; Salabas, E. L.; Schuth, F. *Chem. Mat.* **2007**, *19*, 485.

(64) Shu, P.; Ruan, J. F.; Gao, C. B.; Li, H. C.; Che, S. N. *Microporous Mesoporous Mat.* **2009**, *123*, 314.

(65) Wang, G. X.; Liu, H.; Horvat, J.; Wang, B.; Qiao, S. Z.; Park, J.; Ahn, H. *Chemistry-a European Journal* **2010**, *16*, 11020.

(66) Xia, Y. S.; Dai, H. X.; Jiang, H. Y.; Zhang, L. *Catal. Commun.* **2010**, *11*, 1171.

(67) Zhang, H. J.; Tao, H. H.; Jiang, Y.; Jiao, Z.; Wu, M. H.; Zhao, B. *J. Power Sources* **2010**, *195*, 2950.

(68) Roggenbuck, J.; Waitz, T.; Tiemann, M. *Microporous Mesoporous Mat.* **2008**, *113*, 575.

(69) Jiang, D. E.; Dai, S. *Phys. Chem. Chem. Phys.* **2011**, *13*, 978.

(70) Pang, X. Y.; Liu, C.; Li, D. C.; Lv, C. Q.; Wang, G. C. *ChemPhysChem* **2013**, *14*, 204.

(71) Royer, S.; Duprez, D. *ChemCatChem* **2011**, *3*, 24.

(72) Wang, H. F.; Kavanagh, R.; Guo, Y. L.; Guo, Y.; Lu, G. Z.; Hu, P. *J. Catal.* **2012**, *296*, 110.

(73) In *NIST Standard Reference Database*; National Institute of Standards and Technology; Vol. 2010.

CHAPTER 4

CARBON MONOXIDE OXIDATION ON A NOVEL HKUST-1-TITANIA COMPOSITE

4.1. Introduction

Metal-organic frameworks (MOFs) show promise in a wide array of gas separation and storage applications due to their crystalline structures with tight pore size distributions, high surface areas and pore volumes, and tunable functionality through ligand and metal selection. Much interest has been expressed in rationally designing MOFs to target specific small molecules such as CO_2, H_2, CH_4, CO, NH_3, SO_2, for specific energy-related separations and toxic gas remediation. HKUST-1 is an iconic open-metal site MOF consisting of copper paddle-wheel clusters connected into a three-dimensional framework via benzenetricarboxlyate linkers. It has been widely studied for adsorption and catalytic applications and can be synthesized under a wide variety of conditions.[1-9] HKUST-1 has been grown on supports, including silicon,[10] alumina,[11,12] gold,[8,12] copper,[7] and silica,[12-15] with varying functional groups on the support in some cases. In this work, instead of using a flat oxide support, we use the surface of preformed titania particles to grow HKUST-1, with the intent of encapsulating the titania within the structure of the MOF, as has been done previously with gold[16] and platinum[17] nanoparticles.

Carbon monoxide removal from gas mixtures is relevant to a wide range of applications, including energy and industrial applications. However, the application of interest here is

air purification: removing toxic CO from an air stream at low concentration and pressure. Of particular interest are two applications: personal respirators operating at ambient temperature and larger beds associated with fixed sites or vehicles where waste heat from HVAC or other systems may be available.[18-21] Carbon monoxide adsorption and catalysis has been studied on HKUST-1;[9,22-24] materials supported on HKUST-1, including PdO_2[25] and Ag;[26] and the decomposition products of HKUST-1.[27] PdO_2 on amorphized HKUST-1 reaches 100% conversion by 220°C, a 20°C decrease over the unmodified MOF.[25] In the case of Ag, the HKUST-1 is pre-treated with oxygen, resulting in a loss of MOF structure and an appearance of copper and silver oxides.[26] The untreated HKUST-1 shows no activity at the temperatures measured (below 140°C). The oxidized HKUST-1 reaches 100% conversion by 140°C, and the addition of 5% Ag reduces that by an additional 20°C. The onset of oxidation is reduced from 90°C for the oxidized HKUST-1 to 50°C for Ag/HKUST-1.

Titania is a common support for nanoparticles for carbon monoxide oxidation and other catalytic reactions,[28,29] showing little activity towards CO oxidation on its own but enhancing the activity of the supported material, with CuO/TiO_2 showing higher activity than other metal oxide systems, with an onset temperature around 60°C and complete conversion of CO reached around 150°C.[30] In another study looking at copper oxide supported on titania and zirconia alloys, the CuO/TiO_2 system reached complete conversion at about 200°C, with an onset temperature around 50°C.[31] In this work, we investigate the synergistic effect expected from the intimate contact between disparate

metals commonly found in mixed metal oxides in a MOF system by combining the open metal sites of HKUST-1 with included titania.

4.2. Materials and Experimental Methods

4.2.1. Material Synthesis

$Cu(NO_3)_2 \bullet 6H_2O$ and 1,3,5-benzenetricarboxylic acid (BTC) were obtained from Sigma Aldrich. Titania was obtained from City Chemical. Ethanol was obtained from VWR. All chemicals were used as received. HKUST-1+TiO_2 was synthesized on a variation of the literature procedure for HKUST-1:[1] $Cu(NO_3)_2$ (0.8754 g) in H_2O (12 mL) was combined with 1,3,5-benzenetricarboxylic acid (BTC) (0.4034 g) in ethanol (12 mL). The solutions were then mixed and stirred for 30 min, after which TiO_2 (0.005 g) was added. This was kept at 120°C under constant stirring for 15 hours. The resulting material was washed several times with ethanol before drying. HKUST-1 was synthesized similarly without the addition of TiO_2. Samples were activated at 250°C for 18 hours prior to adsorption experiments.

4.2.2. Experimental Methods

N_2 isotherms at 77K were measured on a Quantachrome Quadrasorb Porous Material Analyzer for pore structure characterization. BET surface areas were calculated over the relative pressure range 0.005-0.03. Powder X-ray diffraction profiles were measured on a PANalytical X-ray diffractometer. Carbon dioxide isotherms were measured on a

Hiden IGA-001 Gas Sorption Analyzer. Carbon monoxide isotherms were measured on a lab-built pressure decay system.

4.2.3. Breakthrough Measurements

Breakthrough was measured on a lab-built system consisting of MKS mass flow controllers feeding a packed powder bed (20-60 mg sample) with a Hiden DSMS as the outlet detector. Samples were activated under He flowing at 50 mL/min. The test gases consisted of 1% CO in air at a total flow rate of 50 mL/min. Breakthrough criteria are defined as 5% of the total CO flow rate, which corresponds to the exposure limit. The m/e monitored are 4 (He), 12 (CO and CO_2), 14 (N_2), 28 (N_2 and CO), 32 (O_2), and 44 (CO_2).

4.3. Results

4.3.1. Material Characterization

Four materials were considered in this work: unmodified HKUST-1 synthesized in an identical method to the composite, unmodified TiO_2, the MOF-oxide composite (HKUST-1+TiO_2), and a physical mixture of as-synthesized HKUST-1 and the unmodified TiO_2 (HKUST-1&TiO_2) in the same ratio as the composite. The physical mixture was investigated in part to determine if the closer contact and confinement effects expected in the composite provided benefit over merely adding the materials together.

The crystal structure and pore characteristics of HKUST-1 were minimally impacted under the synthesis conditions with the titania present (HKUST-1+TiO_2). PXRD of HKUST-1+TiO_2 shows no titania peaks while HKUST-1&TiO_2 containing the same weight percent titania as the composite shows peaks at 27 and 36 (**Figure 4.1**). This lack of distinct long range order assignable to the titania indicates the nanoparticles are well dispersed throughout the MOF network in the composite. There is a slight loss in the calculated surface area per unit mass (**Table 4.1**), as would be expected with the addition of the titania and associated structural defects with its inclusion within the pore system, and a slight hysteresis in the N_2 isotherm (**Figure 4.2**) indicates there could be partial blockage of the MOF pore system.
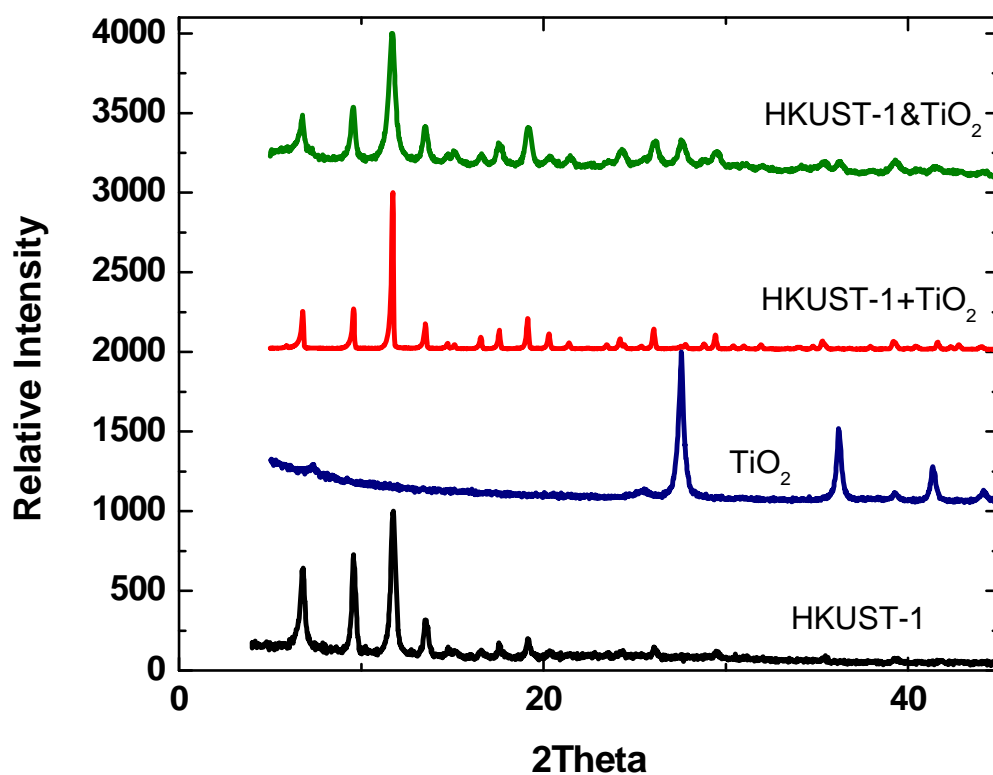
Figure 4.1. PXRD of HKUST-1, HKUST-1+TiO_2, HKUST-1&TiO_2, and TiO_2.

Table 4.1. HKUST-1, Composite, and Physical Mixture Characterization as Synthesized and After CO Isotherms at 25°C.

	BET Surface Area (m^2/g)		Pore Volume (cc/g)	
	As synthesized	After CO[a]	As synthesized	After CO[a]
HKUST-1	1574-1790	1477	0.78-1.1	0.78
HKUST-1+TiO$_2$	999	1192	0.76	0.64
HKUST-1&TiO$_2$	1651	1317	0.84	0.67

[a] after CO isotherm 0-5 bar, 25°C.
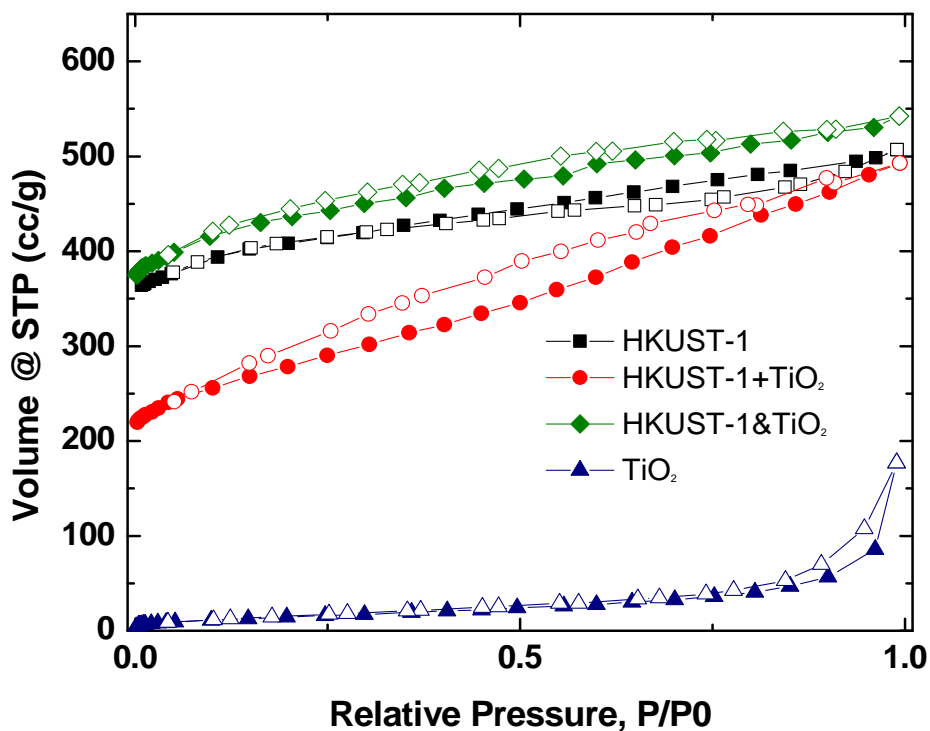
Figure 4.2. N$_2$ isotherms at 77K on as-synthesized HKUST-1, HKUST-1+TiO$_2$, HKUST-1&TiO$_2$, and TiO$_2$.

4.3.2. Carbon Dioxide & Carbon Monoxide Adsorption

Adsorption isotherms were measured for carbon dioxide and carbon monoxide at 25°C

for all materials. The addition of titania with either method does not lower the carbon

dioxide capacity of HKUST-1, nor is any significant enhancement seen; the bulk of the

HKUST-1 pore system remains accessible at room temperature conditions (**Figure 4.3**),

but the addition of the titania does not enhance CO_2 adsorption. For carbon monoxide,

the composite exhibits slightly less capacity than HKUST-1 (**Figure 4.4**). However,

surface areas calculated on the carbon monoxide-exposed samples show the composite

material underwent slight structural changes not seen in the HKUST-1 or HKUST-

1&TiO_2. HKUST-1 and HKUST-1&TiO_2 show a slight decrease in surface area while

HKUST-1+TiO_2 shows a gain in surface area and loss of hysteresis. Carbon monoxide
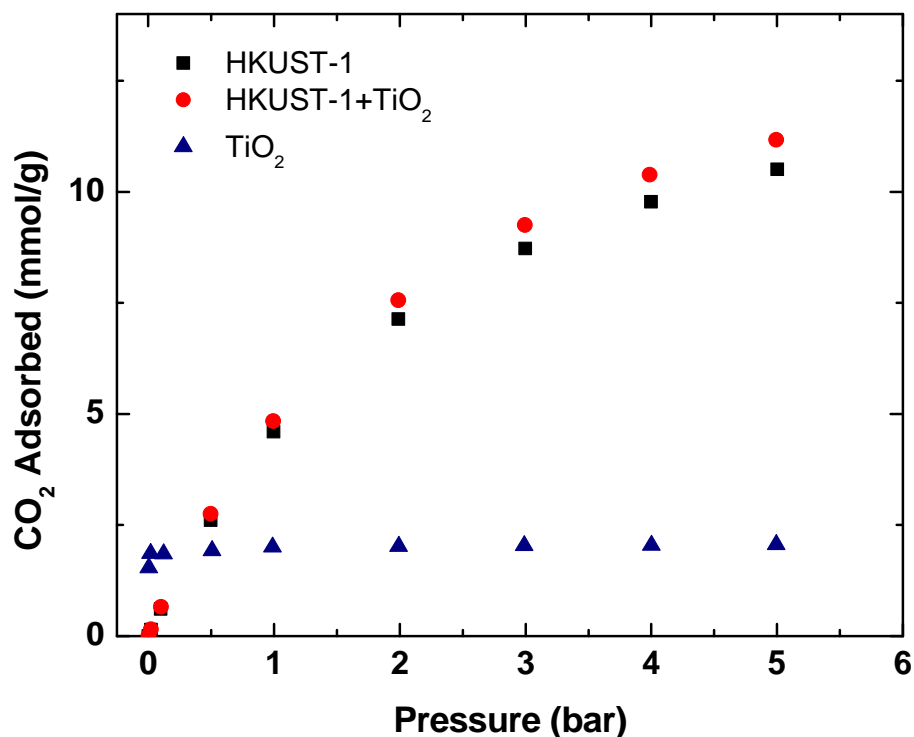
Figure 4.3. CO_2 adsorption on HKUST-1, HKUST-1+TiO_2, and TiO_2 at 25°C.
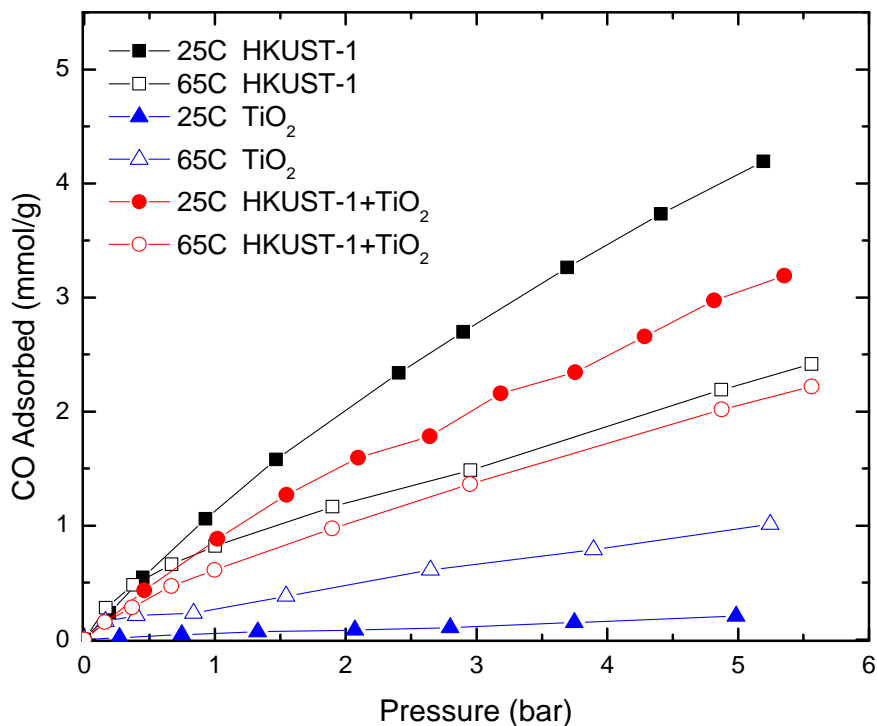
Figure 4.4. CO adsorption on HKUST-1, HKUST-1+TiO₂, and TiO₂ at 25°C and 65°C.

isotherms were also measured at 45 and 65°C on the MOF and composite materials

(**Figure 4.4**). The differences between the MOF and composite decrease with increasing

temperature due to the capacity of the included TiO₂ increasing with temperature in this

range.

4.3.3. Breakthrough

4.3.3.1. Comparison of Composite to Parent Materials

Breakthrough experiments were conducted with carbon monoxide and air to investigate

the potential of these materials for air purification and the oxidation of carbon monoxide

to carbon dioxide. Initial investigations were conducted at 25°C and 250°C, the

temperature at which all samples were activated. At each temperature, the materials were

tested under three sets of conditions: (i) no pretreatment (air and carbon monoxide turned

on simultaneously) to test dynamic separation, (ii) pre-saturation with air to mimic a

respirator or other air purification process, and (iii) pre-saturation with carbon monoxide

for comparison with the proposed mechanism of CO oxidation on HKUST-1.[22] The

carbon monoxide breakthrough times, defined as the time required for the outlet stream to

reach 5% of the inlet (50 ppm), are summarized in **Table 4.2** for all conditions. At room

temperature, the unmodified HKUST-1 has the longest breakthrough time for both the

case of no pretreatment and pretreatment with air (**Figure 4.5**). However, in the case of

pretreatment with carbon monoxide, the breakthrough time for the composite material is

Table 4.2. CO Breakthrough times Without Pretreatment and After Pretreatment with Air or Carbon Monoxide.

	25°C			250°C		
	No Pretreat (min/g)	Air Pretreat (min/g)	Carbon Monoxide Pretreat (min/g)	No Pretreat (min/g)	Air Pretreat (min/g)	Carbon Monoxide Pretreat (min/g)
HKUST-1	148.6	159.2	77.2	149.1	162.8	54.7
TiO$_2$	91.2	101.6	77.7	159.1	178.5	102.4
HKUST-1 +TiO$_2$	120.1	107.5	135.2	180.2	n/a	144.9
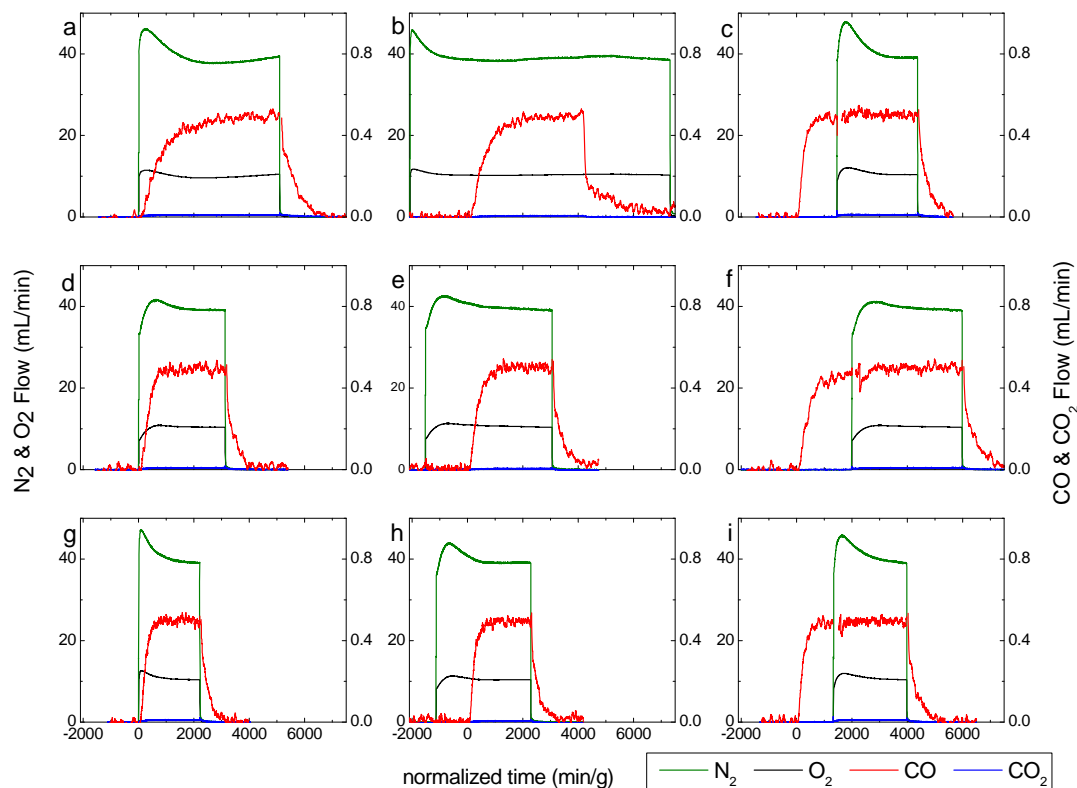
Figure 4.5. Breakthrough at 25°C: Row 1 (a, b, c): HKUST-1, Row 2 (d, e, f): HKUST-1+TiO$_2$, Row 3 (g, h, i): TiO$_2$; Column 1 (a, d, g): no pretreatment, Column2 (b, e, h): pretreated with air, Column 3 (c, f, i): pretreated with CO.

almost double that of either parent material (135 min/g for composite vs ~77 min/g for

each parent).

At 250°C (**Figure 4.6**), the trends change: in the case of no pretreatment, the composite

performs marginally better with respect to breakthrough times and considerably better

(almost 3x longer) in the case of pretreatment with carbon monoxide. At 250°C,

appreciable quantities of carbon dioxide are detected in the outlet stream for both the

parent MOF alone and the composite (**Table 4.3**). For HKUST-1, approximately 60% of

the carbon monoxide is oxidized with no pretreatment or carbon monoxide pretreatment
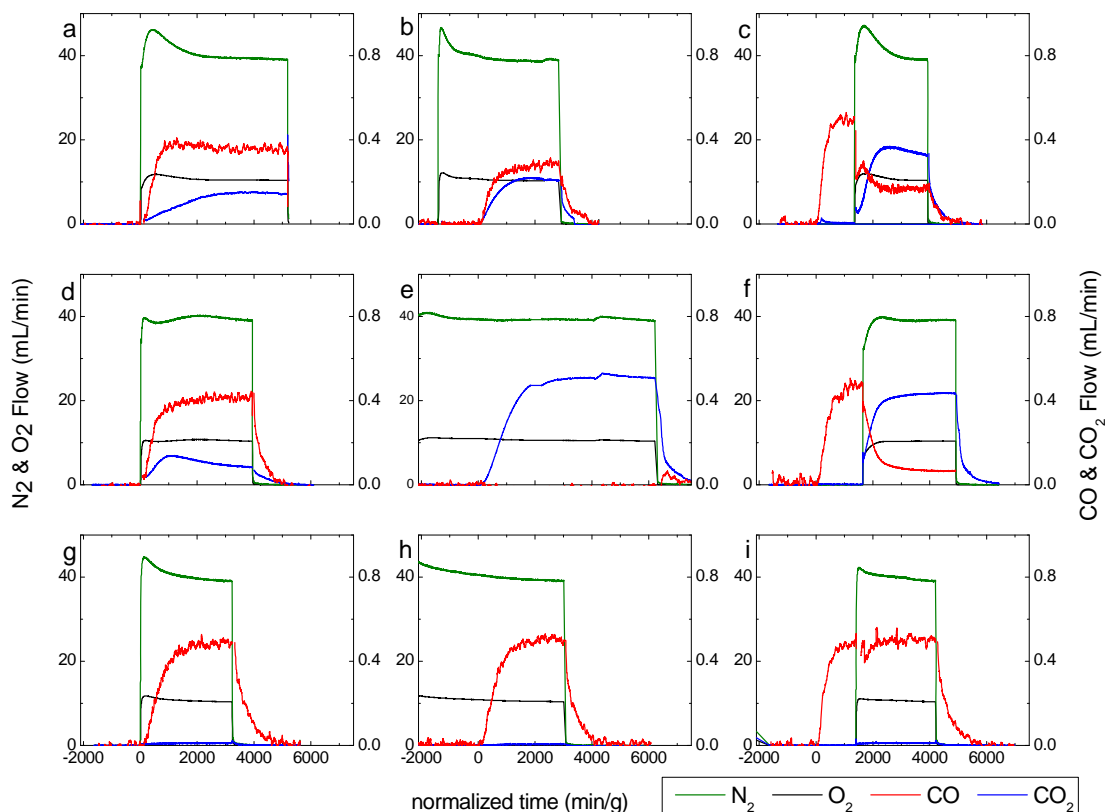
Figure 4.6. Breakthrough at 250°C: Row 1 (a, b, c): HKUST-1, Row 2 (d, e, f): HKUST-1+TiO2, Row 3 (g, h, i): TiO2; Column 1 (a, d, g): no pretreatment, Column2 (b, e, h): pretreated with air, Column 3 (c, f, i): pretreated with CO.

with a slightly lower level of activity in the case of air pretreatment, about 40%. The composite material performs similarly when pretreated with carbon monoxide and worse in the absence of pretreatment. However, in the most realistic case for air purification applications, where the material is pre-saturated with air, the composite material shows almost complete conversion of the carbon monoxide to air.

These results for pure HKUST-1 contrast with previously published results showing complete conversion with HKUST-1 activated under similar conditions by 170°C on lower-surface area material,[23] but agree with findings showing the onset of oxidation

Table 4.3. CO_2 Detected in Outlet Stream.

	25°C			250°C		
	No Pretreat mL / min	Air Pretreat mL / min	Carbon Monoxide Pretreat mL / min	No Pretreat mL / min	Air Pretreat mL / min	Carbon Monoxide Pretreat mL / min
HKUST-1	0.01	0.01	0.01	0.30	0.21	0.33
TiO_2	0.01	0.01	0.01	0.01	0.01	0.01
HKUST-1+TiO_2	0.01	0.01	0.01	0.14	0.53	0.32

above 200°C.[25] The catalytic activity of the material is attributed to both the framework

copper sites and defects, and copper oxide impurities. In fact, amorphized HKUST-1

shows higher catalytic activity than the as-synthesized material,[25] which agrees with other

studies showing higher catalytic activity on the MOF "activated" above its decomposition

temperature.[23] The differences in surface area can be attributed to a difference in

impurities and defects from the different synthesis methods. Due to the constraints on

synthesis conditions necessary to synthesize the composite, optimizing the HKUST-1

was not possible, and it was decided that maintaining consistency in the methods used for

the composite and parent HKUST-1 would allow more relevant comparisons to

determine the relative activity of the composite.

A mechanism for CO oxidation on HKUST-1 has been proposed[22] in which carbon

monoxide adsorbed on two adjacent copper paddlewheel clusters and interacts with a

single gas-phase O_2 molecule. Under this hypothesis, and in agreement with their low temperature experiments, HKUST-1 pre-treated with CO should show higher activity than the other experimental conditions. Our experiments with pure HKUST-1 at 250°C support this hypothesis: carbon monoxide pre-treated samples show slightly higher oxidation than un-pre-treated samples, and both show higher activity than the samples pretreated with air, where the CO must displace O_2 from adjacent copper paddlewheel sites before oxidation may occur. However, with the inclusion of TiO_2, this trend no longer holds. Instead, pre-treatment with CO increases the oxidation over the untreated samples, but the samples pre-treated with air show much greater oxidation instead of less. As has been shown in previous work with carbon monoxide in the presence of TiO_2, titania can act as a source of oxygen[32] or provide nearby sites for O_2 adsorption.[29] Therefore, the close proximity of the oxygen contributor to the copper paddlewheel clusters can enhance oxidation since the hypothesized requirement for adjacent copper sites to be filled by the CO followed by oxygen approaching in the proper orientation is relaxed.

4.3.3.2. Additional Temperatures with Composite

Based on these results, further investigations of the composite material consisted of additional tests under air pretreatment conditions with increasing temperatures at 50°C intervals to gain a better understanding of the necessary temperatures to activate the reaction (**Figure 4.7**). At 50 and 100°C, essentially no carbon dioxide is detected at the outlet of the bed. By 150°C and continuing to 200°C, approximately 3/5 of the carbon monoxide is being converted, indicating partial conversion can be obtained at these lower
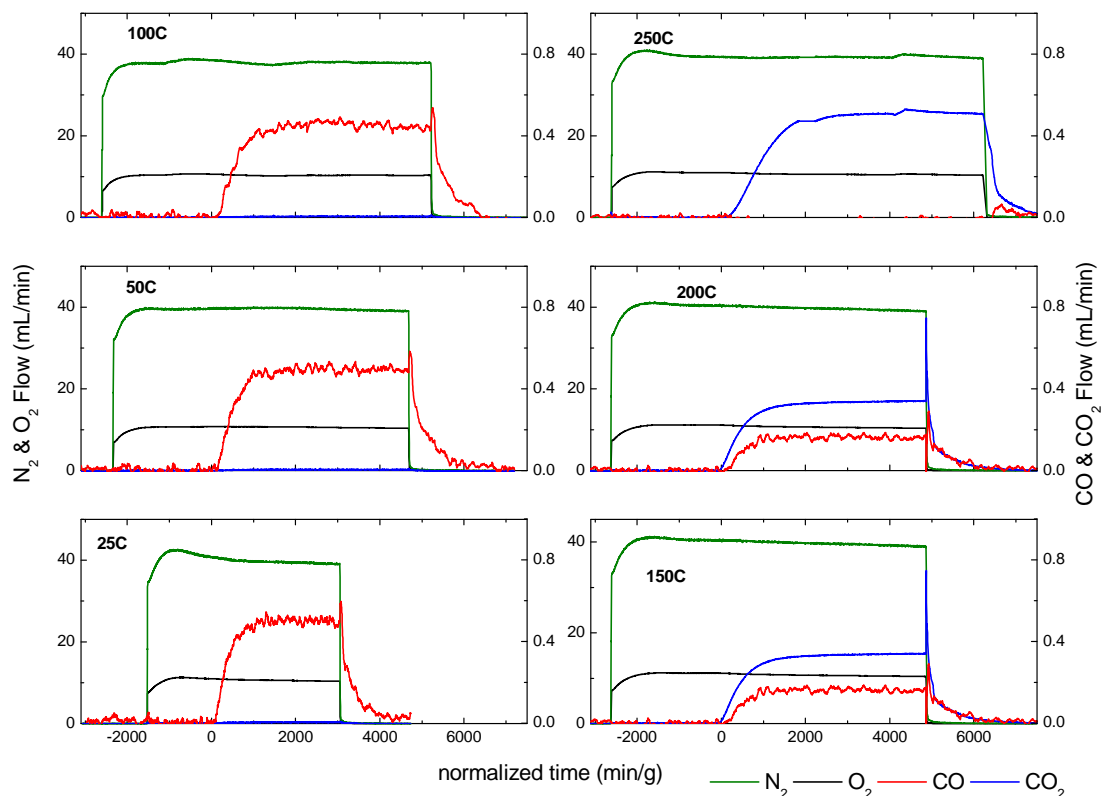
Figure 4.7. Breakthrough on HKUST-1+TiO$_2$ at varying temperatures, pretreated with air.

temperatures. The conversion for HKUST-1 at 250°C under similar conditions is 40% and ~60% under optimal conditions. Notably, these levels of conversion are met in the composite material at temperatures 100°C lower than the parent MOF. Similar results have been seen for PdO$_2$ on HKUST-1, which shows 100% conversion by 220°C. [25] However, this material shows less than 10% conversion at 150°C.[25]

4.4. Conclusions

We have shown here that a composite material consisting of titania and HKUST-1 can be obtained by adding titania to the MOF precursor solution. The sample synthesized thusly

is distinct from a physical mixture of comparable quantities of titania and HKUST-1. The composite material has a higher dynamic capacity of carbon monoxide at room temperature when no air is present and breakthrough times for carbon monoxide comparable to those of the parent HKUST-1 when air enters the system before or with the carbon monoxide. At elevated temperatures, the composite oxidizes a larger fraction of the carbon monoxide present in the gas mixture, showing a maximum conversion in the case of pretreatment with air.

While the composite herein investigated does not enhance the room temperature capture or oxidation of CO, the reduction in temperature for the onset of oxidation over the parent material makes such composites potentially attractive for applications like air purification for fixed sites or vehicles, where waste heat may be available. The reduction in the temperature required for the onset of oxidation demonstrates the benefits in encapsulating oxide nanoparticles within a MOF coating. With optimization or application to other oxide-MOF systems, this technique is promising for increasing activity at lower temperatures. Alternatively, photo-activation could be a route to provide the necessary energy at lower temperatures.

4.5. References

(1) Schlichte, K.; Kratzke, T.; Kaskel, S. *Microporous Mesoporous Mat.* **2004**, *73*, 81.

(2) Tranchemontagne, D. J.; Hunt, J. R.; Yaghi, O. M. *Tetrahedron* **2008**, *64*, 8553.

(3) Chowdhury, P.; Bikkina, C.; Meister, D.; Dreisbach, F.; Gumma, S. *Microporous Mesoporous Mat.* **2009**, *117*, 406.

(4)   Majano, G.; Perez-Ramirez, J. *Advanced Materials* **2013**, *25*, 1052.

(5)   Seo, Y.-K.; Hundal, G.; Jang, I. T.; Hwang, Y. K.; Jun, C.-H.; Chang, J.-S. *Microporous Mesoporous Mat.* **2009**, *119*, 331.

(6)   Li, Z.-Q.; Wang, A.; Guo, C.-Y.; Tai, Y.-F.; Qiu, L.-G. *Dalton Trans.* **2013**, *42*, 13948.

(7)   Jeremias, F.; Henninger, S. K.; Janiak, C. *Chem. Commun.* **2012**, *48*, 9708.

(8)   Zhuang, J.-L.; Ceglarek, D.; Pethuraj, S.; Terfort, A. *Adv. Funct. Mater.* **2011**, *21*, 1442.

(9)   Rubes, M.; Grajciar, L.; Bludsky, O.; Wiersum, A. D.; Llewellyn, P. L.; Nachtigall, P. *ChemPhysChem* **2012**, *13*, 488.

(10)   Redel, E.; Wang, Z.; Walheim, S.; Liu, J.; Gliemann, H.; Woell, C. *Appl. Phys. Lett.* **2013**, *103*.

(11)   Granato, T.; Testa, F.; Olivo, R. *Microporous Mesoporous Mat.* **2012**, *153*, 236.

(12)   Stavila, V.; Volponi, J.; Katzenmeyer, A. M.; Dixon, M. C.; Allendorf, M. D. *Chem. Sci.* **2012**, *3*, 1531.

(13)   Sachse, A.; Ameloot, R.; Coq, B.; Fajula, F.; Coasne, B.; De Vos, D.; Galarneau, A. *Chem. Commun.* **2012**, *48*, 4749.

(14)   Ahmed, A.; Forster, M.; Clowes, R.; Bradshaw, D.; Myers, P.; Zhang, H. *Journal of Materials Chemistry A* **2013**, *1*, 3276.

(15)   Shekhah, O.; Fu, L.; Sougrat, R.; Belmabkhout, Y.; Cairns, A. J.; Giannelis, E. P.; Eddaoudi, M. *Chem. Commun.* **2012**, *48*, 11434.

(16)   Lu, G.; Li, S. Z.; Guo, Z.; Farha, O. K.; Hauser, B. G.; Qi, X. Y.; Wang, Y.; Wang, X.; Han, S. Y.; Liu, X. G.; DuChene, J. S.; Zhang, H.; Zhang, Q. C.; Chen, X. D.; Ma, J.; Loo, S. C. J.; Wei, W. D.; Yang, Y. H.; Hupp, J. T.; Huo, F. W. *Nat. Chem.* **2012**, *4*, 310.

(17)   Wang, P.; Zhao, J.; Li, X. B.; Yang, Y.; Yang, Q. H.; Li, C. *Chem. Commun.* **2013**, *49*, 3330.

(18)   Menzies, K. T., Randel, M.A., Quill, A.L., Roberts, W.C.; Command, U. S. A. M. R. a. D., Ed. Fort Detrick, Frederick, MD, 1989.

(19)   Asimakopoulou, E. K.; Kolaitis, D. I.; Founti, M. A. *Indoor Built Environ.* **2013**, *22*, 750.

(20)   Guerrero, P. A.; Corsi, R. L.; Ashrae In *Ashrae: Transactions 2011, Vol 117, Pt 1*; Amer Soc Heating, Refrigerating and Air-Conditioning Engs: Atlanta, 2011; Vol. 117, p 419.

(21)   Kartel, M. T.; Savelyev, Y. V.; Kanellopoulos, N. In *Methods and Techniques for Cleaning-up Contaminated Sites*; Annable, M. D., Teodorescu, M., Hlavinek, P., Diels, L., Eds.; Springer: Dordrecht, 2008, p 187.

(22)   Noei, H.; Amirjalayer, S.; Muller, M.; Zhang, X. N.; Schmid, R.; Muhler, M.; Fischer, R. A.; Wang, Y. M. *ChemCatChem* **2012**, *4*, 755.

(23)   Qiu, W. G.; Wang, Y.; Li, C. Q.; Zhan, Z. C.; Zi, X. H.; Zhang, G. Z.; Wang, R.; He, H. *Chin. J. Catal.* **2012**, *33*, 986.

(24)   Karra, J. R.; Walton, K. S. *J. Phys. Chem. C* **2010**, *114*, 15735.

(25)   Ye, J. Y.; Liu, C. J. *Chem. Commun.* **2011**, *47*, 2167.

(26)   Zhao, Y.; Zhong, C. L.; Liu, C. J. *Catal. Commun.* **2013**, *38*, 74.

(27)   Zamaro, J. M.; Perez, N. C.; Miro, E. E.; Casado, C.; Seoane, B.; Tellez, C.; Coronas, J. *Chem. Eng. J.* **2012**, *195*, 180.

(28)   Christmann, K.; Schwede, S.; Schubert, S.; Kudernatsch, W. *ChemPhysChem* **2010**, *11*, 1344.

(29)   Diebold, U. *Surf. Sci. Rep.* **2003**, *48*, 53.

(30)   Larsson, P. O.; Andersson, A.; Wallenberg, L. R.; Svensson, B. *J. Catal.* **1996**, *163*, 279.

(31)   Huang, J.; Kang, Y. F.; Wang, L. W.; Yang, T. L.; Wang, Y.; Wang, S. R. *Catal. Commun.* **2011**, *15*, 41.

(32)   Ma, J. B.; Xu, B.; Meng, J. H.; Wu, X. N.; Ding, X. L.; Li, X. N.; He, S. G. *J. Am. Chem. Soc.* **2013**, *135*, 2991.

CHAPTER 5

A MAGNETIC NANOPARTICLE-MOF COMPOSITE

5.1. Introduction

HKUST-1, also known as Cu-BTC or MOF-199, is a MOF consisting of copper paddle-wheel clusters coordinated with benzene-tricarboxylic acid into a three-dimensional pore system and has been studied widely for a variety of gas storage and separation and catalysis applications.[1-9] It has been synthesized on or around a variety of metals and metal oxides.[10-16] Such composites are an attractive way to add multi-functionality. The MOF restricts access to the nanoparticle, adding selectivity to particles that may be insensitive to differences. For example, a nanoparticle used as a sensor generally reacts to a class of molecules and does not differentiate between different members of the family. By adding a pore system around the sensor, access to the sensor can be restricted to smaller molecules. Additionally, adsorption on the MOF near the nanoparticle may change the local environment sufficiently to register, as well.

Removing toxic gases from ambient air mixtures has a wide variety of applications, including respirators and environmental air quality control.[17-20] Carbon monoxide and VOCs such as hexane are prevalent candidates to remove for improving air quality. It is particularly attractive to couple an indicator mechanism with a removal mechanism for such materials, providing information about exposure and device lifetime. By including cobalt iron oxide magnetic nanoparticles (MNPs) that have demonstrated changes in

magnetic field with adsorbed species,[21] a species that may act as an indicator is coupled with a relatively higher-capacity adsorbent.

In this work, HKUST-1 is synthesized around pre-formed magnetic cobalt iron oxide nanoparticles. These composites have been characterized and investigated for framework stabilization and the adsorption of carbon monoxide and hexane.

5.2. Materials and Methods

5.2.1. Material Synthesis

All chemicals were used as received from Acros Organics without further purification: copper nitrate trihydrate ($Cu(NO_3)_2 \bullet 3H_2O$, 99%), benzene tricarboxylic acid (H_3BTC, 99%), and ethanol (EtOH, 99.5%). The composite was synthesized by dissolving $Cu(NO_3)_2 \bullet 3H_2O$ (0.8754 g) in water (10 mL) and H_3BTC (0.4034 g) in ethanol (10 mL). These solutions were combined together with a 4 mL water: ethanol (1:1) solution containing 0.0145 g of 6.1 nm diameter $CoFe_3O_4$ magnetic nanoparticles (MNP) synthesized via literature procedures[21] and functionalized with 0.0126 g BDC by Dan Sabo in the Zhang lab, in the School of Chemistry at Georgia Tech. The solution was placed in a sand bath heated to 120°C and stirred constantly to keep the nanoparticles suspended for 15 hours. After allowing the mixture to cool to room temperature, the blue particles were washed 4 times over 4 days with an excess of ethanol, then dried at ambient conditions. HKUST-1 was also synthesized from $Cu(NO_3)_2 \bullet 3H_2O$ (0.8747 g) in water (12 mL) and H_3BTC (0.4210 g) in ethanol (12 mL) using the same method.

5.2.2. Experimental Methods

Powder XRD was performed on a PANalytical X'Pert Pro (CuKα). Nitrogen physisorption data were collected on a Quantachrome Quadrasorb. Scanning electron microscopy (SEM) images were obtained on a LEO 1530 operated at 10 kV. Transmission electron microscopy (TEM) images were collected on a JEOL 100 CX II (100kV). Thermogravimetric analysis coupled with differential scanning calorimetry (TGA-DSC) was conducted by a NETZSCH STA 449 F1 Jupiter. Samples were heated at a rate of 10°C/min from 0°C to 600°C under a 20 cc/min stream of helium. Carbon dioxide adsorption was performed on a Hiden IGA-001 at 25°C over 0-5 bar. Carbon monoxide adsorption was performed over 0-5 bar at 25°C in a lab-built pressure decay system. Vapor isotherms were measured on a Hiden IGA-003 at 25°C and 1 bar in air up to 90% relative humidity.

5.3. Results and Discussion

5.3.1. Material Characterization

Powder XRD was measured for HKUST-1, the nanoparticles alone, and the composite material (**Figure 5.1**). The composite pattern shows peaks corresponding to HKUST-1 but no peaks that can be indexed to only the nanoparticles. This provides evidence that the nanoparticles are well dispersed throughout the MOF system, as agglomerated nanoparticles should demonstrate enough long-range order to be identifiable in PXRD.
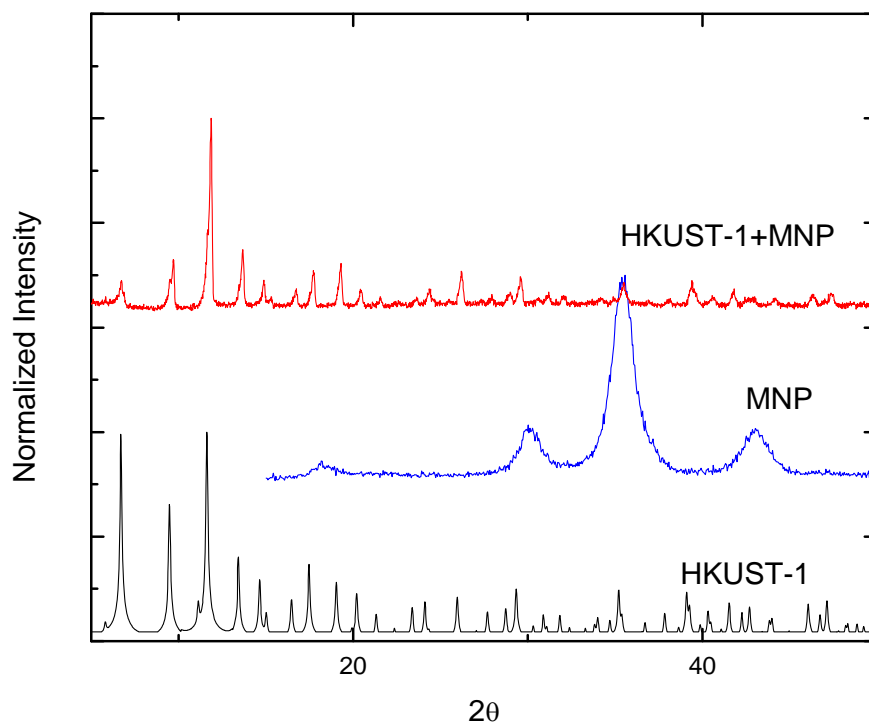
Figure 5.1. Powder XRD for HKUST-1, calculated (black), MNP (blue), and HKUST-1+MNP (red).

All of the composite material remains suspended when a magnet is placed near the sample and inverted while the unmodified HKUST-1 does not, providing additional evidence of the MNP's inclusion. The nanoparticles impact the composite's weight-normalized properties, but the composite retains 72% and 77% of the parent HKUST-1's surface area and pore volume, respectively, as seen in **Table 5.1** and **Figure 5.2**. In fact, when normalized to a per-HKUST-1 basis rather than overall sample mass, the surface area of the material is comparable (1800 m^2/ g HKUST-1).

HKUST-1+MNP shows a slight increase (20-30°C) in decomposition temperature when compared to HKUST-1 synthesized under identical conditions (**Figure 5.3**). The nanoparticles may serve to stabilize the framework itself and may act as a kind of heat
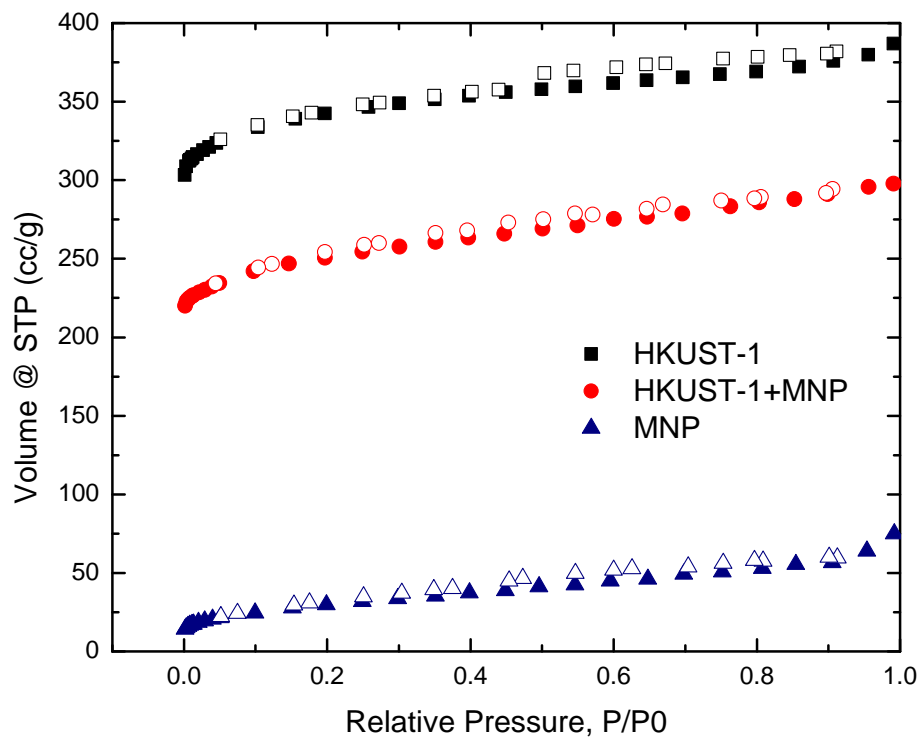
Figure 5.2. N_2 isotherm at 77K; HKUST-1 (□), HKUST-1-MNP (○), and MNP (Δ), open and closed symbols represent adsorption and desorption branches, respectively.

Table 5.1. BET Surface Area and Pore Volume.

| Material	BET Surface Area (m^2/g)	Pore Volume (cc/g)
HKUST-1	1769	0.82
HKUST-1+MNP	1473	0.65
HKUST-1 & MNP physical mixture	1138	0.51
MNP	107	0.082
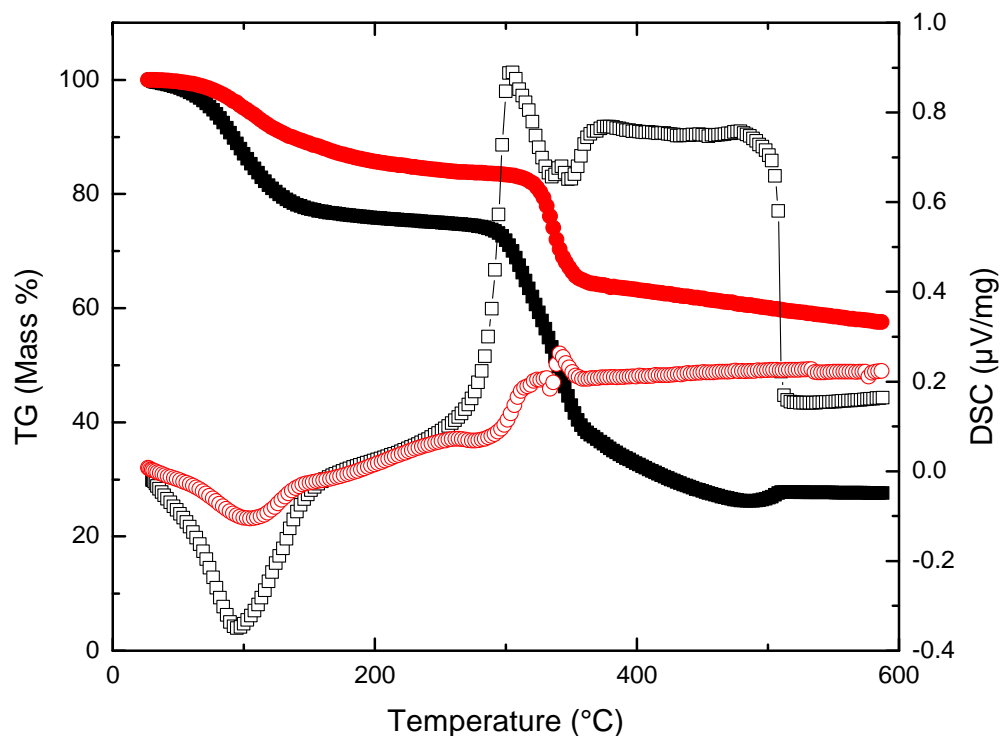
Figure 5.3. Mass lost (closed symbols) and DSC (open symbols) for HKUST-1 (□), HKUST-1-MNP (○) during thermal decomposition.

sink, as seen by the modulation of the DSC curve. The idea of MOF stabilization is supported by the apparent stabilization of the MOF structure in TEM when the nanoparticles are included. HKUST-1 is unstable under TEM, as shown in **Figure 5.4**. Almost immediately upon exposure to a focused TEM electron beam, HKUST-1 deforms, losing crystallinity and its octahedral shape. In contrast, crystals of the composite of comparable size retain their shape and structure for much longer. **Figure 5.5** shows TEM of HKUST-1+MNP. There are clearly regions of nanoparticles or excess reactants unincorporated into the structure of HKUST-1, but the bulk appear to be on or in the MOF structure.
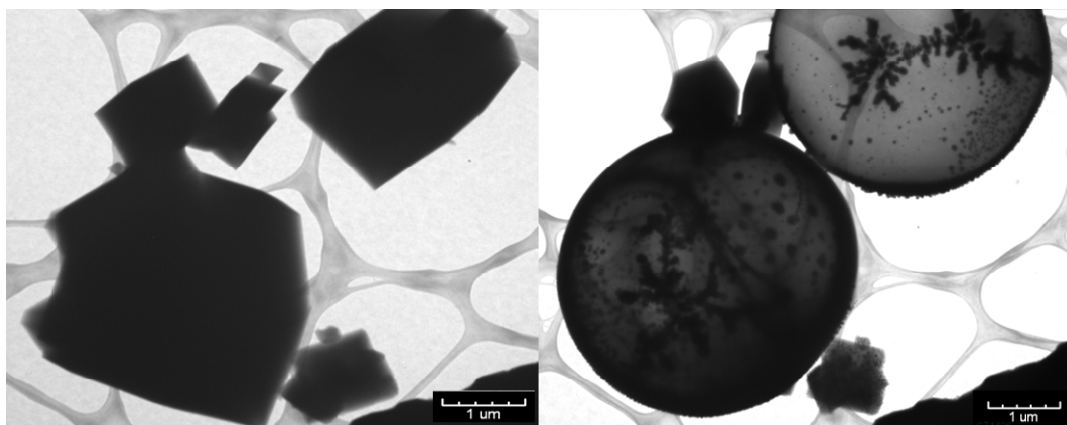
Figure 5.4. TEM of unmodified HKUST-1. HKUST-1 loses crystallinity and shape almost instantaneously when electron beam is focused. Image on right is seconds after image on left, after beam is focused.
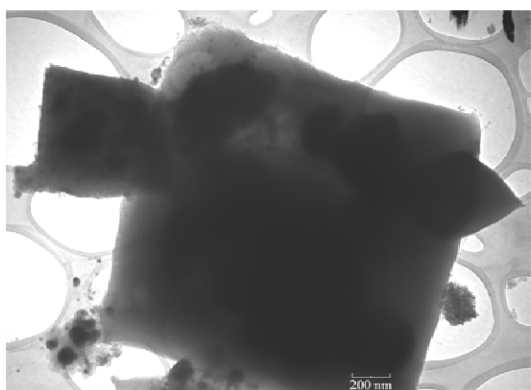
Figure 5.5. TEM of HKUST-1+MNP. Unlike unmodified HKUST-1, the incorporation of nanoparticles results in crystals that retain their shape indefinitely in the electron beam.

5.3.2. Adsorption Isotherms

CO_2 adsorption is not enhanced by the inclusion of nanoparticles in HKUST-1 on the basis of overall composite weight (**Figure 5.6**), with the composite demonstrating a CO_2 capacity 21% less than HKUST-1. When normalized to the HKUST-1 content, the discrepancy decreases, but the composite still has a reduced capacity over the parent
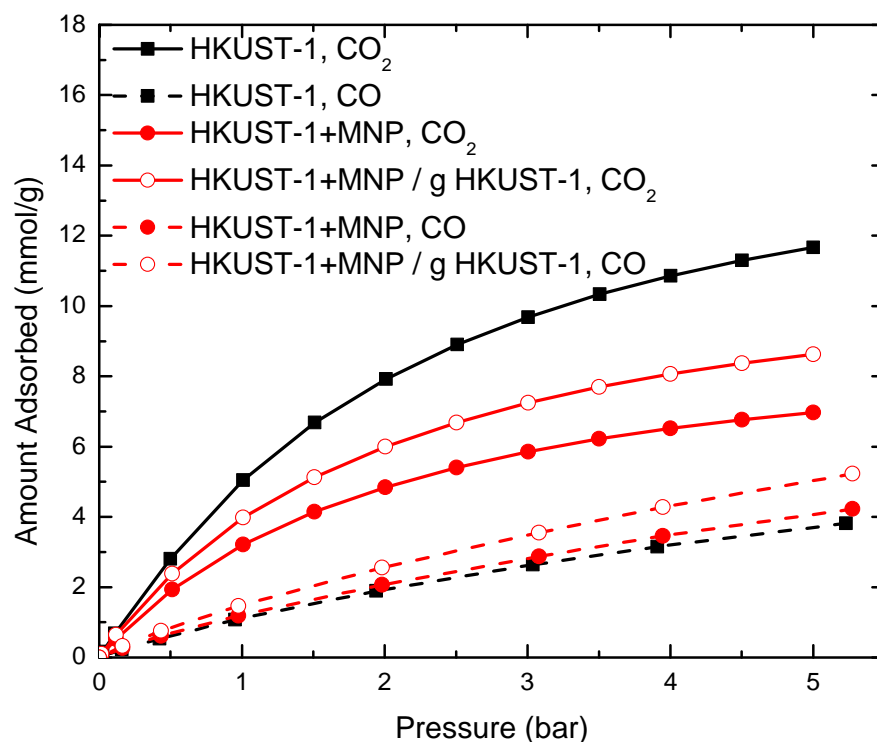
**Figure 5.6**. CO_2 and CO isotherms at 25°C; HKUST-1 and HKUST-1-MNP, closed symbols represent adsorption based on the overall sample weight; open symbols represent adsorption normalized to MOF weight.

material. This is indicative of reduced access to the pore system, and potentially disorder produced from synthesizing the MOF around the nanoparticles. Similarly to CO_2, the composite has slightly lower water capacity than the parent MOF, but the capacity normalized to MOF results in higher water loading (**Figure 5.7**).

In the case of carbon monoxide, the weight-normalized capacity of the parent material and the composite are similar; the stronger adsorbate-sorbent interaction overcomes the added weight and pore blockage from the included nanoparticles (**Figure 5.6**). On a MOF-normalized basis, there is clear enhancement over the unmodified HKUST-1.
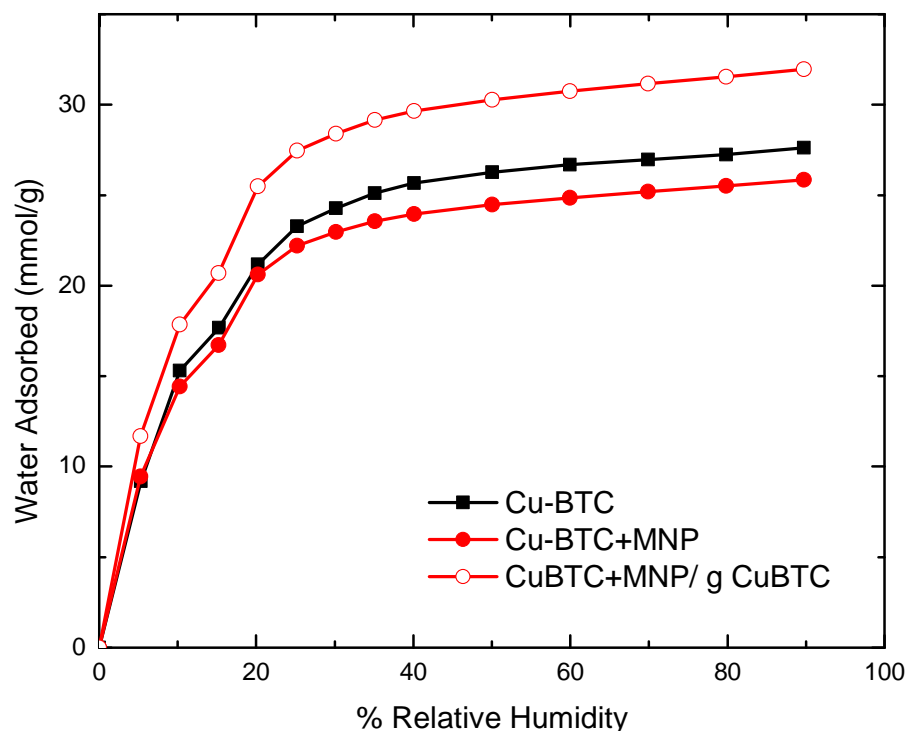
Figure 5.7. Water vapor isotherms at 25°C; closed symbols represent adsorption based on the overall sample weight; open symbols represent adsorption normalized to MOF weight.

Hexane adsorption in HKUST-1 is in good agreement with previously reported values of 401 mg/g,[1] (**Figure 5.8**) but it shows a loss in capacity at 20-30% hexane indicative of partial structural collapse.[2] The HKUST-1+MNP samples adsorbed 40% more hexane than the unmodified parent, and show no loss in structure. This increase in capacity and the stabilizing influence of the nanoparticles makes this an attractive material for VOC removal and air quality improvement. As the MOF is formed around the nanoparticles, the open metal sites should not be impacted by the inclusion of the nanoparticles. This indicates interactions with the nanoparticles dominate over ligand exchange that would lead to a structural collapse.
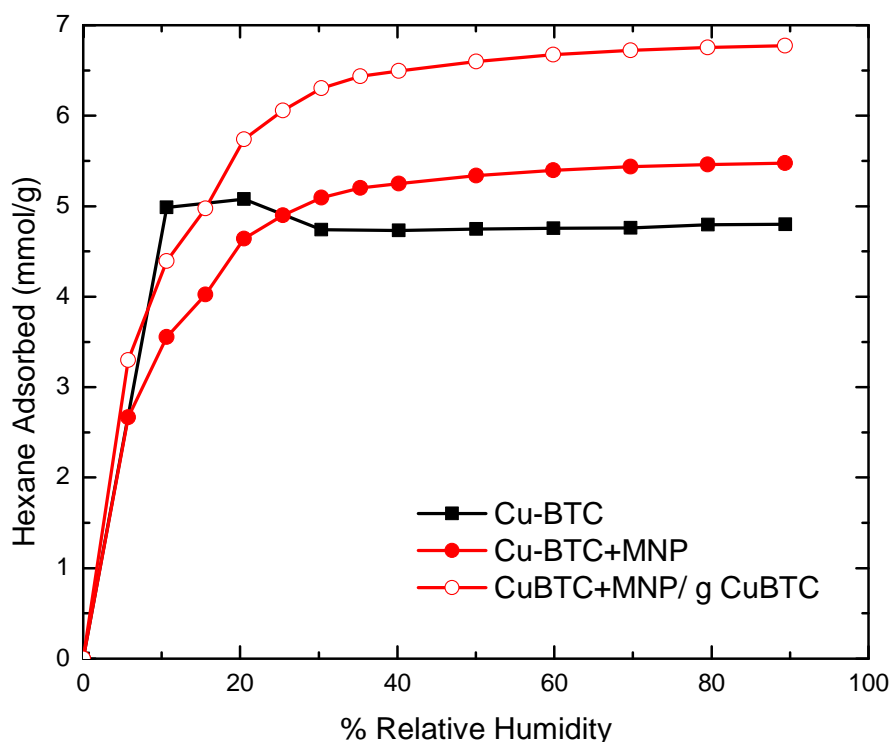
Figure 5.8. Hexane isotherms at 25°C; closed symbols represent adsorption based on the overall sample weight; open symbols represent adsorption normalized to MOF weight.

5.4. Conclusions

A composite consisting of magnetic nanoparticles included in HKUST-1 was synthesized, resulting in a composite that retained the MNP's response to magnetic fields and pore characteristics intermediate between the unmodified HKUST-1 and a physical mixture of MNPs with HKUST-1. The material demonstrates a slight improvement in carbon monoxide capacity compared the parent HKUST-1. HKUST-1+MNP shows a 13% increase in gravimetric hexane capacity and 40% increase when normalized to HKUST-1. This demonstrates composites like these have potential for use as combined sensor-adsorbent systems for the removal of toxic gases and VOCs for air quality improvement.

5.5. References

(1)   Chowdhury, P.; Bikkina, C.; Meister, D.; Dreisbach, F.; Gumma, S. *Microporous Mesoporous Mat.* **2009**, *117*, 406.

(2)   Jeremias, F.; Henninger, S. K.; Janiak, C. *Chem. Commun.* **2012**, *48*, 9708.

(3)   Li, Z.-Q.; Wang, A.; Guo, C.-Y.; Tai, Y.-F.; Qiu, L.-G. *Dalton Trans.* **2013**, *42*, 13948.

(4)   Majano, G.; Perez-Ramirez, J. *Advanced Materials* **2013**, *25*, 1052.

(5)   Rubes, M.; Grajciar, L.; Bludsky, O.; Wiersum, A. D.; Llewellyn, P. L.; Nachtigall, P. *ChemPhysChem* **2012**, *13*, 488.

(6)   Schlichte, K.; Kratzke, T.; Kaskel, S. *Microporous Mesoporous Mat.* **2004**, *73*, 81.

(7)   Seo, Y.-K.; Hundal, G.; Jang, I. T.; Hwang, Y. K.; Jun, C.-H.; Chang, J.-S. *Microporous Mesoporous Mat.* **2009**, *119*, 331.

(8)   Tranchemontagne, D. J.; Hunt, J. R.; Yaghi, O. M. *Tetrahedron* **2008**, *64*, 8553.

(9)   Zhuang, J.-L.; Ceglarek, D.; Pethuraj, S.; Terfort, A. *Adv. Funct. Mater.* **2011**, *21*, 1442.

(10)   Ahmed, A.; Forster, M.; Clowes, R.; Bradshaw, D.; Myers, P.; Zhang, H. *Journal of Materials Chemistry A* **2013**, *1*, 3276.

(11)   Granato, T.; Testa, F.; Olivo, R. *Microporous Mesoporous Mat.* **2012**, *153*, 236.

(12)   Lu, G.; Li, S. Z.; Guo, Z.; Farha, O. K.; Hauser, B. G.; Qi, X. Y.; Wang, Y.; Wang, X.; Han, S. Y.; Liu, X. G.; DuChene, J. S.; Zhang, H.; Zhang, Q. C.; Chen, X. D.; Ma, J.; Loo, S. C. J.; Wei, W. D.; Yang, Y. H.; Hupp, J. T.; Huo, F. W. *Nat. Chem.* **2012**, *4*, 310.

(13)   Redel, E.; Wang, Z.; Walheim, S.; Liu, J.; Gliemann, H.; Woell, C. *Appl. Phys. Lett.* **2013**, *103*.

(14)   Sachse, A.; Ameloot, R.; Coq, B.; Fajula, F.; Coasne, B.; De Vos, D.; Galarneau, A. *Chem. Commun.* **2012**, *48*, 4749.

(15)   Shekhah, O.; Fu, L.; Sougrat, R.; Belmabkhout, Y.; Cairns, A. J.; Giannelis, E. P.; Eddaoudi, M. *Chem. Commun.* **2012**, *48*, 11434.

(16)   Stavila, V.; Volponi, J.; Katzenmeyer, A. M.; Dixon, M. C.; Allendorf, M. D. *Chem. Sci.* **2012**, *3*, 1531.

(17)   Asimakopoulou, E. K.; Kolaitis, D. I.; Founti, M. A. *Indoor Built Environ.* **2013**, *22*, 750.

(18)   Guerrero, P. A.; Corsi, R. L.; Ashrae In *Ashrae: Transactions 2011, Vol 117, Pt 1*; Amer Soc Heating, Refrigerating and Air-Conditioning Engs: Atlanta, 2011; Vol. 117, p 419.

(19)   Kartel, M. T.; Savelyev, Y. V.; Kanellopoulos, N. In *Methods and Techniques for Cleaning-up Contaminated Sites*; Annable, M. D., Teodorescu, M., Hlavinek, P., Diels, L., Eds.; Springer: Dordrecht, 2008, p 187.

(20)   Menzies, K. T., Randel, M.A., Quill, A.L., Roberts, W.C.; Command, U. S. A. M. R. a. D., Ed. Fort Detrick, Frederick, MD, 1989.

(21)   Glover, T. G.; Sabo, D.; Vaughan, L. A.; Rossin, J. A.; Zhang, Z. J. *Langmuir* **2012**, *28*, 5695.

CHAPTER 6

IMPACT OF ACTIVATION CONDITIONS ON CARBON MONOXIDE ADSORPTION IN M-MOF-74

6.1. Introduction

Metal-organic frameworks (MOFs), a relatively new class of porous materials consisting of metal nodes connected via organic linkers, show promise in a wide array of gas separation and storage applications due to their highly regular crystalline structures having well-defined pores with tight pore size distributions, high surface areas and pore volumes, and tunable functionality through ligand and metal selection. Much interest has been expressed in rationally designing MOFs to target specific gases such as CO_2, H_2, CH_4, CO, NH_3, SO_2, and other small molecules for specific energy-related separations and toxic gas remediation. In order to identify trends and draw conclusions to intelligently construct MOFs for specific applications, the interactions of molecules with the ligands and metal centers within a given crystal geometry must be understood. This can be investigated systematically through isostructural MOF families where a portion of the framework is changed while keeping all other portions constant. This was illustrated first through the IRMOF family, consisting of an identical cubic arrangement of zinc nodes with organic linkers varying in either functionality or length from the parent benzenedicarboxylate.[1] More recently, the UiO family, consisting of zirconium nodes connected via organic linkers of varying functionality and length has been investigated to gain additional insight into the role of the organic linker in a more stable coordination environment.[2]

While isoreticular MOF families related through their identical underlying architecture and metal center have received much attention, there are also families of MOFs with the same crystal structure and organic linkers that vary in the metal node. The most widely studied of these families is the M-MOF-74 series, known as CPO-27 or M/DOBDC. These MOFs form as one-dimensional honeycomb channels with dihydroxyterephthalate connecting metal nodes of magnesium,[3] cobalt,[4] nickel,[5] zinc,[6] iron,[7] or manganese.[8] Each metal center is coordinated to a solvent molecule in addition to the structural organic linkers during synthesis, and this molecule can be removed through vacuum activation at elevated temperatures. This leaves the metals with coordinatively unsaturated metal sites, which can function as Lewis acids, making these materials especially attractive for adsorption of Lewis bases. These materials show high capacities for several important gases, including CO_2,[9-18] H_2,[5,12,14] CH_4,[10,14,15,18] CO,[12,18-20] and other energy-related[12,15] or toxic[21,22] gases,[21,22] making the family attractive for further investigation. However, to draw conclusions about the effect of metal sites on the observed adsorption behavior, the differences beyond changing the metal center must be minimized to isolate its impact. This seemingly trivial idea is quite non-trivial in practice.

The published synthesis procedures vary widely in temperature, time, solvent mixtures, metal precursor-to-ligand ratio, and metal precursor-to-solvent ratio, resulting in different yields, crystal imperfections, and potentially different solvent molecules coordinating to the metal centers.[5,9,10,13,18,22] Published activation temperatures vary more than 100°C

between various papers. Within a single study, the activation temperatures are generally less disparate, but the duration can vary by over 24 hours. Additionally, some studies use one activation condition for surface area analysis and different activation conditions before the subsequent adsorption measurements. Due to differences in the strength of the metal-solvent bond, different activation conditions might be necessary for the materials, but similar conditions are attractive for running experiments with different analogs in parallel. Surface area measurements are often used as an indicator of extent of activation or solvent removal, so for this family, the surface areas should follow a trend inverse to the molecular weight of the metal center: Mg-MOF-74, with the lightest metal, should have the highest surface area, and Zn-MOF-74, with the heaviest metal, should have the lowest surface area. Co-DOBDC and Ni-MOF-74 should have comparable surface areas intermediate between the other two analogs. This trend of the measured surface areas should be among the first considerations for ensuring self-consistency within a study investigating the relative merits of such families, but it is often not met in practice. Additionally, consistent activation is more readily applied than methods to minimize or quantify crystal structure imperfections, improving the precision of the trends, even if the accuracy is unaffected.

In this work, we present a systematic study of the activation conditions for M-MOF-74 (M=Co, Mg, Ni, Zn). The relative extent of activation is indicated through BET surface area calculations and carbon monoxide adsorption isotherms to explore the subsequent accessibility and reactivity of the open metal sites.

6.2. Experimental Methods

6.2.1. Synthesis Methods

M-MOF-74 synthesis procedures were modified from literature.[1,2] 2,5-
dihydroxyteephthalic acid (H$_4$DOBDC) (98%), Co(No$_3$)$_2$•6H$_2$O (98%), Mg(NO$_3$)$_2$•6H$_2$O
(98%), Ni(NO$_3$)$_2$•6H$_2$O (99%), Zn(No$_3$)$_2$•6H$_2$O (98%), and n,n-dimethylformamide
(DMF) (99.8%) were obtained from Sigma Aldrich. Ethanol (99%) was obtained from
VWR. All chemicals were used as received.

6.2.1.1. Co-MOF-74

H$_4$DOBDC (0.5 g, 2.5 mmol) and Co(NO$_3$)$_2$•6H$_2$O (1.5 g, 5.2 mmol) were combined.
The solvent mixture, DMF, ethanol, water (70 mL, 70 mL, 70 mL) was added. Once
fully dissolved, it was divided equally into 20 mL vials, capped tightly, and placed in a
pre-heated oven at 100°C for 66 hours.

6.2.1.2. Mg-MOF-74

H$_4$DOBDC (0.111 g, 0.56 mmol) and Mg(NO$_3$)$_2$•6H$_2$O (0.475 g, 1.85 mmol) were
combined. The solvent mixture, DMF, ethanol, water (45 mL, 3 mL, 3 mL) was added.
Once fully dissolved, it was divided equally into 20 mL vials, capped tightly, and placed
in a pre-heated oven at 125°C for 24 hours.

6.2.1.3. Ni-MOF-74

H_4DOBDC (0.5 g, 2.5 mmol) and $Ni(NO_3)_2 \bullet 6H_2O$ (1.5 g, 5.2 mmol) were combined.

The solvent mixture, DMF, ethanol, water (70 mL, 70 mL, 70 mL) was added. Once

fully dissolved, it was divided equally into 20 mL vials, capped tightly, and placed in a

pre-heated oven at 100°C for 66 hours days.

6.2.1.4. Zn-MOF-74

H_4DOBDC (1 g, 5 mmol) and $Zn(NO_3)_2 \bullet 6H_2O$ (4.75 g, 16 mmol) were combined. The

solvent DMF (100 mL) was added. Once fully dissolved, 5 mL water was added, then, it

was divided equally into 20 mL vials, capped tightly, and placed in a pre-heated oven at

110°C for 24 hours.

6.2.1.5. Solvent Exchange and Sample Handling

After cooling to room temperature, each sample was washed several times with DMF.

The DMF was exchanged for methanol, with the solution being decanted and replaced 4

times over 4 days. Samples were stored under methanol and loaded into the adsorption

instrument directly from the methanol solution to minimize exposure to air. The excess

ethanol was allowed to evaporate under vacuum before subsequent activation steps.


6.2.2. Characterization and Isotherm Measurements

TGA-DSC experiments were conducted on a Netzsch STA449 Jupiter under flowing

helium at 20 mL/min. Temperature profiles used were 2°C/min. N_2 isotherms at 77K

were measured on a Quantachrome Quadrasorb Porous Material Analyzer for pore structure characterization. BET surface areas were calculated over the relative pressure range 0.005-0.03. Carbon monoxide isotherms were measured on a lab-built pressure decay system, in which a reference chamber is charged with a known amount of gas that is subsequently allowed to enter the sample chamber. The changes in pressure of the two chambers are used to calculate the amount of gas adsorbed by the sample.

6.3. Results & Discussion

6.3.1. Sufficient Activation and Characterization

When heated under flowing gas, many MOFs exhibit a characteristic weight loss curve consisting of solvent loss at low temperatures, followed by a range of temperatures where the mass remains essentially constant before decomposition begins. Activation temperatures are generally chosen from this plateau at a high enough temperature to ensure complete solvent removal but well below the material's decomposition temperature. M-MOF-74 analogs, on the other hand, show a steep mass loss initially due to solvent removal followed by a more or less gradually sloping section before another steep loss indicating decomposition (**Figure 6.1**). This behavior has been shown previously for Mg-MOF-74[3] and is attributed to the difficulty of fully removing solvent molecules. Co-MOF-74 shows behavior most typical of other MOFs, with an almost flat section between 200°C and 250°C. In contrast, Zn-MOF-74 displays an almost constant loss rate until completely decomposing around 475°C. The lack of a distinct temperature
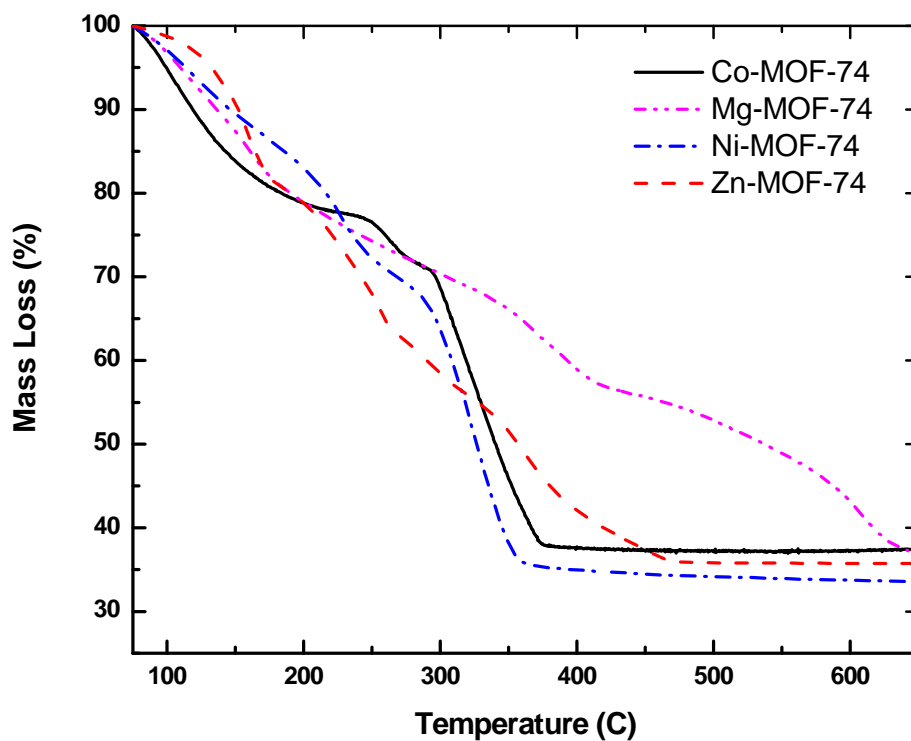
Figure 6.1. Mass loss of as-synthesized M-MOF-74 as a function of temperature.

range after solvent loss and before the onset of decomposition makes it more challenging to choose the proper activation temperature to ensure solvent is completely removed from the metal sites.

Activation conditions reported in the literature[5,9,10,13,18,20,22] range in temperature from 150°C to 265°C with durations varying from 5 to 48 hours (**Table 6.1**). To highlight the issue of self-consistency, predominantly studies including 2 or more of the M-MOF-74 analogs were considered for comparison. These often are not the highest reported values,

Table 6.1. Activation Conditions and Surface Areas from Literature and This Work.

M-MOF-74	Surface Area Activation	BET Surface Area	Sorption Activation	Ref
Co-MOF-74	250°C/5 hr	1080	250°C/5 hr	1
Co-MOF-74	230°C overnight	1093	230°C overnight	4
Co-MOF-74	250°C/24 hr	835		2
Co-MOF-74	250°C/5 hr	1327	100°C/1 hr	5
Co-MOF-74	250°C/12 hr	1326	250°C/12 hr	This work
Mg-MOF-74	250°C/5 hr	1495	250°C/5 hr	1
Mg-MOF-74	240°C/48 hr + 120°C/1 hr	1542	250°C/19 hr	6
Mg-MOF-74	250°C/6 hr	1206		2
Mg-MOF-74	250°C/12 hr	1559	250°C/12 hr	This work
Ni-MOF-74	250°C/5 hr	1070	250°C/5 hr	1
Ni-MOF-74	200°C/19 hr + 110°C/1 hr	1218	200°C/12 hr	6
Ni-MOF-74	230°C overnight	1266	230°C overnight	4
Ni-MOF-74	250°C/5 hr	599		2
Ni-MOF-74	120°C/1 hr	1200	120°C/2 hr	7
Ni-MOF-74	100°C	1083 (Langmuir)	100°C/12 hr; 100°C/20 hr	8
Ni-MOF-74	250°C/12 hr	1484	250°C/12 hr	This work
Zn-MOF-74	250°C/5 hr	816	270°C/16 hr	1
Zn-MOF-74	230°C overnight	806	230°C overnight	4
Zn-MOF-74	150°C/10 hr + 265°C/10 hr	496		2
Zn-MOF-74	250°C/12 hr	1187	250°C/12 hr	This work

but as a representative sample, cover the range of activation temperature and duration. The majority of activation procedures reported were conducted at 250°C, near the upper end of the temperature range where the mass loss of each MOF was still gradual, which should minimize the time required for activation. In this work, to determine the impact of prolonged exposure to high temperature (250°C) under vacuum, each MOF was activated for a varying amount of time, after which the BET surface area was measured. Activation times were varied from 6 to 48 hours for comparison to literature as shown in **Figure 6.2** (18 and 24 hours omitted for clarity). It was found that 6 hours is insufficient to fully activate all analogs of M-MOF-74. Maximum surface areas were obtained after
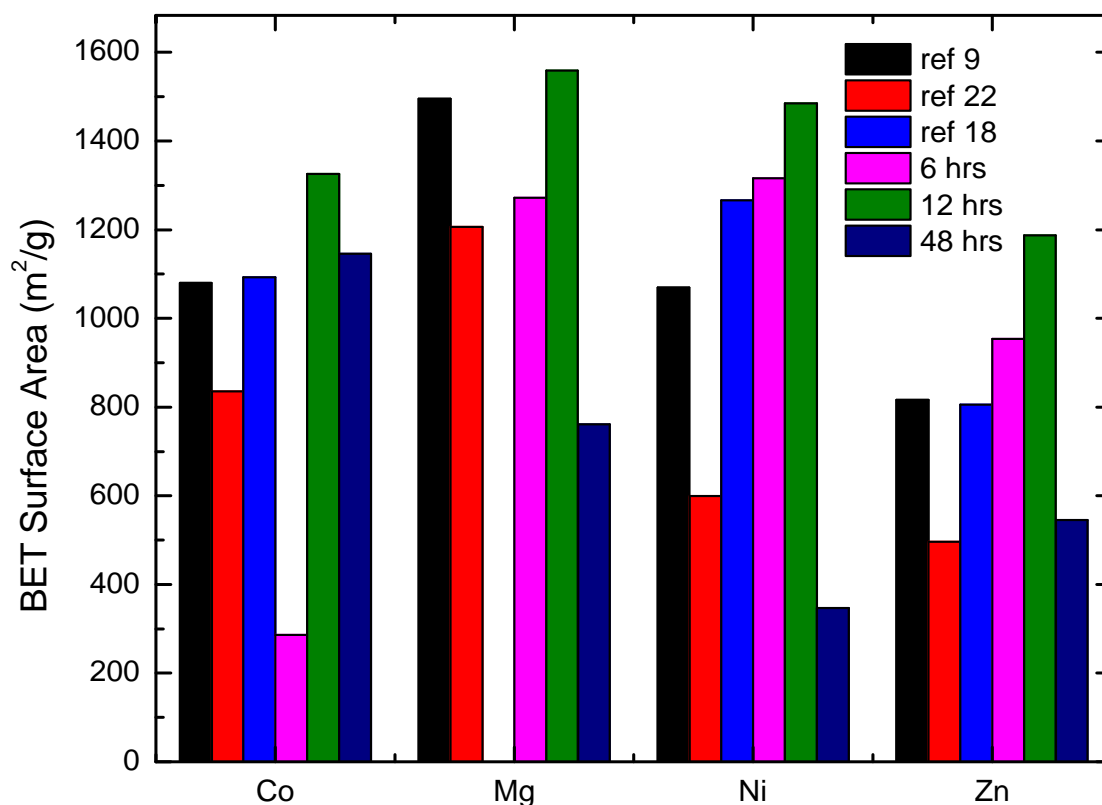

Figure 6.2. BET surface areas obtained under different activation conditions.

12 hours at 250°C, with Co-MOF-74, Mg-MOF-74, and Zn-MOF-74 retaining

comparable surface areas after 18 and 24 hours as well. In the case of Ni-MOF-74, it has

a distinct maximum surface area measured after 12-hour activation, with considerable

loss in surface area apparent after 18 hours. The Co-MOF-74 sample activated for 48

hours retained surface areas comparable to those reported previously in the literature, but

the other three analogs retained less than half of the maximum surface area measured

after prolonged activation. In the case of Zn-MOF-74, this was also accompanied by a

loss in crystallinity. PXRD patterns after surface area measurements after 12 and 48 hour

activations are shown in **Figure 6.3**. A broad peak indicative of nickel oxide formation is

present in the Ni-MOF-74 sample after 48 hours The surface areas measured after 12-

hour activations are listed in **Table 6.1**, and follow the expected trends based on metal

weight indicating comparable extent of activation: Mg-MOF-74 (1559 m^2/g) > Co-MOF-

74 (1326 m^2/g) $\approx$ Ni-MOF-74 (1484 m^2/g) > Zn-MOF-74 (1187 m^2/g).

6.3.2. Carbon Monoxide Adsorption

Carbon monoxide isotherms were measured for each analog at 25°C after activation at

one of three temperatures – 150°C, 200°C, and 250°C – for 12 hours to determine the

impact of activation temperature on adsorption for a model gas that should adsorb

predominantly at the open metal sites. As shown in **Figure 6.4**, the activation conditions

show a varying impact for each analog, generally with higher activation temperatures

resulting in increased capacity. The greatest impact is apparent in Mg-MOF-74, where

activating at 250°C results in an 8-fold increase in carbon monoxide capacity at 1 bar
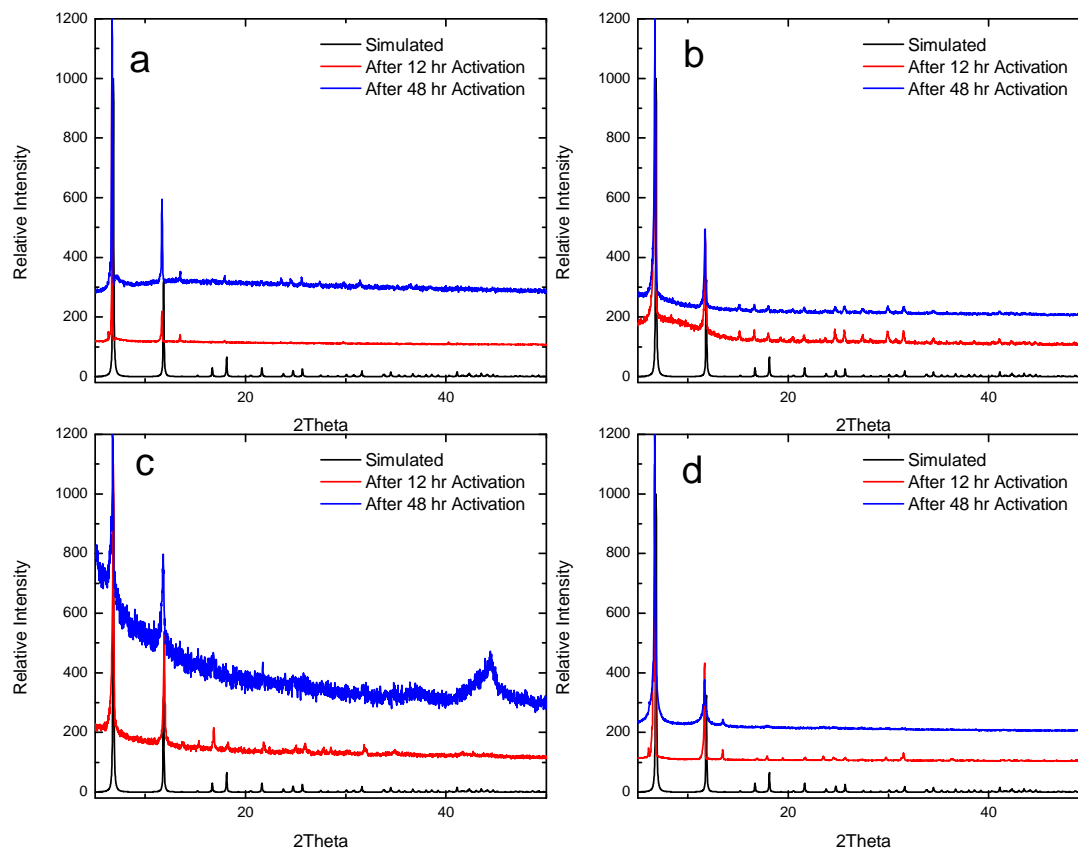
Figure 6.3. PXRD measured after BET from different activation times at 250°C on Co-MOF-74 (a), Mg-MOF-74 (b), Ni-MOF-74 (c) and Zn-MOF-74 (d).

compared to when the material is activated at 150°C. The differences in the CO adsorption behavior for Ni-MOF-74 samples are less pronounced, but samples activated at 250°C exhibit loadings at 5 bar that are approximately 1.7 times greater than the capacity obtained for the samples activated at 150°C. For Ni-MOF-74, the samples activated at 150°C and 200°C show very similar adsorption behavior, but the samples activated at 250°C exhibit a CO capacity that is approximately double the loadings of the other samples at 5 bar. Zn-MOF-74 shows no increase in adsorption with increasing activation temperature; in fact, it shows decreased capacity with the highest activation
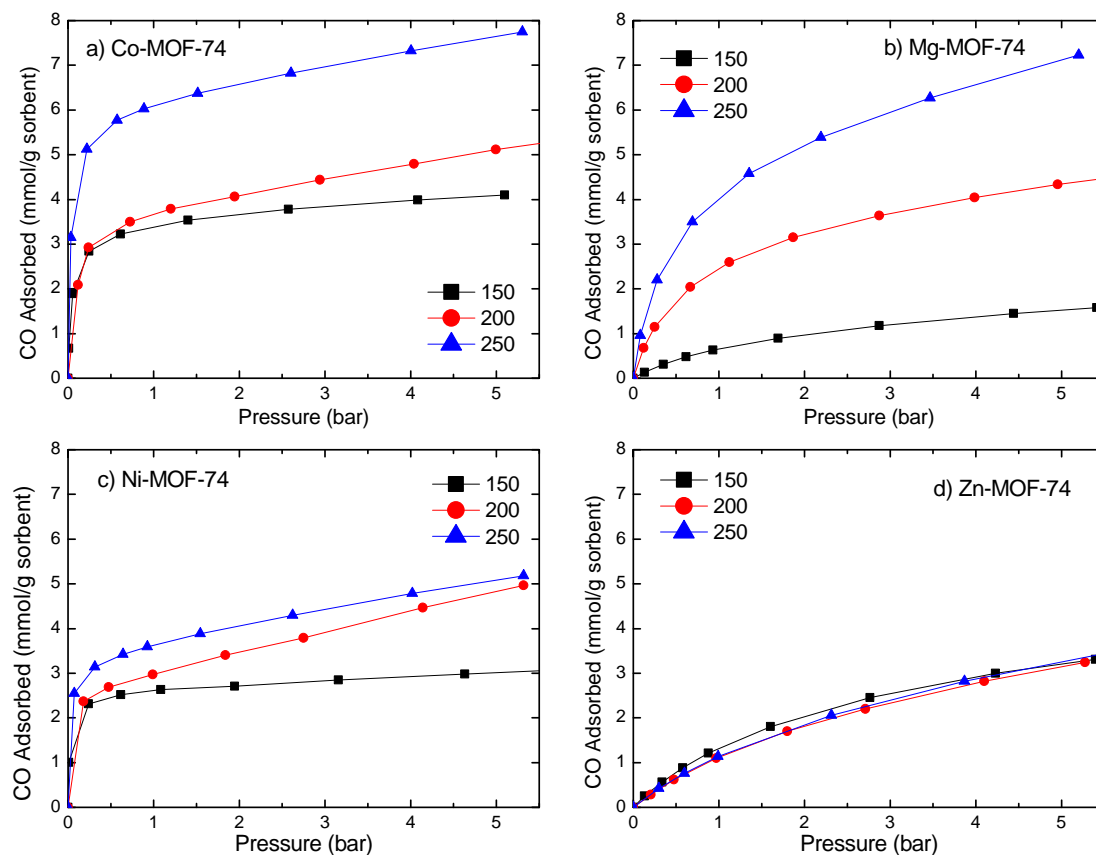
Figure 6.4. Impact of activation temperature on carbon monoxide adsorption on M-MOF-74 at 25°C. Activation for 12 hours at 150°C (■), 200°C (●), 250°C (▲): Co-MOF-74 (a), Mg- MOF-74 (b), Ni-MOF-74 (c), d: Zn- MOF-74 (d).

temperature. This agrees with our findings that Zn-MOF-74 decomposes steadily at lower temperatures than the other analogs.

Carbon monoxide isotherms were measured at 25°C, 45°C, and 65°C on each MOF-74 analog (**Figure 6.5**), and each experimental isotherm was fit to theoretical models, Toth, Langmuir, and Dual-Site Langmuir (see **Table 6.2**). At 25°C, Co-MOF-74 interacts strongly with CO at low pressures, resulting in a distinct Type I isotherm, and it shows the highest capacity of the analogs on a mass basis for all pressures measured. Ni-MOF-74 shows similar strong interactions with carbon monoxide at low pressures but has
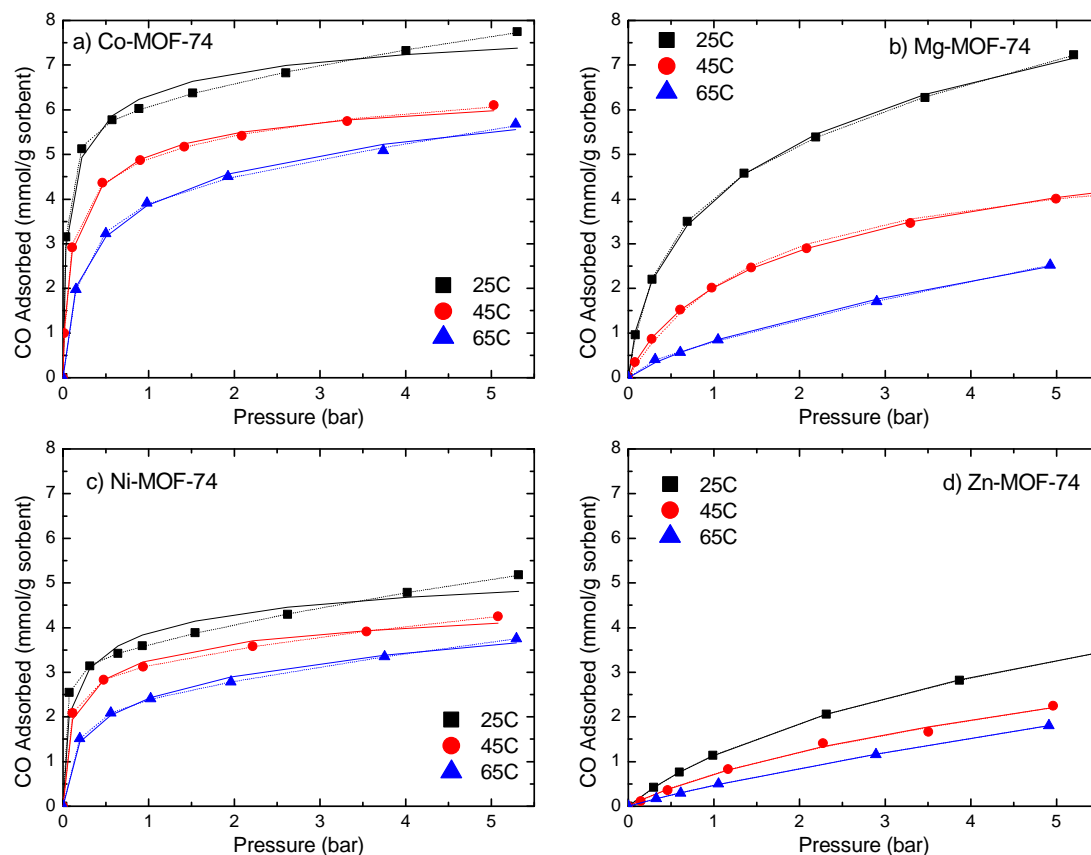
Figure 6.5. Carbon monoxide adsorption at 25°C (■), 45°C (●), 65°C (▲) with Toth (solid line) and Dual-site Langmuir (dotted line) models, a: Co-MOF-74, b: Mg-MOF-74, c: Ni-MOF-74, d: Zn-MOF-74.

a lower overall capacity. At pressures less than approximately 0.5 bar, the nickel analog has the second highest capacity, but by 1 bar, Mg-MOF-74 has exceeded it. Mg-MOF-74, while not exhibiting the strong interaction at the lowest pressures, does have a have a high capacity for CO, approaching 1 molecule per metal site at 5 bar.

On a mass basis, these three analogs greatly exceed the carbon monoxide capacity of any adsorbents reported at ambient pressures and temperature. At 1 bar and 25°C, Zn-MOF-74 (1 mmol/g), the worst performing analog, adsorbs a comparable quantity of carbon

monoxide to Cu-BTC (1.1 mmol/g)[24] and zeolite 5A (1.25 mmol/g),[25] compared to 3.5

mmol/g for Ni-MOF-74, 4 mmol/g for Mg-MOF-74, and 6 mmol/g for Co-MOF-74.

Mg-MOF-74 shows the greatest change in capacity with increasing temperature; at 45°C,

it no longer exceeds the capacity of Ni-MOF-74 at any pressure measured, and at 65°C,

its capacity is comparable with Zn-MOF-74. Our data are in good agreement with the

isotherms reported by Garcia et al. for Co-, Ni-, and Zn-MOF-74 at 303K.[18] The strong

CO-adsorbent interaction seen with Co- and Ni-MOF-74 can be explained through π-

back bonding with the unfilled d-orbitals. Zinc and magnesium do not have partially

filled d-orbitals to contribute to this type of stabilization and therefore do not interact as

strongly with carbon monoxide.

When normalized to an open-metal-site basis, it is evident that many or all of the

theoretical open metal sites for Co-MOF-74, Mg-MOF-74, and Ni-MOF-74 are filled

(100%, 90%, and 80%, respectively), even at pressures below 5 bar. Co-MOF-74 and

Ni-MOF-74 reach their saturation levels below 1 bar, and Co-MOF-74 continues to

adsorb CO in the weaker-binding pore space after its metal sites are filled. This

continued increase as opposed to a leveling-off lends credence to the use of the Dual-Site

Langmuir model and validates the widely disparate parameters for the two types of sites.

The unfilled theoretical open metal sites in Mg-MOF-74 and Ni-MOF-74 may be filled at

higher pressures, but could also be indicative of a higher level of crystal imperfections or

contaminants in these samples compared to the Co-MOF-74.

Table 6.2. Fitting Parameters, M-MOF-74.

		Co-MOF-74							
	25°C			45°C			65°C		
	Toth	Lang-muir	Dual-Site Lang-muir	Toth	Lang-muir	Dual-Site Lang-muir	Toth	Lang-muir	Dual-Site Lang-muir
q1	8.66	6.96	5.73	7.00	5.81	2.52	9.10	5.67	4.32
q2	--	--	6.71	--	--	4.48	--	--	22100
b1	100	16.6	33.3	26.6	8.35	0.371	14.7	2.71	5.24
b2	--	--	0.0814	--	--	16.7	--	--	1.26×10^{-5}
t	0.424	--	--	0.508	--	--	0.369	--	--

		Mg-MOF-74							
	25°C			45°C			65°C		
	Toth	Lang-muir	Dual-Site Lang-muir	Toth	Lang-muir	Dual-Site Lang-muir	Toth	Lang-muir	Dual-Site Lang-muir
q1	16.6	8.05	11.0	7.88	5.29	2.64	100	5.22	12.8
q2	--	--	4.48	--	--	2.64	--	--	0.324
b1	2.24	1.09	0.0725	0.748	0.624	0.624	0.0239	0.183	0.0424
b2	--	--	2.90	--	--	0.624	--	--	7.05
t	0.388	--	--	0.574	--	--	0.281	--	--

Table 6.2 Continued.

	Ni-MOF-74								
	25°C			45°C			65°C		
	Toth	Lang-muir	Dual-Site Lang-muir	Toth	Lang-muir	Dual-Site Lang-muir	Toth	Lang-muir	Dual-Site Lang-muir
q1	6.47	4.47	3.20	5.75	3.95	2.94	12.2	3.71	10.4
q2	--	--	7.24	--	--	4.52	--	--	2.30
b1	100	10.8	49.9	100	7.43	20.6	100	2.37	0.0320
b2	--	--	0.0710	--	--	0.0828	--	--	8.73
t	0.352	--	--	0.338	--	--	0.204	--	--

	Zn-MOF-74								
	25°C			45°C			65°C		
	Toth	Lang-muir	Dual-Site Lang-muir	Toth	Lang-muir	Dual-Site Lang-muir	Toth	Lang-muir	Dual-Site Lang-muir
q1	12.1	6.19	2.74	9.78	4.63	1.61	100	7.10	19737.97
q2	--	--	17.6	--	--	12500	--	--	0.702
b1	0.150	0.22	0.454	0.108	0.181	0.464	0.0062	0.0690	1.39×10^{-5}
b2	--	--	0.0168	--	--	1.8×10^{-5}	--	--	0.381
t	0.599	--	--	0.603	--	--	0.410	--	--

6.4. Conclusions

Activation conditions were found for M-MOF-74 analogs to achieve consistent solvent removal, as characterized by BET surface area, and minimize differences between the analogs in order to draw conclusions on the impact of open metal sites on the adsorption behavior. Co-MOF-74, Mg-MOF-74, and Zn-MOF-74 are stable up to 24 hours at 250°C with minimal surface area loss, but Ni-MOF-74 begins to decompose when activated longer than 12 hours. The transition metal based M-MOF-74 analogs interact quite differently with carbon monoxide compared with the Group II metals. Co- and Ni-MOF-74 show strong low-pressure interaction (< 0.5 bar) with CO due to their π-back bonding capability. Mg-MOF-74 does not interact as strongly at the low-pressure extreme, but shows a high CO capacity at 5 bar, exceeding that of Ni-MOF-74 at moderate pressures and low temperature. Co-MOF-74 has the highest carbon monoxide capacity at 25°C and 1 bar (6 mmol/g), and Mg-MOF-74 shows even greater loadings at higher pressures (7 mmol/g at 5 bar). However, Mg-MOF-74 is much more sensitive to both activation temperature and adsorption temperature compared to Co-MOF-74. This work has shown that activation for 12 hours at 250°C is effective for all analogs to achieve the highest surface areas and consistent adsorption behavior. These results should provide a useful guideline for these popular MOFs and ensure a consistency across future studies to facilitate more direct comparisons of the adsorption performance of the M-MOF-74 family.

6.5. References

(1)   Eddaoudi, M.; Kim, J.; Rosi, N.; Vodak, D.; Wachter, J.; O'Keeffe, M.; Yaghi, O. M. *Science* **2002**, *295*, 469.

(2)   Cavka, J. H.; Jakobsen, S.; Olsbye, U.; Guillou, N.; Lamberti, C.; Bordiga, S.; Lillerud, K. P. *J. Am. Chem. Soc.* **2008**, *130*, 13850.

(3)   Dietzel, P. D. C.; Blom, R.; Fjellvag, H. *Eur. J. Inorg. Chem.* **2008**, 3624.

(4)   Dietzel, P. D. C.; Morita, Y.; Blom, R.; Fjellvag, H. *Angew. Chem.-Int. Edit.* **2005**, *44*, 6354.

(5)   Dietzel, P. D. C.; Panella, B.; Hirscher, M.; Blom, R.; Fjellvag, H. *Chem. Commun.* **2006**, 959.

(6)   Rosi, N. L.; Kim, J.; Eddaoudi, M.; Chen, B. L.; O'Keeffe, M.; Yaghi, O. M. *J. Am. Chem. Soc.* **2005**, *127*, 1504.

(7)   Bloch, E. D.; Murray, L. J.; Queen, W. L.; Chavan, S.; Maximoff, S. N.; Bigi, J. P.; Krishna, R.; Peterson, V. K.; Grandjean, F.; Long, G. J.; Smit, B.; Bordiga, S.; Brown, C. M.; Long, J. R. *J. Am. Chem. Soc.* **2011**, *133*, 14814.

(8)   Zhou, W.; Wu, H.; Yildirim, T. *J. Am. Chem. Soc.* **2008**, *130*, 15268.

(9)   Caskey, S. R.; Wong-Foy, A. G.; Matzger, A. J. *J. Am. Chem. Soc.* **2008**, *130*, 10870.

(10)   Dietzel, P. D. C.; Besikiotis, V.; Blom, R. *J. Mater. Chem.* **2009**, *19*, 7362.

(11)   Valenzano, L.; Civalleri, B.; Chavan, S.; Palomino, G. T.; Arean, C. O.; Bordiga, S. *J. Phys. Chem. C* **2010**, *114*, 11185.

(12)   Valenzano, L.; Vitillo, J. G.; Chavan, S.; Civalleri, B.; Bonino, F.; Bordiga, S.; Lamberti, C. *Catalysis Today* **2012**, *182*, 67.

(13)   Cho, H.-Y.; Yang, D.-A.; Kim, J.; Jeong, S.-Y.; Ahn, W.-S. *Catalysis Today* **2012**, *185*, 35.

(14)   Herm, Z. R.; Krishna, R.; Long, J. R. *Microporous Mesoporous Mat.* **2012**, *151*, 481.

(15)   Hou, X.-J.; He, P.; Li, H.; Wang, X. *J. Phys. Chem. C* **2013**, *117*, 2824.

(16)   Kong, X.; Scott, E.; Ding, W.; Mason, J. A.; Long, J. R.; Reimer, J. A. *J. Am. Chem. Soc.* **2012**, *134*, 14341.

(17) Liu, J.; Tian, J.; Thallapally, P. K.; McGrail, B. P. *J. Phys. Chem. C* **2012**, *116*, 9575.

(18) Garcia, E. J.; Mowat, J. P. S.; Wright, P. A.; Perez-Pellitero, J.; Jallut, C.; Pirngruber, G. D. *J. Phys. Chem. C* **2012**, *116*, 26636.

(19) Valenzano, L.; Civalleri, B.; Sillar, K.; Sauer, J. *J. Phys. Chem. C* **2011**, *115*, 21777.

(20) Chavan, S.; Vitillo, J. G.; Groppo, E.; Bonino, F.; Lamberti, C.; Dietzel, P. D. C.; Bordiga, S. *J. Phys. Chem. C* **2009**, *113*, 3292.

(21) Yu, K.; Kiesling, K.; Schmidt, J. R. *J. Phys. Chem. C* **2012**, *116*, 20480.

(22) Glover, T. G.; Peterson, G. W.; Schindler, B. J.; Britt, D.; Yaghi, O. *Chem. Eng. Sci.* **2011**, *66*, 163.

(23) Schoenecker, P. M.; Carson, C. G.; Jasuja, H.; Flemming, C. J. J.; Walton, K. S. *Ind. Eng. Chem. Res.* **2012**, *51*, 6513.

(24) Karra, J. R.; Walton, K. S. *J. Phys. Chem. C* **2010**, *114*, 15735.

(25) Saha, D.; Deng, S. G. *Journal of Chemical and Engineering Data* **2009**, *54*, 2245.

CHAPTER 7

IMPACT OF AIR EXPOSURE ON ADSORPTION IN A SERIES OF OPEN METAL SITE MOFS

7.1. Introduction

Considerable interest has been shown in the MOF-74 materials for a wide range of small molecule adsorption and separation applications. The MOF-74 family, also known as m(dthp)$_2$, CPO-27, and M/DOBDC, is a series of isostructural materials consisting of dihydroxyterephthalate linkers coordinated to metal centers forming one-dimensional honeycomb channels, where the metal can be magnesium,[1] cobalt,[2] nickel,[3] zinc,[4] iron,[5] or manganese.[6] Each metal center is coordinated to a solvent molecule in addition to the structural linkers. This solvent molecule is removed through activation at elevated temperatures under vacuum, leaving a coordinatively unsaturated metal center or open metal site. Due to these open metal sites, these materials have a high capacity for many gases, including CO_2 (Mg-MOF-74) and CO (Co- and Ni-MOF-74). However, these open metal sites also cause sensitivity to activation conditions and exposure to air or water.

As has been reported previously, these materials are not stable after water vapor adsorption in air, losing 80-95% of their calculated BET surface areas after water adsorption and reactivation.[7] In contrast, several analogs have been shown to be cyclically stable with water exposure when an inert is used as the carrier gas.[1-3] It has

also been found that exposure to ambient air prior to adsorption measurements decreases the measured surface area,[8] leading researchers to store these materials under inert gas or solvent until ready for use. These materials have also been modeled to show that SO_x and NO_x may preferentially adsorb in the open metal sites of these materials.[9] These common pollutants are present in ambient air, potentially contributing to the differences observed between air-exposed and unexposed samples.

Determining the impact on adsorption with air exposure is critical for the future implementation of these and related high-capacity open metal site MOFs in real-world applications. In some cases, the loss in capacity may be small enough to be acceptable, allowing for easy handling. In others, the exceptional performance of the pristine material and large decrease in performance with exposure to ambient conditions may warrant the additional cost and care associated with storing, handling, and shaping. The goal of this work is quantify the differences in air-exposed and unexposed MOF-74 analogs (Co-, Mg-, Ni-, and Zn-) using carbon monoxide capacities. Breakthrough experiments of CO in air and CO in nitrogen at 25°C are used as a model system to investigate the impact oxygen in air has on the CO capacity of these materials.

7.2. Experimental Methods

7.2.1. Synthesis

Materials synthesis procedures were modified from literature as described below.[10,11] All chemicals were used as received: 2,5-dihydroxyterephthalic acid (H₄DOBDC) (98%), $Co(NO_3)_2 \bullet 6H_2O$ (98%), $Mg(NO_3)_2 \bullet 6H_2O$ (98%), $Ni(NO_3)_2 \bullet 6H_2O$ (99%),

$Zn(NO_3)_2 \bullet 6H_2O$ (98%), n,n-dimethylformamide (DMF) (99.8%) obtained from Sigma

Aldrich and ethanol (99%) obtained from VWR.

7.2.1.1. Co-MOF-74

H_4DOBDC (0.5 g, 2.5 mmol) and $Co(NO_3)_2 \bullet 6H_2O$ (1.5 g, 5.2 mmol) were combined.

The solvent mixture, DMF, ethanol, water (70 mL, 70 mL, 70 mL) was added. Once

fully dissolved, it was divided equally into 20 mL vials, capped tightly, and placed in a

pre-heated oven at 100°C for 66 hours.

7.2.1.2. Mg-MOF-74

H_4DOBDC (0.111 g, 0.56 mmol) and $Mg(NO_3)_2 \bullet 6H_2O$ (0.475 g, 1.85 mmol) were

combined. The solvent mixture, DMF, ethanol, water (45 mL, 3 mL, 3 mL) was added.

Once fully dissolved, it was divided equally into 20 mL vials, capped tightly, and placed

in a pre-heated oven at 125°C for 24 hours.

7.2.1.3. Ni-MOF-74

H_4DOBDC (0.5 g, 2.5 mmol) and $Ni(NO_3)_2 \bullet 6H_2O$ (1.5 g, 5.2 mmol) were combined.

The solvent mixture, DMF, ethanol, water (70 mL, 70 mL, 70 mL) was added. Once

fully dissolved, it was divided equally into 20 mL vials, capped tightly, and placed in a

pre-heated oven at 100°C for 66 hours.

7.2.1.4. Zn-MOF-74

H_4DOBDC (1 g, 5 mmol) and $Zn(NO_3)_2 \bullet 6H_2O$ (4.75 g, 16 mmol) were combined. The solvent DMF (100 mL) was added. Once fully dissolved, 5 mL water was added, then, it was divided equally into 20 mL vials, capped tightly, and placed in a pre-heated oven at 110°C for 24 hours.

7.2.2. Sample Handling and Activation

After cooling to room temperature, each sample was washed 3 times over 3 days with DMF. The DMF was exchanged for methanol, with the solution being decanted and replaced daily for 4 days. Samples were stored under methanol.

Samples identified as "unexposed" were loaded into all equipment directly from the methanol solution. The methanol was evaporated under vacuum prior to subsequent treatment. Samples identified as "exposed" or "pre-exposed" were dried in ambient lab air prior to use. Sample activation was conducted at 250°C under vacuum for 12 hours for all materials prior to isotherm measurements. Samples were activated at 250°C for 12 hours under flowing helium prior to breakthrough experiments.

7.2.3. Isotherm Measurements and Breakthrough Experiments

Carbon monoxide isotherms were measured on a lab-built pressure decay system, in which a reference chamber is charged with known amount of gas that is subsequently allowed to enter the sample chamber. The changes in pressure of the two chambers are used to calculate the amount of gas adsorbed by the sample.

Breakthrough experiments were run on a lab-built system consisting of MKS mass flow controllers feeding a packed powder bed (20-60 mg sample) with a Hiden DSMS as the outlet detector. A mixture of 1% CO in air or nitrogen was used to investigate the impact of pre- and concurrent air exposure on CO adsorption. Samples were loaded directly from the methanol solution to the sample cell. Samples were dried at room temperature under a 50 mL/min He stream, then activated at 250°C for 12 hours. After cooling to room temperature, the gas mixture of 0.5 mL/min CO and 49.5 mL/min air or N_2 was started concurrently with the helium stopping. Breakthrough criteria are defined as 5% of the inlet CO flow rate, corresponding to OSHA lower exposure limits.

7.3. Results & Discussion

7.3.1. CO Adsorption

Carbon monoxide isotherms were measured for all analogs at 25°C for samples unexposed to air and activated in situ (unexposed) and samples allowed to dry in ambient conditions prior to measurement (exposed), as shown in **Figure 7.1**. For the exposed samples, the comparative carbon monoxide capacities of the analogs remain similar, with the exposed cobalt analog having the highest capacity along the isotherm and the exposed zinc analog the lowest. Co-MOF-74 exhibited the smallest degradation of all analogs, losing about ¼ of its capacity (24-29%) along the isotherm if allowed to dry in room air prior to isotherm measurement compared to being loaded directly from the methanol solution. Zn-MOF- 74 loses 43-60% of its already low capacity. Ni-MOF-74 does
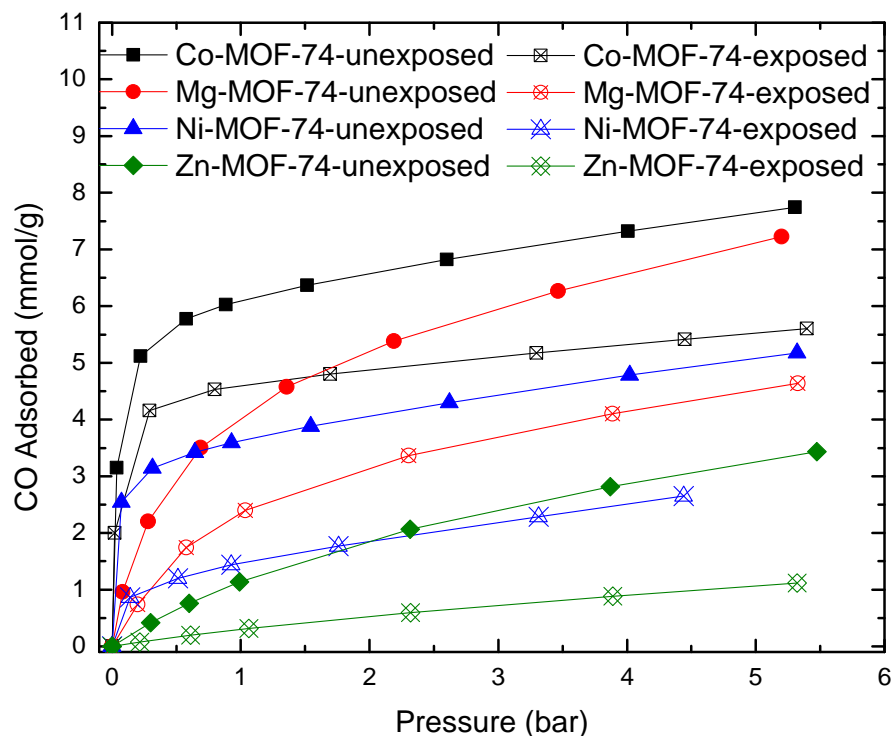
Figure 7.1. CO adsorption at 25°C for M-MOF-74 samples unexposed or exposed to air.

slightly worse, losing 47-67% of its capacity, falling from 3.5 mmol/g CO adsorbed at 1

bar to 1.5 mmol/g for the dry sample. Mg-MOF-74 loses 50-71% of its capacity over the

pressure range measured, with the capacity at 1 bar falling from 4 mmol/g to 2.5 mmol/g.

Co-MOF-74, when exposed to air prior to measurement, has a higher capacity than all

other analogs unexposed to air prior to measurement except wet Mg-MOF-74 above

about 1.5 bar. Exposed Co-MOF-74 reaches 4.5 mmol/g CO adsorbed at 1 bar and 5.5

mmol/g at 5 bar, while unexposed Ni-MOF-74 adsorbs 3.5 mmol/g and 5 mmol/g

respectively. Mg-MOF-74 has weaker low pressure interactions, so the difference

between unexposed Mg-MOF -74 and exposed Co-MOF-74 are highest at low pressures,

reaching 4 and 4.5 mmol/g CO adsorbed, respectively, at 1 bar. Unexposed Mg-MOF-74

surpasses exposed Co-MOF-74 by 1.5 bar, reaching 7 mmol/g at 5 bar compared to exposed Co-MOF-74's 5.5 mmol/g.

7.3.2. Breakthrough Experiments

Breakthrough experiments were conducted with 1% CO in nitrogen or air at 25°C. Zn-MOF-74, showing very little capacity for CO and essentially no remaining surface area after drying was excluded from these experiments. Four sets of conditions were used to investigate the impact of pre-exposure and concurrent exposure to air on the CO capacity of Co-, Ni-, and Mg-MOF-74. The first samples were entirely unexposed to air and were loaded wet as described above, with nitrogen used as the carrier gas, denoted "unexposed in N_2". The second and third sets of samples were exposed to air before the experiment or during the experiment. The second set was dried in ambient air prior to the experiment with nitrogen as the carrier gas, "pre-exposed in N_2" to investigate air exposure on the MOF prior to the experiment, similar to the conditions used for the isotherm measurements. The third set was loaded wet, but the carrier gas was air ("unexposed in air") to investigate the impact of concurrent air exposure on adsorption. The final set of samples was dried in ambient air prior to being run with air as the carrier gas ("pre-exposed in air"). The "unexposed in N_2" samples represent the most ideal lab conditions. The "pre-exposed in air" samples most closely mimic conditions that might be encountered in a real-world system removing carbon monoxide from air. The intermediate conditions serve to isolate air exposure before and during adsorption to investigate the necessity of keeping samples out of contact with air prior to or during

adsorption and help answer the question about the tradeoff between lost equilibrium capacity and ease of handling with dried samples.

Unexpectedly, "pre-exposed in air" Co-MOF-74 had the longest breakthrough time for carbon monoxide (**Figure 7.2**). The other three samples followed the expected trend, with the sample "unexposed in N_2" outperforming the sample "unexposed in air" and the sample "pre-exposed in N_2". The samples run in nitrogen follow the trends predicted from the isotherms, with pre-experimental air exposure reducing the carbon monoxide capacity. The reduced capacity of the "pre-exposed in N_2" sample relative to the "unexposed in air" sample indicates that molecules present in ambient air in addition to
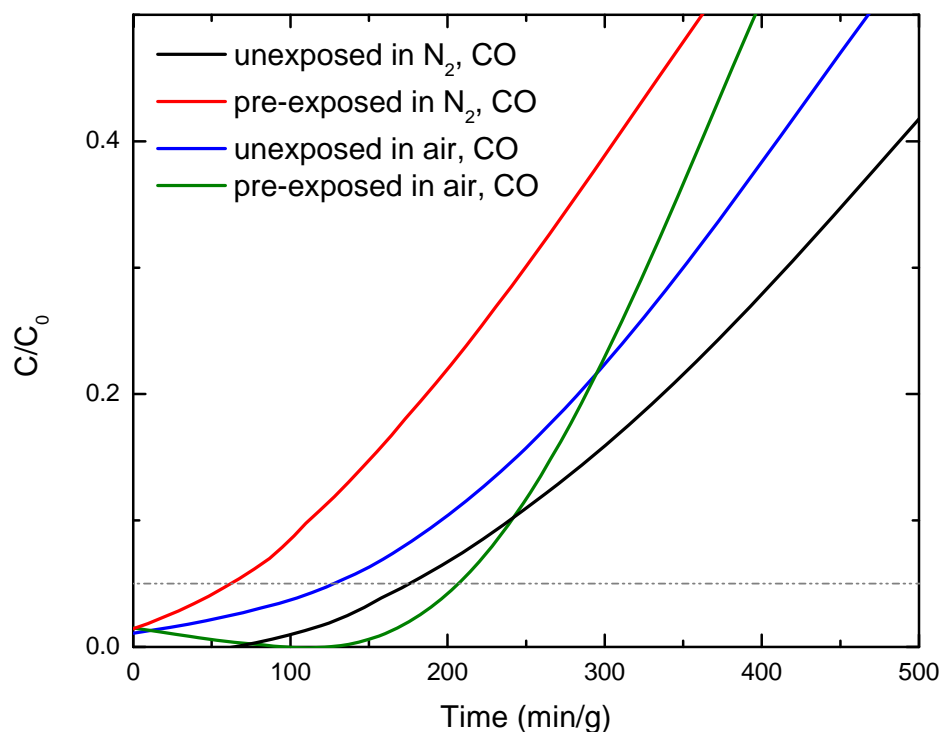
Figure 7.2. Co-MOF-74, 1% CO breakthrough.

oxygen or duration of exposure may contribute to the loss. Breakthrough times are listed in **Table 7.1**.

To understand the apparently anomalous results found with the sample "pre-exposed in air," it is necessary to consider oxidation. Of the Co-MOF-74 samples considered, only this sample resulted in carbon dioxide present in the outlet stream, as shown in **Figure 7.3**. Carbon is detected in the outlet at about the same breakthrough time as the "unexposed in air" sample, but carbon dioxide is initially the dominating species. Since a similar stream is not present for "pre-exposed in N_2," this is not merely carbon dioxide adsorbed from ambient air that was not fully removed during activation but rather carbon

Table 7.1. CO Breakthrough Time for All Conditions.

	Breakthrough Time CO (carbon) in N_2		Breakthrough Time CO (carbon) in Air	
	min / g		min / g	
	un-exposed	pre-exposed	un-exposed	pre-exposed
Co	183	67	132	208
				(124)
Mg	156	376	114	322
				(254)
Ni	485	640	352	319
	(241)	(268)	(252)	(150)
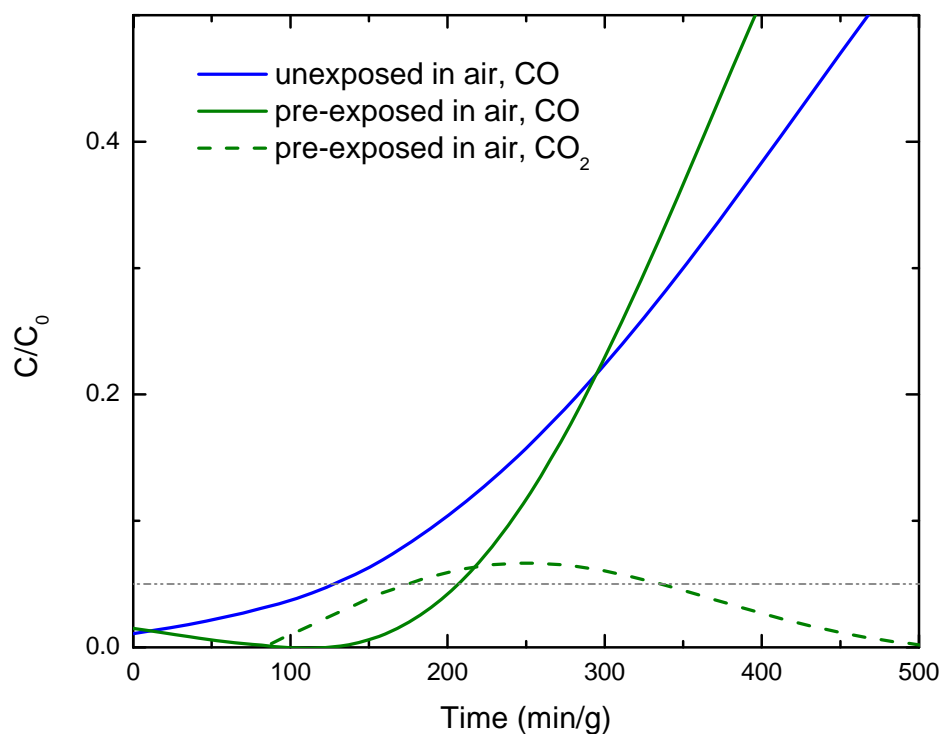
Figure 7.3. Co-MOF-74 sample dried in air prior to breakthrough with 1% CO, balance air CO and CO_2. Co-MOF-74 under the same experimental conditions but unexposed to air prior to breakthrough shown for reference.

monoxide being oxidized. The MOF is unable to sustain the oxidation, which may indicate simultaneous disruption to the framework.

In contrast to Co-MOF-74, the Mg-MOF-74 samples show the opposite trend predicted from the capacity lost with the isotherms in both air and nitrogen: the samples that were exposed to ambient air prior to the experiment had longer breakthrough times than either of the unexposed samples (**Figure 7.4**). The unexposed samples, however, also took longer to reach saturation. Like Co-MOF-74, Mg-MOF-74 "pre-exposed in air" had carbon dioxide in the outlet stream.
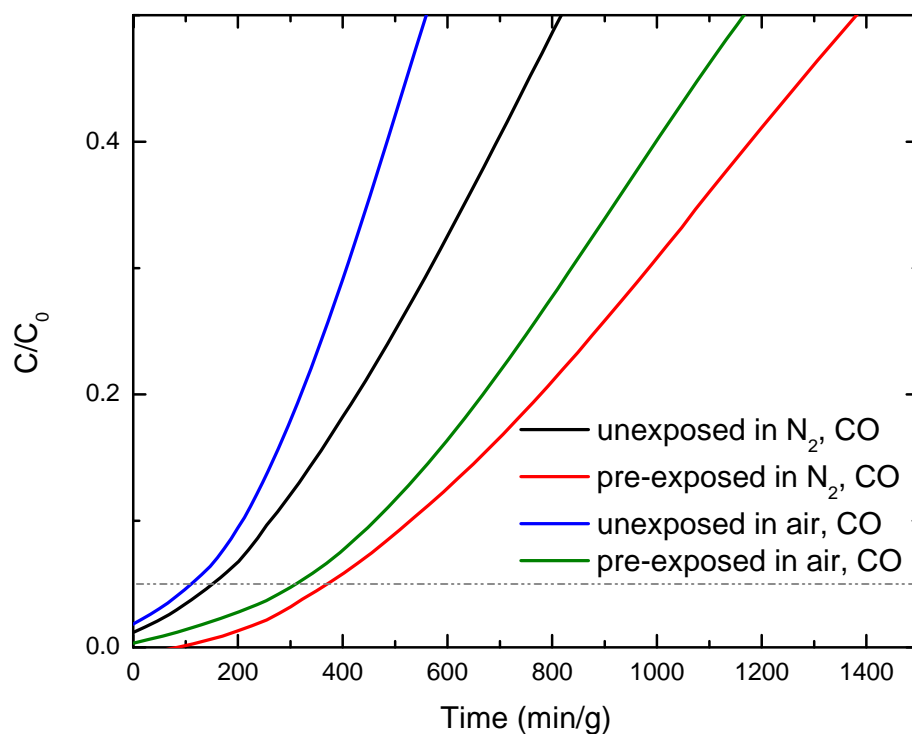
Figure 7.4. Mg-MOF-74, 1% CO breakthrough.

Unlike Co-"pre-exposed in air", the carbon dioxide was not at the beginning of the run but after the sample had reached 80% saturation (**Figure 7.5**). This delay could be related to the higher affinity of Mg-MOF-74 for carbon dioxide. It has been shown that co-adsorbed water generally decreases Mg-MOF-74's capacity for other molecules,[8,11,12] implying that water vapor adsorbed during air exposure prior to the experiment is not the cause. However, Mg-MOF-74 has a much higher capacity for CO_2 than for CO, so the reversal of trends may be due to the adsorption of the carbon dioxide produced, and some pre-exposure to air or pollutants therein is necessary to activate the oxidation.
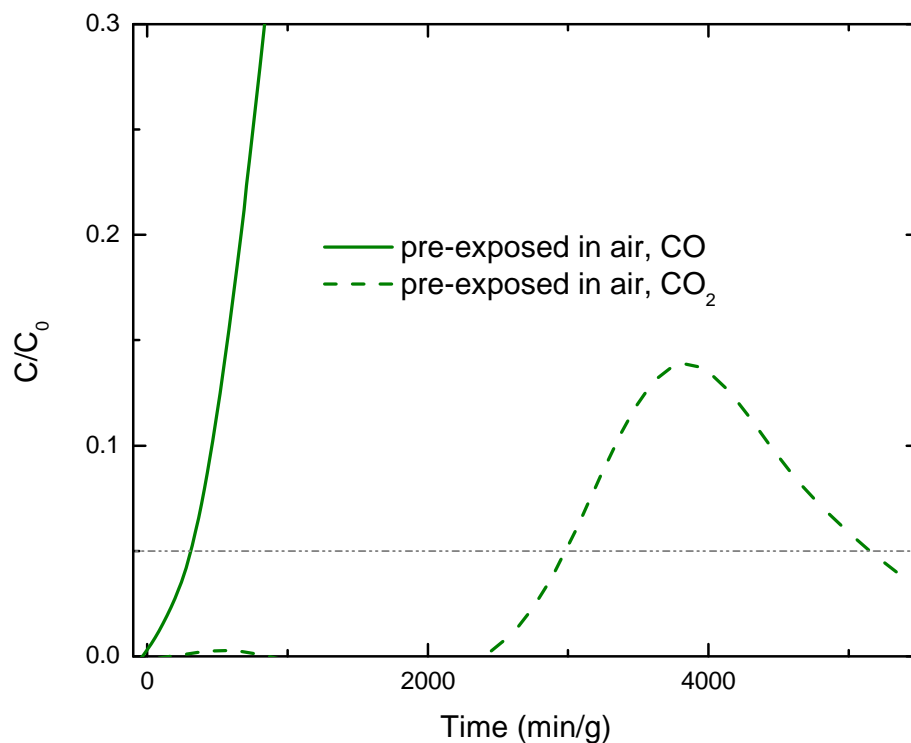
Figure 7.5. Mg-MOF-74 sample dried in air prior to breakthrough with 1% CO, balance air (Co-d-a) showing carbon, CO, and CO_2. Mg-MOF-74 under the same experimental conditions but unexposed to air prior to breakthrough shown for reference.

The CO breakthrough curves for Ni-MOF-74 are shown in **Figure 7.6**. Unlike the previous analogs, Ni-MOF-74 has carbon dioxide present in the outlet under all conditions. When exposed to air prior to the breakthrough experiment, a CO_2 peak similar to that seen in Co-MOF-74-"unexposed in air" is present in both "pre-exposed in air" and "pre-exposed in N_2." However, unlike the previous materials, the peak does not quickly fall to zero. For "pre-exposed in N_2", the steady-state output is 5% of the CO inlet, and for "pre-exposed in air", the output reaches 15% of the CO inlet. Even in the case of the sample "unexposed in N_2," more CO_2 exits the sample bed than in the case of the largest outlet from a Co-MOF-74 sample. When the overall carbon outlet is
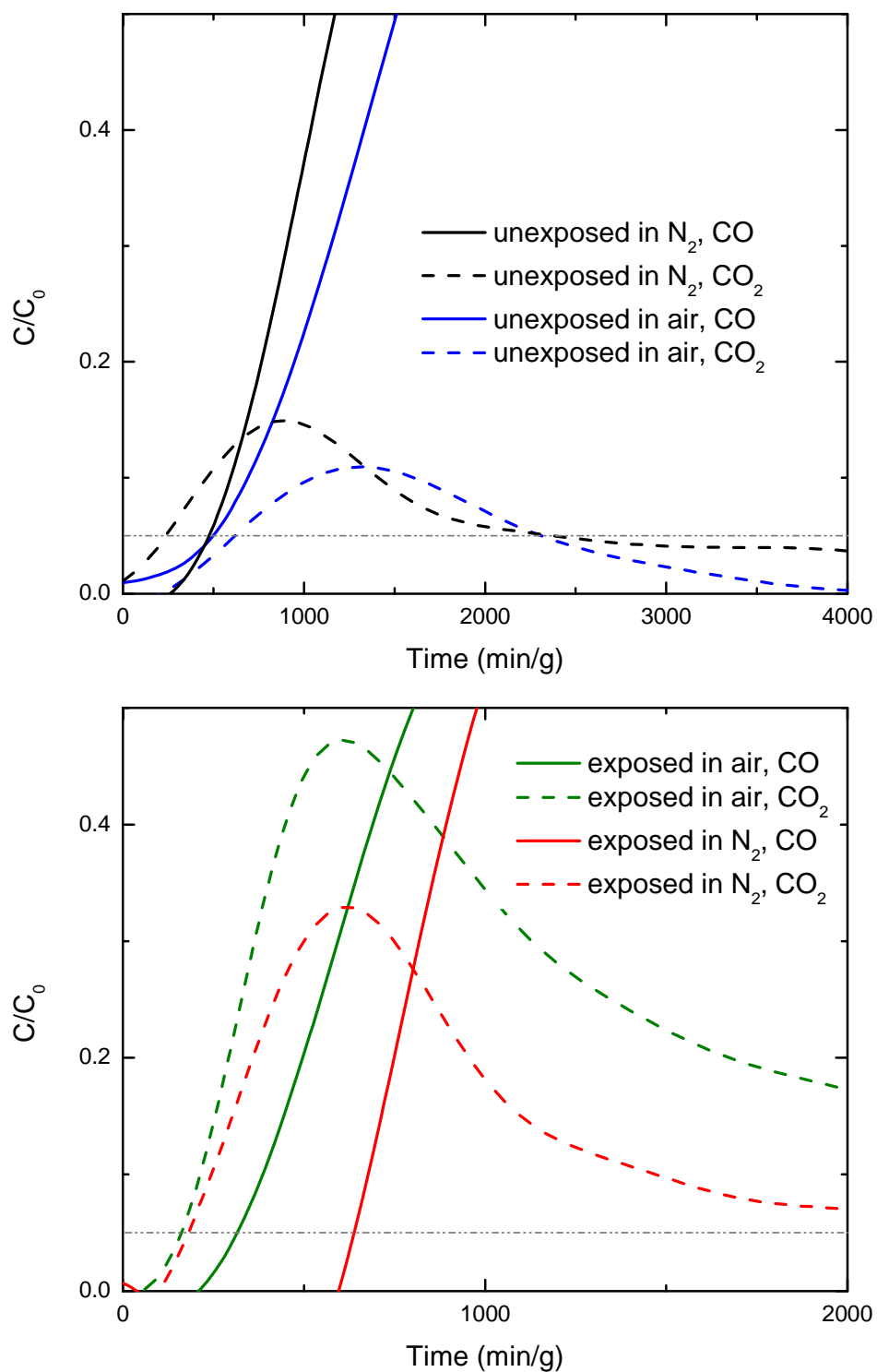
Figure 7.6. Ni-MOF-74, 1% CO breakthrough, unexposed prior to measurement, top; exposed to air prior to measurement, bottom.

considered, the samples under comparable experimental conditions do follow the trends predicted from the isotherm with the unexposed samples having higher capacities than their pre-exposed counterparts, but the generation of carbon dioxide complicates the trends.   In a situation where oxidation may be acceptable or even desirable, the large losses in equilibrium capacity for Ni-MOF-74 may be overcome by the partial room temperature oxidation.

7.4. Conclusions

This work considered the impact of air exposure on subsequent adsorption in MOF-74 analogs. We found that drying the sample prior to isotherm measurement reduces the equilibrium CO capacity across the board, with Co-MOF-74 retaining the highest capacity of the air-exposed analogs. Exposed Co-MOF-74 even surpassed the CO capacity of unexposed Mg-MOF-74 below 1.5 bar and unexposed Zn-MOF-74 and Ni-MOF-74 across the entire pressure range measured.

The uniform reduction in capacity was not seen with breakthrough experiments. For Co-MOF-74 there was a reduction in capacity with air exposure, but in the case of Mg-MOF-74, drying the sample in air prior to the experiment increased the breakthrough time over the unexposed sample in both the air and nitrogen streams. CO_2 was present in the outlet for all Ni-MOF-74 conditions and for Co- and Mg-MOF-74 samples that had been dried under ambient conditions prior to breakthrough in air. Oxygen exposure alone cannot fully explain the differences in breakthrough behavior for these materials. Adsorbed species that are not removed during activation, partial structural collapse, and

contaminants remaining from synthesis may explain the CO_2 production and differing trends between analogs. Further work should be conducted to isolate the relative impact of water vapor, CO_2, and pollutants in ambient air on carbon monoxide adsorption and oxidation.

The complex changes under dynamic conditions with gas mixtures seen with Mg-MOF-74 and Ni-MOF-74 illustrate the difficulty in predicting adsorption from mixtures. This demonstrates the need to critically evaluate material performance under ideal conditions and selectively conduct the appropriate experiments with respect to anticipated operating conditions early in the material selection process to quantify material strengths and weaknesses.

7.5. References

(1)   Dietzel, P. D. C.; Blom, R.; Fjellvag, H. *Eur. J. Inorg. Chem.* **2008**, 3624.

(2)   Dietzel, P. D. C.; Morita, Y.; Blom, R.; Fjellvag, H. *Angew. Chem.-Int. Edit.* **2005**, *44*, 6354.

(3)   Dietzel, P. D. C.; Panella, B.; Hirscher, M.; Blom, R.; Fjellvag, H. *Chem. Commun.* **2006**, 959.

(4)   Rosi, N. L.; Kim, J.; Eddaoudi, M.; Chen, B. L.; O'Keeffe, M.; Yaghi, O. M. *J. Am. Chem. Soc.* **2005**, *127*, 1504.

(5)   Bloch, E. D.; Murray, L. J.; Queen, W. L.; Chavan, S.; Maximoff, S. N.; Bigi, J. P.; Krishna, R.; Peterson, V. K.; Grandjean, F.; Long, G. J.; Smit, B.; Bordiga, S.; Brown, C. M.; Long, J. R. *J. Am. Chem. Soc.* **2011**, *133*, 14814.

(6)   Zhou, W.; Wu, H.; Yildirim, T. *J. Am. Chem. Soc.* **2008**, *130*, 15268.

(7)   Schoenecker, P. M.; Carson, C. G.; Jasuja, H.; Flemming, C. J. J.; Walton, K. S. *Ind. Eng. Chem. Res.* **2012**, *51*, 6513.

(8)   DeCoste, J. B.; Peterson, G. W.; Schindler, B. J.; Killops, K. L.; Browe, M. A.; Mahle, J. J. *Journal of Materials Chemistry A* **2013**, *1*, 11922.

(9)   Yu, K.; Kiesling, K.; Schmidt, J. R. *J. Phys. Chem. C* **2012**, *116*, 20480.

(10)   Caskey, S. R.; Wong-Foy, A. G.; Matzger, A. J. *J. Am. Chem. Soc.* **2008**, *130*, 10870.

(11)   Glover, T. G.; Peterson, G. W.; Schindler, B. J.; Britt, D.; Yaghi, O. *Chem. Eng. Sci.* **2011**, *66*, 163.

(12)   Yu, J. M.; Balbuena, P. B. *J. Phys. Chem. C* **2013**, *117*, 3383.

CHAPTER 8

CONCLUSIONS

8.1. Metal Oxide-MOF Systems via Impregnation

8.1.1. Summary and Conclusions

Composites consisting of metal oxides impregnated into MOFs were successfully synthesized. It was found that targeted functionality could be added to a MOF with minimal pore blocking in UiO-66. UiO-66 does not have a high CO capacity, but it can be enhanced slightly at room temperature through the impregnation and subsequent in situ degradation of cobalt precursors. At 65˚C, the UiO-66-cobalt oxide composites show greatly enhanced capacity, with these capacities even higher than those at 25˚C. This trend is indicative of the chemisorption expected in interactions between carbon monoxide and cobalt oxide.

In contrast, the composites synthesized with MOF-74 did not show enhanced carbon monoxide capacity. There are two likely reasons not present in the UiO-66 system for this. In order to prevent MOF degradation, these samples were kept in methanol, and nitrate loading was conducted thorough a type of solvent exchange or diffusion rather than activation prior to solution contact. The solvent in the pores may not have been effectively displaced, particularly given the strength of the bond between the open metal sites and solvent molecules. Secondly, while UiO-66 is cubic, MOF-74 possesses one-dimensional channels. Each channel in MOF-74 is essentially isolated from all others. If the oxide formed sufficiently large particles to block an entire channel, the interior would be completely blocked from solvent removal and subsequent adsorption. In contrast, a

blocked channel in UiO-66 would limit access to a relatively much smaller portion of the pore system due to the greater degree of interconnectedness.

8.1.2. Recommendations for Future Work

Future work in this area should focus on optimizing systems targeting specific adsorbates and combining impregnants with functionalized MOFs. Cobalt oxide in UiO-66 shows promise; an optimal loading should be identified. These types of materials could be investigated for changing capacities of other toxic gases. This could then be extended to UiO-66 with functionalized organic linkers. The interplay between the functional groups on the structure and the added active sites in the pore space would be interesting to investigate: perhaps targeting different classes of potential adsorbates through the linkers and impregnant could advance towards the goal of broad-spectrum protection in a single material. Additionally, UiO-66 has very little inherent affinity for carbon monoxide. By using a stable material with greater inherent affinity, the CO capacity could be similarly enhanced. However, the challenge with this is apparent in the metal oxide-MOF-74 materials: stability in air and effective activation prior to impregnation are critical for effective composites.

8.2. Metal Oxide-MOF Systems via Encapsulation

8.2.1. Summary and Conclusions

HKUST-1 was successfully synthesized with metal oxides – titania or magnetic cobalt iron oxide nanoparticles – in the framework. The composites were characterized and interrogated with gases and vapors to study the impact of the metal oxide inclusion on the MOF framework and adsorption properties.

The HKUST-1-titania composite was distinct from a physical mixture of the formed MOF and an equivalent amount of titania. It has a higher dynamic capacity of carbon dioxide at room temperature than the parent HKUST-1 in the absence of air and is comparable with the parent when air is present. At 250°C, HKUST-1+TiO$_2$ completely oxidizes the CO to carbon dioxide when presaturated with air. Under the same conditions, HKUST-1 oxidizes about a third of the CO present. The composite reaches the same level of oxidation, a third of the carbon monoxide feed, at 100°C lower.

HKUST-1 was stabilized significantly by the incorporation of the nanoparticles. The composite was sufficiently incorporated into the MOF framework that the entire sample with included magnetic nanoparticles responded to the presence of a magnetic field. When normalized to the quantity of parent HKUST-1 present, it enhanced the MOF's capacity for CO and water vapor. The presence of the particles impacted hexane adsorption the most, with the composite not showing the partial framework collapse seen in the unmodified HKUST-1.

8.2.2. Recommendations for Future Work

HKUST-1 is widely studied and can be synthesized under a wide variety of conditions. However, it lacks stability, making it unattractive for applications where water vapor may be present. Encapsulating metal oxides appears to be an attractive way to add additional functionality while simultaneously increasing framework stability. There is much room for optimization. This method could be pursued with other oxides to target specific applications, particularly those where mixed metal oxides including copper have shown promise. Optimizing the loading may increase stability further, ensuring all particles contain the stabilizing oxide particles.

In addition to HKUST-1, this method of encapsulation could be applied to other MOFs. The criteria that must be met include oxide stability in the MOF synthesis solution and MOF formation under stirring conditions; additionally, a three-dimensional pore system is desirable to ensure sufficient access to the nanoparticle. Attempts to encapsulate metal oxide particles in UiO-66 were unsuccessful due to the highly acidic nature of the MOF precursor zirconium chloride. HKUST-1 was synthesized here with a water-ethanol mixture. Many MOFs can be synthesized in water, ethanol, DMF, and mixtures of the same with precursors that do not produce hydrogen chloride when combined. Additionally, the MOF must nucleate and grow appropriately under stirring conditions. MOFs that nucleate preferentially on surfaces rather than in solution are attractive. The oxide provides sites for heterogeneous nucleation while homogeneous nucleation may result in MOF particles predominantly excluding nanoparticles. Stirring or agitation is important to ensure the nanoparticles remain suspended to provide access to all sides to achieve complete encapsulation. There are MOFs that do not crystallize or result in particles that are too small to effectively encapsulate any nanoparticles under these conditions. Additional understanding of the crystallization of attractive MOFs is critical to rationally choosing systems with the greatest likelihood of success.

8.3. OMS MOFs for Adsorption

8.3.1. Summary and Conclusions

MOF-74 has demonstrated record capacities for adsorption under ideal conditions. This work investigated optimizing activation conditions for a series of MOF-74 analogs containing cobalt, magnesium, nickel, and zinc centers. After optimal conditions were identified, the impact of relaxing ideal conditions on adsorption was investigated. The

primary condition considered was exposure to air before activation and concurrently with the target adsorbate molecules.

Optimal activation conditions were identified for each analog, and it was found that 12 hours at 250°C was uniformly successful for all analogs considered. Co-, Mg-, and Zn-MOF-74 were minimally impacted by increasing activation time up to 24 hours. Ni-MOF-74 began to decompose after 18 hours at this temperature, and peaks indicative of nickel oxide grew over time. Co-MOF-74's carbon monoxide capacity was impacted least by changing the activation temperature. Activation temperature impacted Mg-MOF-74 the most, with a decrease in activation temperature of 100°C reducing its capacity at 25°C from among the best to be comparable to Zn-MOF-74, the worst performing analog considered.

The impact of air exposure on MOF-74 was considered to quantify the change in carbon monoxide capacity with exposure. As expected, the analogs each individually lost CO capacity after short-term exposure to ambient air. However, air-exposed Co-MOF-74 had a higher capacity than the unexposed samples of Ni- and Zn-MOF-74 over the entire pressure range measured and Mg-MOF-74 at low pressures. Under dynamic conditions, the trend seen in the isotherms of a general decrease in capacity applied to Co-MOF-74, with air exposure prior to activation decreasing carbon monoxide capacity, but the Mg-MOF-74 samples showed the opposite trend. All Ni-MOF-74 samples showed oxidation to carbon dioxide, and this complication explains why the equilibrium isotherm trends do not correctly predict the relative behavior under different conditions.

8.3.2. Recommendations for Future Work

This work shows the importance of defining how optimal conditions can be achieved and communicating the details necessary to obtain them within a single laboratory. However, it has been shown with Ni-MOF-74 that even identical conditions may not obtain identical results in various geographic locations. Coupled with the changes seen here for unexposed and air-exposed samples, there is a need to identify the other variables impacting MOF-74 with ambient air exposure. Along with identifying them, their impact must be quantified so informed decisions can be made about whether or not the negative impact outweighs the potential positive gain, or if a perceived negative impact such as loss of surface area actually translates into a related negative impact in adsorption capacity. Water vapor and common environmental pollutants like SO_x and NO_x may be playing a role with oxygen to cause the instability. This also reinforces the idea that equilibrium isotherms may not be the best predictor for separations of multicomponent gas mixtures. Even two-component mixtures such as carbon dioxide-nitrogen separations may not be the best screening tool for MOFs when it is known that oxygen may play a role in their instability. Identifying and communicating the parameters of experiments along with predicted pitfalls under less ideal conditions may better direct future work in moving MOF separations into the realm of practical application.

APPENDIX A

METAL OXIDES INCLUDED IN SBA-15 FOR TOXIC GAS ADSORPTION

A.1. Introduction

Metal oxides included in porous materials have the potential to perform well in separating toxic gases from breathing air. Metal oxides are known to be effective adsorbents, but traditional synthesis methods result in low surface area, and therefore less reactive, materials. We have included magnesium and cobalt oxide in the pores of SBA-15. SBA-15, a silica widely studied for catalytic and adsorption applications, possesses a regular pore structure of meso- and micropores. Synthesizing the oxides within the pore system restricts growth and agglomeration, resulting in small particles with a higher density of edge and defect sites. Metal oxides such as MgO and Co_3O_4 have been successfully synthesized in mesoporous carbons and silicas to form nanoparticles and inverse replicas by many groups who used the composite materials for catalytic oxidation[18-20] and electrochemical applications.[21,22] Most commonly, metal nitrates in water[23-28] or ethanol[18,20-22,29-31] have been used to impregnate the mesoporous material, followed by heating to decompose the nitrate into the metal hydroxide or oxide. Some groups have considered the impact of organic solvents plus water on resulting particle properties.[109]

A.2. Experimental Methods

A.2.1. Synthesis Methods

SBA-15 was synthesized following literature procedures.[110] SBA-15 was then

impregnated per literature procedures[28] with $Mg(NO_3)_2 \bullet 6H_2O$ or $Co(NO_3)_2 \bullet 6H_2O$ using

both wet and incipient wetness techniques and subsequently heated to decompose the

nitrate. Solutions of 1 or 2M nitrate in water or ethanol were added to SBA-15. For wet

impregnation, an excess of solution was added. This mixture was stirred for 24 hours, at

which time the SBA-15 was filtered and dried. For incipient wetness, only enough

solution to wet the sample was added. Each sample was heated at a rate of 2.5°C/min to

200°C and held there for 3 hours to decompose the nitrate. Samples are identified as

follows: metal_(impregnation technique, w = wet, i = incipient wetness)[(nitrate

concentration),(solvent, H= water, E=ethanol)]-(d = dried prior to decomposition, w = no

drying prior to decomposition); for example, SBA-15+Mg_w[1,H]-d was synthesized

from 1M magnesium nitrate hexahydrate in water via wet impregnation and allowed to

dry before decomposition.

A.2.2. Characterization & Isotherms

Nitrogen physisorption data were collected on a Quantachrome Quadrasorb at 77K.

Surface areas were determined using the BET method over the range $0.05<P/P_0<0.3$,

pore sizes using the Quadrasorb built-in DFT calculations, and pore volumes from the

relative pressure closest to $P/P_0=1$. Scanning electron microscopy (SEM) images were

obtained on a LEO 1530 operated at 10 kV to help determine the location of oxide

formation. Transmission electron microscopy (TEM) images were collected on a JEOL

100 CX II (100kV). Thermogravimetric analysis coupled with differential scanning calorimetry (TGA-DSC) was conducted by a NETZSCH STA 449 F1 Jupiter. Carbon dioxide adsorption was performed on a Hiden IGA-001 at 25°C over 0-5 bar or a lab-made pressure decay system at the same temperature and pressures.

A.2.3. Breakthrough

A subset of the composites were chosen for further characterization and evaluation for adsorption of ammonia, sulfur dioxide, cyanogen chloride, and octane: SBA-15, SBA-15+Mg_w[1,H], SBA-15+Co_w[1,H], SBA-15+Mg_i[2,E], and SBA-15+Co_i[2,E]. These experiments were performed at ECBC on a microbreakthrough system described previously.[89]

A.3. Results & Discussion

A.3.1. Composite Characterization

All composites were characterized via nitrogen physisorption. The parent SBA-15 displays a type IV isotherm with hysteresis characteristic of mesoporous materials. Generally, the composite materials exhibited similarly-shaped isotherms while retaining 4-99% of the parent material's surface area (**Table A.1**). The desorption curve for materials retaining high surface areas exhibit shoulders on the hysteresis loop which have been attributed to a cavitation phenomenon occurring when mesopores are partially blocked.[109] Combined with decreased pore sizes and loss of microporosity, this indicates particle formation within the pore system. A subset of the N_2 isotherms, the composites

that were interrogated with toxic gases, are shown in **Figure A.1**: each isotherm exhibits

a shoulder in the desorption branch characteristic of partial pore blockage.

The composites with very little surface area retained were seen in SEM to have

significant oxide formation on the surface of the particles that restricted access to the pore

space, particularly in cases of higher precursor concentration or decomposition without

drying. In the case of saturated precursor, nitrates were likely deposited on the exterior of

the particles during drying, as evidenced in **Figure A.2**. When decomposed wet, even
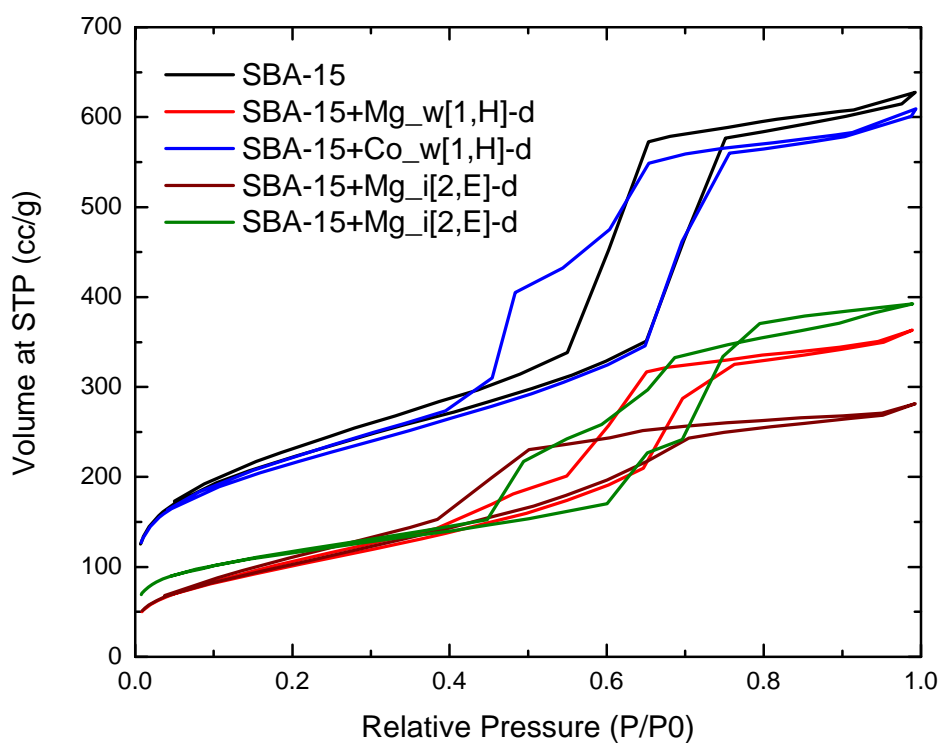
Figure A.1. N_2 adsorption isotherms for SBA-15 and composites evaluated against toxic gases. All tested samples retain relatively high surface areas and exhibit knees in their desorption isotherm characteristic of partial pore blockage.

Table A.1. SBA-15 and Composite Porosity.

Material	BET Surface Area		Pore volume		DFT Pore Sizes	
	m^2/g	%	cm^3/g	%	micro-	meso-
SBA-15	765		0.97		7-8	30-39
Mg_w[1,H]-d	377	49	0.56	58		22-39
Mg_i[sat,H]-d	30	4	0.05	5		25-36
Co_w[1,H]-d	758	99	0.94	97		23-38
Co_i[sat,H]-d	160	21	0.30	31	7-8	25-27, 33-39
Mg_w[1,H]-w	16	2	0.05	5		22-32
Mg_i[1,H]-w	23	3	0.05	5		21-36
Co_w[1,H]-w	249	33	0.35	36		24-40
Co_i[1,H]-w	196	26	0.31	32	7-8	25-27, 31-39
Mg_i[2,H]-d	134	18	0.18	19		15-28
Co_i[2,H]-d	289	38	0.39	40	7-8	25-29, 30-39
Mg_i[2,E]-d	390	51	0.42	43		18-29
Co_i[2,E]-d	404	53	0.61	63		24-31, 33-43
Mg_i[1,H]-d	547	71	0.84	87		29-38
Mg_w[1,E]-d	156	20	0.23	24		21-35
Mg_i[1,E]-d	66	9	0.09	10		18-31
Co_i[1,H]-d	324	42	0.50	51		20-40
Co_w[1,E]-d	379	50	0.78	80		24-31
Co_i[1,E]-d	404	53	0.63	65		22-40

with excess precursor solution removed, the liquid phase present would allow greater

mobility, allowing migration and agglomeration on the exterior surface.

TEM was used to investigate the location of the oxides in the SBA-15 pore system.

Figure A.3 shows TEM of SBA-15+Co_w[1M,H]-d. The darkfield image (**Figure**

A.3.b) shows bright areas associated with the cobalt oxide around the edges of the

particle, not throughout the pore space, but the sizes are consistent with the particles

being distributed inside the SBA-15 in the upper portions of the pore system. **Figure A.4**

shows a TEM of a material synthesized with a higher precursor concentration, SBA-

15+Co_i[2,E]. It shows two distinct phases, with SAD consistent with the oxide being

formed independently from the silica or apparently agglomerated on the surface.
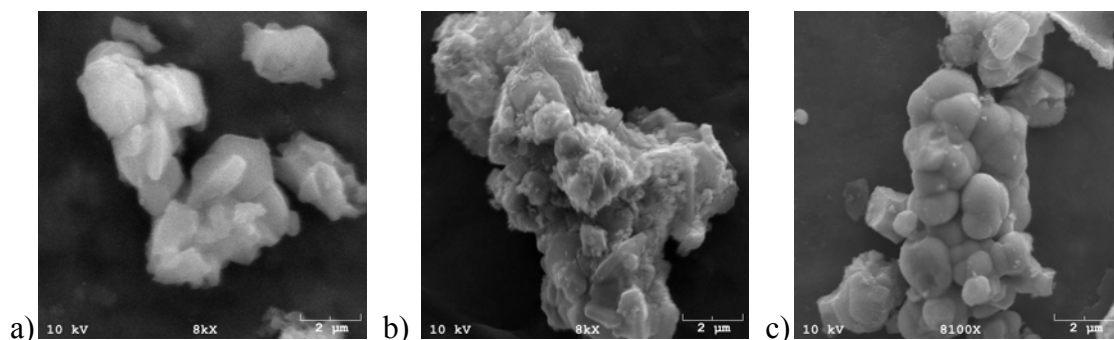
Figure A.2. SEM images of SBA-15 and composites. Lower-concentration precursor solutions help ensure minimal oxide formation on the exterior surface of the material, as seen comparing the parent SBA-15 (a) with a sample synthesized from a 1M nitrate solution, SBA-15-Co_i[1,H]-d (b), and a composite synthesized from saturated precursor solution, SBA-15-Co_i[sat,H]-d (c).
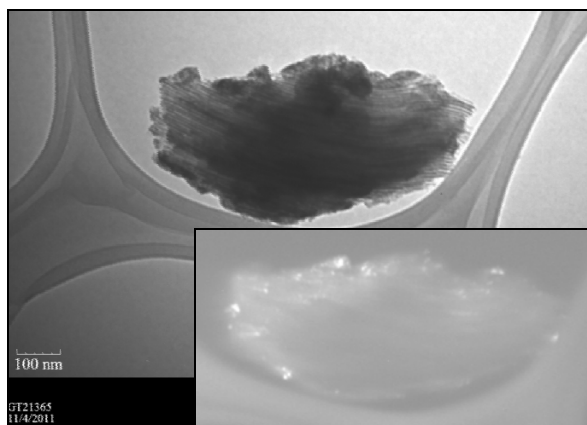
Figure A.3. TEM image of SBA-15+Co_w[1M,H]-d (a) and corresponding darkfield image (b) which indicated cobalt oxide is located predominantly around the edges of the material, with size and distribution consistent with oxide formation in the outer portion of the pore system.
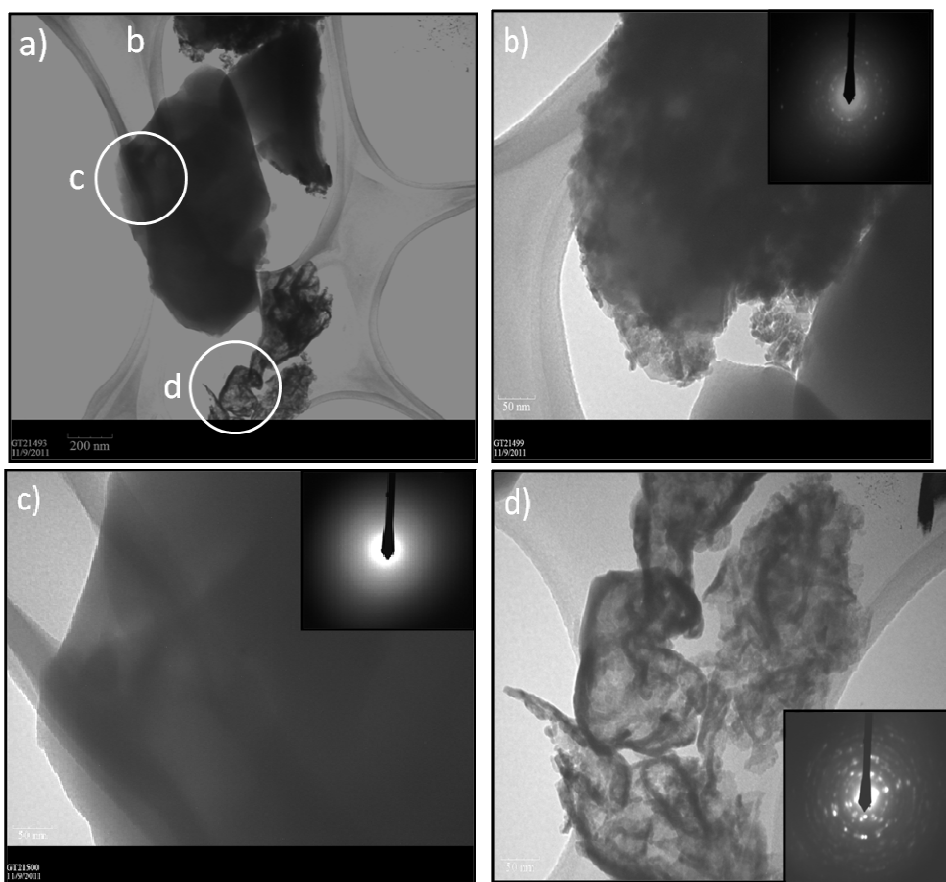
Figure A.4. TEM of SBA-15 + Co_i[2, E], showing two distinct phases of SBA-15 and oxide (a). The silica phase SAD shows only faint rings indicative of the pore system (c). Particles of cobalt oxide have formed independently from the silica (d), but in some areas, the physiology more closely resembles SBA-15 + Co_w[1, H], where the SBA-15 and oxide are in intimate contact, consistent with formation in the pore space (b), with significant agglomeration on the surface.

A.3.2. Carbon Dioxide Adsorption

CO_2 Isotherms were measured for each composite, shown in **Figure A.5** with equilibrium adsorption listed in **Table A.2**. At the pressures considered (up to 5 bar), pore space plays a larger role in CO_2 adsorption than additional functionality from the included oxides when considered on a per-sorbent mass basis.
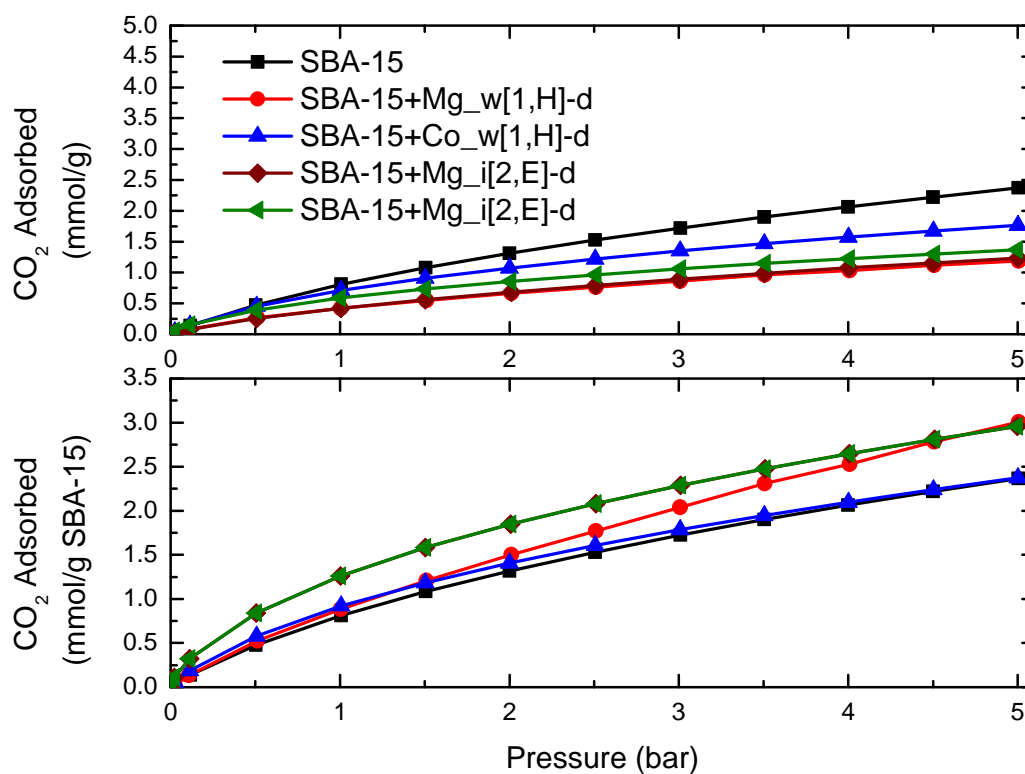
Figure A.5. CO_2 isotherms at 25°C for the composite materials on a mass basis with respect to sorbent mass (top) and with respect to SBA-15 present in the sample (bottom). Isotherms are reversible, so desorption curves were omitted for clarity.

Table A.2. CO_2 Adsorption.

| | Surface Area | | CO$_2$ Adsorbed mmol CO$_2$/g sorbent | | CO$_2$ Adsorbed mmol CO$_2$/g SBA-15 | |
	m^2/g	%	@ 1 bar	@ 5 bar	@ 1 bar	@ 5 bar
SBA-15	765	100	0.81	2.37	0.81	2.37
SBA-15+Mg_w[1,H]-d	377	49	0.42	1.19	0.89	3.00
SBA-15+Co_w[1,H]-d	758	99	0.71	1.77	0.92	2.37
SBA-15+Mg_i[2,E]-d	390	51	0.42	1.24	1.81	5.53
SBA-15+Co_i[2,E]-d	404	53	0.59	1.37	1.26	2.96

A.3.3. Breakthrough

The impregnated samples and the parent SBA-15 were challenged with ammonia, sulfur

dioxide, cyanogen chloride, and octane to determine their potential as toxic gas

adsorbents at 20°C using dry or humid air (80% RH) with a 20 mL/min flow rate using a

microbreakthrough system at ECBC. A challenge concentration of 1,000 mg/m^3 was

used for ammonia, sulfur dioxide, and cyanogen chloride. For octane, the challenge

concentration used was 4,000 mg/m^3.

A.3.3.1. Ammonia

Breakthrough curves for the samples tested are shown in **Figure A.6** for both dry and

humid (80% RH) cases. Ammonia capacities are listed in **Table A.3**. SBA-15+Co_w[1,

H] outperformed SBA-15 under dry conditions. All samples showed increased saturation

Figure A.6. Ammonia breakthrough for composites in dry air (a) and 80% relative humidity (b).
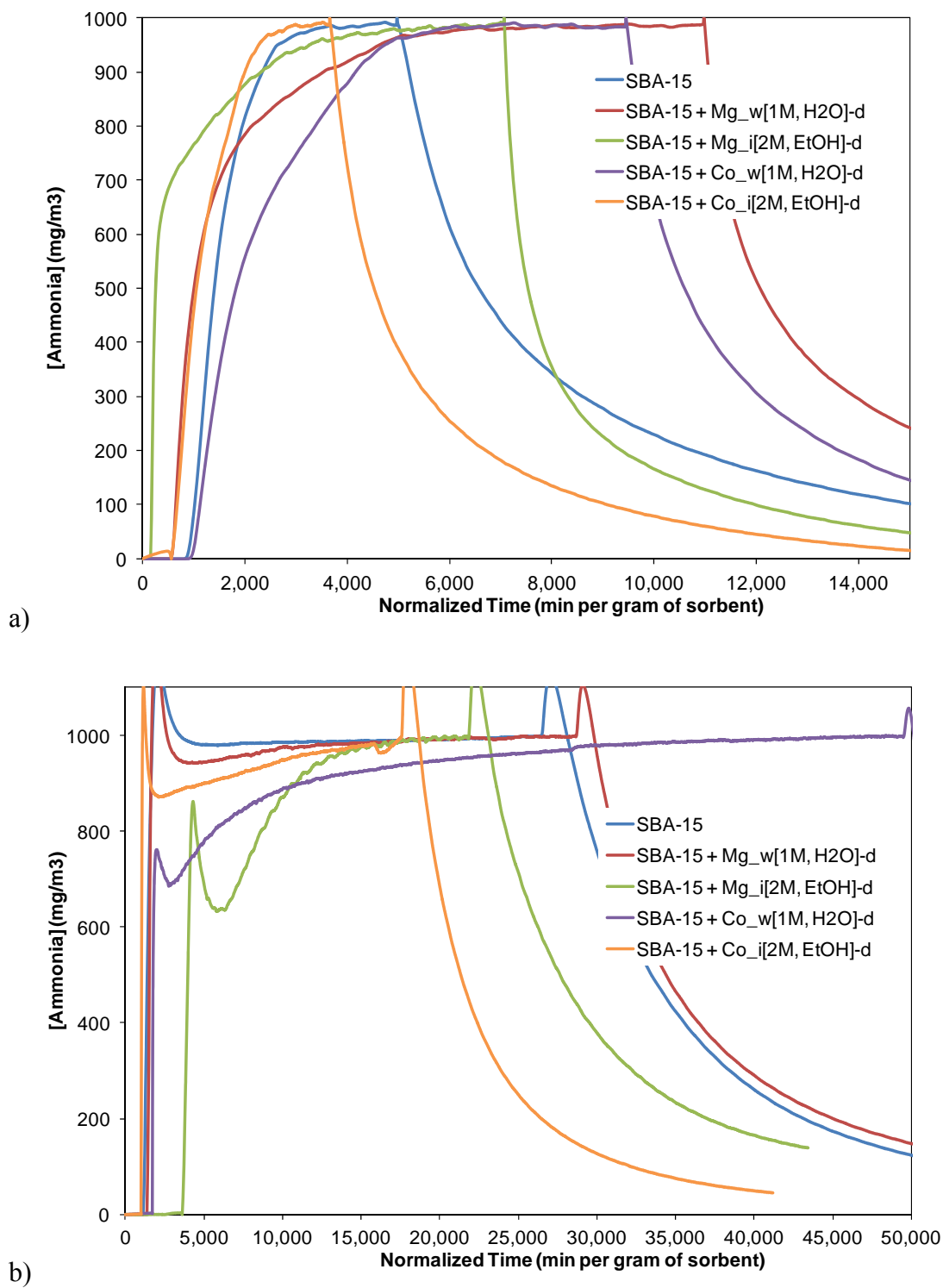
**Table A.3.** Ammonia Adsorption for Composites Under Dry and Humid Conditions.

	% SBA-15	Humidity Conditions	Sample Mass g	Loading mol/kg sorbent		Loading mol/kg SBA-15	
				Saturation	With Desorption	Saturation	With Desorption
SBA-15	100	dry	0.009	1.86	0	1.86	0
		80% RH	0.009	1.82	0	1.82	0
SBA-15+ Mg_w[1,H]	60	dry	0.007	1.94	0	3.23	0
		80% RH	0.009	2.28	0	3.80	0
SBA-15+ Co_w[1,H]	81	dry	0.009	2.74	0	3.38	0
		80% RH	0.01	5.62	0	6.94	0
SBA-15+ Mg_i[2,E]	25	dry	0.014	0.97	0	3.88	0
		80% RH	0.015	6.92	0	27.68	0
SBA-15+ Co_i[2,E]	47	dry	0.018	1.45	0	3.09	0
		80% RH	0.016	2.43	0	5.17	0

loading under humid conditions, with SBA-15+Mg_i[2, E] demonstrating the greatest

enhancement. All impregnated materials show enhancement over the parent SBA-15 on

a per-SBA-15 basis. No samples retained ammonia upon desorption.

A.3.3.2. Sulfur Dioxide

Breakthrough curves for the samples tested are shown in **Figure A.7** for both dry and

humid (80% RH) cases. Sulfur dioxide capacities are listed in **Table A.4**. SBA-

15+Co_w[1, H] performed well under both wet and dry conditions and retained 70-80%

Figure A.7. Sulfur dioxide breakthrough for composites in dry air (a) and 80% relative humidity (b).
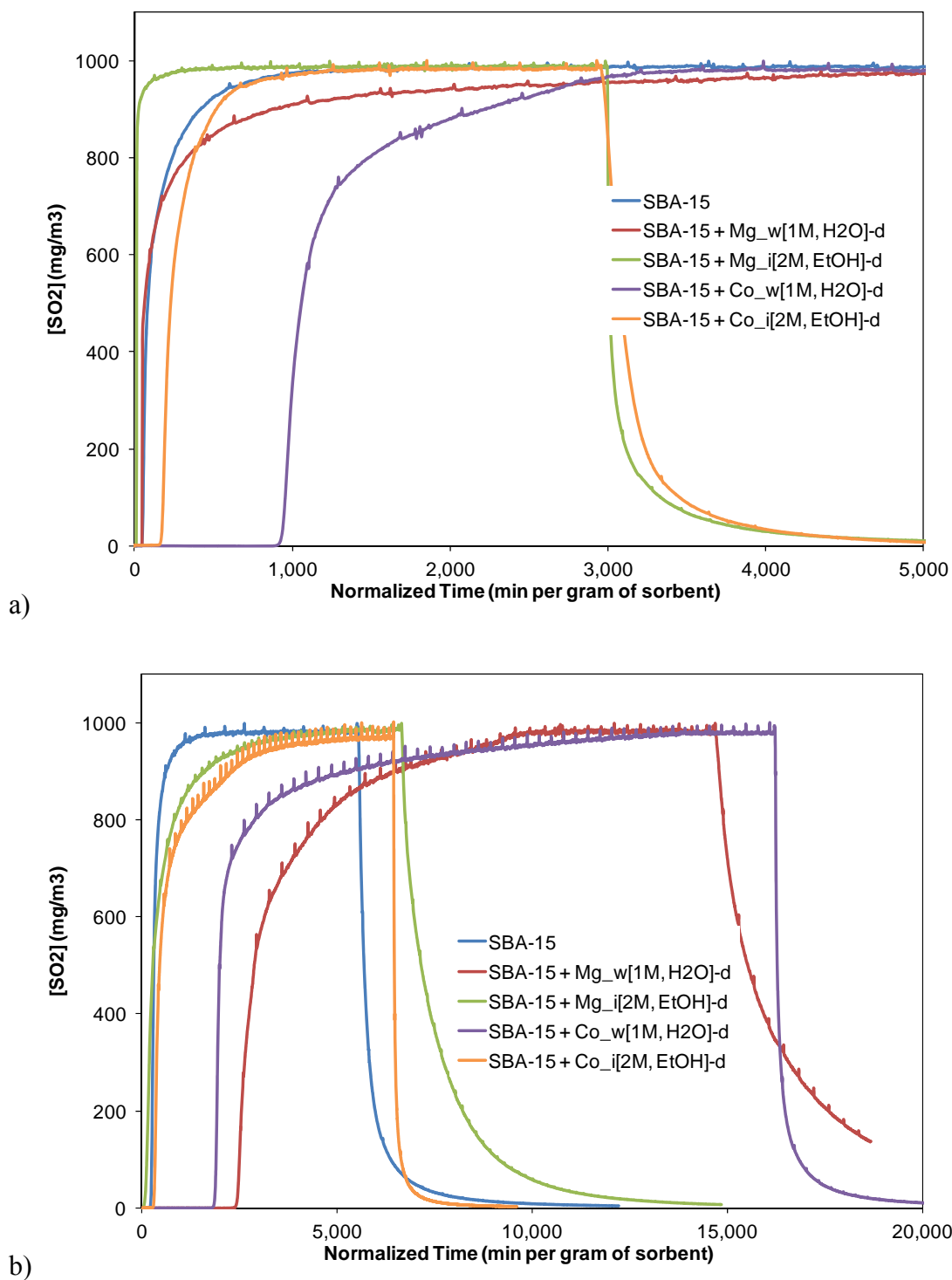
Table A.4. Sulfur Dioxide Adsorption for Composites Under Dry and Humid Conditions.

	% SBA-15	Humidity Conditions	Sample Mass g	Loading mol/kg sorbent		Loading mol/kg SBA-15	
				Saturation	With Desorption	Saturation	With Desorption
SBA-15	100	dry	0.006	0.1	0	0.10	0
		80% RH	0.007	0.14	0.02	0.14	0.02
SBA-15+ Mg_w[1,H]	60	dry	0.007	0.16	0	0.27	0
		80% RH	0.007	1.19	0.75	1.98	1.25
SBA-15+ Co_w[1,H]	81	dry	0.008	0.43	0.31	0.53	0.38
		80% RH	0.008	0.95	0.81	1.17	1.00
SBA-15+ Mg_i[2,E]	25	dry	0.018	0.02	0	0.08	0
		80% RH	0.015	0.21	0.13	0.84	0.52
SBA-15+ Co_i[2,E]	47	dry	0.011	0.11	0.03	0.23	0.06
		80% RH	0.019	0.31	0.28	0.66	0.60

of the adsorbed SO_2 upon desorption. All samples performed better under humid

conditions, with SBA-15+Co_w[1, H] showing the greatest enhancement.

A.3.3.3. Cyanogen Chloride

Breakthrough curves for the samples tested are shown in **Figure A.7** for both dry and

humid (80% RH) cases. Cyanogen chloride (CK) capacities are listed in **Table A.5**. The

parent material had the highest adsorption of CK under dry conditions. SBA-15+
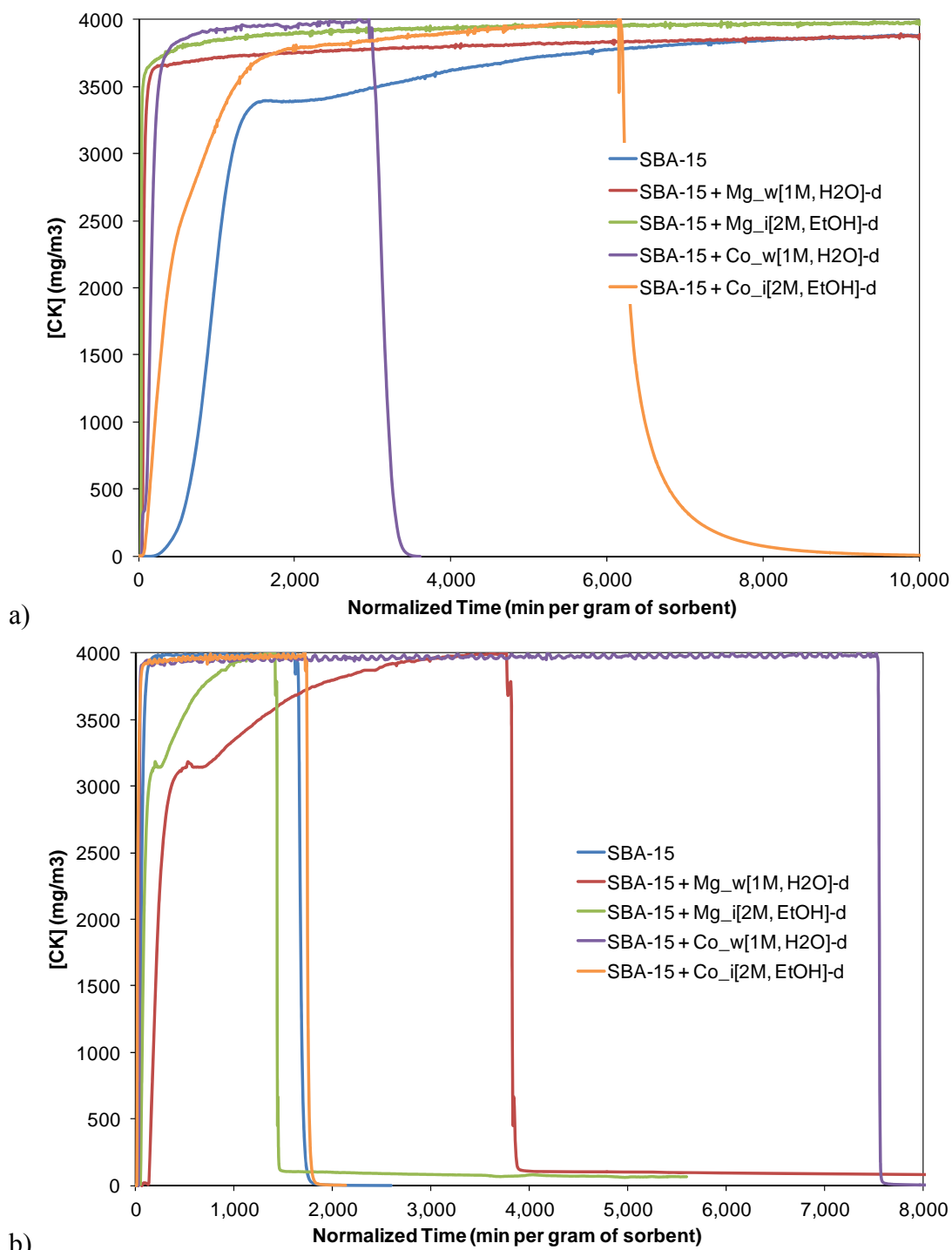
Figure A.8. Cyanogen chloride breakthrough for composites in dry air (a) and 80% relative humidity (b).

Table A.5. Cyanogen Chloride Adsorption for Composites Under Dry and Humid Conditions.

	% SBA-15	Humidity Conditions	Sample Mass g	Loading mol/kg sorbent		Loading mol/kg SBA-15	
				Saturation	With Desorption	Saturation	With Desorption
SBA-15	100	dry	0.005	2.45	1.68	2.45	1.68
		80% RH	0.01	0.09	0.01	0.09	0.01
SBA-15+ Mg_w[1,H]	60	dry	0.006	1.14	0.91	1.90	1.52
		80% RH	0.007	0.66	0.66	1.10	1.10
SBA-15+ Co_w[1,H]	81	dry	0.01	0.27	0.03	0.33	0.04
		80% RH	0.009	0.14	0.1	0.17	0.12
SBA-15+ Mg_i[2,E]	25	dry	0.013	0.29	0.28	1.16	1.12
		80% RH	0.02	0.11	0.1	0.44	0.40
SBA-15+ Co_i[2,E]	47	dry	0.012	0.9	0.52	1.91	1.11
		80% RH	0.019	0.06	0.02	0.13	0.04

Mg_w[1, H] showed high adsorption under dry and humid conditions, with little loss under desorption dry and no loss under humid conditions.

A.3.3.4. Octane

Breakthrough curves for the samples tested are shown in **Figure A.9** for both dry and humid (80% RH) cases. Ammonia capacities are listed in **Table A.6**. SBA-15 adsorbed

more octane than any composites, with adsorption decreasing with decreasing pore volume. As expected, octane adsorption decreases under humid conditions.

a)

b)
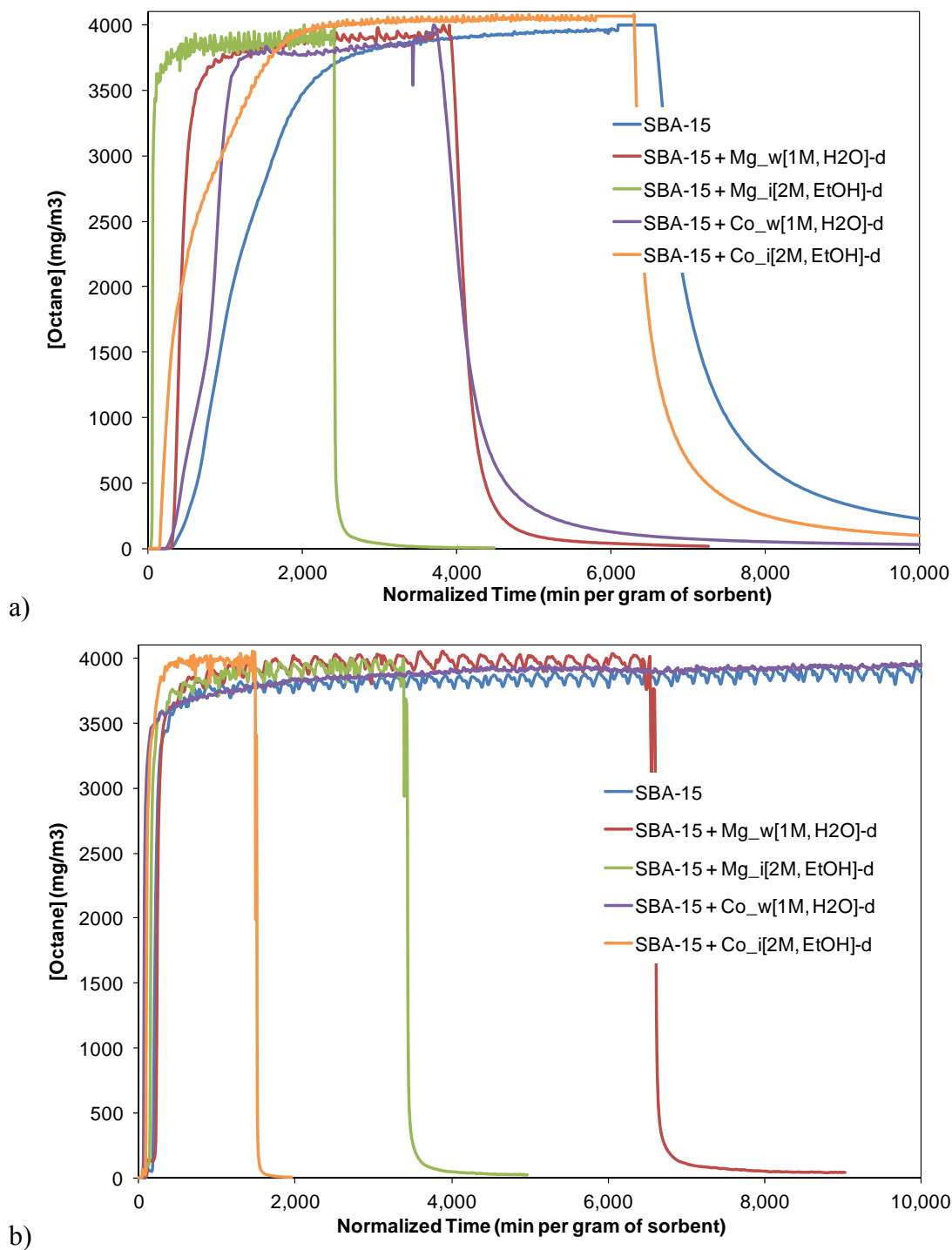
Figure A.9. Octane breakthrough for composites in dry air (a) and 80% relative humidity (b).

Table A.6. Octane Adsorption for Composites Under Dry and Humid Conditions.

	% SBA-15	Humidity Conditions	Sample Mass g	Loading mol/kg sorbent		Loading mol/kg SBA-15	
				Saturation	With Desorption	Saturation	With Desorption
SBA-15	100	dry	0.009	0.93	0.15	0.93	0.15
		80% RH	0.006	0.56	0.38	0.56	0.38
SBA-15+ Mg_w[1,H]	60	dry	0.009	0.4	0.21	0.67	0.35
		80% RH	0.005	0.24	0.05	0.40	0.08
SBA-15+ Co_w[1,H]	81	dry	0.009	0.64	0.22	0.79	0.27
		80% RH	0.01	0.3	0.2	0.37	0.25
SBA-15+ Mg_i[2,E]	25	dry	0.018	0.11	0.01	0.44	0.04
		80% RH	0.007	0.19	0.13	0.76	0.52
SBA-15+ Co_i[2,E]	47	dry	0.016	0.42	0.01	0.89	0.02
		80% RH	0.012	0.1	0.06	0.21	0.13

A.4. Conclusions

This work shows that including metal oxides in porous materials can enhance adsorption

of toxic chemicals. While no single material is a clear winner under all conditions,

several composites show promising results against individual gases. In the magnesium

composites, adsorption tends to be enhanced by humidity. Additional work is indicated

to further quantify these materials to optimize metal oxide loading for enhanced TIC adsorption.

A.5. References

(1)   Garcia, T.; Agouram, S.; Sanchez-Royo, J. F.; Murillo, R.; Mastral, A. M.; Aranda, A.; Vazquez, I.; Dejoz, A.; Solsona, B. *Appl. Catal. A-Gen.* **2010**, *386*, 16.

(2)   Lopes, I.; Davidson, A.; Thomas, C. *Catal. Commun.* **2007**, *8*, 2105.

(3)   Xia, Y. S.; Dai, H. X.; Jiang, H. Y.; Zhang, L. *Catal. Commun.* **2010**, *11*, 1171.

(4)   Wang, G. X.; Liu, H.; Horvat, J.; Wang, B.; Qiao, S. Z.; Park, J.; Ahn, H. *Chemistry-a European Journal* **2010**, *16*, 11020.

(5)   Zhang, H. J.; Tao, H. H.; Jiang, Y.; Jiao, Z.; Wu, M. H.; Zhao, B. *J. Power Sources* **2010**, *195*, 2950.

(6)   Bhagiyalakshmi, M.; Lee, J. Y.; Jang, H. T. *International Journal of Greenhouse Gas Control* **2010**, *4*, 51.

(7)   Deng, J. G.; Zhang, L.; Dai, H. X.; Xia, Y. S.; Jiang, H. Y.; Zhang, H.; He, H. *J. Phys. Chem. C* **2010**, *114*, 2694.

(8)   Khodakov, A. Y.; Zholobenko, V. L.; Bechara, R.; Durand, D. *Microporous Mesoporous Mat.* **2005**, *79*, 29.

(9)   Roggenbuck, J.; Koch, G.; Tiemann, M. *Chem. Mat.* **2006**, *18*, 4151.

(10) Roggenbuck, J.; Tiemann, M. *J. Am. Chem. Soc.* **2005**, *127*, 1096.

(11) Roggenbuck, J.; Waitz, T.; Tiemann, M. *Microporous Mesoporous Mat.* **2008**, *113*, 575.

(12) Rumplecker, A.; Kleitz, F.; Salabas, E. L.; Schuth, F. *Chem. Mat.* **2007**, *19*, 485.

(13) Shu, P.; Ruan, J. F.; Gao, C. B.; Li, H. C.; Che, S. N. *Microporous Mesoporous Mat.* **2009**, *123*, 314.

(14) Tuysuz, H.; Lehmann, C. W.; Bongard, H.; Tesche, B.; Schmidt, R.; Schuth, F. *J. Am. Chem. Soc.* **2008**, *130*, 11510.

(15)   van der Meer, J.; Bardez-Giboire, I.; Mercier, C.; Revel, B.; Davidson, A.; Denoyel, R. *J. Phys. Chem. C* **2010**, *114*, 3507.

(16)   Hicks, J. C.; Drese, J. H.; Fauth, D. J.; Gray, M. L.; Qi, G. G.; Jones, C. W. *J. Am. Chem. Soc.* **2008**, *130*, 2902.

(17)   Glover, T. G.; Peterson, G. W.; Schindler, B. J.; Britt, D.; Yaghi, O. *Chem. Eng. Sci.* **2011**, *66*, 163.

APPENDIX B

METAL OXIDE-MOF COMPOSITES FOR CARBON MONOXIDE

ADSORPTION

B.1. Introduction

MOF-74 is a widely studied metal organic framework (MOF) that can be synthesized isostructurally with different metals, commonly magnesium,[1] cobalt,[2] nickel,[3] zinc,[4]. Upon solvent removal and activation, these metals are coordinatively unsaturated, leaving desirable sites for adsorption. Mg-MOF-74 has shown very high equilibrium CO_2 capacities, and Co-MOF-74 and Ni-MOF-74 are quite promising for carbon monoxide adsorption. A unique quality to MOFs, unlike some other well-studied porous materials such as activated carbons, is that their adsorption capacity does not always scale linearly with surface area.[5] Interactions with the pore walls can be more critical than raw surface area available. For many small gas molecules, the molecules group around favorable sites along the pore walls, leaving a void space in the interior of the pore. This work considers impregnating Co- and Mg-MOF-74 with cobalt or magnesium oxide in the same manner as UiO-66 discussed in Chapter 3 to provide additional active sites for adsorption and provide mixed oxide properties.

B.2. Experimental Methods

B.2.1. Synthesis Methods

Co- and Mg-MOF-74 synthesis procedures were modified from literature.[6,7] 2,5-dihydroxyteephthalic acid (H$_4$DOBDC) (98%), Co(NO$_3$)$_2$•6H$_2$O (98%) ,

$Mg(NO_3)_2 \bullet 6H_2O$ (98%), , and n,n-dimethylformamide (DMF) (99.8%) were obtained from Sigma Aldrich. Ethanol (99%) was obtained from VWR. All chemicals were used as received.

B.2.1.1. Co-MOF-74

H_4DOBDC (0.5 g, 2.5 mmol) and $Co(NO_3)_2 \bullet 6H_2O$ (1.5 g, 5.2 mmol) were combined. The solvent mixture, DMF, ethanol, water (70 mL, 70 mL, 70 mL) was added. Once fully dissolved, it was divided equally into 20 mL vials, capped tightly, and placed in a pre-heated oven at 100°C for 66 hours.

B.2.1.2. MgMOF-74

H_4DOBDC (0.111 g, 0.56 mmol) and $Mg(NO_3)_2 \bullet 6H_2O$ (0.475 g, 1.85 mmol) were combined. The solvent mixture, DMF, ethanol, water (45 mL, 3 mL, 3 mL) was added. Once fully dissolved, it was divided equally into 20 mL vials, capped tightly, and placed in a pre-heated oven at 125°C for 24 hours.

B.2.1.3. Sample Handling and Composite Synthesis

After cooling to room temperature, each sample was washed several times with DMF. The DMF was exchanged for methanol, with the solution being decanted and replaced 4 times over 4 days. Samples were stored under methanol until required.

To synthesize each composite, the MOF sample was placed in a nitrate solution for 24 hours. Both MOFs were contacted with the following dissolved in 20 mL methanol: 0.25 M $Mg(NO_3)_2$, 0.5 M $Mg(NO_3)_2$, 0.25 M $Co(NO_3)_2$, and 0.5 M $Co(NO_3)_2$. Samples are designated with the parent MOF and impregnant: #[MO](M-MOF), where # is the precursor concentration, MO is the impregnant, and M is the MOF metal, i.e. ¼Mg(Co-MOF-74) is Co-MOF-74 impregnated with 0.25 M $Mg(NO_3)_2$.

Samples were removed directly from the nitrate solution and loaded into each instrument. The excess methanol was allowed to evaporate, and the sample was heated to 250°C and held there under vacuum for 12 hours to decompose the nitrate and activate the MOF.

B.2.2. Characterization and Isotherms

Samples were characterized via N_2 physisorption at 77K using a Quantachrome Quadrasorb. BET surface areas were calculated over the pressure rang 0.005-0.03. Carbon dioxide and carbon monoxide isotherms were measured using a lab-built pressure decay system at room temperature at pressures up to 5 bar.

B.3. Results & Discussion

B.3.1. Composite Characterization

Each sample was characterized via N_2 physisorption at 77K. The calculated BET surface areas are shown in **Table B.1**. For the impregnated Co-MOF-74 samples, the surface areas ranged from 85% of the parent MOF up to more than double. The measurements

Table B.1. BET Surface Area for Each Composite.

Sample	BET Surface Area m^2 / g	Fraction of Parent MOF
Co-MOF-74	1020	
Mg-MOF-74	1199	
¼Mg(Co-MOF-74)	1050	1.03
½Mg(Co-MOF-74)	2831	2.78
¼Co(Co-MOF-74)	869	0.85
½Co(Co-MOF-74)	1555	1.53
¼Mg(Mg-MOF-74)	363	0.30
½Mg(Mg-MOF-74)	785	0.66
¼Co(Mg-MOF-74)	899	0.75
½Co(Mg-MOF-74)	500	0.42

over 1.5 times the surface area are due to measurement error rather than actual increase in

porosity. The Mg-MOF-74 based composites range from 30-75% of the parent MOF's

surface area.

B.3.2. Carbon Dioxide and Carbon Monoxide Adsorption

Unlike UiO-66 previously discussed in Chapter 3, metal oxides included in MOF-74 via

this procedure do not enhance adsorption. **Figure B.1** shows the carbon dioxide and

carbon monoxide isotherms for samples based on Co-MOF-74. The sample with the

lower loading of cobalt oxide shows comparable CO_2 adsorption to the unmodified Co-
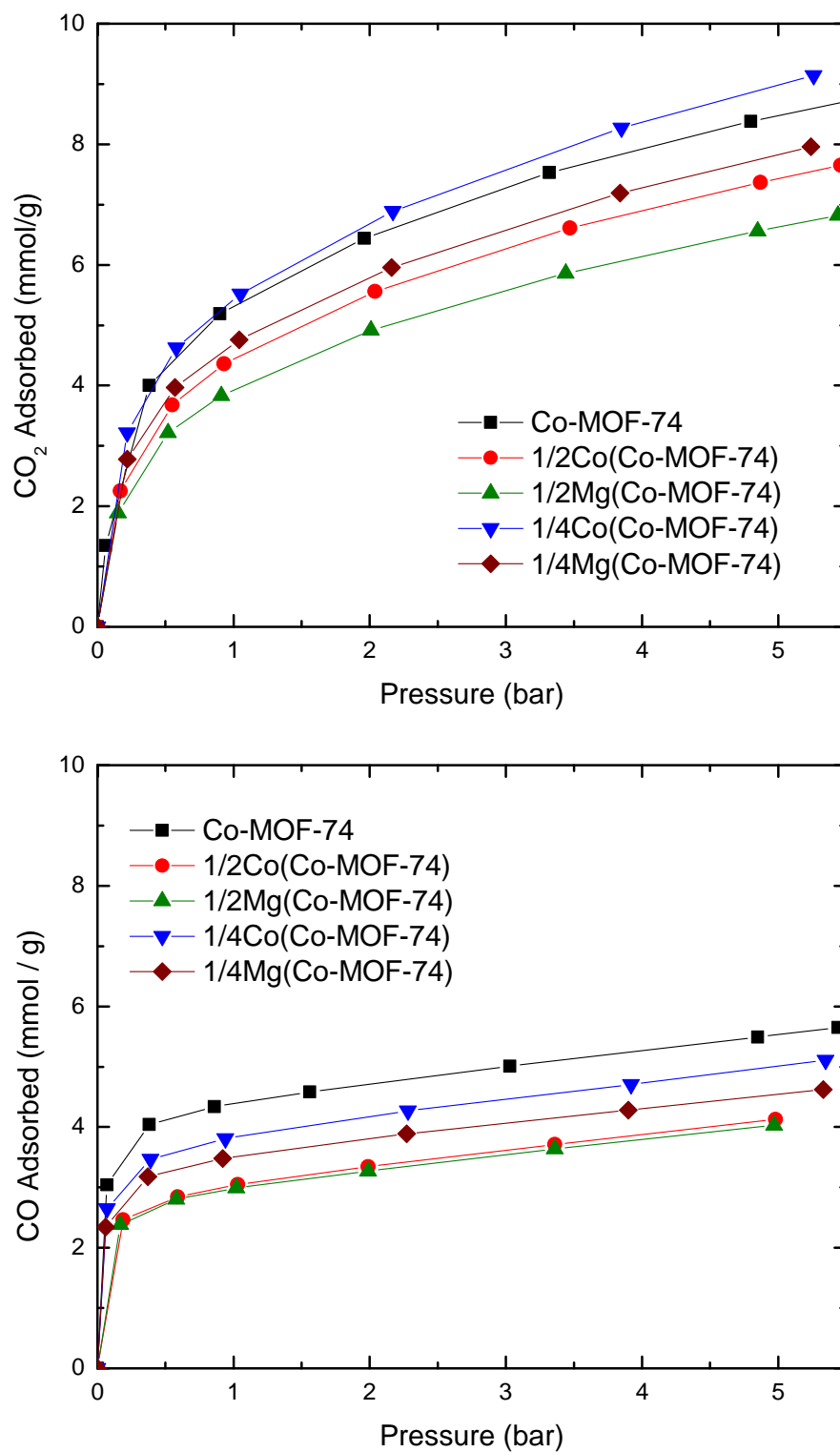
Figure B.1. CO_2 and CO adsorption on Co-MOF-74-based composites.

MOF-74, essentially within instrument error. The samples with the higher loading of

both magnesium and cobalt oxides show larger losses in capacity than the sample with

the lower loading of magnesium oxide. For CO, all samples show a loss in capacity

compared to the unmodified Co-MOF-74, following the same trends seen with carbon

dioxide. **Figure B.2** shows isotherms for the samples with the lower loading based on

Mg-MOF-74. Like Co-MOF-74, the sample with the other oxide (magnesium oxide in

the cobalt-based MOF and cobalt oxide in the magnesium-based MOF) shows the larger

loss in surface area compared to the oxide with the same metal as the parent MOF. In

contrast to Co-MOF-74, the Mg-MOF-74 with the lower level of loading of magnesium

oxide shows no decrease in carbon monoxide capacity, reaching similar capacity as the

unmodified Mg-MOF-74.

Adsorption losses are larger for MOF-74 compared to UiO-66. This is likely due

predominantly to the difference in pore systems. UiO-66 is cubic, and MOF-74

possesses one-dimensional channels. If a pore in MOF-74 is fully blocked, there is no

alternate access path, while the greater interconnectedness of UiO-66 prevents large

portions of the pore space being inaccessible because of one or two blocked pores.

Additionally, for the MO-MOF-74 synthesis, the samples were not activated prior to

contact with the precursor solution to reduce inherent capacity loss due to exposure of the

MOF-74 to air. This may result in insufficient precursor loading coupled with

incomplete solvent removal upon activation. Preparing the samples under inert may be a

possible solution to prevent air exposure.
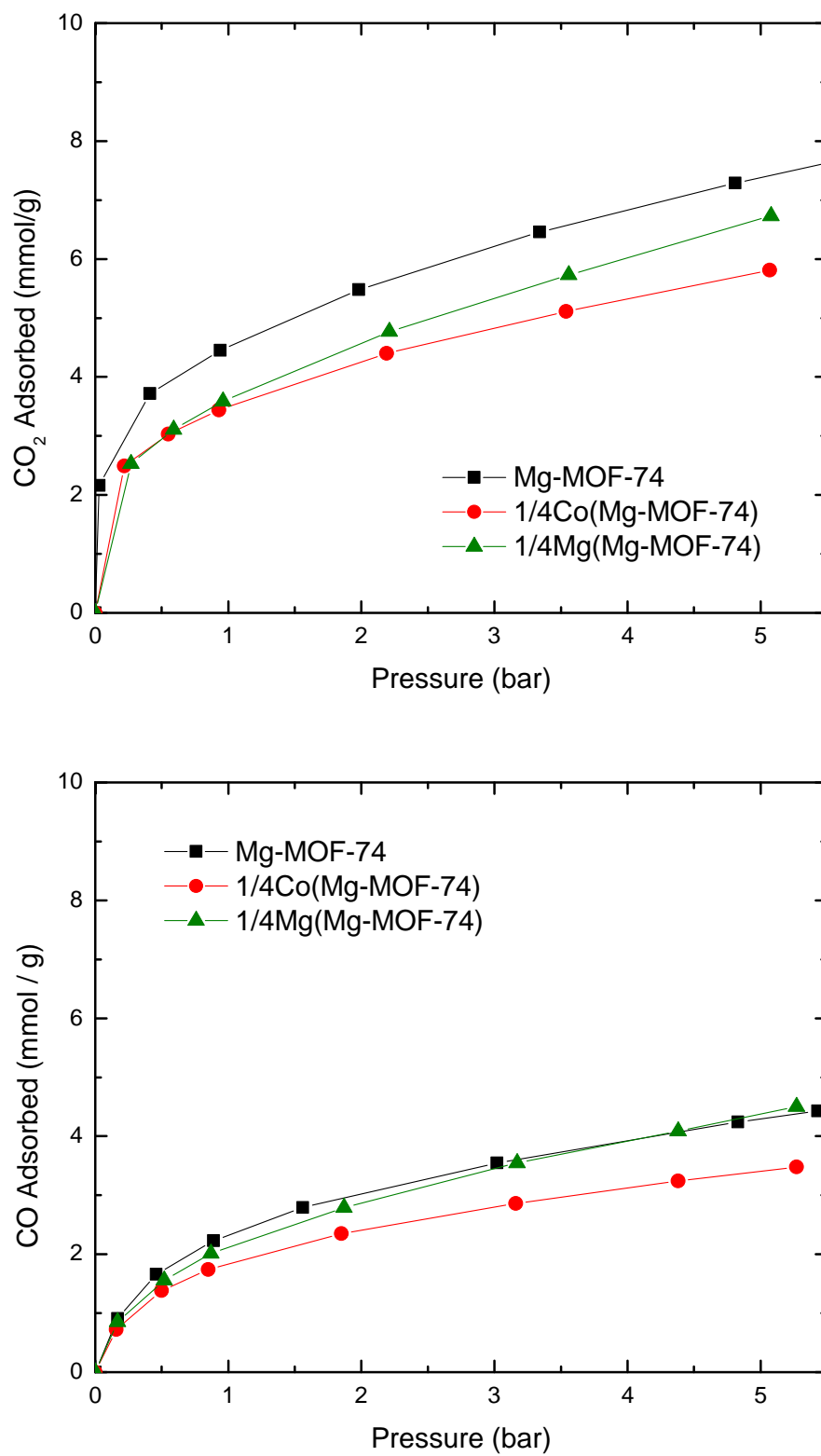
Figure B.2. CO_2 and CO adsorption on Mg-MOF-74-based composites.

B.4. Conclusions

Co-MOF-74 and Mg-MOF-74 were impregnated with magnesium oxide and cobalt

oxide. Surface area and CO_2 capacity losses were consistent with partial pore blockage.

Enhancement hypothesized for CO adsorption with MgO-(Co-MOF-74) and Co_3O_4-(Mg-

MOF-74) were not seen, in contrast to Co_3O_4 in UiO-66.

Appropriately selecting MOFs to be modified via impregnation is critical to success. A

highly-connected pore structure is vital to ensure the bulk of the pore system is not cut off

from access by a small percentage of filled pores. Additionally, evacuation and

subsequent impregnation is preferred over a solution exchange mechanism when open

metal sites are involved.

B.5. References

(1)   Dietzel, P. D. C.; Blom, R.; Fjellvag, H. *Eur. J. Inorg. Chem.* 2008, 3624.

(2)   Dietzel, P. D. C.; Morita, Y.; Blom, R.; Fjellvag, H. *Angew. Chem.-Int. Edit.* 2005, *44*, 6354.

(3)   Dietzel, P. D. C.; Panella, B.; Hirscher, M.; Blom, R.; Fjellvag, H. *Chem. Commun.* 2006, 959.

(4)   Rosi, N. L.; Kim, J.; Eddaoudi, M.; Chen, B. L.; O'Keeffe, M.; Yaghi, O. M. *J. Am. Chem. Soc.* 2005, *127*, 1504.

(5)   *Metal-Organic Frameworks*; Farrusseng, D., Ed.; Wiley-VCH Verlag & Co: Weinheim, Germany, 2011.

(6)   Caskey, S. R.; Wong-Foy, A. G.; Matzger, A. J. *J. Am. Chem. Soc.* 2008, *130*, 10870.

(7)   Glover, T. G.; Peterson, G. W.; Schindler, B. J.; Britt, D.; Yaghi, O. *Chem. Eng. Sci.* 2011, *66*, 163.

APPENDIX C

RAW DATA

C.1. Metal Oxide-UiO-66 Systems

Table C.1. Nitrogen Isotherms at 77K for UiO-Co1w, -Co1i, -Co2w, and –Co2i.

UiO-Co1w		UiO-Co1i		UiO-Co2w		UiO-Co2i	
P/P_0	N_2 cc /g	P/P_0	N_2 cc /g	P/P_0	N_2 cc /g	P/P_0	N_2 cc /g
0.00	140.92	0.00	222.99	0.00	110.63	0.00	14.64
0.00	157.88	0.00	244.62	0.00	121.45	0.00	15.86
0.01	165.75	0.01	259.06	0.01	132.64	0.01	17.29
0.01	169.69	0.01	264.16	0.01	135.00	0.01	17.68
0.01	174.20	0.01	270.07	0.01	138.10	0.01	18.13
0.01	177.69	0.01	274.90	0.01	139.73	0.01	18.37
0.02	185.59	0.02	286.53	0.02	146.02	0.02	19.14
0.03	203.20	0.03	311.86	0.03	152.32	0.03	20.10
0.04	208.42	0.04	318.21	0.04	157.35	0.04	21.15
0.05	212.89	0.05	324.59	0.05	161.19	0.05	21.68
0.10	224.09	0.11	340.80	0.10	169.12	0.10	22.71
0.15	229.90	0.16	347.27	0.15	174.22	0.16	23.42
0.20	235.15	0.20	352.88	0.20	179.03	0.20	23.91
0.25	239.30	0.25	358.86	0.25	183.52	0.25	24.32
0.31	244.58	0.30	363.28	0.30	188.00	0.30	24.67
0.35	247.98	0.35	367.32	0.35	192.37	0.35	25.20
0.40	252.53	0.40	370.91	0.40	196.79	0.40	25.53
0.45	255.85	0.45	377.08	0.45	202.34	0.45	25.81
0.50	260.94	0.50	380.93	0.50	206.76	0.50	26.33
0.55	263.89	0.55	384.58	0.55	211.58	0.55	26.62
0.60	269.00	0.61	388.19	0.60	216.67	0.60	27.24
0.65	272.06	0.65	395.87	0.65	222.17	0.65	27.53
0.70	278.68	0.70	400.48	0.70	226.20	0.70	28.21
0.75	282.73	0.75	405.19	0.75	232.45	0.75	28.56
0.81	290.41	0.81	409.85	0.80	236.70	0.80	29.27
0.85	294.75	0.86	420.78	0.85	244.92	0.86	29.96
0.91	305.81	0.90	427.66	0.91	254.28	0.90	30.87
0.96	317.40	0.95	448.47	0.95	264.19	0.96	31.96
1.00	400.44	1.00	535.73	0.99	298.43	0.99	35.25
0.94	318.67	0.94	450.07	0.92	263.16	0.92	31.36
0.87	304.54	0.86	428.59	0.90	258.20	0.86	30.25
0.85	303.14	0.85	429.67	0.81	246.17	0.84	29.80
0.79	296.75	0.76	416.41	0.80	246.38	0.77	28.94
0.75	291.61	0.74	418.93	0.75	240.85	0.75	28.89
0.67	282.03	0.67	409.92	0.70	236.08	0.67	28.45
0.65	281.54	0.65	406.61	0.65	232.62	0.65	28.07
0.60	276.06	0.57	401.01	0.58	226.40	0.57	27.57
0.52	268.60	0.55	397.62	0.55	222.54	0.55	27.33
0.50	267.81	0.50	393.41	0.50	219.19	0.47	26.79
0.45	263.17	0.43	383.66	0.45	214.75	0.45	26.55
0.40	258.61	0.40	380.85	0.40	209.07	0.40	26.13
0.32	250.88	0.32	373.21	0.32	200.65	0.32	25.49
0.30	248.97	0.30	370.41	0.30	199.22	0.30	25.28
0.25	244.58	0.22	362.85	0.25	193.71	0.23	24.62
0.18	236.30	0.20	359.53	0.18	184.38	0.20	24.30
0.15	233.13	0.15	352.21	0.15	181.86	0.12	23.42
0.10	225.60	0.07	336.40	0.07	169.13	0.10	23.11
0.04	210.74	0.05	328.82	0.05	164.02	0.04	21.59

Table C.2. Nitrogen Isotherms at 77K for UiO-Mg1w, -Mg1i, -Mg2w, and -Mg2i.

UiO-Mg1w		UiO-Mg1i		UiO-Mg2w		UiO-Mg2i	
P/P_0	N_2	P/P_0	N_2	P/P_0	N_2	P/P_0	N_2
	cc /g		cc /g		cc /g		cc /g
0.00	142.83	0.00	155.31	0.00	125.73	0.00	149.60
0.00	156.35	0.00	170.56	0.00	139.12	0.00	161.71
0.01	163.08	0.01	180.58	0.01	145.73	0.01	172.43
0.01	168.41	0.01	184.18	0.01	148.75	0.01	175.80
0.01	171.01	0.01	188.54	0.01	152.10	0.01	179.67
0.01	173.00	0.01	191.47	0.01	154.14	0.01	182.91
0.02	181.22	0.02	198.68	0.02	159.07	0.02	189.88
0.03	188.41	0.03	204.63	0.03	164.23	0.03	195.39
0.04	190.98	0.04	209.16	0.04	168.24	0.04	199.97
0.05	193.99	0.05	213.16	0.05	170.87	0.05	203.68
0.10	202.76	0.11	223.50	0.10	178.90	0.10	212.93
0.15	207.34	0.15	227.82	0.15	184.47	0.15	218.83
0.20	210.68	0.20	231.53	0.20	188.71	0.20	224.01
0.25	214.15	0.25	235.49	0.25	192.79	0.25	228.41
0.30	216.95	0.30	239.11	0.30	196.63	0.30	233.00
0.35	220.28	0.35	242.60	0.35	200.36	0.35	237.23
0.40	222.66	0.40	245.72	0.40	204.16	0.40	240.82
0.45	224.91	0.45	248.70	0.45	207.04	0.45	244.91
0.50	227.71	0.50	252.27	0.50	210.83	0.50	248.87
0.55	229.83	0.55	255.21	0.55	215.19	0.55	252.56
0.60	231.94	0.60	259.14	0.60	218.38	0.60	257.16
0.65	235.62	0.65	261.53	0.65	222.79	0.65	261.40
0.70	237.98	0.70	266.43	0.70	225.84	0.70	265.31
0.75	241.64	0.75	269.31	0.75	231.04	0.75	270.38
0.80	244.56	0.81	275.72	0.81	237.23	0.81	276.92
0.90	255.61	0.85	281.00	0.85	241.50	0.86	281.70
0.92	259.38	0.91	286.98	0.94	259.99	0.90	289.13
0.95	267.11	0.95	298.68	0.96	267.97	0.98	313.76
0.99	315.78	0.99	331.22	0.99	325.33	0.99	332.27
0.95	274.73	0.93	296.00	0.94	266.17	0.93	298.72
0.87	254.37	0.88	288.90	0.86	247.42	0.86	287.40
0.81	248.41	0.83	282.23	0.85	245.36	0.85	286.07
0.80	247.29	0.76	276.05	0.80	241.54	0.78	280.19
0.72	242.47	0.75	276.39	0.72	233.39	0.75	276.99
0.67	240.13	0.67	269.62	0.70	231.10	0.68	269.38
0.65	238.29	0.65	268.10	0.62	225.54	0.65	268.17
0.57	233.54	0.60	265.51	0.60	223.99	0.57	261.92
0.55	231.94	0.55	263.01	0.55	219.50	0.55	259.81
0.48	227.74	0.50	258.86	0.50	217.16	0.50	256.22
0.45	227.02	0.42	252.82	0.45	213.34	0.45	251.27
0.38	222.88	0.40	252.15	0.37	206.56	0.37	245.09
0.35	221.61	0.32	245.81	0.35	205.34	0.35	243.16
0.30	218.46	0.30	244.55	0.27	198.48	0.30	238.90
0.23	215.21	0.25	240.13	0.25	196.64	0.25	233.65
0.20	213.01	0.17	232.78	0.20	192.41	0.18	225.73
0.15	208.73	0.15	230.42	0.12	183.42	0.15	223.10
0.10	203.76	0.08	219.99	0.10	180.62	0.10	215.14
0.05	194.14	0.05	215.37	0.05	171.18	0.05	205.47

Table C3. Nitrogen Isotherms at 77K for UiO-Co1w2, -Co1w3, -Co2w2, -Co2w3.

UiO-Co1w2		UiO-Co1w3		UiO-Co2w2		UiO-Co2w3	
P/P_0	N_2 cc /g	P/P_0	N_2 cc /g	P/P_0	N_2 cc /g	P/P_0	N_2 cc /g
0.00	113.14	0.00	75.41	0.01	139.33	0.00	52.71
0.01	116.09	0.00	77.25	0.01	140.95	0.01	53.76
0.01	118.36	0.01	79.35	0.01	143.55	0.01	55.11
0.01	122.84	0.01	81.32	0.01	146.37	0.01	56.36
0.01	124.15	0.01	82.35	0.01	148.35	0.01	57.23
0.02	127.67	0.02	84.80	0.02	154.38	0.02	59.13
0.03	135.28	0.03	87.26	0.03	159.51	0.03	61.21
0.04	136.85	0.04	90.61	0.04	163.42	0.04	63.18
0.05	139.16	0.05	92.13	0.05	169.06	0.05	64.27
0.10	144.88	0.10	97.73	0.10	183.06	0.10	68.31
0.15	149.62	0.15	102.50	0.15	197.05	0.15	70.95
0.20	153.44	0.20	106.78	0.20	207.11	0.20	74.13
0.25	155.96	0.25	110.71	0.25	221.40	0.25	77.45
0.30	159.33	0.30	114.95	0.30	230.08	0.30	79.84
0.35	161.65	0.35	119.35	0.35	245.73	0.35	82.47
0.40	164.49	0.40	123.39	0.40	253.17	0.40	85.14
0.45	167.27	0.45	127.72	0.45	261.35	0.45	88.48
0.50	168.69	0.50	132.56	0.50	280.50	0.50	90.38
0.55	171.42	0.55	136.80	0.55	287.60	0.55	93.68
0.60	173.96	0.60	141.70	0.60	305.88	0.60	95.51
0.65	174.97	0.65	146.41	0.65	313.53	0.65	98.54
0.70	177.29	0.70	150.71	0.70	317.68	0.70	102.20
0.75	179.86	0.75	155.28	0.75	330.88	0.75	104.11
0.80	181.93	0.80	159.14	0.81	346.10	0.80	105.54
0.85	184.76	0.86	165.54	0.85	369.98	0.85	109.27
0.91	188.71	0.90	170.53	0.91	377.27	0.90	111.35
0.96	196.16	0.95	177.84	0.95	406.70	0.95	114.19
1.00	240.57	0.99	194.89	0.99	440.81	0.99	127.69
0.94	190.95	0.92	168.67	0.91	396.08	0.92	112.22
0.86	183.96	0.86	159.73	0.90	383.67	0.86	104.73
0.85	182.72	0.85	155.61	0.81	367.22	0.85	103.18
0.76	177.51	0.76	147.41	0.80	377.79	0.76	97.35
0.75	177.31	0.74	146.34	0.72	348.18	0.75	95.82
0.68	173.91	0.67	139.17	0.70	344.18	0.68	91.34
0.65	174.50	0.65	136.66	0.62	328.13	0.65	91.58
0.57	170.42	0.57	130.66	0.60	321.97	0.60	88.77
0.55	170.61	0.55	128.67	0.52	297.73	0.55	87.50
0.47	166.70	0.50	124.82	0.50	292.89	0.50	84.95
0.45	166.64	0.42	119.79	0.45	275.31	0.42	82.34
0.37	162.67	0.40	118.35	0.37	254.83	0.39	81.92
0.35	162.92	0.33	113.99	0.35	254.70	0.35	79.80
0.27	159.10	0.30	112.14	0.27	231.88	0.28	76.76
0.25	157.21	0.23	107.47	0.25	225.84	0.25	75.64
0.18	152.82	0.20	105.81	0.18	208.84	0.20	73.93
0.15	151.52	0.12	99.53	0.15	202.44	0.12	69.61
0.10	146.31	0.10	97.21	0.10	186.87	0.10	68.27
0.05	140.48	0.05	91.52	0.04	168.02	0.04	63.62
0.01	121.77	0.01	80.71	0.01	145.69	0.01	56.33

Table C.4. Nitrogen Isotherms at 77K for UiO-Mg1w2, -Mg1w3, -Mg2w2, -Mg2w3.

UiO-Mg1w2		UiO-Mg1w3		UiO-Mg2w2		UiO-Mg2w3	
P/P_0	N_2 cc /g	P/P_0	N_2 cc /g	P/P_0	N_2 cc /g	P/P_0	N_2 cc /g
0.00	133.65	0.01	134.07	0.01	106.70	0.01	10.87
0.01	139.89	0.01	136.01	0.01	107.70	0.01	11.15
0.01	141.68	0.01	138.25	0.01	109.13	0.01	11.47
0.01	143.63	0.01	140.24	0.01	110.90	0.01	11.80
0.01	145.02	0.01	141.80	0.01	112.08	0.01	12.07
0.02	148.90	0.02	145.30	0.02	115.05	0.02	12.75
0.03	154.96	0.03	149.11	0.03	117.59	0.03	13.48
0.04	156.71	0.04	152.07	0.04	119.90	0.04	14.23
0.05	158.88	0.05	155.96	0.05	122.36	0.05	15.21
0.10	165.85	0.10	166.50	0.10	129.28	0.10	18.49
0.15	171.35	0.15	176.93	0.15	134.97	0.15	21.53
0.20	175.70	0.20	187.21	0.20	140.21	0.20	25.17
0.25	179.15	0.25	196.44	0.25	145.84	0.25	28.72
0.30	183.30	0.30	206.90	0.30	151.36	0.30	32.28
0.35	186.11	0.35	217.00	0.35	156.77	0.35	35.39
0.40	189.65	0.40	226.41	0.40	161.31	0.40	39.51
0.45	192.04	0.45	236.44	0.45	166.11	0.45	43.77
0.50	193.86	0.50	244.36	0.50	170.86	0.50	46.89
0.55	197.56	0.55	253.99	0.55	175.64	0.55	51.05
0.60	198.69	0.60	266.20	0.60	180.22	0.60	55.85
0.65	200.32	0.65	276.92	0.65	184.10	0.65	59.35
0.70	204.75	0.70	284.62	0.70	189.93	0.70	62.75
0.76	206.13	0.75	292.46	0.75	195.35	0.75	70.13
0.81	207.73	0.80	300.10	0.80	199.79	0.80	72.88
0.85	210.33	0.85	310.84	0.87	207.66	0.85	77.23
0.91	215.15	0.90	316.58	0.91	212.41	0.91	82.00
0.95	219.28	0.99	363.40	0.95	217.46	0.95	86.46
0.99	240.22	1.00	415.83	0.99	247.04	0.99	105.60
0.92	211.75	0.92	316.63	0.95	220.56	0.92	81.34
0.88	208.56	0.90	307.49	0.86	206.63	0.87	77.54
0.81	205.38	0.81	288.83	0.81	200.02	0.82	70.90
0.78	201.54	0.80	284.60	0.80	198.33	0.76	66.11
0.75	203.15	0.75	272.66	0.72	191.77	0.75	62.39
0.68	197.41	0.67	258.65	0.70	189.42	0.67	56.58
0.65	196.27	0.65	250.74	0.62	183.82	0.65	53.22
0.59	195.54	0.57	234.29	0.60	180.45	0.57	45.31
0.55	193.41	0.55	226.37	0.52	174.68	0.55	42.95
0.47	190.29	0.50	217.95	0.50	173.48	0.47	37.92
0.45	188.85	0.42	204.05	0.42	166.19	0.45	36.66
0.37	186.03	0.40	200.44	0.40	164.57	0.40	34.65
0.35	184.90	0.33	192.62	0.35	160.19	0.32	30.18
0.28	180.69	0.27	187.28	0.30	155.60	0.30	28.53
0.25	178.48	0.25	184.09	0.25	150.51	0.22	24.78
0.20	174.66	0.17	172.85	0.18	142.55	0.20	23.74
0.12	168.14	0.15	170.83	0.12	135.76	0.12	19.65
0.10	166.26	0.07	157.80	0.10	133.70	0.10	18.46
0.04	157.51	0.05	153.09	0.04	123.29	0.05	15.96
0.01	142.80	0.01	136.28	0.01	111.91	0.01	12.42

Table C.5. Carbon Dioxide Isotherms at 25°C for UiO-Co1w, -Co1i, -Co2w, and -Co2i.

UiO-Co1w		UiO-Co1i		UiO-Co2w		UiO-Co2i	
P	CO_2	P	CO_2	P	CO_2	P	CO_2
bar	mmol /g	bar	mmol /g	bar	mmol /g	bar	mmol /g
0.00	0.01	0.00	0.00	0.00	0.01	0.00	0.02
0.02	0.07	0.02	0.07	0.02	0.07	0.02	0.08
0.50	0.78	0.50	0.75	0.51	0.66	0.50	0.79
1.00	1.23	1.00	1.24	1.01	1.03	1.00	1.25
1.51	1.59	1.51	1.64	1.51	1.30	1.50	1.61
2.01	1.88	2.01	1.97	2.01	1.53	2.00	1.90
2.51	2.14	2.50	2.27	2.51	1.73	2.50	2.17
3.01	2.37	3.01	2.53	3.01	1.90	3.00	2.40
3.50	2.58	3.50	2.77	3.51	2.05	3.50	2.61
4.00	2.78	4.00	2.99	4.01	2.19	4.00	2.80
4.50	2.96	4.50	3.20	4.50	2.32	4.50	2.98
5.00	3.13	5.00	3.39	5.01	2.44	5.00	3.15
4.00	2.78	4.00	3.00	4.00	2.21	4.00	2.80
3.00	2.38	3.00	2.55	3.00	1.93	3.00	2.41
2.00	1.89	2.00	2.00	2.00	1.57	2.00	1.92
1.00	1.24	1.00	1.27	1.00	1.08	1.00	1.27
0.01	0.03	0.01	0.07	0.01	0.11	0.01	0.04

Table C.6. Carbon Dioxide Isotherms at 25°C for UiO-Mg1w, -Mg1i, -Mg2w, and -Mg2i.

UiO-Mg1w		UiO-Mg1i		UiO-Mg2w		UiO-Mg2i	
P	CO_2	P	CO_2	P	CO_2	P	CO_2
bar	mmol /g	bar	mmol /g	bar	mmol /g	bar	mmol /g
0.00	0.01	0.00	0.04	0.00	0.04	0.00	0.01
0.02	0.08	0.02	0.09	0.02	0.09	0.02	0.07
0.50	0.86	0.50	0.86	0.50	0.78	0.50	0.84
1.00	1.36	0.99	1.37	1.00	1.23	1.00	1.34
1.51	1.74	1.49	1.78	1.50	1.58	1.49	1.73
2.00	2.04	2.00	2.12	2.00	1.87	2.00	2.05
2.50	2.32	2.50	2.42	2.50	2.12	2.50	2.33
3.00	2.56	2.99	2.68	3.00	2.33	2.99	2.58
3.50	2.77	3.50	2.92	3.50	2.52	3.50	2.80
4.00	2.97	4.00	3.14	4.00	2.69	4.00	3.01
4.50	3.15	4.49	3.34	4.50	2.84	4.49	3.19
5.00	3.31	5.00	3.54	5.00	2.98	5.00	3.37
3.99	3.01	3.99	3.14	3.99	2.70	4.00	3.01
2.98	2.64	3.00	2.69	2.99	2.36	3.00	2.60
2.00	2.17	2.00	2.14	1.99	1.93	2.00	2.08
1.00	1.51	1.00	1.40	1.00	1.32	0.99	1.38
0.00	0.25	0.01	0.09	0.00	0.17	0.01	0.08

Table C.7. Carbon Monoxide Isotherms for UiO-Co1w and -Co1i.

UiO-66		UiO-Co1w				UiO-Co1i			
CO, 25°C		CO, 25°C		CO, 65°C		CO, 25°C		CO, 65°C	
P bar	CO mmol / g	P bar	CO mmol / g	P bar	CO mmol / g	P bar	CO mmol / g	P bar	CO mmol / g
0.00	0.00	0.00	0.00	0.00	0.00	0.00	0.00	0.00	0.00
0.13	0.06	0.15	0.19	0.16	0.67	0.15	0.06	0.13	0.87
0.40	0.13	0.35	0.26	0.56	1.05	0.34	0.12	0.39	1.14
0.75	0.21	0.65	0.36	1.04	1.78	0.85	0.33	0.77	1.27
1.24	0.33	1.13	0.51	1.91	2.11	1.49	0.57	1.42	1.64
1.83	0.47	2.08	0.80	3.30	2.65	2.46	0.88	2.67	1.98
2.89	0.72	3.78	1.37	4.50	3.05	3.50	1.25	3.96	2.42
4.76	1.15	5.27	1.79			5.10	1.83	5.33	2.56
5.44	1.29								

Table C.8. Carbon Monoxide Isotherms for UiO-Co2w and -Co2i.

UiO-Co2w				UiO-Co2i			
CO, 25°C		CO, 65°C		CO, 25°C		CO, 65°C	
P bar	CO mmol / g	P bar	CO mmol / g	P bar	CO mmol / g	P bar	CO mmol / g
0.00	0.00	0.00	0.00	0.00	0.00	0.00	0.00
0.16	0.10	0.15	0.37	0.16	0.07	0.15	0.07
0.35	0.19	0.55	0.88	0.34	0.14	0.41	0.22
0.65	0.31	1.05	1.20	0.84	0.33	0.79	0.42
1.13	0.47	1.90	2.44	1.48	0.59	1.43	0.74
2.08	0.81	3.29	3.15	2.45	0.88	2.68	1.33
3.76	1.46	4.48	3.80	3.48	1.20	3.97	1.82
5.25	1.93			5.09	1.71	5.34	2.27

Table C.9. Carbon Monoxide Isotherms for UiO-Mg1w and -Mg1i.

UiO-Mg1w				UiO-Mg1i			
CO, 25°C		CO, 65°C		CO, 25°C		CO, 65°C	
P bar	CO mmol / g	P bar	CO mmol / g	P bar	CO mmol / g	P bar	CO mmol / g
0.00	0.00	0.00	0.00	0.00	0.00	0.00	0.00
0.17	0.06	0.16	0.18	0.14	0.05	0.31	0.12
0.45	0.17	0.50	0.24	0.43	0.13	0.88	0.17
0.82	0.31	0.95	0.39	0.92	0.28	2.02	0.32
1.16	0.44	2.10	0.57	1.94	0.52	2.64	0.44
1.99	0.72	3.43	0.77	3.26	0.85		
3.32	1.22	4.62	0.92	4.22	1.06		
5.06	1.90			5.54	1.37		

Table C.10. Carbon Monoxide Isotherms for UiO-Mg2w and -Mg2i.

UiO-Mg2w				UiO-Mg2i			
CO, 25°C		CO, 65°C		CO, 25°C		CO, 65°C	
P	CO	P	CO	P	CO	P	CO
bar	mmol / g	bar	mmol / g	bar	mmol / g	bar	mmol / g
0.00	0.00	0.00	0.00	0.00	0.00	0.00	0.00
0.17	0.10	0.17	0.05	0.14	0.11	0.31	0.00
0.45	0.22	0.50	0.16	0.43	0.19	0.88	0.06
0.82	0.38	0.96	0.27	0.92	0.35	2.02	0.22
1.15	0.50	2.10	0.50	1.93	0.64	2.64	0.30
1.98	0.77	3.42	0.70	3.25	1.00		
3.30	1.23	4.62	0.88	4.21	1.27		
5.05	1.79			5.53	1.62		

Table C.11. Carbon Monoxide Isotherms for UiO-Co1w2, -Co1w3, -Co2w2, -Co2w3.

UiO-Co1w2, 25°C		UiO-Co1w3, 25°C		UiO-Co2w2, 25°C		UiO-Co2w3, 25°C	
P	CO	P	CO	P	CO	P	CO
bar	mmol / g	bar	mmol / g	bar	mmol / g	bar	mmol / g
0.25	0.12	0.00	0.00	0.25	0.11	0.00	0.00
0.60	0.22	0.13	0.11	0.60	0.22	0.13	0.08
1.03	0.36	0.51	0.24	1.03	0.36	0.51	0.20
1.93	0.59	1.01	0.39	1.92	0.59	1.01	0.35
3.07	0.92	1.83	0.61	3.06	0.93	1.83	0.54
4.24	1.23	2.94	0.91	4.24	1.23	2.93	0.80
5.17	1.48	4.18	1.23	5.17	1.45	4.16	1.07
		5.29	1.48			5.28	1.31

Table C.12. Carbon Monoxide Isotherms for UiO-Mg1w2, -Mg1w3, -Mg2w2, -Mg2w3.

UiO-Mg1w2, 25°C		UiO-Mg1w3, 25°C		UiO-Mg2w2, 25°C		UiO-Mg2w3, 25°C	
P	CO	P	CO	P	CO	P	CO
bar	mmol / g	bar	mmol / g	bar	mmol / g	bar	mmol / g
0.00	0.00	0.00	0.00	0.00	0.00	0.00	0.00
0.17	0.07	0.13	0.05	0.18	0.05	0.13	0.03
0.51	0.18	0.61	0.20	0.51	0.13	0.61	0.14
0.90	0.31	1.12	0.32	0.90	0.24	1.12	0.25
1.88	0.64	1.92	0.54	1.88	0.52	1.92	0.42
3.03	0.96	3.17	0.85	3.02	0.79	3.16	0.70
4.08	1.22	4.42	1.14	4.07	1.02	4.41	0.96
5.18	1.53	5.46	1.37	5.16	1.27	5.45	1.13

C.2. HKUST-1-Titania Systems

Table C.13. Nitrogen Isotherms at 77K for HKUST-1 and TiO_2.

HKUST-1 as synthesized		HKUST-1 after CO exposure		TiO_2 as synthesized	
P/P_0	N_2 cc /g	P/P_0	N_2 cc /g	P/P_0	N_2 cc /g
0.01	363.80	0.00	327.59	0.00	3.99
0.01	365.14	0.00	336.89	0.00	5.43
0.01	365.84	0.01	338.58	0.01	5.84
0.02	367.84	0.01	340.23	0.01	6.24
0.03	370.07	0.01	341.84	0.01	6.64
0.04	372.67	0.01	342.81	0.01	6.84
0.05	376.04	0.02	345.74	0.02	7.48
0.11	393.69	0.03	348.83	0.03	8.05
0.15	402.23	0.04	352.87	0.04	8.68
0.20	408.35	0.05	357.85	0.05	9.26
0.25	414.18	0.10	370.62	0.10	11.11
0.30	419.41	0.15	380.88	0.15	12.69
0.35	427.17	0.20	389.42	0.20	14.46
0.40	432.65	0.25	397.41	0.25	15.90
0.45	438.62	0.30	404.97	0.30	17.32
0.50	444.36	0.35	411.74	0.36	19.53
0.56	451.08	0.40	419.81	0.41	20.81
0.60	456.34	0.45	426.24	0.45	22.05
0.65	462.22	0.50	433.17	0.50	24.18
0.70	468.28	0.55	440.37	0.56	26.14
0.76	475.28	0.60	448.96	0.60	27.39
0.81	480.95	0.65	453.97	0.65	30.15
0.85	485.04	0.70	461.93	0.70	32.61
0.94	494.77	0.75	466.47	0.75	36.06
0.96	498.28	0.81	476.86	0.80	40.60
0.99	506.78	0.86	484.91	0.85	47.00
0.92	483.99	0.90	489.00	0.90	56.64
0.86	470.49	0.96	497.95	0.96	85.86
0.84	467.63	0.99	505.79	0.99	176.79
0.76	457.04	0.95	500.12	0.95	107.63
0.75	454.51	0.85	489.31	0.89	69.93
0.68	448.74	0.85	489.47	0.85	52.92
0.65	447.59	0.80	485.65	0.78	42.40
0.57	443.19	0.75	481.58	0.74	38.70
0.55	442.06	0.67	471.60	0.68	34.80
0.47	434.20	0.65	470.21	0.65	33.36
0.45	432.85	0.60	465.28	0.58	29.22
0.40	429.07	0.55	458.46	0.55	28.90
0.33	422.71	0.50	451.02	0.47	25.41
0.30	420.04	0.45	445.45	0.45	24.42
0.25	415.07	0.37	431.57	0.37	21.58
0.18	407.71	0.35	427.85	0.35	20.94
0.15	403.30	0.30	418.72	0.28	18.38
0.08	388.66	0.25	409.60	0.25	17.38
0.05	377.86	0.20	401.45	0.18	14.51
		0.12	382.28	0.12	12.50
		0.10	376.07	0.10	11.57

Table C.14. Nitrogen Isotherms at 77K for HKUST-1+ TiO_2 and HKUST-1&TiO_2.

HKUST-1+TiO_2 as synthesized		HKUST-1+TiO_2 after CO exposure		HKUST-1&TiO_2 as synthesized		HKUST-1&TiO_2 after CO exposure	
P/P_0	N_2 cc /g	P/P_0	N_2 cc /g	P/P_0	N_2 cc /g	P/P_0	N_2 cc /g
0.00	219.71	0.00	268.67	0.00	374.65	0.00	295.27
0.00	221.61	0.00	270.68	0.00	377.99	0.00	299.74
0.01	223.88	0.01	272.80	0.01	380.43	0.01	301.90
0.01	225.06	0.01	274.51	0.01	382.46	0.01	303.67
0.01	226.72	0.01	276.02	0.01	383.90	0.01	305.20
0.01	227.67	0.01	276.70	0.01	384.65	0.01	306.02
0.02	230.76	0.02	279.20	0.02	387.48	0.02	308.57
0.03	234.75	0.03	282.26	0.03	390.35	0.03	311.52
0.04	240.55	0.04	285.07	0.04	394.18	0.04	314.62
0.05	244.39	0.05	288.94	0.05	398.84	0.05	318.33
0.10	255.87	0.10	299.92	0.10	415.62	0.10	328.63
0.15	268.22	0.15	308.62	0.16	430.38	0.15	335.59
0.20	278.26	0.20	315.91	0.20	436.52	0.20	341.90
0.25	290.08	0.25	322.25	0.25	443.03	0.25	348.28
0.30	301.81	0.30	327.25	0.30	450.25	0.30	352.51
0.36	313.97	0.35	333.54	0.35	456.48	0.35	356.41
0.40	322.64	0.40	338.07	0.40	466.44	0.40	360.26
0.45	334.34	0.45	343.68	0.45	471.71	0.45	365.01
0.50	345.54	0.50	348.46	0.50	475.86	0.50	367.75
0.55	359.47	0.55	353.19	0.56	479.57	0.55	374.83
0.60	372.59	0.60	359.55	0.60	492.15	0.60	378.29
0.65	388.64	0.65	362.19	0.65	496.23	0.65	381.40
0.70	404.17	0.70	368.48	0.70	500.62	0.70	384.46
0.75	416.19	0.75	372.23	0.75	503.64	0.75	389.84
0.81	438.05	0.81	378.32	0.80	513.09	0.81	395.97
0.86	449.71	0.85	385.11	0.85	517.17	0.86	398.96
0.90	462.39	0.91	389.13	0.90	525.36	0.95	414.65
0.95	480.68	0.95	397.08	0.96	530.34	0.97	419.65
0.99	492.83	0.99	414.22	0.99	542.27	0.99	433.29
0.91	471.87	0.92	395.66	0.91	528.72	0.92	414.15
0.90	477.32	0.90	394.54	0.90	528.13	0.90	409.70
0.81	448.60	0.81	388.80	0.84	526.39	0.81	404.26
0.80	449.35	0.79	388.17	0.75	516.77	0.80	405.16
0.75	443.03	0.75	384.86	0.74	517.81	0.72	394.75
0.67	429.29	0.67	378.55	0.70	515.68	0.70	393.83
0.65	420.33	0.65	376.14	0.62	505.51	0.65	389.02
0.60	411.74	0.59	373.10	0.60	504.98	0.60	385.50
0.55	399.63	0.55	367.67	0.55	500.38	0.53	379.36
0.50	389.73	0.50	363.64	0.47	487.18	0.50	378.38
0.45	372.59	0.42	354.13	0.45	485.40	0.42	369.79
0.37	353.19	0.40	350.67	0.37	472.36	0.40	368.55
0.35	345.20	0.32	340.88	0.35	470.59	0.32	360.50
0.30	333.78	0.30	338.48	0.30	462.09	0.30	357.56
0.25	315.85	0.25	332.60	0.25	453.45	0.24	352.90
0.17	289.96	0.20	325.21	0.20	444.71	0.17	343.42
0.15	281.94	0.12	310.45	0.12	427.66	0.15	339.78
0.07	251.96	0.10	305.14	0.10	421.08	0.08	325.58
0.05	241.42	0.04	288.78	0.04	396.52	0.05	319.48

Table C.15. Carbon Dioxide and Carbon Monoxide Isotherms for HKUST-1.

CO_2, 25°C		CO, 25°C		CO, 45°C		CO, 65°C	
P	CO_2	P	CO	P	CO	P	CO
bar	mmol / g	bar	mmol / g	bar	mmol / g	bar	mmol / g
0.00	0.00	0	0	0.00	0.00	0	0
0.02	0.14	0.19	0.23	0.15	0.20	0.16	0.28
0.10	0.61	0.45	0.54	0.38	0.35	0.37	0.48
0.50	2.61	0.93	1.06	0.72	0.49	0.67	0.66
1.00	4.59	1.47	1.58	1.04	0.73	1.00	0.82
1.99	7.13	2.41	2.34	1.73	1.15	1.90	1.17
3.00	8.72	2.90	2.70	2.83	1.67	2.95	1.49
4.00	9.77	3.69	3.26	4.20	2.28	4.87	2.19
5.00	10.50	4.41	3.73	5.18	2.70	5.56	2.42
		5.19	4.19				

Table C.16. Carbon Dioxide and Carbon Monoxide Isotherms for HKUST-1+TiO_2.

CO_2, 25°C		CO, 25°C		CO, 45°C		CO, 65°C	
P	CO_2	P	CO	P	CO	P	CO
bar	mmol / g	bar	mmol / g	bar	mmol / g	bar	mmol / g
0.00	0.01	0	0	0.00	0.00	0	0
0.02	0.15	0.46	0.43	0.15	0.10	0.16	0.15
0.10	0.65	1.02	0.88	0.37	0.24	0.37	0.28
0.50	2.75	1.55	1.27	0.71	0.46	0.67	0.47
0.99	4.84	2.09	1.59	1.02	0.69	1.00	0.61
1.99	7.56	2.64	1.78	1.71	1.08	1.90	0.98
3.00	9.25	3.19	2.16	2.81	1.58	2.95	1.36
3.99	10.38	3.75	2.34	4.18	2.14	4.88	2.02
4.99	11.17	4.29	2.66	5.16	2.54	5.56	2.22
		4.82	2.97				
		5.35	3.19				

Table C.17. Carbon Dioxide and Carbon Monoxide Isotherms for HKUST-1&TiO_2.

CO_2, 25°C		CO, 25°C		CO, 45°C		CO, 65°C	
P	CO_2	P	CO	P	CO	P	CO
bar	mmol / g	bar	mmol / g	bar	mmol / g	bar	mmol / g
0.00	0.00	0	0	0.00	0.00	0	0
0.03	0.18	0.51	0.48	0.18	0.14	0.16	0.23
0.11	0.69	1.11	0.90	0.47	0.35	0.40	0.40
0.51	2.89	1.65	1.29	0.88	0.57	0.83	0.67
0.99	5.03	2.22	1.66	1.65	0.96	1.54	1.01
2.00	8.02	2.78	1.90	2.50	1.35	2.64	1.43
2.99	9.82	3.32	2.24	3.60	1.83	3.89	1.90
4.00	11.07	3.90	2.62	5.12	2.41	5.25	2.37
4.99	11.92	4.44	2.92				
		4.98	2.67				
		5.51	2.96				

Table C.18. Carbon Dioxide and Carbon Monoxide Isotherms for TiO_2.

CO_2, 25°C		CO, 25°C		CO, 45°C		CO, 65°C	
P	CO_2	P	CO	P	CO	P	CO
bar	mmol / g	bar	mmol / g	bar	mmol / g	bar	mmol / g
0.00	1.54	0	0	0.00	0.00	0	0
0.02	1.86	0.27	0.02	0.16	0.00	0.16	0.16
0.12	1.85	0.75	0.04	0.46	0.06	0.40	0.21
0.51	1.93	1.33	0.07	0.86	0.11	0.84	0.23
0.99	2.01	2.07	0.09	1.56	0.25	1.54	0.38
1.99	2.03	2.80	0.11	2.51	0.36	2.65	0.61
2.99	2.04	3.75	0.15	3.40	0.50	3.90	0.79
4.00	2.04	4.98	0.21	4.31	0.63	5.24	1.01
4.99	2.06			5.29	0.76		

C.3. HKUST-1+MNP Systems

Table C.19. Nitrogen Isotherms at 77K for HKUST-1, MNP, and HKUST-1+MNP.

HKUST-1		MNP		HKUST-1+MNP	
P/P_0	N_2 cc /g	P/P_0	N_2 cc /g	P/P_0	N_2 cc /g
0.00	303.29	0.00	14.16	0.00	220.06
0.00	308.84	0.00	15.08	0.00	222.70
0.01	312.16	0.01	15.95	0.01	224.02
0.01	312.84	0.01	16.63	0.01	225.14
0.01	313.86	0.01	17.20	0.01	226.21
0.01	314.62	0.01	17.51	0.01	226.61
0.02	316.63	0.02	18.47	0.02	228.47
0.03	319.00	0.03	19.43	0.03	230.20
0.04	321.13	0.04	20.58	0.04	232.19
0.05	323.63	0.05	21.44	0.05	234.53
0.10	333.64	0.10	24.49	0.10	242.09
0.16	339.14	0.15	27.70	0.15	246.94
0.20	342.48	0.20	29.86	0.20	250.58
0.26	346.55	0.25	31.78	0.25	254.48
0.30	348.86	0.30	33.76	0.30	257.55
0.35	351.35	0.35	35.19	0.35	260.57
0.40	353.62	0.40	37.43	0.40	263.37
0.45	355.90	0.45	38.72	0.45	265.92
0.50	357.81	0.50	41.17	0.50	269.06
0.55	359.73	0.55	42.42	0.55	271.21
0.60	361.82	0.60	44.93	0.60	275.26
0.65	363.63	0.65	45.99	0.65	276.69
0.70	365.30	0.70	49.19	0.70	278.68
0.75	367.51	0.75	50.67	0.76	283.25
0.80	369.11	0.81	53.06	0.80	285.96
0.86	372.17	0.85	55.55	0.85	287.85
0.91	375.86	0.91	56.73	0.90	291.03
0.96	379.92	0.95	63.94	0.96	295.77
0.99	386.89	0.99	74.97	0.99	297.66
0.91	381.88	0.91	59.54	0.91	294.36
0.90	380.61	0.90	59.95	0.90	291.89
0.85	379.62	0.81	57.58	0.81	289.18
0.80	378.39	0.80	58.00	0.80	288.33
0.75	377.29	0.75	56.10	0.75	287.02
0.67	374.23	0.70	53.87	0.67	284.52
0.65	373.70	0.63	52.67	0.65	281.65
0.60	371.73	0.60	51.84	0.57	278.13
0.54	369.83	0.55	49.84	0.55	278.66
0.50	368.19	0.47	46.53	0.50	274.97
0.44	357.62	0.45	44.97	0.45	272.92
0.40	356.27	0.38	40.12	0.40	268.07
0.35	353.65	0.35	39.47	0.35	266.26
0.27	349.38	0.30	37.12	0.27	260.04
0.25	348.19	0.25	34.86	0.25	258.75
0.18	342.82	0.18	30.86	0.20	254.25
0.15	340.56	0.15	29.66	0.12	246.66
0.10	335.10	0.07	24.30	0.10	244.37
0.05	326.05	0.05	22.26	0.04	234.21

Table C.20. Carbon Dioxide and Carbon Monoxide Isotherms for HKUST-1 and HKUST-1+MNP.

HKUST-1				HKUST-1+MNP			
CO$_2$, 25°C		CO, 25°C		CO, 45°C		CO, 65°C	
P	CO$_2$	P	CO	P	CO	P	CO
bar	mmol / g	bar	mmol / g	bar	mmol / g	bar	mmol / g
0.00	0.00	0.00	0.00	0.00	0.00	0.00	0.00
0.03	0.16	0.16	0.22	0.02	0.08	0.16	0.26
0.11	0.68	0.42	0.53	0.12	0.52	0.43	0.61
0.50	2.81	0.95	1.08	0.51	1.93	0.97	1.19
1.01	5.04	1.94	1.89	1.01	3.21	1.98	2.07
1.51	6.68	3.04	2.64	1.51	4.14	3.08	2.87
2.01	7.92	3.91	3.15	2.00	4.84	3.95	3.45
2.51	8.90	5.23	3.82	2.50	5.40	5.27	4.23
3.00	9.69			3.00	5.85		
3.51	10.33			3.50	6.22		
4.00	10.86			4.00	6.52		
4.50	11.30			4.50	6.77		
5.00	11.67			5.00	6.97		

Table C.21. Water and Hexane Isotherms for HKUST-1 and HKUST-1+MNP.

HKUST-1				HKUST-1+MNP			
Water, 25°C		Hexane, 25°C		Water, 25°C		Hexane, 25°C	
RH	Water	RH	Hexane	RH	Water	RH	Hexane
%	mmol / g	%	mmol / g	%	mmol / g	%	mmol / g
0.00	0.00	0.00	0.00	0.00	0.00	5.73	2.67
5.30	9.20	10.64	4.99	5.29	9.45	10.65	3.55
10.27	15.30	20.50	5.08	10.27	14.43	15.59	4.02
15.24	17.68	30.33	4.74	15.24	16.72	20.50	4.64
20.22	21.18	40.19	4.73	20.21	20.60	25.42	4.90
25.19	23.27	50.03	4.75	25.18	22.20	30.34	5.09
30.15	24.27	59.88	4.76	30.15	22.96	35.27	5.20
35.12	25.10	69.72	4.76	35.12	23.57	40.19	5.25
40.09	25.67	79.55	4.80	40.09	23.97	50.04	5.34
50.03	26.26	89.41	4.80	50.03	24.47	59.87	5.39
59.96	26.68	79.56	4.77	59.96	24.85	69.71	5.44
69.89	26.97	59.88	4.75	69.89	25.19	79.54	5.46
79.82	27.24	40.18	4.73	79.82	25.50	89.39	5.48
89.75	27.61	20.49	4.67	89.76	25.84	79.54	5.45
79.82	27.37	0.00		79.82	25.62	59.87	0.74
59.96	26.86			59.96	25.11	40.19	0.73
40.09	26.05			40.09	24.37	20.50	0.73
20.22	22.52			20.22	21.47	0.00	0.36
0.00	2.31			0.00	5.02		

C.4. M-MOF-74

Table C.22. Nitrogen Isotherms at 77K for Co-MOF-74.

6-hr Activation		12-hr Activation		18-hr Activation		24-hr Activation		48-hr Activation	
P/P_0	N_2 cc /g	P/P_0	N_2 cc /g	P/P_0	N_2 cc /g	P/P_0	N_2 cc /g	P/P_0	N_2 cc /g
0.00	49.87	0.01	416.65	0.00	274.43	0.00	307.48	0.00	255.74
0.00	58.13	0.01	418.32	0.01	279.08	0.01	309.05	0.01	260.28
0.01	59.95	0.01	420.72	0.01	283.32	0.01	311.04	0.01	261.39
0.01	61.71	0.01	423.39	0.01	284.21	0.01	313.13	0.01	262.97
0.01	62.97	0.01	425.06	0.01	284.83	0.01	314.34	0.01	264.08
0.02	64.56	0.02	428.55	0.02	287.01	0.02	316.70	0.02	266.72
0.03	66.17	0.03	431.62	0.03	289.30	0.03	318.70	0.03	268.97
0.04	67.57	0.04	434.10	0.04	291.59	0.04	320.08	0.04	271.04
0.05	68.99	0.05	437.13	0.05	293.25	0.05	321.72	0.05	272.99
0.10	71.88	0.10	443.03	0.10	297.22	0.10	325.39	0.10	277.88
0.15	74.03	0.15	448.85	0.15	300.33	0.15	328.37	0.15	281.41
0.20	76.68	0.20	452.97	0.20	302.59	0.20	330.99	0.20	284.43
0.25	79.38	0.25	457.23	0.25	304.73	0.25	333.08	0.25	287.01
0.30	81.88	0.30	462.04	0.30	306.58	0.30	335.36	0.30	289.87
0.35	84.08	0.35	466.87	0.35	308.70	0.35	337.88	0.36	292.14
0.40	87.09	0.40	472.34	0.41	310.20	0.40	340.25	0.40	294.56
0.46	88.60	0.45	476.30	0.45	312.02	0.45	342.55	0.45	297.16
0.50	91.72	0.50	483.89	0.50	313.23	0.50	344.19	0.50	299.19
0.55	93.10	0.55	485.15	0.55	315.38	0.55	347.18	0.55	301.80
0.60	96.44	0.60	490.29	0.60	316.53	0.60	349.46	0.60	304.43
0.65	97.57	0.65	494.14	0.65	318.51	0.65	351.83	0.65	306.70
0.70	101.22	0.70	500.11	0.70	319.44	0.70	354.82	0.70	309.56
0.75	103.06	0.75	502.97	0.75	321.73	0.75	356.91	0.75	312.95
0.80	105.99	0.80	506.15	0.80	322.72	0.80	359.50	0.80	315.10
0.85	106.49	0.85	510.71	0.85	324.95	0.85	362.46	0.86	319.17
0.95	113.02	0.90	516.56	0.90	325.92	0.95	367.10	0.90	322.23
0.97	112.73	0.95	521.95	0.95	328.67	0.97	369.84	0.98	329.77
1.00	121.28	0.99	533.06	0.99	443.37	1.00	375.22	1.00	335.11
0.91	113.77	0.95	526.63	0.94	329.55	0.95	369.07	0.91	325.26
0.90	113.19	0.86	522.60	0.90	329.17	0.90	368.46	0.89	325.53
0.81	111.01	0.84	520.93	0.80	326.27	0.80	364.70	0.81	321.57
0.80	111.15	0.80	521.05	0.80	326.39	0.79	364.07	0.80	321.04
0.75	110.08	0.75	517.87	0.72	324.54	0.75	362.50	0.75	319.64
0.70	109.36	0.67	509.22	0.70	324.21	0.67	359.33	0.70	317.63
0.62	106.63	0.65	509.79	0.65	323.02	0.65	359.04	0.62	313.54
0.60	104.58	0.57	502.63	0.60	322.06	0.60	357.33	0.60	312.67
0.52	101.71	0.55	501.80	0.54	319.68	0.55	354.68	0.55	310.47
0.49	100.92	0.47	493.03	0.50	318.31	0.47	349.96	0.48	306.66
0.45	99.44	0.45	494.35	0.42	314.14	0.45	348.95	0.43	300.97
0.40	97.35	0.40	487.48	0.40	313.35	0.40	346.33	0.40	299.22
0.32	94.57	0.32	479.46	0.35	310.90	0.34	344.04	0.32	294.67
0.30	94.18	0.30	477.14	0.27	307.49	0.27	339.43	0.30	293.59
0.22	90.25	0.24	469.62	0.25	306.13	0.25	338.51	0.22	288.73
0.20	89.12	0.17	460.04	0.18	302.14	0.17	333.45	0.20	287.45
0.12	85.24	0.15	457.20	0.15	300.20	0.15	331.82	0.12	281.77
0.10	83.88	0.10	450.55	0.07	294.58	0.07	325.29	0.10	279.81
0.04	80.05	0.04	437.85	0.05	292.20	0.05	322.82	0.04	272.78
0.01	76.66	0.01	423.78	0.01	281.21	0.01	310.95	0.01	262.27

Table C.23. Nitrogen Isotherms at 77K for Mg-MOF-74.

6-hr Activation		12-hr Activation		24-hr Activation		48-hr Activation	
P/P_0	N_2 cc /g	P/P_0	N_2 cc /g	P/P_0	N_2 cc /g	P/P_0	N_2 cc /g
0.00	278.41	0.00	341.30	0.00	334.47	0.01	165.95
0.01	280.50	0.01	347.61	0.01	342.33	0.01	167.29
0.01	283.40	0.01	352.33	0.01	346.67	0.01	169.11
0.01	286.78	0.01	354.65	0.01	350.23	0.01	171.22
0.01	289.00	0.01	356.43	0.01	351.84	0.01	172.41
0.02	293.49	0.02	360.76	0.02	358.70	0.02	175.13
0.03	297.55	0.03	368.31	0.03	361.61	0.03	177.86
0.04	300.77	0.04	369.75	0.04	366.87	0.04	179.81
0.05	303.88	0.05	372.63	0.05	368.77	0.05	182.59
0.10	311.39	0.10	379.23	0.10	375.51	0.10	188.52
0.15	316.70	0.15	384.61	0.15	380.76	0.15	192.78
0.20	321.81	0.20	388.23	0.20	384.83	0.20	196.53
0.25	325.81	0.25	391.81	0.25	388.85	0.25	201.53
0.30	330.22	0.30	394.99	0.30	391.52	0.30	204.83
0.35	333.70	0.35	398.40	0.35	394.44	0.35	210.35
0.40	337.09	0.40	400.95	0.40	397.86	0.40	213.69
0.45	340.92	0.45	403.84	0.45	400.26	0.45	216.71
0.50	343.82	0.50	406.46	0.50	402.93	0.50	221.44
0.55	347.76	0.55	409.00	0.55	405.39	0.55	225.72
0.60	351.63	0.60	411.70	0.60	408.05	0.60	228.48
0.65	354.55	0.65	413.49	0.65	410.76	0.65	233.43
0.70	358.89	0.70	416.48	0.70	413.87	0.70	238.73
0.75	362.24	0.75	419.51	0.75	415.75	0.75	244.05
0.80	366.17	0.80	421.38	0.80	417.22	0.80	248.96
0.85	369.99	0.85	424.81	0.86	419.60	0.86	257.63
0.90	374.74	0.90	428.34	0.90	423.34	0.90	267.56
0.96	381.71	0.95	433.15	0.95	426.13	0.99	300.49
0.99	390.49	1.00	465.57	0.99	439.11	1.00	327.65
0.91	377.52	0.93	432.18	0.92	425.10	0.91	286.90
0.90	377.29	0.90	430.85	0.87	421.90	0.90	285.91
0.81	373.51	0.80	428.07	0.85	421.40	0.81	281.11
0.80	371.97	0.80	426.94	0.76	418.62	0.80	280.96
0.75	370.26	0.75	425.49	0.75	418.54	0.75	277.23
0.70	368.09	0.67	422.37	0.70	416.81	0.70	275.30
0.62	364.06	0.65	421.29	0.62	413.66	0.65	271.59
0.60	362.56	0.60	419.35	0.60	412.96	0.60	268.21
0.52	356.61	0.56	416.79	0.55	411.18	0.55	265.45
0.50	355.43	0.47	412.04	0.48	406.93	0.50	261.03
0.42	347.09	0.45	409.53	0.45	405.28	0.43	231.64
0.40	344.96	0.37	402.95	0.40	400.78	0.40	228.03
0.34	340.30	0.35	401.55	0.32	395.18	0.35	222.90
0.30	336.59	0.27	395.90	0.30	394.45	0.30	218.38
0.23	329.54	0.25	394.04	0.25	390.58	0.25	213.82
0.20	327.30	0.17	388.13	0.20	386.82	0.17	205.63
0.15	321.76	0.15	386.17	0.12	380.14	0.15	203.72
0.07	310.89	0.08	377.21	0.10	376.87	0.10	196.24
0.05	306.61	0.05	373.18	0.04	368.08	0.04	186.98
0.01	286.81	0.01	352.27	0.01	350.86	0.01	176.26

Table C.24. Nitrogen Isotherms at 77K for Ni-MOF-74.

6-hr Activation		12-hr Activation		18-hr Activation		24-hr Activation		48-hr Activation	
P/P_0	N_2 cc /g	P/P_0	N_2 cc /g	P/P_0	N_2 cc /g	P/P_0	N_2 cc /g	P/P_0	N_2 cc /g
0.00	280.29	0.00	319.82	0.00	209.44	0.00	217.48	0.00	66.12
0.01	284.57	0.01	324.86	0.01	212.50	0.01	223.91	0.01	67.53
0.01	292.92	0.01	330.84	0.01	216.82	0.01	225.63	0.01	69.30
0.01	294.93	0.01	333.82	0.01	222.16	0.01	228.19	0.01	71.25
0.01	296.48	0.01	336.09	0.01	225.75	0.01	230.09	0.01	72.52
0.02	301.04	0.02	341.20	0.02	233.85	0.02	234.41	0.02	75.55
0.03	308.97	0.03	346.11	0.03	241.85	0.03	238.77	0.03	78.75
0.04	311.18	0.04	349.84	0.04	248.01	0.04	242.35	0.04	81.28
0.05	314.19	0.05	353.38	0.05	254.82	0.05	245.37	0.05	84.33
0.10	321.74	0.11	362.72	0.10	269.76	0.10	253.54	0.10	92.75
0.15	326.99	0.16	366.32	0.15	279.78	0.15	259.70	0.15	99.54
0.20	330.69	0.20	369.99	0.20	288.23	0.20	264.60	0.20	105.42
0.25	334.99	0.25	372.76	0.25	296.47	0.25	268.88	0.25	110.89
0.30	338.11	0.30	375.63	0.30	306.35	0.30	273.22	0.30	117.07
0.35	340.97	0.35	378.21	0.35	313.56	0.35	277.72	0.35	123.42
0.40	343.07	0.40	380.50	0.40	318.55	0.40	281.97	0.40	130.72
0.45	346.84	0.45	382.93	0.45	326.46	0.45	285.76	0.45	136.36
0.50	349.26	0.50	385.55	0.50	329.45	0.50	289.19	0.50	143.59
0.55	351.72	0.55	387.19	0.55	333.71	0.55	292.06	0.55	151.32
0.60	353.33	0.61	389.17	0.61	338.85	0.60	295.37	0.61	161.49
0.65	355.88	0.65	391.81	0.65	343.00	0.66	298.27	0.65	170.20
0.70	359.91	0.70	394.67	0.70	343.83	0.70	301.66	0.70	183.27
0.75	362.02	0.75	395.78	0.75	347.75	0.75	304.37	0.75	197.52
0.80	364.57	0.80	399.37	0.80	351.52	0.80	307.80	0.80	222.11
0.85	365.55	0.85	402.14	0.86	350.73	0.86	312.60	0.87	283.08
0.94	373.86	0.90	404.33	0.90	354.79	0.90	316.26	0.91	359.30
0.97	375.02	0.95	407.03	0.95	362.12	0.95	318.41	0.95	478.71
1.00	385.80	0.99	411.83	0.99	427.98	1.00	329.96	1.00	566.97
0.90	373.35	0.95	409.64	0.92	368.78	0.95	322.43	0.93	503.29
0.90	371.66	0.90	408.79	0.90	368.59	0.86	317.62	0.89	452.51
0.82	370.54	0.81	404.43	0.81	365.44	0.85	316.62	0.85	349.67
0.80	368.98	0.80	402.93	0.80	363.73	0.80	313.45	0.79	248.89
0.72	367.02	0.75	402.99	0.75	363.29	0.75	310.86	0.74	215.56
0.70	364.81	0.70	401.55	0.67	354.43	0.70	308.82	0.69	194.69
0.62	362.41	0.62	398.52	0.65	358.42	0.64	305.41	0.64	183.80
0.60	360.87	0.60	397.25	0.59	354.99	0.60	303.49	0.57	168.95
0.53	356.70	0.55	395.50	0.54	352.71	0.55	301.21	0.55	165.10
0.50	356.69	0.50	393.16	0.47	345.64	0.50	297.82	0.48	152.38
0.45	352.96	0.45	390.95	0.45	343.41	0.45	294.52	0.45	148.77
0.37	349.13	0.39	387.66	0.37	330.01	0.40	290.84	0.37	135.59
0.35	347.79	0.35	385.03	0.35	325.92	0.35	285.78	0.35	133.29
0.27	341.39	0.27	379.37	0.30	316.27	0.27	277.90	0.30	125.38
0.25	340.22	0.25	378.13	0.23	302.78	0.25	275.25	0.25	118.53
0.20	334.91	0.17	371.12	0.20	297.53	0.20	270.52	0.20	111.37
0.12	327.10	0.15	369.14	0.13	280.86	0.12	260.20	0.15	103.10
0.10	324.82	0.07	358.31	0.07	266.48	0.10	256.96	0.08	90.41
0.04	312.97	0.05	353.38	0.05	258.01	0.04	244.82	0.05	85.66
0.01	293.48	0.01	330.15	0.01	221.78	0.01	226.10	0.01	69.63

Table C.25. Nitrogen Isotherms at 77K for Zn-MOF-74.

6-hr Activation		12-hr Activation		18-hr Activation		24-hr Activation		48-hr Activation	
P/P$_0$	N$_2$ cc /g	P/P$_0$	N$_2$ cc /g	P/P$_0$	N$_2$ cc /g	P/P$_0$	N$_2$ cc /g	P/P$_0$	N$_2$ cc /g
0.00	212.38	0.00	264.45	0.00	225.34	0.00	248.50	0.00	111.26
0.00	213.46	0.01	266.69	0.00	227.30	0.01	254.01	0.01	114.21
0.01	217.84	0.01	271.32	0.01	234.29	0.01	257.58	0.01	116.77
0.01	218.65	0.01	272.35	0.01	235.33	0.01	258.55	0.01	118.50
0.01	219.32	0.01	273.15	0.01	236.08	0.01	259.37	0.01	119.78
0.02	221.47	0.02	275.55	0.02	238.88	0.02	261.76	0.02	122.73
0.03	223.73	0.03	280.30	0.03	242.25	0.03	266.95	0.03	125.80
0.04	225.93	0.04	281.72	0.04	244.78	0.04	268.76	0.04	128.46
0.05	227.80	0.05	284.00	0.05	247.63	0.05	271.08	0.05	131.53
0.10	232.99	0.10	290.11	0.10	255.09	0.11	279.16	0.10	139.12
0.15	236.49	0.15	294.47	0.15	260.57	0.15	283.34	0.15	145.24
0.21	240.40	0.20	297.63	0.20	265.26	0.20	287.31	0.20	150.81
0.26	242.52	0.25	300.94	0.25	270.11	0.25	290.50	0.25	156.27
0.30	245.30	0.30	303.12	0.30	274.02	0.30	293.63	0.30	161.83
0.35	247.15	0.35	305.55	0.35	276.90	0.35	296.43	0.35	166.44
0.40	249.29	0.40	307.72	0.41	279.67	0.40	298.85	0.40	169.97
0.45	250.89	0.45	309.44	0.45	282.56	0.45	300.88	0.45	173.45
0.50	253.70	0.50	311.44	0.50	287.51	0.50	303.08	0.50	176.23
0.55	255.17	0.55	313.20	0.55	289.69	0.55	304.81	0.55	178.31
0.60	256.41	0.60	314.82	0.60	291.11	0.61	307.00	0.60	180.40
0.65	257.60	0.65	316.48	0.65	296.82	0.65	308.58	0.65	182.41
0.71	258.17	0.70	318.45	0.70	298.46	0.70	310.14	0.70	184.47
0.75	262.62	0.75	319.96	0.75	299.61	0.75	311.03	0.75	186.53
0.80	263.90	0.80	321.39	0.80	305.89	0.80	312.48	0.80	187.42
0.85	264.35	0.90	324.46	0.85	307.47	0.85	314.00	0.86	190.19
0.90	266.97	0.92	324.48	0.91	308.88	0.90	314.99	0.91	192.10
0.95	268.22	0.96	326.60	0.96	313.61	0.95	316.88	0.95	194.38
0.99	272.23	0.99	330.00	0.99	535.74	1.00	321.69	1.00	226.23
0.95	269.38	0.91	325.93	0.93	318.01	0.91	316.76	0.91	196.08
0.86	266.47	0.90	325.93	0.85	313.05	0.90	316.58	0.89	195.80
0.85	266.25	0.82	324.47	0.84	313.36	0.81	314.85	0.81	193.61
0.76	264.57	0.80	324.19	0.75	307.92	0.79	315.08	0.79	193.73
0.75	264.34	0.72	322.79	0.74	311.66	0.72	313.68	0.75	192.33
0.70	263.58	0.70	322.43	0.70	305.63	0.70	313.41	0.70	191.24
0.62	261.36	0.65	321.28	0.65	306.72	0.62	311.35	0.65	190.05
0.60	261.12	0.60	320.23	0.58	299.97	0.60	311.15	0.60	188.42
0.52	258.37	0.55	319.07	0.55	301.17	0.52	308.68	0.55	187.08
0.50	258.27	0.47	315.71	0.47	293.53	0.50	308.11	0.50	185.37
0.42	254.33	0.45	314.72	0.45	291.82	0.43	305.07	0.42	180.77
0.40	253.71	0.40	312.49	0.37	286.52	0.40	302.89	0.40	179.12
0.32	249.43	0.32	308.19	0.35	284.09	0.32	298.29	0.32	170.99
0.30	248.47	0.30	307.22	0.30	280.58	0.30	296.94	0.30	169.09
0.22	243.79	0.22	302.08	0.25	275.30	0.25	293.39	0.23	160.40
0.20	242.72	0.20	300.66	0.18	267.15	0.18	287.93	0.20	157.34
0.15	239.18	0.13	294.47	0.12	260.66	0.13	282.96	0.12	147.79
0.08	232.60	0.10	292.15	0.10	257.29	0.10	280.22	0.09	143.16
0.05	229.67	0.04	283.72	0.04	245.76	0.05	272.19	0.04	134.01
0.01	218.27	0.01	271.45	0.01	229.62	0.01	259.03	0.01	121.44

Table C.26. Carbon Monoxide Isotherms at 25°C, 200°C Activation.

Co-MOF-74			Mg-MOF-74			Ni-MOF-74			Zn-MOF-74		
P bar	CO mmol / g	CO molec / CUS	P bar	CO mmol / g	CO molec / CUS	P bar	CO mmol / g	CO molec / CUS	P bar	CO mmol / g	CO molec / CUS
0.00	0.00	0.00	0.00	0.00	0.00	0.00	0.00	0.00	0.00	0.00	0.00
0.12	2.09	0.33	0.12	0.68	0.08	0.18	2.37	0.37	0.21	0.28	0.05
0.24	2.93	0.46	0.25	1.15	0.14	0.48	2.68	0.42	0.48	0.62	0.10
0.73	3.49	0.54	0.67	2.04	0.25	0.99	2.97	0.46	0.97	1.10	0.18
1.20	3.79	0.59	1.12	2.60	0.32	1.84	3.41	0.53	1.80	1.70	0.28
1.95	4.06	0.63	1.87	3.15	0.38	2.75	3.79	0.59	2.71	2.20	0.36
2.94	4.44	0.69	2.87	3.64	0.44	4.14	4.47	0.70	4.10	2.82	0.46
4.04	4.79	0.75	3.98	4.04	0.49	5.32	4.97	0.77	5.28	3.25	0.53
4.99	5.11	0.80	4.96	4.33	0.53						
5.66	5.30	0.83	5.63	4.50	0.55						

Table C.27. Carbon Monoxide Isotherms for Co-MOF-74, 250°C Activation.

25°C			45°C			65°C		
P bar	CO mmol / g	CO molec / CUS	P bar	CO mmol / g	CO molec / CUS	P bar	CO mmol / g	CO molec / CUS
0.00	0.00	0.00	0.00	0.00	0.00	0.00	0.00	0.00
0.00	0.78	0.12	0.11	2.78	0.43	0.15	1.98	0.31
0.05	2.60	0.41	0.45	4.12	0.64	0.50	3.22	0.50
0.45	3.99	0.62	0.92	4.63	0.72	0.98	3.91	0.61
1.22	4.37	0.68	2.21	5.18	0.81	1.92	4.50	0.70
2.11	4.61	0.72	3.55	5.54	0.86	3.74	5.08	0.79
3.42	4.89	0.76	5.08	5.97	0.93	5.28	5.67	0.88
5.17	5.22	0.81						

Table C.28. Carbon Monoxide Isotherms for Mg-MOF-74, 250°C Activation.

25°C			45°C			65°C		
P bar	CO mmol / g	CO molec / CUS	P bar	CO mmol / g	CO molec / CUS	P bar	CO mmol / g	CO molec / CUS
0.00	0.00	0.00	0.00	0.00	0.00	0.00	0.00	0.00
0.08	0.96	0.12	0.08	0.41	0.05	0.32	0.40	0.05
0.28	2.20	0.27	0.27	1.03	0.13	0.61	0.56	0.07
0.69	3.50	0.42	0.61	1.82	0.22	1.05	0.85	0.10
1.36	4.58	0.56	0.97	2.39	0.29	2.90	1.70	0.21
2.19	5.39	0.65	1.44	2.94	0.36	4.93	2.52	0.31
3.46	6.27	0.76	2.08	3.45	0.42			
5.20	7.23	0.88	3.29	4.11	0.50			
			5.00	4.73	0.57			
			5.83	5.03	0.61			

Table C.29. Carbon Monoxide Isotherms for Ni-MOF-74, 250°C Activation.

25°C			45°C			65°C		
P bar	CO mmol / g	CO molec / CUS	P bar	CO mmol / g	CO molec / CUS	P bar	CO mmol / g	CO molec / CUS
0.00	0.00	0.00	0.00	0.00	0.00	0.00	0.00	0.00
0.08	0.14	0.02	0.11	2.09	0.32	0.20	1.51	0.24
0.30	2.85	0.44	0.47	2.83	0.46	0.56	2.08	0.34
0.77	4.22	0.66	0.94	3.13	0.51	1.03	2.40	0.39
2.53	4.51	0.70	2.21	3.58	0.58	1.96	2.78	0.45
3.60	4.73	0.74	3.54	3.91	0.64	3.75	3.34	0.54
5.22	5.14	0.80	5.08	4.25	0.69	5.30	3.75	0.61

Table C.30. Carbon Monoxide Isotherms for Zn-MOF-74, 250°C Activation.

25°C			45°C			65°C		
P bar	CO mmol / g	CO molec / CUS	P bar	CO mmol / g	CO molec / CUS	P bar	CO mmol / g	CO molec / CUS
0.00	0.00	0.00	0.00	0.00	0.00	0.00	0.00	0.00
0.10	0.04	0.01	0.15	0.11	0.02	0.33	0.17	0.03
0.49	0.43	0.07	0.46	0.36	0.06	0.61	0.29	0.05
0.94	0.89	0.15	1.17	0.83	0.13	1.06	0.50	0.08
2.52	1.40	0.23	2.28	1.41	0.23	2.89	1.16	0.19
3.57	1.98	0.32	4.96	2.00	0.33	4.91	1.80	0.29
5.17	2.63	0.43						

Table C.31. Carbon Monoxide Isotherms for Air-dried Co-, Mg, and Ni-MOF-74, 25°C.

Co-MOF-74		Mg-MOF-74		Ni-MOF-74	
P bar	CO mmol / g	P bar	CO mmol / g	P bar	CO mmol / g
0.00	0.00	0.00	0.00	0.00	0.00
0.02	2.00	0.20	0.74	0.14	0.87
0.29	4.16	0.58	1.74	0.51	1.20
0.80	4.53	1.04	2.40	0.93	1.44
1.70	4.81	2.30	3.37	1.76	1.77
3.30	5.18	3.89	4.10	3.31	2.28
4.45	5.42	5.33	4.64	4.44	2.65
5.40	5.60				

C.6. Metal Oxide-SBA-15 Systems

Table C.32. Nitrogen Isotherms at 77K for Samples Interrogated with Toxic Gases, SBA-15, +Mg_w[1,H]-d, +Co_w[1,H]-d, +Mg_i[2,E]-d, and +Co_i[2,E]-d.

SBA-15		SBA-15+ Mg_w[1,H]-d		SBA-15+ Co_w[1,H]-d		SBA-15+ Mg_i[2,E]-d		SBA-15+ Co_i[2,E]-d	
P/P_0	N_2 cc /g	P/P_0	N_2 cc /g	P/P_0	N_2 cc /g	P/P_0	N_2 cc /g	P/P_0	N_2 cc /g
0.01	125.17	0.01	50.28	0.00	0.28	0.01	49.14	0.01	69.34
0.01	131.40	0.01	51.67	0.00	40.62	0.01	50.59	0.01	70.73
0.01	133.58	0.01	52.70	0.00	48.23	0.01	52.02	0.01	71.94
0.02	145.02	0.02	58.20	0.00	52.30	0.02	55.46	0.02	77.86
0.03	156.85	0.03	62.77	0.00	54.61	0.03	59.58	0.03	82.98
0.04	161.08	0.04	66.92	0.00	55.14	0.04	63.89	0.04	87.34
0.05	170.71	0.05	69.93	0.00	69.37	0.05	67.42	0.05	90.16
0.10	193.37	0.10	80.99	0.01	77.13	0.10	78.55	0.10	101.53
0.15	206.99	0.15	91.90	0.01	79.47	0.16	91.07	0.15	108.50
0.20	223.37	0.20	101.79	0.01	82.69	0.20	98.91	0.20	115.99
0.25	234.05	0.25	109.36	0.01	84.50	0.25	107.43	0.25	121.35
0.31	249.00	0.30	119.67	0.02	89.38	0.30	116.93	0.30	127.97
0.35	258.70	0.35	128.02	0.03	97.67	0.36	128.18	0.35	133.60
0.41	272.29	0.40	137.14	0.04	100.44	0.40	136.70	0.40	140.20
0.45	283.76	0.45	149.49	0.05	104.62	0.45	147.41	0.45	146.31
0.50	298.25	0.50	159.55	0.11	121.28	0.51	160.62	0.50	153.74
0.56	313.20	0.55	173.85	0.15	130.19	0.55	171.99	0.55	160.99
0.60	328.61	0.60	191.20	0.20	138.94	0.60	188.44	0.60	170.47
0.65	350.91	0.65	209.52	0.25	146.53	0.65	208.49	0.65	226.90
0.70	463.44	0.70	287.21	0.31	155.64	0.70	232.74	0.70	241.36
0.75	576.47	0.76	325.03	0.35	162.42	0.75	238.85	0.75	333.88
0.80	583.92	0.80	330.10	0.40	169.71	0.81	244.97	0.79	370.41
0.86	593.21	0.85	335.59	0.45	177.86	0.85	248.36	0.85	378.76
0.90	601.06	0.90	341.72	0.50	187.82	0.91	253.89	0.91	384.48
0.98	614.82	0.95	349.89	0.55	196.80	0.95	257.25	0.95	388.77
0.99	627.48	0.99	363.46	0.60	209.28	0.99	269.64	0.99	392.40
0.91	608.21	0.95	350.76	0.65	223.22	0.95	259.72	0.94	382.35
0.90	606.31	0.90	344.39	0.70	335.94	0.90	256.52	0.90	371.08
0.82	597.67	0.85	339.42	0.75	372.12	0.85	254.51	0.85	362.49
0.80	595.11	0.80	335.45	0.80	375.30	0.80	251.49	0.80	354.42
0.75	588.39	0.75	329.83	0.86	379.01	0.75	249.31	0.75	347.13
0.68	578.49	0.68	322.00	0.90	381.55	0.70	245.28	0.69	332.54
0.65	572.46	0.65	316.65	0.97	389.16	0.65	240.73	0.65	296.78
0.60	452.93	0.60	256.89	0.99	442.54	0.60	233.14	0.59	258.13
0.55	338.25	0.55	201.02	0.92	384.36	0.55	226.46	0.55	242.36
0.49	314.30	0.48	181.24	0.87	381.36	0.50	220.78	0.49	217.11
0.44	296.63	0.45	169.51	0.82	378.50	0.45	190.63	0.45	152.58
0.39	283.55	0.38	142.50	0.77	375.93	0.38	146.22	0.40	145.17
0.33	267.81	0.35	136.77	0.74	373.82	0.35	137.65	0.35	137.56
0.28	254.14	0.28	121.73	0.68	370.14	0.29	124.33	0.30	130.76
0.25	245.33	0.25	115.90	0.64	359.63	0.25	116.61	0.24	122.49
0.19	227.19	0.18	101.73	0.60	312.50	0.19	104.44	0.20	117.44
0.15	217.17	0.15	95.47	0.54	281.40	0.14	92.76	0.15	110.69
0.09	192.26	0.08	78.36	0.50	267.96	0.10	84.37	0.08	97.64
0.05	173.07	0.05	69.11	0.45	198.42	0.04	65.31	0.04	89.50
				0.40	172.39				

Table C.33. Nitrogen Isotherms at 77K for SBA-15+Mg_w[1,H]-w, +Mg_i[1,H]-w +Co_w[1,H]-w, and +Co_i[1,H]-w.

SBA-15+ Mg_w[1,H]-w		SBA-15+ Mg_i[1,H]-w		SBA-15+ Co_w[1,H]-w		SBA-15+ Co_i[1,H]-w	
P/P_0	N_2 cc /g	P/P_0	N_2 cc /g	P/P_0	N_2 cc /g	P/P_0	N_2 cc /g
0.01	1.63	0.01	1.83	0.01	42.74	0.01	34.41
0.01	1.66	0.01	1.83	0.01	43.34	0.01	35.89
0.01	1.69	0.01	1.86	0.01	43.87	0.01	36.23
0.02	1.83	0.02	2.05	0.02	47.44	0.02	38.36
0.03	1.99	0.03	2.25	0.03	50.77	0.03	40.80
0.04	2.17	0.04	2.46	0.04	53.68	0.04	42.68
0.05	2.30	0.05	2.69	0.05	54.79	0.05	45.01
0.10	2.86	0.11	3.62	0.10	63.03	0.10	49.58
0.16	3.37	0.16	4.44	0.16	68.57	0.15	53.47
0.20	3.82	0.21	5.20	0.20	71.85	0.20	56.67
0.26	4.34	0.25	5.89	0.26	76.99	0.25	59.35
0.30	4.77	0.30	6.77	0.30	80.13	0.31	62.30
0.36	5.19	0.35	7.64	0.35	84.18	0.35	64.94
0.40	5.56	0.40	8.52	0.40	87.99	0.40	67.67
0.45	6.26	0.45	9.59	0.45	91.98	0.45	70.77
0.50	6.79	0.51	10.62	0.50	96.67	0.50	73.62
0.55	7.63	0.56	11.52	0.55	101.87	0.55	77.58
0.60	8.73	0.60	12.80	0.60	108.03	0.60	81.18
0.65	11.59	0.65	16.84	0.65	116.14	0.66	87.00
0.70	13.03	0.70	19.36	0.70	143.84	0.70	104.73
0.75	13.62	0.75	20.52	0.75	197.93	0.75	136.24
0.80	14.25	0.80	21.84	0.81	202.14	0.81	138.14
0.85	14.46	0.85	23.27	0.85	203.40	0.88	142.05
0.90	15.74	0.90	24.89	0.94	206.76	0.90	144.51
0.95	17.05	0.95	27.46	0.96	210.18	0.95	161.26
1.00	32.79	0.99	33.97	1.00	226.08	0.99	198.72
0.93	17.46	0.91	27.41	0.94	209.26	0.95	174.47
0.86	16.19	0.86	26.10	0.87	205.36	0.89	145.89
0.85	16.46	0.84	26.77	0.81	202.73	0.83	140.58
0.76	15.29	0.75	25.26	0.78	201.97	0.77	137.92
0.75	15.50	0.75	25.72	0.74	199.87	0.75	137.32
0.70	15.19	0.67	24.58	0.68	196.68	0.68	135.05
0.63	14.29	0.65	24.72	0.65	189.96	0.65	131.69
0.60	14.26	0.57	21.66	0.60	140.45	0.60	100.32
0.52	13.05	0.55	20.38	0.54	116.59	0.55	89.36
0.50	12.51	0.47	16.57	0.49	108.26	0.49	84.53
0.44	8.50	0.45	15.27	0.45	92.56	0.45	73.74
0.40	7.73	0.37	12.86	0.39	83.44	0.39	68.73
0.35	7.12	0.35	12.26	0.33	77.76	0.34	65.35
0.27	6.01	0.27	10.32	0.28	72.83	0.30	63.49
0.25	5.80	0.25	9.58	0.24	68.49	0.24	59.77
0.18	4.58	0.18	7.37	0.18	62.64	0.18	56.21
0.15	4.24	0.15	6.57	0.14	57.12	0.14	53.09
0.07	2.88	0.07	3.99	0.08	49.76	0.09	49.22
0.05	2.42	0.05	3.18	0.05	42.94	0.05	45.51
				0.04	39.76	0.04	43.71
				0.03	36.41	0.03	41.92
				0.02	34.00	0.02	40.67

Table C.34. Nitrogen Isotherms at 77K for SBA-15+Mg_i[1,H]-d, +Mg_i[2,H]-d, +Mg_i[sat,H]-d, +Co_i[1,H]-d, +Co_i[2,H]-d, +Co_i[sat,H]-d.

SBA-15+ Mg_i[1,H]-d		SBA-15+ Mg_i[2,H]-d		SBA-15+ Mg_i[sat,H]-d		SBA-15+ Co_i[1,H]-d		SBA-15+ Co_i[2,H]-d		SBA-15+ Co_i[sat,H]-d	
P/P_0	N_2 cc /g	P/P_0	N_2 cc /g	P/P_0	N_2 cc /g	P/P_0	N_2 cc /g	P/P_0	N_2 cc /g	P/P_0	N_2 cc /g
0.00	52.35	0.01	17.48	0.01	4.06	0.00	78.97	0.01	48.77	0.01	28.13
0.00	64.65	0.01	18.16	0.01	4.26	0.00	98.74	0.01	49.79	0.01	29.33
0.01	69.27	0.01	18.33	0.01	4.38	0.01	106.57	0.01	50.61	0.01	29.61
0.01	72.38	0.02	19.83	0.02	4.69	0.01	113.24	0.02	55.05	0.02	31.35
0.01	75.59	0.03	21.27	0.03	5.04	0.01	118.75	0.03	59.09	0.03	33.08
0.01	78.11	0.04	22.56	0.04	5.54	0.01	122.08	0.04	62.47	0.04	34.63
0.02	83.68	0.05	24.00	0.05	5.83	0.02	131.81	0.05	63.94	0.05	36.52
0.03	90.22	0.11	28.70	0.10	6.75	0.03	141.41	0.10	71.92	0.10	40.39
0.04	95.63	0.15	31.76	0.15	7.43	0.04	149.09	0.15	77.84	0.15	43.32
0.05	100.48	0.20	34.81	0.20	8.14	0.05	156.61	0.21	83.07	0.20	45.97
0.10	121.60	0.25	38.03	0.25	8.77	0.10	186.77	0.25	86.82	0.25	48.43
0.15	134.98	0.30	41.31	0.30	9.47	0.15	213.03	0.31	91.99	0.30	50.85
0.20	147.59	0.35	44.72	0.35	10.13	0.20	236.21	0.35	95.62	0.35	53.41
0.25	161.27	0.40	47.52	0.40	10.90	0.25	259.48	0.41	101.18	0.40	55.76
0.30	171.57	0.45	51.97	0.45	11.67	0.30	280.81	0.45	105.53	0.45	58.25
0.36	186.73	0.50	56.39	0.50	12.58	0.35	305.73	0.50	111.21	0.50	61.03
0.40	197.71	0.55	61.06	0.55	13.53	0.40	327.77	0.55	116.75	0.55	64.38
0.46	213.41	0.60	67.07	0.61	15.00	0.45	355.45	0.60	123.64	0.60	67.76
0.50	225.57	0.65	72.56	0.65	21.57	0.50	378.01	0.65	131.05	0.65	71.89
0.55	243.49	0.70	75.68	0.70	27.56	0.55	402.15	0.70	152.52	0.70	86.58
0.60	261.82	0.75	77.55	0.75	28.08	0.60	438.30	0.75	220.55	0.76	110.55
0.65	282.08	0.80	79.45	0.80	28.46	0.66	476.29	0.81	225.75	0.80	112.33
0.70	349.01	0.86	81.81	0.85	28.82	0.70	571.86	0.85	228.06	0.87	117.68
0.75	457.90	0.90	84.02	0.90	29.18	0.75	753.19	0.90	230.99	0.91	123.37
0.80	477.23	0.95	86.37	0.96	29.95	0.81	795.16	0.95	233.87	0.95	145.07
0.89	493.65	1.00	112.94	0.99	31.84	0.85	806.87	1.00	253.81	0.99	193.56
0.91	499.74	0.93	85.70	0.93	29.80	0.90	838.13	0.94	235.86	0.95	172.48
1.00	532.71	0.86	85.07	0.87	29.43	0.97	859.75	0.86	232.62	0.89	125.63
1.00	545.28	0.85	85.73	0.82	29.13	0.99	892.50	0.82	231.30	0.83	115.14
0.92	508.65	0.79	84.59	0.77	28.85	0.95	866.50	0.80	230.68	0.80	112.95
0.90	506.45	0.75	83.77	0.73	28.58	0.90	861.46	0.72	227.66	0.75	110.85
0.82	493.89	0.67	82.41	0.68	28.27	0.85	857.43	0.70	226.96	0.69	108.93
0.80	491.50	0.65	81.97	0.63	27.80	0.75	819.34	0.65	216.83	0.65	105.76
0.73	480.55	0.60	80.35	0.59	25.69	0.74	828.84	0.60	156.85	0.60	80.01
0.70	475.41	0.52	77.98	0.55	17.76	0.70	811.31	0.55	142.55	0.55	73.05
0.63	449.35	0.50	78.24	0.49	14.59	0.65	785.77	0.50	130.46	0.50	69.65
0.60	360.49	0.45	70.32	0.44	11.95	0.59	606.16	0.45	116.93	0.45	60.60
0.55	276.54	0.39	58.18	0.38	11.06	0.52	505.85	0.39	109.74	0.39	55.50
0.49	252.17	0.33	53.28	0.34	10.27	0.50	488.47	0.33	103.14	0.34	53.19
0.43	233.24	0.30	50.74	0.29	9.53	0.45	443.39	0.28	97.79	0.30	50.86
0.40	223.83	0.23	44.28	0.24	8.80	0.40	413.46	0.23	92.41	0.25	48.37
0.33	202.69	0.18	40.51	0.19	8.01	0.33	362.83	0.18	86.85	0.20	45.91
0.30	193.17	0.14	37.76	0.14	7.22	0.30	350.46	0.14	80.95	0.15	43.20
0.23	172.34	0.10	33.96	0.08	6.28	0.25	321.31	0.09	73.16	0.10	40.17
0.18	155.95	0.04	28.04	0.05	5.48	0.18	267.63	0.05	66.41	0.05	35.96
0.13	139.77					0.15	254.20	0.04	63.13		
0.08	120.51					0.08	198.81	0.03	59.98		
0.05	104.48					0.05	169.83	0.02	57.76		

Table C.35. Nitrogen Isotherms at 77K for SBA-15+Mg_w[1,E]-d, +Mg_i[1,E]-d, +Co_w[1,E]-d, +Co_i[1,E]-d.

SBA-15+ Mg_w[1,E]-d		SBA-15+ Mg_i[1,E]-d		SBA-15+ Co_w[1,E]-d		SBA-15+ Co_i[1,E]-d	
P/P_0	N_2 cc /g	P/P_0	N_2 cc /g	P/P_0	N_2 cc /g	P/P_0	N_2 cc /g
0.00	1.92	0.01	7.33	0.01	56.76	0.00	10.53
0.00	2.29	0.01	7.38	0.01	58.18	0.00	29.39
0.01	2.33	0.01	7.50	0.01	58.55	0.01	33.42
0.01	2.57	0.02	8.06	0.02	62.82	0.01	37.28
0.01	2.99	0.03	8.75	0.03	68.50	0.01	39.63
0.01	3.06	0.04	9.38	0.04	71.73	0.01	40.16
0.02	3.92	0.05	10.06	0.05	77.21	0.02	43.51
0.03	4.83	0.10	12.07	0.10	89.59	0.03	47.55
0.04	5.85	0.15	14.04	0.15	101.99	0.04	50.71
0.05	7.72	0.21	16.26	0.20	106.32	0.05	54.53
0.10	14.42	0.25	18.10	0.25	120.28	0.10	69.80
0.15	21.57	0.30	20.25	0.30	127.93	0.15	83.29
0.20	28.64	0.35	22.49	0.35	139.78	0.20	96.18
0.25	36.26	0.40	25.07	0.40	145.74	0.25	107.84
0.30	45.35	0.45	27.50	0.45	163.84	0.30	119.43
0.35	53.68	0.50	30.22	0.50	169.13	0.35	132.43
0.40	63.38	0.55	33.30	0.55	196.51	0.40	142.90
0.45	75.42	0.60	36.29	0.60	205.49	0.45	156.18
0.50	85.79	0.65	40.79	0.65	237.09	0.51	172.60
0.55	99.26	0.70	44.05	0.70	314.82	0.55	184.51
0.60	111.49	0.75	46.34	0.75	417.38	0.60	197.48
0.66	138.23	0.80	48.56	0.80	434.36	0.65	214.22
0.70	151.60	0.85	50.34	0.85	431.15	0.70	250.08
0.75	164.99	0.90	50.56	0.90	456.57	0.75	337.23
0.80	177.72	0.96	54.00	0.95	453.71	0.81	356.35
0.86	195.90	0.99	60.81	1.00	537.38	0.85	362.70
0.90	207.38	0.95	54.54	0.91	464.92	0.91	376.58
0.95	225.00	0.89	54.35	0.90	493.74	0.95	381.89
0.99	262.56	0.84	53.56	0.85	496.50	0.99	405.22
0.91	224.14	0.79	52.57	0.80	473.42	0.91	381.36
0.90	225.69	0.74	51.61	0.75	467.88	0.90	380.98
0.81	210.11	0.69	50.57	0.70	476.16	0.85	375.62
0.80	211.28	0.65	48.71	0.65	452.72	0.80	365.15
0.75	204.99	0.60	48.44	0.60	432.97	0.75	360.82
0.67	188.97	0.55	46.94	0.55	415.43	0.70	350.03
0.65	184.64	0.50	44.71	0.50	396.05	0.65	335.47
0.60	175.32	0.45	39.12	0.45	229.64	0.59	248.39
0.53	149.20	0.40	33.16	0.37	208.64	0.54	215.09
0.50	143.25	0.35	29.89	0.35	195.70	0.50	203.62
0.43	122.12	0.30	26.42	0.30	183.49	0.43	172.47
0.40	115.20	0.25	23.28	0.25	164.01	0.40	164.76
0.32	95.37	0.20	21.21	0.17	132.23	0.33	143.78
0.30	88.32	0.15	18.18	0.15	121.26	0.30	137.40
0.23	69.43	0.10	14.59	0.07	83.82	0.24	117.39
0.18	53.98	0.05	10.56	0.05	70.50	0.20	107.62
0.15	47.28					0.13	85.26
0.08	23.77					0.10	76.55
0.05	16.70					0.04	50.98

Table C.36. Carbon Dioxide Isotherms at 25°C for Samples Interrogated with Toxic Gases, SBA-15, +Mg_w[1,H]-d, +Co_w[1,H]-d, +Mg_i[2,E]-d, and +Co_i[2,E]-d.

P bar	CO_2 mmol /g	P bar	CO_2 mmol /g	P bar	CO_2 mmol /g	P bar	CO_2 mmol /g	P bar	CO_2 mmol /g
0.00	0.00	0.00	0.01	0.00	0.00	0.00	0.00	0.00	0.00
0.02	0.03	0.02	0.02	0.03	0.04	0.02	0.02	0.02	0.05
0.12	0.14	0.11	0.08	0.11	0.15	0.11	0.08	0.11	0.15
0.50	0.47	0.51	0.27	0.51	0.45	0.51	0.25	0.51	0.39
1.01	0.81	1.01	0.42	1.01	0.71	1.00	0.42	1.00	0.59
1.51	1.08	1.51	0.55	1.50	0.91	1.50	0.56	1.50	0.73
2.00	1.31	2.01	0.66	2.00	1.07	2.01	0.68	2.01	0.86
2.51	1.53	2.51	0.76	2.51	1.22	2.51	0.79	2.51	0.96
3.01	1.72	3.01	0.86	3.01	1.35	3.01	0.89	3.01	1.06
3.51	1.90	3.51	0.96	3.50	1.47	3.50	0.98	3.51	1.15
4.00	2.06	4.01	1.03	4.00	1.57	4.00	1.08	4.01	1.23
4.50	2.22	4.51	1.12	4.50	1.67	4.50	1.16	4.51	1.30
5.00	2.37	5.01	1.19	5.00	1.77	5.00	1.24	5.00	1.37
4.00	2.06	4.00	1.07	4.00	1.58	4.00	1.09	4.00	1.23
3.00	1.71	3.00	0.90	3.00	1.35	3.00	0.92	3.00	1.07
2.00	1.31	2.00	0.71	2.00	1.08	2.00	0.71	2.00	0.87
1.00	0.80	1.00	0.48	1.00	0.71	1.00	0.47	1.00	0.61
0.50	0.47	0.50	0.32	0.50	0.46	0.50	0.30	0.50	0.41
0.00	0.01	0.00	0.09	0.00	0.01	0.00	0.04	0.00	0.07

C.6. Metal Oxide-MOF-74 Systems

Table C.37. Nitrogen Isotherms at 77K for Co-MOF-74 and MO-Co-MOF-74's.

Co-MOF-74		[1/4Mg](Co-M74)		[1/4Co](Co-M74)		[1/2Mg](Co-M74)		[1/2Co](Co-M74)	
P/P_0	N_2 cc /g	P/P_0	N_2 cc /g	P/P_0	N_2 cc /g	P/P_0	N_2 cc /g	P/P_0	N_2 cc /g
0.01	230.33	0.00	234.51	0.00	168.22	0.00	606.00	0.00	338.31
0.01	231.60	0.00	236.97	0.01	178.58	0.01	622.48	0.01	347.37
0.01	233.18	0.01	239.41	0.01	186.73	0.01	628.99	0.01	351.36
0.01	234.69	0.01	241.36	0.01	190.51	0.01	635.59	0.01	354.61
0.01	235.72	0.01	242.64	0.01	193.36	0.01	639.27	0.01	356.89
0.02	237.93	0.02	245.01	0.02	197.38	0.02	649.73	0.02	360.86
0.03	239.83	0.03	247.12	0.03	200.82	0.03	660.82	0.03	364.61
0.04	241.46	0.04	249.06	0.04	204.48	0.04	669.36	0.04	367.70
0.05	243.50	0.05	251.00	0.05	208.36	0.05	679.57	0.05	371.46
0.10	248.17	0.10	257.14	0.10	217.48	0.10	710.73	0.10	382.44
0.15	251.74	0.15	262.77	0.15	227.49	0.15	735.44	0.15	390.51
0.20	255.26	0.20	267.69	0.20	235.96	0.21	765.42	0.20	401.36
0.25	258.18	0.25	274.23	0.25	247.57	0.25	788.44	0.25	409.77
0.30	260.42	0.30	280.27	0.30	257.11	0.30	809.58	0.30	418.32
0.35	263.77	0.35	285.59	0.35	270.39	0.35	833.05	0.35	429.44
0.40	266.72	0.40	293.43	0.40	279.86	0.40	859.14	0.40	437.58
0.45	268.72	0.45	298.75	0.45	294.01	0.45	882.05	0.45	448.16
0.50	272.74	0.50	307.50	0.50	303.18	0.50	915.85	0.50	462.16
0.56	275.94	0.55	316.13	0.56	321.96	0.55	936.72	0.55	470.07
0.61	278.53	0.60	326.75	0.60	334.69	0.60	967.69	0.60	484.74
0.65	281.23	0.65	332.32	0.65	352.92	0.65	999.86	0.65	493.03
0.70	285.41	0.70	343.97	0.70	362.78	0.70	1016.64	0.70	503.54
0.76	284.26	0.75	355.04	0.75	381.33	0.76	1053.42	0.75	520.93
0.80	291.48	0.81	369.07	0.81	403.22	0.80	1080.29	0.81	530.67
0.85	296.21	0.85	375.80	0.85	427.12	0.85	1092.77	0.88	547.44
0.90	297.79	0.91	392.07	0.90	438.36	0.91	1137.14	0.91	554.29
0.95	302.40	0.95	405.13	0.95	465.36	0.95	1162.56	0.95	565.41
0.99	305.17	1.00	536.45	1.00	604.88	0.99	1268.29	0.99	601.12
0.91	301.94	0.95	419.92	0.94	471.68	0.92	1153.09	0.91	557.18
0.90	303.98	0.86	406.46	0.86	458.41	0.86	1135.91	0.89	561.72
0.81	299.42	0.84	406.39	0.84	460.18	0.84	1131.36	0.81	537.85
0.80	300.97	0.78	399.41	0.77	436.07	0.80	1106.40	0.79	543.78
0.75	299.76	0.75	394.15	0.75	434.05	0.75	1084.60	0.75	529.82
0.70	297.68	0.67	380.54	0.67	414.30	0.68	1051.89	0.67	518.92
0.62	293.49	0.65	377.24	0.65	407.70	0.65	1048.32	0.65	513.70
0.60	290.54	0.58	363.65	0.57	384.45	0.57	1009.26	0.57	499.79
0.55	288.68	0.52	351.25	0.55	379.20	0.55	1002.74	0.55	496.30
0.47	284.32	0.50	347.19	0.48	357.43	0.47	965.84	0.47	482.66
0.45	282.78	0.43	333.29	0.45	351.34	0.45	952.03	0.45	477.32
0.39	279.01	0.40	325.07	0.38	327.08	0.40	917.91	0.40	466.30
0.32	273.46	0.33	308.64	0.35	319.49	0.32	873.74	0.33	450.31
0.30	271.14	0.30	303.14	0.27	298.60	0.30	860.29	0.30	440.10
0.22	265.12	0.23	288.05	0.25	291.62	0.22	807.42	0.23	422.74
0.20	262.38	0.20	284.23	0.18	272.41	0.20	789.28	0.20	416.10
0.12	254.21	0.12	270.86	0.12	257.59	0.12	736.14	0.12	399.88
0.10	251.72	0.10	266.67	0.10	251.62	0.10	716.47	0.10	394.55
0.03	240.84	0.04	256.82	0.04	237.03	0.04	667.04	0.05	381.14
0.01	232.76	0.01	247.91	0.01	225.09	0.01	609.98	0.01	363.33

Table C.38. Nitrogen Isotherms at 77K for Mg-MOF-74 and MO-Mg-MOF-74's.

Mg-MOF-74		[1/4Mg](Mg-M74)		[1/4Co](Mg-M74)		[1/2Mg](Mg-M74)		[1/2Co](Mg-M74)	
P/P_0	N_2 cc /g	P/P_0	N_2 cc /g	P/P_0	N_2 cc /g	P/P_0	N_2 cc /g	P/P_0	N_2 cc /g
0.00	258.02	0.01	132.02	0.00	194.71	0.00	168.91	0.01	111.63
0.01	262.18	0.01	126.68	0.01	198.41	0.00	172.35	0.01	111.82
0.01	266.04	0.01	122.26	0.01	201.37	0.01	175.44	0.01	112.45
0.01	269.29	0.01	115.28	0.01	203.55	0.01	177.54	0.01	113.14
0.01	271.51	0.02	107.24	0.01	204.77	0.01	178.62	0.01	113.62
0.02	276.39	0.02	101.71	0.02	207.99	0.02	181.33	0.02	115.41
0.03	280.02	0.03	95.32	0.03	210.56	0.03	183.76	0.03	117.10
0.04	284.93	0.04	92.84	0.04	214.27	0.04	186.56	0.04	118.82
0.05	287.64	0.05	89.12	0.05	216.38	0.05	188.77	0.05	120.46
0.10	298.03	0.10	93.98	0.10	226.39	0.10	197.77	0.10	127.64
0.15	304.76	0.15	99.87	0.15	234.52	0.15	204.06	0.15	133.58
0.20	312.24	0.20	101.98	0.20	243.05	0.20	211.58	0.20	139.62
0.25	316.77	0.25	103.90	0.25	252.05	0.25	217.59	0.25	145.77
0.30	322.62	0.30	106.76	0.30	261.12	0.30	227.46	0.30	152.52
0.35	328.74	0.35	115.62	0.35	270.27	0.35	233.66	0.35	157.23
0.40	334.51	0.40	117.01	0.40	279.52	0.40	244.34	0.40	163.02
0.45	342.17	0.45	125.66	0.45	292.87	0.45	250.21	0.45	169.40
0.50	346.48	0.50	128.24	0.50	306.94	0.50	258.41	0.50	179.95
0.55	354.56	0.55	134.72	0.55	315.95	0.55	270.02	0.55	184.22
0.60	358.97	0.60	143.11	0.60	332.97	0.60	280.35	0.60	195.73
0.65	365.64	0.65	159.16	0.65	341.24	0.65	290.45	0.65	201.27
0.70	371.81	0.70	164.51	0.70	353.69	0.70	298.79	0.70	214.84
0.75	375.52	0.75	186.57	0.75	372.19	0.75	307.91	0.75	221.66
0.80	387.81	0.80	196.58	0.80	387.53	0.80	323.76	0.81	239.93
0.86	390.93	0.86	224.06	0.85	401.96	0.85	335.34	0.85	244.65
0.90	403.31	0.90	238.62	0.91	426.09	0.93	358.71	0.95	273.29
0.95	410.30	0.96	564.29	0.95	438.01	0.96	366.25	0.97	287.79
1.00	503.03	0.99	2683.86	1.00	584.81	1.00	530.07	0.99	311.16
0.92	409.38	0.95	403.86	0.93	442.28	0.93	380.01	0.95	292.97
0.89	406.72	0.87	300.26	0.90	440.99	0.86	362.92	0.86	283.21
0.85	403.90	0.85	296.27	0.81	429.31	0.85	363.98	0.84	288.35
0.80	402.62	0.76	258.08	0.80	420.69	0.76	350.91	0.80	279.24
0.75	394.04	0.75	259.66	0.72	407.01	0.75	350.70	0.74	277.71
0.70	390.63	0.68	232.18	0.70	407.31	0.67	338.66	0.70	270.58
0.62	380.10	0.65	220.69	0.65	402.10	0.65	335.07	0.65	264.31
0.59	380.89	0.57	180.08	0.57	380.50	0.60	328.21	0.57	248.55
0.55	374.62	0.55	170.56	0.55	377.77	0.54	313.64	0.55	244.82
0.47	363.45	0.50	133.18	0.47	356.88	0.48	298.23	0.47	228.10
0.44	360.35	0.44	89.12	0.45	348.58	0.45	293.09	0.45	223.15
0.40	353.15	0.40	55.26	0.37	325.75	0.37	272.43	0.37	203.12
0.32	341.41	0.32	6.04	0.35	320.19	0.35	264.86	0.35	197.88
0.30	338.15	0.30	-38.00	0.28	297.38	0.30	254.46	0.30	187.64
0.22	325.70	0.23	-96.20	0.25	288.22	0.23	235.83	0.22	169.26
0.20	323.05	0.20	-133.27	0.18	262.81	0.20	230.03	0.20	162.50
0.12	307.79	0.13	-195.73	0.15	254.80	0.13	211.60	0.12	142.01
0.10	302.67	0.10	-218.61	0.08	225.42	0.10	206.06	0.10	136.08
0.05	290.52	0.04	-260.73	0.05	216.11	0.04	188.71	0.04	116.96
0.01	268.76	0.01	-312.22	0.01	194.70	0.01	173.83	0.01	103.12

Table C.39. Carbon Dioxide and Carbon Monoxide Isotherms for Co-MOF-74 and Mg-MOF-74.

Co-MOF-74				Mg-MOF-74			
CO₂, 25°C		CO, 25°C		CO₂, 25°C		CO, 25°C	
P	CO	P	CO	P	CO	P	CO
bar	mmol / g	bar	mmol / g	bar	mmol / g	bar	mmol / g
0.00	0.00	0.00	0.00	0.00	0.00	0.00	0.00
0.06	1.35	0.07	3.04	0.03	2.16	0.17	0.91
0.38	4.00	0.38	4.04	0.41	3.72	0.46	1.66
0.90	5.19	0.86	4.34	0.94	4.45	0.89	2.23
1.96	6.44	1.56	4.58	1.98	5.48	1.56	2.79
3.32	7.53	3.03	5.01	3.34	6.46	3.02	3.55
4.80	8.38	4.85	5.49	4.81	7.29	4.83	4.24
5.63	8.77	5.44	5.65	5.63	7.69	5.43	4.43

Table C.40. Carbon Dioxide and Carbon Monoxide Isotherms for [1/2Co](Co-MOF-74) and [1/2Mg](Co-MOF-74).

CO₂, 25°C		CO, 25°C		CO₂, 25°C		CO, 25°C	
P	CO	P	CO	P	CO	P	CO
bar	mmol / g	bar	mmol / g	bar	mmol / g	bar	mmol / g
0.00	0.00	0.00	0.00	0.00	0.00	0.00	0.00
0.17	2.25	0.19	2.46	0.15	1.89	0.17	2.38
0.55	3.68	0.59	2.84	0.52	3.22	0.58	2.80
0.93	4.36	1.03	3.05	0.91	3.83	1.02	2.99
2.04	5.56	1.99	3.34	2.01	4.92	1.99	3.27
3.47	6.61	3.36	3.71	3.44	5.86	3.36	3.64
4.87	7.37	4.98	4.13	4.85	6.56	4.97	4.03
5.46	7.65			5.44	6.82		

Table C.41. Carbon Dioxide and Carbon Monoxide Isotherms for [1/4Co](Co-MOF-74) and [1/4Mg](Co-MOF-74).

CO₂, 25°C		CO, 25°C		CO₂, 25°C		CO, 25°C	
P	CO	P	CO	P	CO	P	CO
bar	mmol / g	bar	mmol / g	bar	mmol / g	bar	mmol / g
0.00	0.00	0.00	0.00	0.00	0.00	0.00	0.00
0.22	3.22	0.07	2.65	0.22	2.78	0.06	2.34
0.58	4.63	0.39	3.47	0.57	3.97	0.37	3.18
1.05	5.52	0.94	3.81	1.04	4.76	0.92	3.48
2.17	6.89	2.28	4.27	2.16	5.96	2.27	3.89
3.85	8.27	3.92	4.71	3.84	7.19	3.90	4.28
5.26	9.14	5.35	5.11	5.24	7.96	5.33	4.62

Table C.42. Carbon Dioxide and Carbon Monoxide Isotherms for[1/4Co](Mg-MOF-74) and [1/4Mg](Mg-MOF-74).

CO_2, 25°C		CO, 25°C		CO_2, 25°C		CO, 25°C	
P	CO	P	CO	P	CO	P	CO
bar	mmol / g	bar	mmol / g	bar	mmol / g	bar	mmol / g
0.00	0.00	0.00	0.00	0.00	0.00	0.00	0.00
0.22	2.49	0.16	0.72	0.27	2.53	0.17	0.85
0.55	3.03	0.50	1.38	0.59	3.11	0.52	1.56
0.93	3.44	0.85	1.74	0.96	3.59	0.87	2.01
2.19	4.40	1.85	2.35	2.21	4.77	1.87	2.79
3.54	5.11	3.16	2.86	3.56	5.73	3.17	3.55
5.07	5.81	4.38	3.24	5.08	6.73	4.38	4.09
		5.27	3.48			5.27	4.50